

Syracuse University

## SURFACE at Syracuse University

---

Dissertations - ALL

SURFACE at Syracuse University

---

1-24-2024

# Exploring the Electrochemical Performance of Calcium-Ion Batteries With Novel Cathodes and Electrolytes

Paul Alexis Chando  
*Syracuse University*

Follow this and additional works at: <https://surface.syr.edu/etd>

 Part of the [Chemical Engineering Commons](#)

---

### Recommended Citation

Chando, Paul Alexis, "Exploring the Electrochemical Performance of Calcium-Ion Batteries With Novel Cathodes and Electrolytes" (2024). *Dissertations - ALL*. 1843.  
<https://surface.syr.edu/etd/1843>

This Dissertation is brought to you for free and open access by the SURFACE at Syracuse University at SURFACE at Syracuse University. It has been accepted for inclusion in Dissertations - ALL by an authorized administrator of SURFACE at Syracuse University. For more information, please contact [surface@syr.edu](mailto:surface@syr.edu).

# ABSTRACT

The development of electric vehicles and energy storage devices are part of larger international efforts to create a sustainable future. Lithium-ion batteries have become crucial components to powering these technologies. However, the growing dependence of this singular battery chemistry to power an ever expanding landscape of technologies raises sustainability issues around lithium. Exploration of alternate battery chemistries have become part of research efforts to meet global energy demands. Calcium has emerged as one such battery system that could help alleviate stresses placed on lithium with its energy density and cost. Battery chemistries are unique, and each battery possesses its own set of challenges. Regarding calcium, one such challenge is the identification of suitable cathodes. Open framework oxides, based on previous work, have been identified as the most promising cathode structures for calcium intercalation chemistry. However, many oxides have yet to be experimentally evaluated. In addition to the issues surrounding cathodes for calcium batteries, another challenge surrounding calcium chemistry is the use of suitable electrolytes that would allow for calcium metal to be used as anodes. Calcium electrolytes form passivation layers on calcium metal electrodes that quickly prevent any calcium diffusion from occurring in the battery. Recent efforts on calcium electrolytes have focused on engineering the solid electrolyte interphase to form phases that are more accommodating with calcium diffusion. This dissertation describes my efforts at experimentally exploring two cathodes for calcium-ion batteries along with an effort at engineering the solid electrolyte interphase for calcium batteries by using an electrolyte that is not native to calcium.

The electrochemical activity within a cathode, when using intercalation chemistry, produces structural changes to the electrode that can be tracked with x-ray diffraction (XRD). My first

project with this dissertation was focused on the design and fabrication of an in situ XRD cell that could track the structural changes to a cathode as it was cycled. I implemented a glassy carbon window that would be transparent to x-rays and validated the functionality of the cell with an established battery system for intercalation chemistry. Lithium Cobalt Oxide ( $\text{LiCoO}_2$ ) was cycled against a lithium metal anode within the in situ cell. The cell was cycled at a rate of C/40 and achieved reversible capacities of 32 mAh/g. Structural changes to the (003), (101), (009), (107) and (018) lattice planes were tracked with the in situ cell and validated its functionality.

My following efforts were aimed at evaluating the electrochemical activity of calcium manganese oxide ( $\text{CaMn}_2\text{O}_4$ ) post-spinel and its capacity to function as a cathode for calcium-ion batteries. The  $\text{CaMn}_2\text{O}_4$  post-spinel cathode was synthesized using a solid-state synthesis method and verified with XRD. The electrochemical activity of the cathode was first analyzed with cyclic voltammetry and galvanostatic cycling. Oxidation potentials of the cathode were identified at 0.2 and 0.5 V while broad insertion potentials were identified at -1.5 V. A maximum charge of the cathode was performed at a rate of C/200, yielding a maximum capacity of 100 mAh/g. Structural characterization of the electrode was performed and compared to theoretical models, confirming the redox activity of the cathode. Cycling capabilities of the cathode were also performed in coin cell configurations. Using a c-rate of C/33, the cathode was measured to reversibly cycle 52 mAh/g and was further verified with Energy-Dispersive X-ray Spectroscopy (EDS) and X-ray Photoelectron Spectroscopy (XPS). The results from the evaluation revealed that  $\text{CaMn}_2\text{O}_4$  is a promising cathode for calcium-ion batteries.

Beyond the successful cycling of  $\text{CaMn}_2\text{O}_4$ , the next goal of my dissertation was focused on a similar line of testing with calcium iron oxide ( $\text{CaFe}_2\text{O}_4$ ). The  $\text{CaFe}_2\text{O}_4$  post-spinel was synthesized through an auto-combustion route and its phase was also verified with XRD. Cyclic

voltammetry studies were performed on the cathode and reported limited oxidative behavior at approximately 0.3 V and was not reproduced on subsequent CV cycles. There was no reinsertion activity observed with the post-spinel. Galvanostatic cycling of the cathode was also performed on  $\text{CaFe}_2\text{O}_4$  at a c-rate of C/100, cycling a capacity of 50 mAh/g. Postmortem XRD of the cathode revealed one structural development within the crystal structure of  $\text{CaFe}_2\text{O}_4$  that aligned with theoretical calculations of the post-spinel. The data collected on  $\text{CaFe}_2\text{O}_4$  concluded that this cathode had limited electrochemical activity and would not be a feasible candidate for calcium-ion batteries.

The last efforts of my dissertation were focused on addressing SEI issues that occur when using calcium metal anodes with calcium electrolytes. Previous research on designing SEIs for calcium batteries have used alternate electrolytes to produce phases that are more ionically conductive. My project was aimed at using a similar strategy, immersing calcium metal electrodes in a potassium electrolyte and cycle charge. Using potassium hexafluorophosphate ( $\text{KPF}_6$ ) in a ternary mixture of carbonate solvents, calcium symmetrical cells were cycled with a charge density of  $0.025 \text{ mA/cm}^2$  with a capacity of  $0.15 \text{ mAh/cm}^2$  for over 200 hours. Throughout plating and stripping, overpotentials were maintained below 1.8 V. The phases formed in the SEI were a combination of permanent and transient phases that were verified with XRD, EDS and Fourier Transform Infrared (FTIR) spectroscopy. Increased cycling of calcium in the symmetrical cells was further verified with in situ Raman spectroscopy and the calcium content was measured with inductively coupled plasma mass spectrometry (ICP-MS). The results confirm the effectiveness of potassium electrolytes being used to tailor a hybrid SEI for calcium plating and maintaining cycling stability throughout testing.

In summary, the contributions in this dissertation offer an experimental evaluation of cathodes for calcium-ion batteries along with identifying a new electrolyte to be used for engineering interphases. These findings can offer better insights for future strategies with calcium batteries.

EXPLORING THE ELECTROCHEMICAL PERFORMANCE OF CALCIUM-ION  
BATTERIES WITH NOVEL CATHODES AND ELECTROLYTES

by

Paul Alexis Chando

B.S., Rensselaer Polytechnic Institute, 2009

M.S., CUNY City College, 2013

Dissertation

Submitted In Partial Fulfillment of the Requirements for the Degree of

DOCTOR OF PHILOSOPHY IN CHEMICAL ENGINEERING

Syracuse University

December 2023

Copyright © Paul Alexis Chando, 2023  
All Rights Reserved

## ACKNOWLEDGEMENTS

I would like to start by thanking my advisor, Dr. Ian Dean Hosein, for all his help during my time at Syracuse University. He took a risk on me and let me transfer into his lab at the end 2019. Since I started in his lab, he has provided continuous support on my numerous projects, building up my confidence as a researcher and professional. His collaborative nature towards research always provided a safe space to explore ideas and to embrace the mistakes that eventually lead to successful projects. He's given me opportunities not only to improve my research skills, but to also mentor students in the lab and grow as a leader. He has been a terrific mentor and I will always be grateful for all he has taught me.

I would also like to thank my defense committee, Dr. Jesse Bond, Dr. Shikha Nangia, Dr. Viktor Cybulskis, Dr. Theodore Walker, and Dr. Jay Thomas for serving as chair. I want to thank Dr. Viktor Cybulskis for his help with his X-ray diffractometer. He not only gave me access to his Rigaku diffractometer, which was critical to my work, but also helped provide insights that were critical to the successful design of my in situ cell and its operation.

I am thankful for the help provided by Dr. Manuel Smeu and his student Sihe Chen of Binghamton University. They were instrumental in performing the theoretical calculations in my dissertation. The theoretical XRD patterns generated from their work provided critical information to compare my experimental work and I am thankful for how helpful and accommodating they have been with helping me refine my work.

I'd also like to thank Dr. Jon Zubieta for letting me audit his class and giving me a crash course in crystallography. It was a terrific learning experience that gave me a deeper appreciation for the nuances involved with x-ray diffraction.

I want to acknowledge the staff at Syracuse University. Jason Markle, Amelia Rae Forbes and Emilia Stojanovski of the Biomedical and Chemical Engineering Department have always been extremely helpful during my time at Syracuse and have made navigating all aspects of administrative tasks an easy process. I also want to acknowledge William Dossert. He has been a brilliant machinist and friend to me during my time at Syracuse University. Working with him has been a re-education on properly designing equipment. He helped me become a better designer and engineer. The success of the in situ cell is heavily credited to him and all the iterations he helped build.

The research projects in this dissertation would not have been possible without the funding support from The Syracuse Center of Excellence (CoE) and the National Science Foundation (NSF) under grant number CMMI-1751621. I would also like to acknowledge the support provided by the research assistantships from the College of Engineering and Computer Science at Syracuse University. Analysis of calcium cathodes with x-ray photoelectron spectroscopy (XPS) was performed at Cornell University and I would like to acknowledge the Cornell Center for Materials Research Shared Facilities, which is supported by the NSF MRSEC program (DMR-1719875). I also want to thank Dr. John Wright of Cornell University for performing XPS analysis with my samples and providing feedback on all my questions regarding XPS analysis.

My research in the Hosein lab would not have been as successful without the help from the great colleagues I have worked with. Dr. Shreyas Pathreker was instrumental in helping me get started in the lab and was always a great sounding board for ideas. I would also like to thank Dr. Fran Genier. She always brought such enormous positivity to the lab and with every project she worked on. I also want to acknowledge Xinlu Wang. Working with her in the lab has been such a positive and collaborative experience. She has always been willing to help with all aspects of research and

lab maintenance. Dr. Robson Schuarca has been in the trenches with me since we both started in Fall 2017. We've spent the past six years encouraging each other with our research projects and always trying to enjoy all that Syracuse has to offer when we weren't in lab. It's been great walking through this journey with him as a comrade. I am also immensely grateful for the talented undergraduate students I have worked with during my time in the Hosein lab. Jacob Shellhamer and Elizabeth Wall were the first undergraduate students I mentored, and they were both instrumental in helping create a foundation for my research. Gabriel Quintero has been another exceptional student in the lab, and I am thankful for his work on the various projects I had him help me with.

I am grateful to Dr. Shelby Buffington who has been a terrific friend throughout my time at Syracuse University and helped me maintain my sanity throughout the PhD process. She has always been effective at giving me an objective opinion on the many projects and hurdles I have had to overcome. Similarly, I would also like to acknowledge Justin Siefker of University College London. I've known Justin since we were undergraduates at Rensselaer Polytechnic Institute, and he has always been a source of encouragement with all my projects. I am thankful for knowing him all these years.

I would also like to thank my advisor during my time at The City College of New York, Dr. Daniel Steingart. He has been a great mentor and a great friend with helping me navigate several challenging moments in my life.

Lastly, I want to thank my family. My parents, Brigitte Courty and Arnaud Thieffry, have always been a foundation of incredible support and always believed in what I was capable of accomplishing. My brother, Marc Chando, has always given me a sense of belonging and has been so generous with sharing advice and knowledge with me. I also want to thank my sister-in-law,

Sandra Restrepo, for her love and kindness. I am extremely grateful to my nephew, Connor Chando, who has given me so many reasons to smile and be happy. I want to thank my grandfather, Jacques Courty, for introducing me to what is so beautiful about engineering. I would not be finishing my doctorate today if it wasn't for the love and support you all gave me throughout this journey. Thank you all!

# **DEDICATION**

I dedicate this dissertation to my family.

# TABLE OF CONTENTS

CHAPTER 1 GENERAL INTRODUCTION .....	1
1.1 Introduction.....	2
1.2 Lithium-Ion Batteries.....	4
1.3 Next Generation Batteries.....	7
1.4 Cathodes for Calcium-Ion Batteries.....	9
1.5 Electrolytes for Calcium-Ion Batteries .....	13
1.6 Outline of Dissertation.....	15
References.....	19
CHAPTER 2 DESIGN AND VALIDATION OF IN SITU X-RAY DIFFRACTION CELL.....	26
2.1 Introduction.....	27
2.2 Materials and Methods.....	29
2.2.1 Materials .....	29
2.2.2 Electrode Preparation.....	30
2.2.3 Electrolyte Preparation.....	30
2.2.4 Electrochemistry .....	30
2.2.5 Electrode Characterization.....	31
2.2.6 In situ Cell and Sample Holder Design.....	31
2.3 Results and Discussion .....	35
2.4 Conclusion .....	39
Supplemental Information .....	40
References.....	58
CHAPTER 3 EXPLORING CALCIUM MANGANESE OXIDE AS A PROMISING CATHODE MATERIAL FOR CALCIUM-ION BATTERIES.....	61
3.1 Introduction.....	62

3.2 Experimental Section .....	64
3.2.1 Materials .....	64
3.2.2 Synthesis of $\text{CaMn}_2\text{O}_4$ .....	64
3.2.3 Electrode Preparation .....	65
3.2.4 Electrolyte Preparation .....	66
3.2.5 Electrochemistry .....	67
3.2.6 Electrode Characterization .....	68
3.2.7 Ab-Initio Calculations .....	69
3.3 Results and Discussion .....	69
3.4 Conclusion .....	82
Supplemental Information .....	84
References .....	100
<b>CHAPTER 4 A STUDY OF CALCIUM ION INTERCALATION IN POST-SPINEL CALCIUM IRON OXIDE .....</b>	<b>107</b>
4.1 Introduction .....	108
4.2 Materials and Methods .....	110
4.2.1 Materials .....	110
4.2.2 Synthesis of $\text{CaFe}_2\text{O}_4$ .....	110
4.2.3 Electrode Preparation .....	111
4.2.4 Electrolyte Preparation .....	112
4.2.5 Electrochemistry .....	112
4.2.6 Electrode Characterization .....	113
4.2.7 Ab-Initio Calculations .....	114
4.3 Results and Discussion .....	114
4.4 Conclusion .....	124

Supplemental Information .....	126
References.....	128
CHAPTER 5 PLATING AND STRIPPING CALCIUM METAL IN POTASSIUM HEXAFLUOROPHOSPHATE ELECTROLYTE TOWARDS A STABLE HYBRID SOLID ELECTROLYTE INTERPHASE.....	132
5.1 Introduction.....	133
5.2 Experimental Section .....	134
5.2.1 Materials .....	134
5.2.2 Electrolyte Preparation.....	135
5.2.3 Electrode Preparation.....	135
5.2.4 Electrochemistry .....	136
5.2.5 Electrode Characterization.....	137
5.3 Results and Discussion .....	138
5.4 Conclusion .....	149
Supplemental Information .....	151
References.....	154
CHAPTER 6 CONCLUSIONS AND FUTURE WORK.....	158
6.1 Conclusions.....	159
6.2 Future Work .....	161
6.2.1 Synthesis of $\text{Ca}_{0.66}\text{Mn}_{1.4}\text{Fe}_{0.6}\text{O}_4$ .....	163
Materials .....	163
Synthesis .....	163
Results.....	164
References.....	166
APPENDICES .....	168
APPENDIX I: PERMISSION FROM ACS PUBLICATION FOR FIGURE 1.1 .....	169

APPENDIX II: PERMISSION FROM ACS PUBLICATION FOR FIGURE 1.2 .....	170
APPENDIX III: PERMISSION FROM ACS CHEMISTRY OF MATERIALS FOR PUBLISHED ARTICLE.....	171
APPENDIX IV: PERMISSION FROM ACS APPLIED ENERGY MATERIALS FOR PUBLISHED ARTICLE.....	173
CURRICULUM VITAE.....	175

# LIST OF FIGURES

<b>Figure 1.1</b> - Schematic of lithium-ion battery. Adapted from reference 27.....	5
<b>Figure 1.2</b> - Comparison of lithium and calcium batteries a) comparison of reduction potentials b) comparisons of gravimetric and volumetric capacities (Adapted from reference 41 <a href="https://pubs.acs.org/doi/10.1021/acsenergylett.1c00593">https://pubs.acs.org/doi/10.1021/acsenergylett.1c00593</a> . Future permissions of material excerpted should be directed to ACS ).....	9
<b>Figure 2.1</b> - In situ cell a) Schematic of in situ XRD cell b) Photo of assembled in situ cell .....	32
<b>Figure 2.2</b> - In situ cell with Rigaku Miniflex 600 a) Installation of in situ cell inside Rigaku Miniflex 600 b) XRD diffraction of baseline in situ cell.....	33
<b>Figure 2.3</b> - XRD diffraction of the LiCoO <sub>2</sub> powder and freestanding electrode as it is assembled inside of in situ cell.....	34
<b>Figure 2.4</b> - LiCoO <sub>2</sub> cycling inside of in situ cell a) Voltage-time curves with 10 cycles of testing b) Voltage-capacity curves for the LiCoO <sub>2</sub> .....	36
<b>Figure 2.5</b> - In situ XRD diffraction of LiCoO <sub>2</sub> cathode as it is charged and discharged .....	37
<b>Figure 2.6</b> - In situ XRD of LiCoO <sub>2</sub> during first 3 cycles of testing a) XRD evolution of the (003) lattice plane b) Deconvolution of XRD peaks after first charge of LiCoO <sub>2</sub> .....	38
<b>Figure 2.7</b> - XRD of LiCoO <sub>2</sub> for first 3 cycles of testing a) XRD spectra of (101) lattice plane b) XRD spectra of (109), (107) and (108) planes .....	39
<b>Figure SI 2.1</b> - In situ cell assembly .....	40
<b>Figure SI 2.2</b> - In situ cell sub-assembly .....	41
<b>Figure SI 2.3</b> - Sample holder sub-assembly .....	42
<b>Figure SI 2.4</b> - Part 1 - Sample holder block .....	43
<b>Figure SI 2.5</b> - Part 2 - Sample holder top.....	44
<b>Figure SI 2.6</b> - Part 3 - Screw wheel.....	45
<b>Figure SI 2.7</b> - Part 4 - Bottom cap.....	46
<b>Figure SI 2.8</b> - Part 5 - Screw interface .....	47
<b>Figure SI 2.9</b> - Part 6 - PTFE electrode insulator .....	48

<b>Figure SI 2.10</b> - Part 7 - Electrode contact .....	49
<b>Figure SI 2.11</b> - Part 8 - In situ o-ring .....	50
<b>Figure SI 2.12</b> - Part 9 - In situ neck.....	51
<b>Figure SI 2.13</b> - Part 10 - PTFE insulation .....	52
<b>Figure SI 2.14</b> - Part 11 - Spring.....	53
<b>Figure SI 2.15</b> - Part 12 - Brass piston.....	54
<b>Figure SI 2.16</b> - Part 13 - Glassy carbon window.....	55
<b>Figure SI 2.17</b> - Part 14 - Top cap (before machining aperture) .....	56
<b>Figure SI 2.18</b> - Part 14 - Top cap (with machined aperture).....	57
<b>Figure 3.1</b> - Synthesis of post-spinel $\text{CaMn}_2\text{O}_4$ . a) XRD diffraction of $\text{CaMn}_2\text{O}_4$ (inset of lattice parameters, space group and unit cell) b) SEM image of $\text{CaMn}_2\text{O}_4$ powders (Scale bar of 10 microns) c) Close up SEM image of $\text{CaMn}_2\text{O}_4$ particles (Scale bar of 0.5 microns). .....	70
<b>Figure 3.2</b> - a) Cyclic voltammetry of $\text{CaMn}_2\text{O}_4$ . b) In situ EIS measurements of the $\text{CaMn}_2\text{O}_4$ (inset shows equivalent circuit used for impedance analysis and charge transfer resistance plot). .....	71
<b>Figure 3.3</b> - a) Maximum charge of the $\text{CaMn}_2\text{O}_4$ (C/200) and discharge b) XRD of lattice plane (020). c) XRD of lattice plane (132) before and after charging (dashed lines denoting emergence of peak at $44.5^\circ$ ). .....	75
<b>Figure 3.4</b> - XPS of $\text{CaMn}_2\text{O}_4$ for average oxidation of manganese a) Mn 3s binding energy b) Mn 2p binding energy of charged sample c) Mn 2p binding energy of baseline sample. ....	77
<b>Figure 3.5</b> - Galvanostatic cycling of the $\text{CaMn}_2\text{O}_4$ a) Voltage-time curve of selected cycles (inset of full 100 cycle testing with $\text{CaMn}_2\text{O}_4$ ) b) Capacity-voltage curves of selected cycles of $\text{CaMn}_2\text{O}_4$ c) EDS of the $\text{CaMn}_2\text{O}_4$ before and after galvanostatic cycling. ....	80
<b>Figure 3.6</b> - In situ cell cycling of $\text{CaMn}_2\text{O}_4$ a) voltage-capacity curves of $\text{CaMn}_2\text{O}_4$ b) XRD of $\text{CaMn}_2\text{O}_4$ during charge and discharge within in situ cell (inset of interplanar spacing during charge and discharge). .....	82
<b>Figure SI 3.1</b> - Calibration of reference electrodes a) CV test of $\text{Ag}/\text{Ag}^+$ reference electrode (0.01 M $\text{AgNO}_3$ in 0.5 M $\text{Ca}(\text{TFSI})_2$ DME) with 50 mM ferrocene dissolved in 0.5 M $\text{Ca}(\text{TFSI})_2$ in DME with Pt working electrode and AC counter electrode b) OCV of the activated carbon is -0.187 V vs. $\text{Ag}/\text{Ag}^+$ .....	84

<b>Figure SI 3.2</b> - Linear Stability Window of Ca(TFSI) <sub>2</sub> in DME using 316 stainless steel blocking and calcium nonblocking electrode at 0.5 mV/s.....	85
<b>Figure SI 3.3</b> - In situ cell a) Schematic of in situ cell used for CaMn <sub>2</sub> O <sub>4</sub> b) photo of the in situ cell assembled.....	85
<b>Figure SI 3.4</b> - a) Installation of in situ cell inside of the Rigaku XRD b) baseline XRD scan of CaMn <sub>2</sub> O <sub>4</sub> inside of in situ cell. ....	86
<b>Figure SI 3.5</b> - Nyquist plots of impedance for CaMn <sub>2</sub> O <sub>4</sub> after charge and discharge cycling....	86
<b>Figure SI 3.6</b> - DFT Calculations of CaMn <sub>2</sub> O <sub>4</sub> a) Voltage profile of CaMn <sub>2</sub> O <sub>4</sub> as calcium is removed. Voltage values were calculated with stable concentrations of calcium in CaMn <sub>2</sub> O <sub>4</sub> with the convex hull. b) Convex hull of CaMn <sub>2</sub> O <sub>4</sub> . Three concentrations of calcium were on the hull and connected by the line.....	87
<b>Figure SI 3.7</b> - Structural models of Ca <sub>1-x</sub> Mn <sub>2</sub> O <sub>4</sub> deinsertion a) x = 0 b) x = 0.25 c) x = 0.5 d) x = 0.5 e) x = 0.5 f) x = 0.75 g) x = 1.0.....	88
<b>Figure SI 3.8</b> - Theoretical XRD patterns of Ca <sub>1-x</sub> Mn <sub>2</sub> O <sub>4</sub> deinsertion a) x = 0 b) x = 0.25 c) x = 0.5 d) x = 0.5 e) x = 0.5 f) x = 0.75 g) x = 1.0 .....	88
<b>Figure SI 3.9</b> - Rietveld refinement of CaMn <sub>2</sub> O <sub>4</sub> cathode a) post-maximum charge b) post-discharge .....	97
<b>Figure SI 3.10</b> - XRD changes with CaMn <sub>2</sub> O <sub>4</sub> from maximum charge a) Full experimental XRD of CaMn <sub>2</sub> O <sub>4</sub> from its pristine electrode and after maximum charge of the CaMn <sub>2</sub> O <sub>4</sub> b) Theoretical XRD of the CaMn <sub>2</sub> O <sub>4</sub> with 25% vacancies from the pristine electrode .....	98
<b>Figure SI 3.11</b> - Galvanostatic cycling of the CaMn <sub>2</sub> O <sub>4</sub> at C/39 a) Voltage-time curve of 30 cycles of testing b) Capacity-voltage curves of selected cycles of CaMn <sub>2</sub> O <sub>4</sub> .....	99
<b>Figure SI 3.12</b> - XRD of the CaMn <sub>2</sub> O <sub>4</sub> before after galvanostatic cycling of the CaMn <sub>2</sub> O <sub>4</sub> .....	99
<b>Figure 4.1</b> - Synthesis of post-spinel CaFe <sub>2</sub> O <sub>4</sub> .....	115
<b>Figure 4.2</b> - SEM images of CaFe <sub>2</sub> O <sub>4</sub> powders a) Overview image of CaFe <sub>2</sub> O <sub>4</sub> (Scale bar of 5 microns) b) Close up SEM image of CaFe <sub>2</sub> O <sub>4</sub> (Scale bar of 1 microns).....	116
<b>Figure 4.3</b> - Cyclic voltammetry of CaFe <sub>2</sub> O <sub>4</sub> working electrode, activated carbon counter electrode and Ag/Ag <sup>+</sup> reference electrode at 0.5 mV/s scan rate .....	117
<b>Figure 4.4</b> - XRD of CaFe <sub>2</sub> O <sub>4</sub> synthesized powder and in situ XRD of CaFe <sub>2</sub> O <sub>4</sub> .....	118
<b>Figure 4.5</b> - Maximum charge of the CaFe <sub>2</sub> O <sub>4</sub> inside of the in situ cell at C/50 .....	120

<b>Figure 4.6</b> - In situ XRD of the CaFe <sub>2</sub> O <sub>4</sub> a) in situ XRD overview of CaFe <sub>2</sub> O <sub>4</sub> from maximum charge b) In situ XRD of the (200) lattice planes over course of charging .....	120
<b>Figure 4.7</b> - Galvanostatic cycling of CaFe <sub>2</sub> O <sub>4</sub> a) Voltage-time curve of cycling b) Capacity-voltage curves of cycled of CaFe <sub>2</sub> O <sub>4</sub> .....	121
<b>Figure 4.8</b> - Overview XRD of CaFe <sub>2</sub> O <sub>4</sub> from galvanostatic cycling (asterisk in figure are reflections from aluminum current collector) .....	123
<b>Figure 4.9</b> - XRD of the CaFe <sub>2</sub> O <sub>4</sub> before and after galvanostatic cycling with (103) lattice planes .....	123
<b>Figure 4.10</b> - EDS of the CaFe <sub>2</sub> O <sub>4</sub> before and after galvanostatic cycling.....	124
<b>Figure SI 4.1</b> - N <sub>2</sub> isotherm CaFe <sub>2</sub> O <sub>4</sub> .....	126
<b>Figure SI 4.2</b> - Theoretical XRD Patterns of CaFe <sub>2</sub> O <sub>4</sub> a) XRD with 100% calcium occupancy b) XRD with 75% calcium occupancy .....	126
<b>Figure SI 4.3</b> - Crystal structure of CaFe <sub>2</sub> O <sub>4</sub> a) 100% calcium occupancy b) 75% calcium occupancy .....	127
<b>Figure 5.1</b> - Galvanostatic cycling a) Plating and stripping of the Ca//Ca symmetric cell b) Voltage vs. capacity curves c) CV of the Ca//Ca symmetric cell d) Cross-sectional of SEI on calcium electrode after 10 cycles of galvanostatic cycling. ....	139
<b>Figure 5.2</b> - XRD of galvanostatic cycling with calcium electrodes a) XRD profiles of plating at -0.5 V and -1.8 V along with XRD of stripping at 1.8 V in a calcium symmetric cell. b) XRD profiles of plating and stripping between the diffraction angles of 40°-70° c) FTIR on the calcium plated and stripped materials .....	142
<b>Figure 5.3</b> - SEM/EDX from plating and stripping (a-g) EDX of calcium electrode from -0.5 V plating. (h-n) EDX of calcium electrode from -1.8 V. (o-u) EDX analysis after stripping at 1.8 V. ....	143
<b>Figure 5.4</b> - Plating onto gold electrode a) XRD profiles from plating onto a gold working electrode at -0.5 V and -1.8 V. b) XRD profiles from plating onto gold between diffraction angles of 10°-40° c) EDX of plated gold electrode at -0.5 V and -1.8 V. ....	144
<b>Figure 5.5</b> - In situ EIS of calcium electrodes during galvanostatic cycling. a) Nyquist plot from in situ EIS b) Hybrid SEI resistance from in situ EIS. Inset in (b) is equivalent circuit for SEI resistance.....	146
<b>Figure 5.6</b> - Raman analysis of electrolyte a) Gaussian fits of PF <sub>6</sub> <sup>-</sup> interactions in KPF <sub>6</sub> electrolyte (pristine) b) Gaussian fits of PF <sub>6</sub> <sup>-</sup> interactions in KPF <sub>6</sub> electrolyte (cycled) .....	147

<b>Figure SI 5.1</b> – Plating and stripping Ca//Ca symmetric cell with dedicated calcium reference electrode .....	151
<b>Figure SI 5.2</b> - XRD of pristine and pressed calcium pellets .....	151
<b>Figure SI 5.3</b> - Linear stability window of KPF <sub>6</sub> EC/DMC/EMC using a gold blocking electrode and calcium nonblocking electrode at 0.5 mV/s .....	152
<b>Figure SI 5.4</b> - Nyquist plots of impedance for galvanostatic cycling and after each plating and stripping .....	152
<b>Figure SI 5.5</b> - Transference number measurement of KPF <sub>6</sub> EC/DMC/EMC (uncycled) .....	153
<b>Figure 6.1</b> - XRD of synthesized Ca <sub>0.66</sub> Mn <sub>1.4</sub> Fe <sub>0.6</sub> O <sub>4</sub> .....	164

## LIST OF TABLES

<b>Table SI 3.1</b> - Calculated lattice parameters of $\text{Ca}_{1-x}\text{Mn}_2\text{O}_4$ deinsertion a) $x = 0$ b) $x = 0.25$ c) $x = 0.5$ d) $x = 0.5$ e) $x = 0.5$ f) $x = 0.75$ g) $x = 1.0$ .....	89
<b>Table SI 3.2</b> - Atomic $x, y, z$ coordinates and occupancy of $\text{Ca}_{1-x}\text{Mn}_2\text{O}_4$ deinsertion with $x = 0$ (a) .....	90
<b>Table SI 3.3</b> - Atomic $x, y, z$ coordinates and occupancy of $\text{Ca}_{1-x}\text{Mn}_2\text{O}_4$ deinsertion with $x = 0.25$ (b) .....	91
<b>Table SI 3.4</b> - Atomic $x, y, z$ coordinates and occupancy of $\text{Ca}_{1-x}\text{Mn}_2\text{O}_4$ deinsertion with $x = 0.5$ (c) .....	92
<b>Table SI 3.5</b> - Atomic $x, y, z$ coordinates and occupancy of $\text{Ca}_{1-x}\text{Mn}_2\text{O}_4$ deinsertion with $x = 0.5$ (d) .....	94
<b>Table SI 3.6</b> - Atomic $x, y, z$ coordinates and occupancy of $\text{Ca}_{1-x}\text{Mn}_2\text{O}_4$ deinsertion with $x = 0.5$ (e) .....	95
<b>Table SI 3.7</b> - Atomic $x, y, z$ coordinates and occupancy of $\text{Ca}_{1-x}\text{Mn}_2\text{O}_4$ deinsertion with $x = 0.75$ (f) .....	96
<b>Table SI 3.8</b> - Atomic $x, y, z$ coordinates and occupancy of $\text{Ca}_{1-x}\text{Mn}_2\text{O}_4$ deinsertion with $x = 1.0$ (g) .....	97
<b>Table SI 3.9</b> - Refined parameters for $\text{CaMn}_2\text{O}_4$ .....	97
<b>Table SI 3.10</b> - Refined parameters for $\text{Mn}_3\text{O}_4$ .....	98
<b>Table SI 3.11</b> - Refined parameters for $\text{MnO}$ .....	98

## LIST OF PUBLISHED PAPERS

1. **Chando, P. A.**; Chen, S.; Shellhamer, J. M.; Wall, E.; Wang, X.; Schuarca, R.; Smeu, M.; Hosein, I. D. Exploring Calcium Manganese Oxide as a Promising Cathode Material for Calcium-Ion Batteries. *Chem. Mater.* **2023**.

<https://doi.org/10.1021/acs.chemmater.3c00659>.

This published work was used as Chapter 3 in this dissertation

2. **Chando, P.A.**; Shellhamer, J.M.; Wall, E.; He, W.; Hosein, I.D. Plating and Stripping Calcium Metal in Potassium Hexafluorophosphate Electrolyte toward a Stable Hybrid Solid Electrolyte Interphase. *ACS Appl. Energy Mater.* **2023**, 6 (7), 3924–3932.

<https://doi.org/10.1021/acsaem.3c00098>.

This published work was used as Chapter 5 in this dissertation

# **CHAPTER 1**

## **GENERAL INTRODUCTION**

## 1.1 Introduction

The need for technologies that minimize carbon footprints along with an infrastructure to support them has been a focus of numerous studies and government initiatives. Most notably, the Paris Agreement of 2016 is a global effort to address climate change with several strategies that include the development of renewable energy sources (RES) and electric vehicles.<sup>[1-3]</sup> The widespread adoption of these technologies is impacted largely by balancing performance and cost. Projects developing wind and solar energy have made significant advances in decreasing technology cost. Environmental reports on solar energy have forecasted a 43% drop for solar photovoltaics by 2025, allowing for further market penetration and projecting a more substantial role in energy supply by 2050.<sup>[4,5]</sup> Regarding electric vehicles, countries such as the USA and China are investing \$2.4 billion and \$15 billion in electric cars. While lithium-ion batteries have one of the highest densities (100-265 Wh/kg), the driving range of current electric vehicles is still considerably lower than cars fueled by gasoline. Investments into next generation electric vehicles are aiming to achieve performance metrics of 300 miles per charge and battery costs being reduced to \$125 kWh<sup>-1</sup>.<sup>[1,6]</sup> The energy portfolio from all these technologies is dependent on lithium-ion batteries (LIB) to power them. Lithium, with a gravimetric capacity of 3863 mAh/g and energy density above 150 Wh/kg, is the primary battery chemistry being used to power electric vehicles.<sup>[1,7,8]</sup> Regarding its role with solar and wind energy, lithium-ion batteries are an established energy storage solution (ESS) that are effective at managing these intermittent energy sources and providing a more consistent energy to the national grid. Currently, lithium-ion batteries make up 78% of current battery solutions used for storing energy from renewable sources.<sup>[9-14]</sup>

The use of lithium with these broader applications has caused increased demands of lithium metal to meet manufacturing and research needs. Global demand has doubled every 5 years with LIB

capacities reaching 125 GWh (2020), 220 GWh (2025) and 390 GWh (2030).<sup>[1,15]</sup> The global market for automotive LIB will grow from \$7.8 billion in 2015 to \$30.6 billion in 2024. Similarly, energy demands of lithium to serve as storage solutions for wind and solar energy are also on a trajectory of steep growth. According to the Department of Energy (DOE) Global Energy Storage Database, 1,364 energy storage projects using 174 GWs of energy are in operation globally with an additional 334 energy projects totaling 18 GWs in development.<sup>[12-14]</sup>

The rising demand for lithium has also led to rising costs and geopolitical concerns since lithium reserves are unevenly distributed around the world.<sup>[16]</sup> According to estimates from the US Geological Survey (USGS) in 2011, the total lithium resources are calculated to be 29 Mts. The largest resources are in Bolivia (9 Mts), Chile (7.5 Mts), China (5.4 Mts) and Argentina (2.6 Mts).<sup>[1,17]</sup> Historically, lithium was refined for a multitude of different applications with batteries occupying less than 5% of lithium manufacturing. The projected use of lithium is as follows: 9760 tons of lithium in 2015 being 30% market share. By 2020, 12,160 tons of lithium are mined accounting for 37% and by 2025, 21,520 tons of lithium will be mined accounting for 66% of the market share of lithium with most lithium batteries being used for electric vehicles.<sup>[18-22]</sup> The increased use of lithium along with its finite availability has caused the price of raw materials for lithium-ion batteries to increase. A 2022 US mineral commodity report summarized the use of lithium and tracked a 21% manufacturing increase of lithium in 2021 with market volatility causing the price of lithium to increase from \$7,000/ton to \$26,200/ton.<sup>[23]</sup> The volatility with lithium prices is exacerbated by studies projecting that global lithium resources will be exhausted by 2030 from manufacturing demand.<sup>[20,24,25]</sup> Based on the rising energy demands of ever expanding technologies and market volatility of lithium, alternative battery chemistries need to be

explored to mitigate the rising costs of raw materials that may price out technologies that we need for a sustainable future.

## 1.2 Lithium-Ion Batteries

Lithium-ion batteries, since their commercialization in 1991, have fundamentally changed our everyday lives. They power an ever-expanding range of technologies and are the dominant battery chemistry we depend on. The discovery and development of this line of batteries is the product of considerable research efforts since the 1970s. The discovery of lithium cathodes being able to reversibly intercalate charge for battery applications belongs to John B. Goodenough, M. Stanley Whittingham and Akira Yoshino and was recognized in 2019 with their Nobel Prize.<sup>[26-28]</sup> Since their market introduction, researchers have focused on maximizing the energy density of lithium-ion batteries to further their applicability towards new and developing technologies.

Lithium-ion batteries consist of 4 components which include the cathode, anode, electrolyte, and separator. A schematic of the lithium-ion battery is outlined in Figure 1 with Lithium Cobalt Oxide ( $\text{LiCoO}_2$ ) as the cathode, graphite as the anode and a lithium-rich electrolyte. Lithium-ion batteries function on intercalation chemistry, which is the reversible insertion of ions into a host material.<sup>[29]</sup> During the charging process of Figure 1, electrons are transferred from the  $\text{LiCoO}_2$  to the graphite through an external circuit, powering a device. In addition to the transfer of electrons, cations deintercalate from the  $\text{LiCoO}_2$ , causing changes in the interplanar spacing of the cathode, and migrate to the graphite using the electrolyte as a conductive pathway. The delithiation reaction at the cathode is outlined by reaction 1 (1.1) while the insertion of lithium into the anode is represented by reaction 2 (1.2). The separator functions as a physical barrier between the anode and cathode to prevent a short circuit. During the discharge of the LIB, the charging process is reversed and ions flow from the graphite back into the  $\text{LiCoO}_2$ , reinserting back into the crystal

framework and undoing the structural changes observed during charging. This overview of intercalation chemistry in lithium-ion batteries has become the staple of powering billions of electrical devices.<sup>[27,30]</sup>

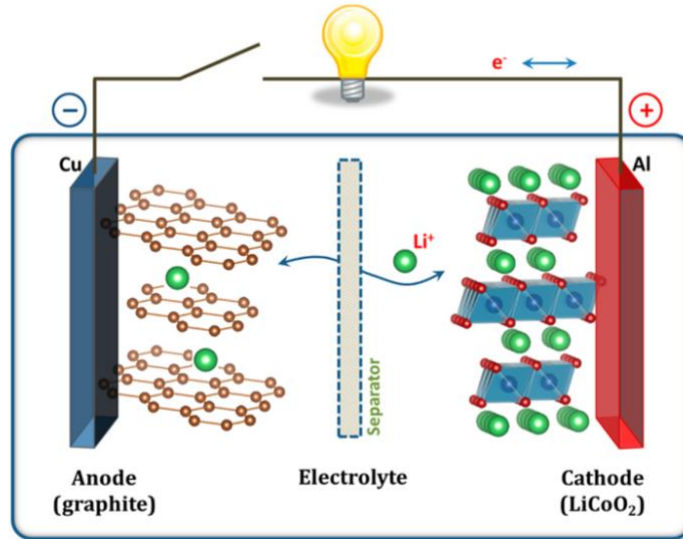
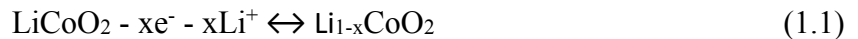


**Figure 1.1** - Schematic of lithium-ion battery. Adapted from reference 27



The mechanism of intercalation chemistry has considerable benefits including high reversibility, round trip efficiency and stability. The reversible shuttling of ions in and out of the cathode is dependent on cycling a certain capacity within the battery. Overcharging of a lithium-ion battery involves removing a large amount of lithium ions from the cathode which can lead to significant structural changes and cause phase changes to occur.<sup>[31]</sup> Such developments have considerable impacts on the remaining cycle life of a lithium-ion battery and charge that can be cycled. The performance of a lithium-ion battery requires a reversible capacity with the cathode to be identified. The reversible capacity is the amount of charge that can be cycled in and out of the

electrode without causing permanent structural changes to the electrode. The magnitude of the reversible capacity and charging rates of the cathode are dependent on establishing the theoretical capacity of a cathode. The theoretical capacity is the total possible charge that can be extracted from a battery. For a lithium-ion battery, it is dictated by the cathode, which serves as the source of lithium ions. The theoretical capacity of a cathode is outlined by the following equation (1.3):

$$\textit{Theoretical capacity (mAh/g)} = \frac{n * F * 1000}{MW * 3600} \quad (1.3)$$

where F is Faraday's constant (96,485 C/mol), n is the number of electrons transferred, and MW is the molecular weight of the active material in the electrode. Research efforts on optimizing the energy density of lithium-ion batteries have focused on achieving high operating voltages and maximizing the reversible capacity.<sup>[32]</sup> For attaining higher operating voltages, lithium-ion batteries have relied on the use of aprotic electrolytes since aqueous electrolytes would be limited to a voltage limit of 1.2 V. Regarding the reversible capacity of lithium-ion batteries, achieving higher capacities for such systems has involved modifying the active materials used in the cathodes. Such modifications have included increasing the ratio of active material used, making lithium-ion batteries lighter to achieve higher gravimetric capacities, and exploring other crystal structures for LIBs including spinels and NASICON frameworks.<sup>[32,33]</sup> Outside of achieving higher capacities for LIBs, the greatest possible increase in the energy density of lithium batteries would occur from raising the average operating voltage by using a lithium metal anode. Lithium metal would be the ideal anode for lithium batteries because of their theoretical capacities (3860 mAh/g) and low reduction potentials (-3.04 V vs. Standard Hydrogen Electrode (SHE))<sup>[32,34]</sup> However, lithium metal anodes are known to not plate evenly and are prone to forming dendrites which forms "dead" lithium and can ultimately cause battery shorts and fires.<sup>[34]</sup> Based on this safety hazard, lithium metal anodes have been used primarily for research purposes with lithium based cathodes.

Commercial LIBs have focused on using graphite anodes to avoid the safety hazards associated with lithium metal. While effective, the use of graphite limits the average operating voltage and, consequently, the energy density of the battery. Given the demands from electric vehicles and other technologies for higher energy densities, along with the previously described sustainability issues surrounding lithium, other battery chemistries will have to be explored since lithium is reaching a saturation point with its attainable energy densities.<sup>[35,36]</sup>

### **1.3 Next Generation Batteries**

Several alternate battery chemistries beyond lithium have been explored including sodium, magnesium, and calcium. Sodium-ion batteries have considerable development since they are a monovalent system that use similar reaction mechanisms to lithium and have comparable electrolytes along with similar types of cathodes for intercalation chemistry. Other factors that enhance the candidacy of sodium-ion batteries is the natural abundance of raw materials for it and low cost as a result. However, the drawback of this type of battery chemistry is the larger ionic radius and weight of sodium, which causes sodium batteries to have a lower energy density than lithium batteries.<sup>[37,38]</sup> Magnesium is an alternate battery chemistry of large research efforts due to its divalency and favorable gravimetric capacity of 2205 mAh/g. Magnesium also has a similar ionic radius (0.72 Å) to lithium (0.76 Å) which opens up the possibility of many intercalation hosts being used with lithium-ion batteries also being used for magnesium. Despite these advantages, some of the major challenges surrounding magnesium batteries is the identification of suitable electrolytes that can plate and strip magnesium without the formation of passivation layers along with electrolytes being able to function at higher voltages.<sup>[37,39]</sup>

An additional post-lithium battery chemistry that is being explored is calcium. Calcium is a particularly interesting alternative to lithium due to several factors. Calcium is the 5th most abundant element in earth's crust, making the economics associated with processing its raw materials relatively inexpensive.<sup>[37]</sup> The previously mentioned 2022 US mineral commodity report reported on the production of lime (CaO), which is the raw materials that calcium metal is refined from. The report concluded that the US produced 17 million tonnes of lime in 2021 at a price of \$140/ton.<sup>[23]</sup> Compared to the previously described lithium market volatility, the price point of calcium is particularly attractive for initiatives focused on driving down the price per kilowatt-hour of new and developing technologies.

Other factors that support the candidacy of calcium as an alternative battery chemistry is the similar redox potential calcium has to lithium along with competitive volumetric capacities. (Figure 1.2) While the gravimetric capacity of lithium (3864 mAh/g) is considerably higher than that of calcium (1337 mAh/g) both metals have similar volumetric capacities. The volumetric capacity of lithium is recorded to be 2062 mAh/cm<sup>3</sup> while the volumetric capacity of calcium is 2072 mAh/cm<sup>3</sup>.<sup>[40,41]</sup> The superior gravimetric capacity of lithium makes it a suitable battery system for mobile applications over calcium. However, for more stationary applications, both systems would be compatible. Calcium also has a standard reduction potential of -2.87 V (vs. SHE). Compared to the standard reduction potential of lithium, which is -3.04 V (vs. SHE), the calcium potential is only 0.17 V higher than lithium, The similar redox potentials outlines both systems capable of achieving high energy densities using their respective metal anodes and volumetric capacities. Lithium metal anodes include the deposition of lithium on the anode surface as dendrites, increasing the surface area and potentially leading to thermal runaway. However, it has been shown that multivalent metals can deposit uniformly with minimal dendritic growth.<sup>[37,42]</sup> Additionally,

more electrons are exchanged per charge carrier in multivalent batteries, allowing multivalent chemistries to reach the same energy and power densities of monovalent batteries with less ions..<sup>[43]</sup>

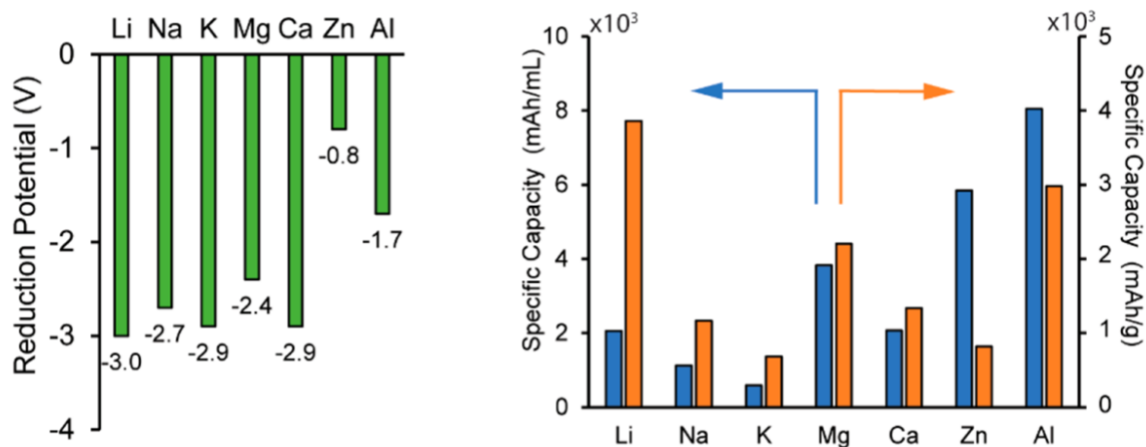


**Figure 1.2** - Comparison of lithium and calcium batteries a) comparison of reduction potentials b) comparisons of gravimetric and volumetric capacities (Adapted from reference 41 <https://pubs.acs.org/doi/10.1021/acseenergylett.1c00593>. Future permissions of material excerpted should be directed to ACS )

#### 1.4 Cathodes for Calcium-Ion Batteries

Cathodes are an essential component to calcium ion batteries. They largely influence the working voltage, capacity, and energy density of the battery.<sup>[44]</sup> While cathodes for systems such as lithium-ion batteries have been well established, the multivalency of calcium ions carries with it a unique set of challenges for successful cycling of calcium. Cathodes for calcium batteries must possess certain properties including a high-capacity, ability to run at high-voltage, structural stability during cycling, and possessing stable transport pathways for calcium diffusion in and out of the structure.<sup>[45,46]</sup> Calcium, with a divalent charge and larger ionic radius than lithium, has more ionic interactions with its surroundings and is subject to sluggish diffusion kinetics as a result. Ideal cathodes for calcium-ion batteries should possess frameworks that allow fast diffusion of ions,

allowing for faster capacity cycling.<sup>[40,45]</sup> Additional parameters for assessing the viability of cathodes for calcium-ion batteries include theoretical capacity, phase stability, conductivity, average voltage of operation and volume change from intercalation chemistry.<sup>[47-49]</sup> Several classes of calcium cathodes have been explored for use in calcium-ion batteries including prussian blue analogues (PBA), sodium superior ionic conductors (NASICON), organic, layered, and open-tunnel oxides.<sup>[47]</sup> PBAs are porous electrodes that have a cage-like structure. The formula for such cathodes is  $A_x[B(CN)_6]_yH_2O$  with A and B being transition metal ions. The A and B atoms are coordinated to form large cubic voids in the structure. These voids are pathways for cations to diffuse through the crystal structure. While this framework does serve as an effective means for achieving high cyclability and insertion potentials, it is limited with a low specific capacity.<sup>[47,50,51]</sup> NASICON is a popular class of cathodes for its fast ion insertion. The formula for NASICON materials is  $AMM'(PO_4)_3$  where A is for alkali ions, M is for a trivalent transition metal ion and M' is for a tetravalent transition metal ion. A NASICON electrode in calcium-ion batteries is  $Ca_xV_2(PO_4)_3$ . The NASICON structure includes corner-shared  $VO_6$  octahedra and  $PO_4$  tetrahedra. The NASICON structure also has alkali metals at 6b and 18e sites. During charging, the ions at 6b sites are stationary while the ions at 18e sites are removed, allowing for cycling of multivalent ions. The NASICON cathodes have high cycling stability and insertion potentials. However, the drawbacks with this class of cathodes are the low specific capacity and need for operating at high temperatures.<sup>[47,52,53]</sup> Another class of cathodes that has significant potential with multivalent ion batteries are organic compounds. Ionically conductive polymers are frequently used in this line of cathodes with polyaniline, polypyrrole and polythiophene being the most commonly used polymers. The benefits of such cathodes include their low cost and high rate-capability. However, limitations for these systems include low cyclic stability and low volumetric capacities.<sup>[47,54,55]</sup>

Layered oxides are another class of cathodes that have promising performance for multivalent-ion chemistry. This particular class of cathodes consists of transition metal octahedra bonded together into 2D planes. The planes are connected to neighboring sites through van der Waals interactions. The removal and insertion of cations into these structures modifies the interplanar spacing between the 2D planes and is the same mechanism of capacity cycling with  $\text{LiCoO}_2$  as it is used in lithium-ion batteries. Regarding the use of layered oxides with calcium-ion batteries, the most typical transition metal used for it is vanadium due to the different oxidation states it can accommodate.<sup>[56]</sup> Use of layered oxides have reported high-rate performance and a relatively high specific capacity. However, the issue associated with layered oxides is the cost associated with their synthesis, which would be difficult for large scale production.<sup>[47,57,58]</sup>

The last class of cathodes for calcium-ion batteries is open-tunnel transition metal oxides. This particular type of cathode is regarded as the most promising candidate for calcium-ion batteries since the 1D tunnels for charge migration provide a framework that can accommodate the larger ionic radius of calcium ions.<sup>[47]</sup> The compounds in this class of cathodes are typically manganese based, but recent work has also shown open tunnel structures to exist with compounds such as molybdenum vanadium oxide. The movement of cations is dependent on large pores within these cathodes that can allow for fast diffusion. For higher capacities, hexagonal or larger pores are needed for multivalent ions. When compared to alternate cathode classes, open tunnel oxides were found to have the best overall battery performance with energy densities of 300-500 Wh/kg.

Based on the superior battery performance of open tunnel oxides, several types of transition metal oxides have been explored using ab-initio calculations.<sup>[47,59,60]</sup>

One such system that has been evaluated theoretically and has an open tunnel structure for multivalent ion diffusion are spinels. Spinel possess a  $\text{AB}_2\text{O}_4$  formula with A being the cation of

choice and B being the transition metal oxide. In such a structure, the A cations are tetrahedrally coordinated while the B ions are in octahedral coordinations.<sup>[61]</sup> Density functional theory (DFT) has emerged as a tool for screening potential cathodes and modeling the performance of promising candidates. Theoretical calculations performed on spinels have reported migration barriers of 600 meV. Previous theoretical studies on the successful diffusion of calcium ions have concluded that migration barriers in electrodes that are 525 meV correspond to an ionic diffusivity of  $10^{-12} \text{ cm}^2\text{s}^{-1}$  and have served as a benchmark for ideal cationic diffusion.<sup>[46]</sup> The 600 meV migration barrier in spinels reports that calcium ions would be able to diffuse through the structure at higher charge and discharge rates. This low diffusion barrier is possible from the tetrahedral coordination of calcium functioning in a metastable state.<sup>[62]</sup> Spinel, based on DFT calculations, have been identified as strong candidates for cycling calcium ions. Theoretical calculations on such spinels have also predicted volume variations of 20% which could lead to phase instability as calcium is cycled.<sup>[62]</sup> However, there are no experimental evaluations to corroborate or refute theoretical predictions made of such spinels due to the processing needed for their formation. The more naturally occurring variants of the spinel structure are post-spinels.<sup>[63]</sup> Post-spinels also possess the 1D conduction pathways that make open-tunnel transition metal oxides attractive candidates for multivalent-ion batteries. Calcium-ions are projected to move in the post-spinel structure through one-dimensional chains that are formed by  $\text{MO}_6$  octahedrals in “double-rutile chains.”<sup>[63]</sup> However, the calcium ions in such structures are in octahedral coordinations. While more thermodynamically stable, this also raises the diffusion barrier from 600 meV to 1.8 eV for calcium diffusion. This drastic change in migration barriers limits the charge and discharge rates for these calcium cathodes. As a result of the high diffusion barriers calculated for post-spinel structures, little work has been dedicated to the experimental evaluation of such systems.<sup>[63,64]</sup> One of the aims

of this dissertation is the exploration of such post-spinels for the implementation in calcium-ion batteries.

### **1.5 Electrolytes for Calcium-Ion Batteries**

The high energy densities of calcium-ion batteries are contingent on the capacity cycling from suitable cathodes and the use of calcium metal anodes to elevate the operating voltage of the battery. The use of calcium metal anodes for such applications is challenged by the solid electrolyte interphase (SEI) that forms on the calcium in native calcium electrolytes. The SEI is the product of salt and solvent reduction reactions with an electrode that form a film on the electrode surface. It serves as an ionically conducting and electrically insulating layer on an electrode that prevents short circuits within the battery. The SEI phases that have formed with lithium-ion batteries include lithium fluoride (LiF), lithium chloride (LiCl) and lithium oxide (Li<sub>2</sub>O). These phases have functioned as electrically insulating and ionically conductive mediums that allow the batteries to cycle charge.<sup>[65,66]</sup> With calcium electrolytes and anodes, the phases in the SEI have included calcium fluoride (CaF<sub>2</sub>), calcium chloride (CaCl<sub>2</sub>) and calcium oxide (CaO). These analogous phases to lithium-ion SEIs are electrically and ionically insulating. These highly insulating layers reduce ionic conductivity and cause increases in the operating voltage as a result of the developing charge transfer resistance. Calcium ions cannot move in and out of the SEI and the coulombic efficiency of such a system was reported to be 5%.<sup>[67]</sup> The lack of diffusion from the SEI causes an increase in the resistance of the SEI and prompts the use of higher voltages that eventually lead to an inability for the SEI to function any longer.<sup>[68,69]</sup>

The possibility of using calcium based electrolytes was not considered feasible because of the passivation layers that form on the calcium metal electrode. However, recent developments in the

field of calcium electrolytes have created renewed interest in work focused on calcium metal anodes with electrolytes. In 2016, reversible calcium deposition was reported by Ponrouch on stainless steel electrodes at elevated temperatures. The electrolyte used was calcium tetrafluoroborate ( $\text{Ca}(\text{BF}_4)_2$ ) in a solvent mixture of ethylene carbonate (EC) and propylene carbonate (PC) at 75-100°C.<sup>[70]</sup> The work outlined by the reversible plating and stripping of calcium in that system elucidated the importance of salt and solvent combinations and how the SEI resistance could be bypassed with elevated temperatures. Other efforts at attaining reversible calcium plating and stripping included the use of the same salt and solvent combination and cycling at room temperature.<sup>[71]</sup> Using current densities lower than 0.4 mA/cm<sup>2</sup>, coulombic efficiencies larger than 95% were obtained with calcium deposition thicknesses of 20 μm. The use of lower current densities also managed to bypass the formation of  $\text{CaF}_2$  phases. While the current densities for the system may have been orders of magnitude lower than those for lithium systems, it established the functionality of calcium plating and stripping at room temperature while also providing insight into the dependence some SEI phases have with overpotentials.<sup>[69,72]</sup> Other efforts at trying to cycle calcium at room temperature have focused on the use of borate salts.<sup>[73-75]</sup> Spectroscopic studies of calcium borohydride ( $\text{Ca}(\text{BH}_4)_2$ ) in tetrahydrofuran (THF) revealed that the calcium ions are weakly coordinated with the  $\text{BH}_4^-$  anions and could efficiently deposit on gold and platinum electrodes with coulombic efficiencies of 95%.<sup>[68]</sup> The work with borate salts also revealed a dependence calcium electrodeposition has on current density. Under small current densities, the calcium deposition on gold and platinum electrodes was reported to have globular morphologies while higher current densities have more dendritic features.<sup>[73,76]</sup> This development does outline the possibility of dendritic formations that may occur if there are current density inhomogeneities with the SEI formation.

One of the latest efforts for implementing calcium metal electrodes at room temperature has been interphase engineering with non-calcium electrolytes. The passivation layers that limit the kinetics of plating and stripping are specific to calcium electrolytes and is exemplified by plating and stripping work with calcium hexafluorophosphate ( $\text{Ca}(\text{PF}_6)_2$ ).<sup>[77]</sup> Recent research into interphase engineering reported on the successful plating and stripping of calcium using sodium electrolytes.<sup>[77,78]</sup> The strategy leverages the similar ionic radius of sodium (227 ppm) and calcium (231 ppm) while also designing a hybrid sodium/calcium SEI layer with more ionically conductive phases such as sodium oxide ( $\text{Na}_2\text{O}$ ). The hybrid SEI lowers the charge transfer kinetics and achieves consistent plating and stripping of calcium. The hybrid SEI approach is also effective at maintaining low overpotentials by mitigating the continuous production of the  $\text{CaF}_2$  phase that occurs with fluorinated carbonate electrolytes. Similar efforts have been made using a hybrid lithium and calcium SEI and have also been successful with lowering overpotentials for calcium plating and stripping and enhancing cycling stability. The morphology of deposited calcium from hybrid SEIs has also been reported to have uniform planar growth and avoids the dendritic structures that have been observed with other strategies.<sup>[79]</sup> One of the aims of this dissertation is to explore an alternate electrolyte that can effectively form a hybrid SEI and maintain cycling stability as calcium is plated and stripped.

## **1.6 Outline of Dissertation**

This dissertation is composed of six chapters. It also fulfills the requirements set by the “Guidelines for Doctoral Dissertations and Master’s Theses” by the Graduate School at Syracuse University. The dissertation is organized by the following chapters.

Chapter 1 introduces the financial and environmental factors that lead to the increased use of lithium for powering multiple technologies. It segues to the sustainability issues surrounding the continued use of lithium and creates financial and electrochemical cases for the use of calcium. A brief overview of the current cathodes used in calcium-ion batteries is discussed while also identifying transition metal oxide post-spinels as promising candidates. The introductory chapter also discusses current challenges over the use of calcium metal anodes and efforts at addressing it. Lastly, the introductory chapter includes the dissertation structure and contributions from each project covered in this work.

Chapter 2 presents the development of an operando in situ cell for tracking structural changes of electrodes via X-ray diffraction (XRD). The chapter discusses design considerations for the in situ cell and validation of the cell with a study performed on  $\text{LiCoO}_2$ . All design files for reproducing the in situ cell are included in the supplemental information. The in situ cell successfully tracks the interplanar spacing changes that occur in  $\text{LiCoO}_2$  as it is cycled and the use of glassy carbon as an XRD window is verified. This study demonstrates the development of equipment for tracking structural changes in cathodes for calcium-ion battery intercalation chemistry.

Chapter 3 outlines the exploration of post-spinel Calcium Manganese Oxide ( $\text{CaMn}_2\text{O}_4$ ) as a cathode in calcium-ion batteries. A maximum capacity of 100 mAh/g is charged from the post-spinel. The results from the characterization and cycling of the  $\text{CaMn}_2\text{O}_4$  identify some phase transformations that occur within the cathode that facilitate the cycling of the cathode. The redox activity of the cathode is investigated with Cyclic Voltammetry (CV) and Galvanostatic (GS) cycling, identifying oxidation potentials at 0.2 and 0.5 V, and insertion potentials that begin at -1.0 and -1.5 V. The  $\text{CaMn}_2\text{O}_4$  can cycle at capacities of 52 mAh/g at a rate of C/33, and calcium cycling is verified with Energy-Dispersive X-ray Spectroscopy (EDS) and X-ray Photoelectron

Spectroscopy (XPS). The results from this work conclude that  $\text{CaMn}_2\text{O}_4$  is a promising cathode for calcium-ion batteries.

Chapter 4 examines Calcium Iron Oxide ( $\text{CaFe}_2\text{O}_4$ ) as a cathode for calcium-ion batteries. The results from testing revealed that the  $\text{CaFe}_2\text{O}_4$  has limited redox activity and produces minor structural variations with the cathode. While able to cycle, much of the electrochemical activity is due to electrolyte side reactions rather than decalciation of the  $\text{CaFe}_2\text{O}_4$ . The findings from the chapter effectively outline a negative result for this post-spinel to function as a cathode for calcium-ion batteries.

Chapter 5 investigates the use of  $\text{KPF}_6$  salt for a hybrid SEI in calcium metal batteries. The hybrid SEI strategy is effective at mitigating the continued production of passivation layers that exist with native calcium electrolytes. Plating and stripping overpotentials in a symmetric calcium cell do not exceed 2 V and last for over 200 hours of operation. Analysis of the plating and stripping data reveals the plating and stripping of calcium below 0.5 V. XRD analysis of the SEI that forms on the calcium is a combination of permanent and transient phases that facilitate cycling. FTIR identifies the parallel plating of both calcium and potassium in galvanostatic data. Raman spectroscopy of the electrolyte identifies compositional changes that increase plating and stripping of calcium. The results from this work indicate that potassium electrolytes are a possible route for reversible cycling of calcium electrodes and may be a strategy for integrating calcium anodes into calcium batteries.

Chapter 6 outlines the findings from the works presented in this dissertation and offers an assessment of future work regarding calcium batteries. The chapter concludes with preliminary

data on the alloying of iron and manganese to form a cathode that is primarily manganese and manages to have the more favorable  $\text{CaFe}_2\text{O}_4$ -type crystal structure for faster cycling.

## References

1. Ding, Y.; Cano, Z. P.; Yu, A.; Lu, J.; Chen, Z. Automotive Li-Ion Batteries: Current Status and Future Perspectives. *Electrochemical Energy Reviews* **2019**, *2* (1), 1–28.
2. Dimitrov, R. S. The Paris Agreement on Climate Change: Behind Closed Doors. *Global Environmental Politics* **2016**, *16* (3), 1–11.
3. Rogelj, J.; den Elzen, M.; Höhne, N.; Fransen, T.; Fekete, H.; Winkler, H.; Schaeffer, R.; Sha, F.; Riahi, K.; Meinshausen, M. Paris Agreement Climate Proposals Need a Boost to Keep Warming Well below 2 °C. *Nature* **2016**, *534* (7609), 631–639.
4. Kebede, A. A.; Kalogiannis, T.; Van Mierlo, J.; Berecibar, M. A Comprehensive Review of Stationary Energy Storage Devices for Large Scale Renewable Energy Sources Grid Integration. *Renewable Sustainable Energy Rev.* **2022**, *159*, 112213.
5. IRENA. *The Power to Change: Solar and Wind Cost Reduction Potential to 2025*; **2016**.
6. Liu, P.; Ross, R.; Newman, A. Long-Range, Low-Cost Electric Vehicles Enabled by Robust Energy Storage. *MRS Energy & Sustainability* **2015**, *2* (1), 12.
7. Liu, W.; Placke, T.; Chau, K. T. Overview of Batteries and Battery Management for Electric Vehicles. *Energy Reports* **2022**, *8*, 4058–4084.
8. Zeng, X.; Li, M.; Abd El-Hady, D.; Alshitari, W.; Al-Bogami, A. S.; Lu, J.; Amine, K. Commercialization of Lithium Battery Technologies for Electric Vehicles. *Adv. Energy Mater.* **2019**, *9* (27), 1900161.
9. Dehghani-Sani, A. R.; Tharumalingam, E.; Dusseault, M. B.; Fraser, R. Study of Energy Storage Systems and Environmental Challenges of Batteries. *Renewable Sustainable Energy Rev.* **2019**, *104*, 192–208.
10. Yoo, H. D.; Markevich, E.; Salitra, G.; Sharon, D.; Aurbach, D. On the Challenge of Developing Advanced Technologies for Electrochemical Energy Storage and Conversion. *Mater. Today* **2014**, *17* (3), 110–121.
11. Bashir, T.; Ismail, S. A.; Song, Y.; Irfan, R. M.; Xu, W. A Review of the Energy Storage Aspects of Chemical Elements for Lithium-Ion Based Batteries. *Energy Materials* **2021**. <https://doi.org/10.20517/energymater.2021.20>.
12. Choi, D.; Shamim, N.; Crawford, A.; Huang, Q.; Vartanian, C. K.; Viswanathan, V. V.; Paiss, M. D.; Alam, M. J. E.; Reed, D. M.; Sprenkle, V. L. Li-Ion Battery Technology for Grid Application. *J. Power Sources* **2021**, *511*, 230419.

13. Hesse, H. C.; Schimpe, M.; Kucevic, D.; Jossen, A. Lithium-Ion Battery Storage for the Grid—A Review of Stationary Battery Storage System Design Tailored for Applications in Modern Power Grids. *Energies* **2017**, *10* (12), 2107.
14. Chen, T.; Jin, Y.; Lv, H.; Yang, A.; Liu, M.; Chen, B.; Xie, Y.; Chen, Q. Applications of Lithium-Ion Batteries in Grid-Scale Energy Storage Systems. *Trans. Tianjin Univ.* **2020**, *26* (3), 208–217.
15. Zubi, G.; Dufo-López, R.; Carvalho, M.; Pasaoglu, G. The Lithium-Ion Battery: State of the Art and Future Perspectives. *Renewable Sustainable Energy Rev.* **2018**, *89*, 292–308.
16. IRENA. Battery Storage for Renewables : Market Status and Technology Outlook. *Irena* **2015**, No. January, 60.
17. Forster, J.: A lithium shortage: are electric vehicles under threat? Swiss Federal Institute of Technology Zurich. <http://www.files.ethz.ch/cepe/Top10/Forster.pdf> (**2011**).
18. Desjardins, J.: Lithium: the future of the green revolution. <http://www.visualcapitalist.com/lithium-fuel-green-revolution/> (2017).
19. Blomgren, G. E. The Development and Future of Lithium Ion Batteries. *J. Electrochem. Soc.* **2016**, *164* (1), A5019.
20. Wanger, T. C. The Lithium Future—resources, Recycling, and the Environment. *Conservation Letters* **2011**, *4* (3), 202–206.
21. Miatto, A.; Wolfram, P.; Reck, B. K.; Graedel, T.E. Uncertain Future of American Lithium: A Perspective until 2050. *Environ. Sci. Technol.* **2021**, *55* (23), 16184–16194.
22. Vikström, H.; Davidsson, S.; Höök, M. Lithium Availability and Future Production Outlooks. *Appl. Energy* **2013**, *110*, 252–266.
23. Bolen, W. P. Mineral Commodity Summaries 2022. US Geological Survey: Reston, VA, USA 2022, 202.
24. Shekhar, A. R.; Parekh, M. H.; Pol, V. G. Worldwide Ubiquitous Utilization of Lithium-Ion Batteries: What We Have Done, Are Doing, and Could Do Safely Once They Are Dead? *J. Power Sources* **2022**, *523*, 231015.
25. Neumann, J.; Petranikova, M.; Meeus, M.; Gamarra, J. D.; Younesi, R.; Winter, M.; Nowak, S. Recycling of Lithium-ion Batteries—current State of the Art, Circular Economy, and next Generation Recycling. *Adv. Energy Mater.* **2022**, 2102917.

26. Mizushima, K.; Jones, P. C.; Wiseman, P. J.; Goodenough, J. B.  $\text{Li}_x\text{CoO}$  ( $0 < x < 1$ ): A NEW CATHODE MATERIAL FOR BATTERIES OF HIGH ENERGY DENSITY. *Plan. Perspect.* **1980**, 783, 789.
27. Goodenough, J. B.; Park, K.-S. The Li-Ion Rechargeable Battery: A Perspective. *J. Am. Chem. Soc.* **2013**, 135 (4), 1167–1176.
28. Nitta, N.; Wu, F.; Lee, J. T.; Yushin, G. Li-Ion Battery Materials: Present and Future. *Mater. Today* **2015**, 18 (5), 252–264.
29. Intercalation Chemistry. In *Encyclopedia of Inorganic and Bioinorganic Chemistry*; Scott, R. A., Ed.; John Wiley & Sons, Ltd: Chichester, UK, 2011; Vol. 2, p 29.
30. Reimers, J. N.; Dahn, J. R. Electrochemical and In Situ X-Ray Diffraction Studies of Lithium Intercalation in  $\text{Li}_x\text{CoO}_2$ . *J. Electrochem. Soc.* **1992**, 139 (8), 2091.
31. Shu, J.; Shui, M.; Huang, F.; Ren, Y.; Wang, Q.; Xu, D.; Hou, L. A New Look at Lithium Cobalt Oxide in a Broad Voltage Range for Lithium-Ion Batteries. *J. Phys. Chem. C* **2010**, 114 (7), 3323–3328.
32. Placke, T.; Kloepsch, R.; Dühnen, S.; Winter, M. Lithium Ion, Lithium Metal, and Alternative Rechargeable Battery Technologies: The Odyssey for High Energy Density. *J. Solid State Electrochem.* **2017**, 21 (7), 1939–1964.
33. Goodenough, J. B. Evolution of Strategies for Modern Rechargeable Batteries. *Acc. Chem. Res.* **2013**, 46 (5), 1053–1061.
34. Zheng, J.; Tang, T.; Zhao, Q.; Liu, X.; Deng, Y.; Archer, L. A. Physical Orphaning versus Chemical Instability: Is Dendritic Electrodeposition of Li Fatal? *ACS Energy Lett.* **2019**, 4 (6), 1349–1355.
35. Yang, Y.; Bremner, S.; Menictas, C.; Kay, M. Battery Energy Storage System Size Determination in Renewable Energy Systems: A Review. *Renewable Sustainable Energy Rev.* **2018**, 91, 109–125.
36. Deng, J.; Bae, C.; Denlinger, A.; Miller, T. Electric Vehicles Batteries: Requirements and Challenges. *Joule* **2020**, 4 (3), 511–515.
37. Gummow, R. J.; Vamvounis, G.; Kannan, M. B.; He, Y. Calcium-Ion Batteries: Current State-of-the-Art and Future Perspectives. *Adv. Mater.* **2018**, 30 (39), e1801702.
38. Hwang, J.-Y.; Myung, S.-T.; Sun, Y.-K. Sodium-Ion Batteries: Present and Future. *Chem. Soc. Rev.* **2017**, 46 (12), 3529–3614.

39. Yoo, H. D.; Shterenberg, I.; Gofer, Y.; Gershinshy, G.; Pour, N.; Aurbach, D. Mg Rechargeable Batteries: An on-Going Challenge. *Energy Environ. Sci.* **2013**, *6* (8), 2265–2279.
40. Maroni, F.; Dongmo, S.; Gauckler, C.; Marinaro, M.; Wohlfahrt-Mehrens, M. Through the Maze of Multivalent-ion Batteries: A Critical Review on the Status of the Research on Cathode Materials for Mg<sup>2+</sup> and Ca<sup>2+</sup> Ions Insertion. *Batter. Supercaps* **2021**, *4* (8), 1221–1251.
41. Hosein, I. D. The Promise of Calcium Batteries: Open Perspectives and Fair Comparisons. *ACS Energy Lett.* **2021**, 1560–1565.
42. Canepa, P.; Sai Gautam, G.; Hannah, D. C.; Malik, R.; Liu, M.; Gallagher, K. G.; Persson, K. A.; Ceder, G. Odyssey of Multivalent Cathode Materials: Open Questions and Future Challenges. *Chem. Rev.* **2017**, *117* (5), 4287–4341.
43. Park, J.; Xu, Z.-L.; Yoon, G.; Park, S. K.; Wang, J.; Hyun, H.; Park, H.; Lim, J.; Ko, Y.-J.; Yun, Y. S.; Kang, K. Stable and High-Power Calcium-Ion Batteries Enabled by Calcium Intercalation into Graphite. *Adv. Mater.* **2019**, e1904411.
44. Ji, B.; He, H.; Yao, W.; Tang, Y. Recent Advances and Perspectives on Calcium-Ion Storage: Key Materials and Devices. *Adv. Mater.* **2021**, *33* (2), e2005501.
45. Arroyo-de Dompablo, M. E.; Ponrouch, A.; Johansson, P.; Palacín, M. R. Achievements, Challenges, and Prospects of Calcium Batteries. *Chem. Rev.* **2019**. <https://doi.org/10.1021/acs.chemrev.9b00339>.
46. Rong, Z.; Malik, R.; Canepa, P.; Sai Gautam, G.; Liu, M.; Jain, A.; Persson, K.; Ceder, G. Materials Design Rules for Multivalent Ion Mobility in Intercalation Structures. *Chem. Mater.* **2015**, *27* (17), 6016–6021.
47. Lakhnot, A. S.; Panchal, R. A.; Datta, J.; Mahajani, V.; Bhimani, K.; Jain, R.; Datta, D.; Koratkar, N. Intercalation Hosts for Multivalent-ion Batteries. *Small Struct.* **2022**, 2200290.
48. Chen, S.; Zhao, D.; Chen, L.; Liu, G.; Ding, Y.; Cao, Y.; Chen, Z. Emerging Intercalation Cathode Materials for Multivalent Metal-ion Batteries: Status and Challenges. *Small Structures* **2021**, No. sstr.202100082, 2100082.
49. Rutt, A.; Shen, J.-X.; Horton, M.; Kim, J.; Lin, J.; Persson, K. A. Expanding the Material Search Space for Multivalent Cathodes. *ACS Appl. Mater. Interfaces* **2022**, *14* (39), 44367–44376.
50. Tojo, T.; Sugiura, Y.; Inada, R.; Sakurai, Y. Reversible Calcium Ion Batteries Using a Dehydrated Prussian Blue Analogue Cathode. *Electrochim. Acta* **2016**, *207*, 22–27.

51. Li, Y.; Dang, Q.; Chen, W.; Tang, L.; Hu, M. Recent Advances in Rechargeable Batteries with Prussian Blue Analogs Nanoarchitectonics. *J. Inorg. Organomet. Polym. Mater.* **2021**, *31* (5), 1877–1893.
52. Tekliye, D. B.; Kumar, A.; Weihang, X.; Mercy, T. D.; Canepa, P.; Gautam, G. S. Exploration of NaSICON Frameworks as Calcium-Ion Battery Electrodes, 2022.
53. Chen, C.; Shi, F.; Zhang, S.; Su, Y.; Xu, Z.-L. Ultrastable and High Energy Calcium Rechargeable Batteries Enabled by Calcium Intercalation in a NASICON Cathode. *Small* **2022**, 2107853.
54. Nagappan, S.; Duraivel, M.; Elayappan, V.; Muthuchamy, N.; Mohan, B.; Dhakshinamoorthy, A.; Prabakar, K.; Lee, J.-M.; Park, K. H. Metal–organic Frameworks-based Cathode Materials for Energy Storage Applications: A Review. *Energy Technol.* **2023**, 2201200.
55. Ye, H.; Li, Y. Review on Multivalent Rechargeable Metal–Organic Batteries. *Energy Fuels* **2021**, *35* (9), 7624–7636.
56. Das, T.; Tosoni, S.; Pacchioni, G. Layered Oxides as Cathode Materials for beyond-Li Batteries: A Computational Study of Ca and Al Intercalation in Bulk V<sub>2</sub>O<sub>5</sub> and MoO<sub>3</sub>. *Comput. Mater. Sci.* **2021**, *191*, 110324.
57. Park, H.; Bartel, C. J.; Ceder, G.; Zapol, P. Layered Transition Metal Oxides as ca Intercalation Cathodes: A Systematic First-principles Evaluation. *Adv. Energy Mater.* **2021**, 2101698.
58. Zhao, X.; Mao, L.; Cheng, Q.; Liao, F.; Yang, G.; Lu, X.; Chen, L. Interlayer Engineering of Preintercalated Layered Oxides as Cathode for Emerging Multivalent Metal-Ion Batteries: Zinc and Beyond. *Energy Storage Materials* **2021**, *38*, 397–437.
59. Xiong, Y.; Lin, Y.; Xue, Q. Review—Open-Framework Structure Based Cathode Materials Coupled with Metallic Anodes for Rechargeable Multivalent Ion Batteries. *J. Electrochem. Soc.* **2020**, *167* (16), 160530.
60. Lu, W.; Wang, J.; Sai Gautam, G.; Canepa, P. Searching Ternary Oxides and Chalcogenides as Positive Electrodes for Calcium Batteries. *Chem. Mater.* **2021**, *33* (14), 5809–5821.
61. Sickafus, K. E.; Wills, J. M.; Grimes, N. W. Structure of Spinel. *J. Am. Ceram. Soc.* **2004**, *82* (12), 3279–3292.
62. Liu, M.; Rong, Z.; Malik, R.; Canepa, P.; Jain, A.; Ceder, G.; Persson, K. A. Spinel Compounds as Multivalent Battery Cathodes: A Systematic Evaluation Based on Ab Initio Calculations. *Energy Environ. Sci.* **2015**, *8* (3), 964–974.

63. Ling, C.; Mizuno, F. Phase Stability of Post-Spinel Compound  $\text{AMn}_2\text{O}_4$  (A = Li, Na, or Mg) and Its Application as a Rechargeable Battery Cathode. *Chem. Mater.* **2013**, *25* (15), 3062–3071.
64. Dompablo, M. E. A.; Krich, C.; Nava-Avendaño, J.; Biškup, N.; Palacín, M. R.; Bardé, F. A Joint Computational and Experimental Evaluation of  $\text{CaMn}_2\text{O}_4$  Polymorphs as Cathode Materials for Ca Ion Batteries. *Chem. Mater.* **2016**, *28* (19), 6886–6893.
65. Peled, E.; Menkin, S. Review—SEI: Past, Present and Future. *J. Electrochem. Soc.* **2017**, *164* (7), A1703.
66. Wang, A.; Kadam, S.; Li, H.; Shi, S.; Qi, Y. Review on Modeling of the Anode Solid Electrolyte Interphase (SEI) for Lithium-Ion Batteries. *npj Computational Materials* **2018**, *4* (1), 1–26.
67. Meitav, A.; Peled, E. Solid Electrolyte Interphase (SEI) electrode—V. the Formation and Properties of the Solid Electrolyte Interphase on Calcium in Thionyl Chloride Solutions. *Electrochim. Acta* **1988**, *33* (8), 1111–1121.
68. Song, H.; Wang, C. Current Status and Challenges of Calcium Metal Batteries. *Adv Energy and Sustain Res* **2022**, 2100192.
69. Melemed, A. M.; Khurram, A.; Gallant, B. M. Current Understanding of Nonaqueous Electrolytes for Calcium-Based Batteries. *Batter Supercaps* **2020**, *3* (7), 570–580.
70. Ponrouch, A.; Frontera, C.; Bardé, F.; Palacín, M. R. Towards a Calcium-Based Rechargeable Battery. *Nat. Mater.* **2016**, *15* (2), 169–172.
71. Biria, S.; Pathreker, S.; Li, H.; Hosein, I. D. Plating and Stripping of Calcium in an Alkyl Carbonate Electrolyte at Room Temperature. *ACS Appl. Energy Mater.* **2019**, *2* (11), 7738–7743.
72. Wei, Q.; Zhang, L.; Sun, X.; Liu, T. L. Progress and Prospects of Electrolyte Chemistry of Calcium Batteries. *Chem. Sci.* **2022**, *13* (20), 5797–5812.
73. Shyamsunder, A.; Blanc, L. E.; Assoud, A.; Nazar, L. F. Reversible Calcium Plating and Stripping at Room Temperature Using a Borate Salt. *ACS Energy Letters* **2019**, *4* (9), 2271–2276.
74. Ta, K.; Zhang, R.; Shin, M.; Rooney, R. T.; Neumann, E. K.; Gewirth, A. A. Understanding Ca Electrodeposition and Speciation Processes in Nonaqueous Electrolytes for Next-Generation Ca-Ion Batteries. *ACS Appl. Mater. Interfaces* **2019**, *11* (24), 21536–21542.

75. Melemed, A. M.; Skiba, D. A.; Gallant, B. M. Toggling Calcium Plating Activity and Reversibility through Modulation of Ca<sup>2+</sup> Speciation in Borohydride-Based Electrolytes. *J. Phys. Chem. C* **2022**. <https://doi.org/10.1021/acs.jpcc.1c09400>.
76. Pu, S. D.; Gong, C.; Gao, X.; Ning, Z.; Yang, S.; Marie, J.-J.; Liu, B.; House, R. A.; Hartley, G. O.; Luo, J.; Bruce, P. G.; Robertson, A. W. Current-Density-Dependent Electroplating in Ca Electrolytes: From Globules to Dendrites. *ACS Energy Lett.* **2020**, *5* (7), 2283–2290.
77. Song, H.; Su, J.; Wang, C. Hybrid Solid Electrolyte Interphases Enabled Ultralong Life Ca-Metal Batteries Working at Room Temperature. *Adv. Mater.* **2021**, *33* (2), e2006141.
78. Song, H.; Wang, C. Artificial Hybrid Solid Electrolyte Mediated Ca-metal for Ultra-durable Room-temperature 5 V Calcium Batteries. *Energy Environ. Mater.* **2021**. <https://doi.org/10.1002/eem2.12325>.
79. Song, H.; Su, J.; Wang, C. Multi-ions Electrolyte Enabled High Performance Voltage Tailorable Room-temperature Ca-metal Batteries. *Adv. Energy Mater.* **2021**, *11* (10), 2003685.

## **CHAPTER 2**

# **DESIGN AND VALIDATION OF IN SITU X-RAY DIFFRACTION CELL**

## 2.1 Introduction

Lithium-ion batteries since their commercialization in 1991 have fundamentally changed our everyday lives.<sup>[1]</sup> They power an ever-expanding range of technologies and are the dominant battery chemistry we depend on. To further the number of applications for these batteries, research continues exploring how to optimize these systems. Data on how battery electrodes behave as a function of cycling and degradation mechanisms provide critical insights into strategies for improving lithium-ion batteries.<sup>[2]</sup>

The common mechanism of lithium-ion batteries is the use of intercalation chemistry which is the reversible insertion and removal of ions with a host structure. The shuttling of ions within the host structure causes the breaking and reforming of bonds and can also lead to volumetric changes in the electrode.<sup>[3]</sup> The resulting structural changes that occur in an electrode because of intercalation chemistry are tracked on the atomic scale using X-ray diffraction (XRD). Depending on the degree of charge cycled with the electrode, phase changes can occur with the crystal structure along with other events such as microcracking. These permanent changes to the crystal structure have large impacts on the reversible capacity of the electrode and its lifetime.<sup>[4]</sup> The research into optimizing the performance and lifetime of lithium-ion batteries has relied heavily on techniques such as XRD to identify events that occur within the electrode as it is cycled.

The use of XRD to track structural changes in an electrode have typically been *ex situ* characterizations which involve the assembly and disassembly of a battery. While insightful, limitations to the characterization approach exist. The use of snapshots of an electrode after it is removed from the battery configuration do not accurately represent the electrode as it is being cycled. Factors such as atmospheric contamination or relaxation of the electrodes may take effect and limit the conclusions that can be drawn from the data. Operando characterization of an electrode provides critical information into the behavior of an electrode as it exists assembled

within a battery. While operando cells provide invaluable information into the performance of an electrode, the design and functionality of the cell must meet criteria for successful electrochemical operation and use in the X-ray diffractometer.<sup>[5-7]</sup>

Several strategies for operando XRD cells have been developed to track the behavior of electrodes as they are cycled.<sup>[8-14]</sup> Most notably, coin cells and pouch cells for batteries have been modified with an opening that is sealed with Kapton tape. These inexpensive solutions address a number of considerations for an in situ cell. Coin cells and pouch cells are easy to assemble inside of a glovebox. The kapton tape serves as a transparent window for x-rays to penetrate and the kapton tape itself is inert with electrochemical components. The drawbacks of such approaches include the kapton tape not being rigid enough to handle the distribution of pressure inside the cell, which causes variations in the structural data collected. Additionally, the thin film of kapton tape allows for x-rays to penetrate different components of the electrochemical cell, making it difficult to discern which components contribute to the XRD spectra taken.<sup>[7,15]</sup> Other strategies for in situ cells have involved the assembly of swagelok-type cells with beryllium windows. These designs are effective at maintaining uniform pressure distributions within the cell and the beryllium window is transparent to x-rays. However, the continued use of beryllium does eventually cause the window to oxidize and become toxic.<sup>[7]</sup> Other windows such as glassy carbon have been used for XRD analysis in transmission and reflection modes.<sup>[9,16]</sup> Glassy carbon is particularly attractive since it is electrochemically inert, electrically conductive, structurally rigid and does not form any toxic byproducts with its use. In addition to the criteria set by the transparent XRD window, an in situ cell needs to be easy to assemble, fit within the XRD diffractometer chamber, align with the XRD beamline, and achieve reproducible results.

Here, we propose an in situ cell and cell holder that can operate in XRD reflection geometry. The inexpensive in situ cell and in situ cell holder are fabricated from stock sources commercially available. Glassy carbon is used as the in situ cell window. The in situ cell is easily assembled inside of a glovebox and the in situ cell holder can easily fit with the goniometer of an X-ray diffractometer while also adjusting the height of the in situ cell. The functionality of the in situ cell is verified with the electrochemical cycling of lithium cobalt oxide ( $\text{LiCoO}_2$ ) as the working electrode and lithium metal (Li) as the counter electrode. The reversible capacity of the  $\text{LiCoO}_2$  is demonstrated with XRD spectra that successfully tracks the structural changes to the electrode as lithium is cycled. This demonstration of the in situ cell serves as an effective means for tracking other cathode materials as they are cycled.

## **2.2 Materials and Methods**

### **2.2.1 Materials**

Lithium Cobalt Oxide ( $\text{LiCoO}_2$ ), 3Å molecular sieves and Polytetrafluoroethylene (PTFE) preparation (60% wt) were purchased from Sigma-Aldrich. Additionally, the lithium electrolyte of Lithium Hexafluorophosphate ( $\text{LiPF}_6$ ) in a binary mixture of Ethylene Carbonate (EC) and Dimethyl Carbonate (DMC) was also purchased from Sigma-Aldrich. Super P Carbon Black and 15 mm Lithium metal chips were purchased from MTI Corporation, USA. Glassy carbon (Sigradur-G) disks were used as the XRD window for the in situ cell and were purchased from Hochtemperatur-Werkstoffe GmbH (HTW). All materials used in the construction of the in situ cell, including the 316 stainless steel spring and PTFE o-rings, were purchased from McMaster-Carr.

### 2.2.2 Electrode Preparation

To prepare a freestanding electrode, powders of  $\text{LiCoO}_2$  (65% wt) and carbon black (5% wt) were mixed with PTFE Binder (30% wt).<sup>[16,17]</sup> The active material was mixed with carbon black in a ball miller. The components were mixed at 19.67 Hz for 90 minutes.<sup>[18]</sup> After ball milling, the mixture was placed in a mortar and pestle where PTFE binder was added and suspended in excess ethanol. The materials were mixed until all excess ethanol evaporated. The freestanding electrode would then be processed in a hot roll press at 80°C and subsequently vacuum dried overnight at 80°C.

### 2.2.3 Electrolyte Preparation

The electrolyte used in all electrochemistry experiments was 1.0 M  $\text{Li}(\text{PF}_6)$  in EC/DMC. As the stock electrolyte was purchased from Sigma-Aldrich, the only modification needed was to dry the electrolyte over 3 Å molecular sieves for 48 hours to remove any residual moisture. Water content in the electrolyte was evaluated and found to be below 50 ppm using a Karl Fischer Titrator (899 Coulometer, Metrohm).

### 2.2.4 Electrochemistry

Galvanostatic experiments were carried out with the two-electrode in situ cell setup with  $\text{LiCoO}_2$  as the working electrode (5 mm diameter) and lithium metal (Li) as the counter electrode (15 mm diameter). 80  $\mu\text{L}$  of 1.0 M  $\text{Li}(\text{PF}_6)$  in EC/DMC was used with the in situ cell and all assemblies were performed in an argon filled glovebox. Testing began with a 2 hour open circuit voltage to allow components to equilibrate before testing. In situ cell cycling was performed on an Arbin battery tester at room temperature with a c-rate of C/40 and cutoff voltages of 3.0 V (v.  $\text{Li}/\text{Li}^+$ ) and 4.2 V (v.  $\text{Li}/\text{Li}^+$ ). The upper and lower limits of the voltages are selected based on the extensive

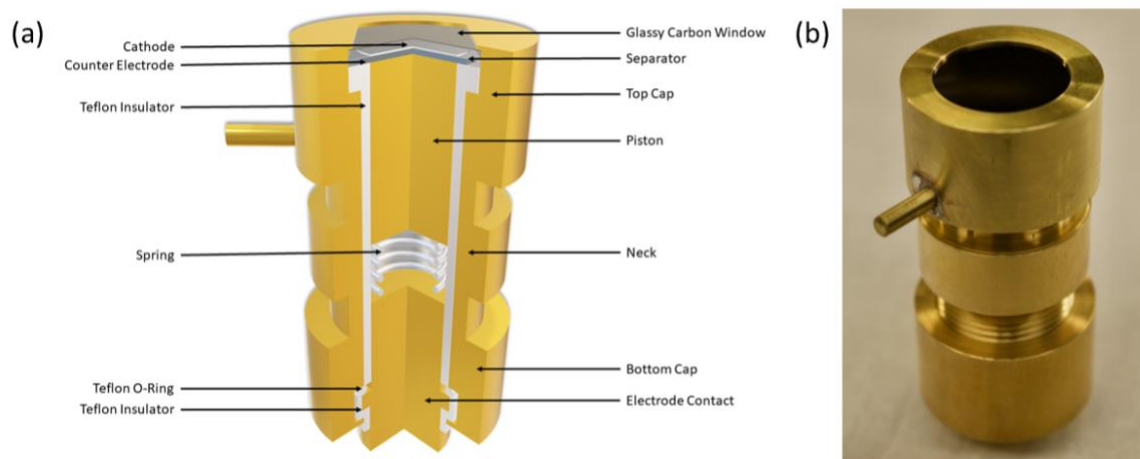
research that has been already performed on  $\text{LiCoO}_2$  and preventing overcharging and overdischarging.<sup>[19]</sup>

### **2.2.5 Electrode Characterization**

A Rigaku Miniflex diffractometer was used for the collection of X-ray diffraction data. Copper (Cu)  $K\alpha$  radiation was used to collect data in the range of  $10\text{-}80^\circ$  at a scan rate of  $5^\circ/\text{min}$ . Once the charging or discharging of the  $\text{LiCoO}_2$  was completed, the in situ cell was placed inside of the Rigaku XRD. The XRD data collection was performed at room temperature. In situ XRD measurements were performed with a custom in situ cell. (Figure 2.1) Rietveld refinement of each material was performed using Highscore Plus software.<sup>[20]</sup> The Materials Project was used for the identification of phases.<sup>[21]</sup>

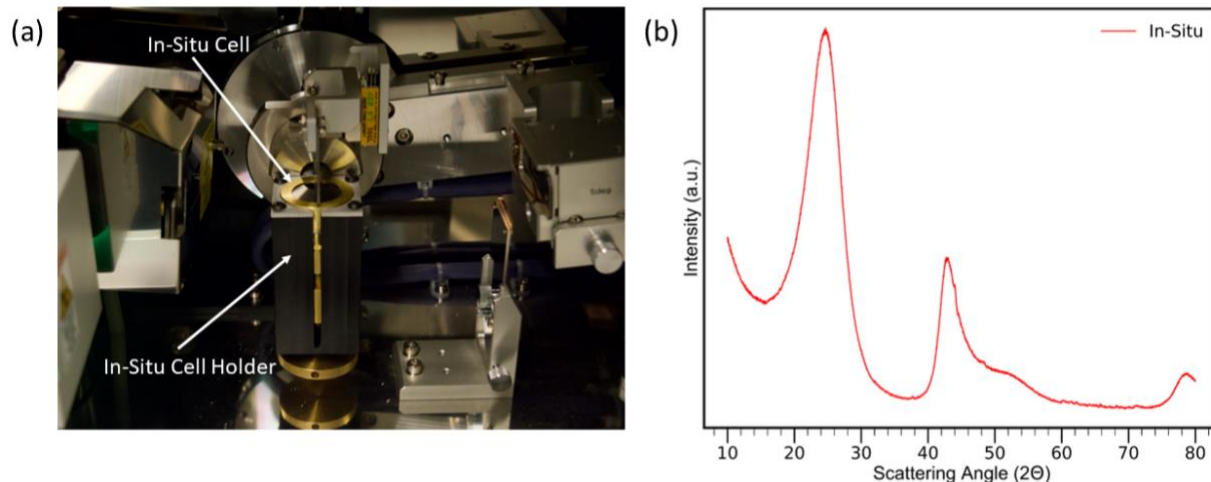
### **2.2.6 In situ Cell and Sample Holder Design**

Figure 2.1a is a schematic of the fabricated in situ cell and Figure 2.1b is a photo of the assembled in situ cell. The design of the cell is a modified version of an in situ cell developed by Sottman.<sup>[16]</sup> Beryllium windows were not used for the in situ cell due to their toxicity and, instead, glassy carbon was used. The glassy carbon from HTW has a thickness of 0.0415 inches and a diameter of 0.875 inches. The thickness of the glassy carbon is sufficient to allow x-rays to penetrate the window while also being rigid enough to prevent any uneven pressure distribution inside the in situ cell. The aperture of the in situ cell has a width of 0.5906 inches and manages to be larger than the irradiated area width of 0.4331 inches, making sure that all of the XRD measurements generated are from the glassy carbon and working electrode only. The glassy carbon window has a considerable amorphous background below  $30^\circ$  ( $2\theta$ ) in the XRD pattern and can be observed in Figure 2.2b.



**Figure 2.1** - In situ cell a) Schematic of in situ XRD cell b) Photo of assembled in situ cell

The battery components inside of the in situ cell are assembled below the glassy carbon window and can also be viewed in the schematic of Figure 2.1a. The working electrode is assembled directly underneath the glassy carbon window. To avoid any overlapping XRD reflections, the working electrode is processed as a freestanding electrode and is placed directly on the glassy carbon.<sup>[16,17]</sup> Beneath the working electrode, an electrolyte soaked separator maintains a physical barrier between the working and counter electrode. Contact between the working and counter electrodes are maintained by a stainless steel spring and brass piston. Teflon (PTFE) is used for its chemically and electrically inert nature, serving as insulation between components of the in situ cell and preventing short circuits. The casing of the in situ cell being brass, along with the glassy carbon, serve as an electrical contact for the working electrode while the brass piston and stainless steel spring serve as contact for the counter electrode. The teflon insulation, when contacted with the glassy carbon disk and casing, forms a hermetic seal with the in situ cell.



**Figure 2.2** - In situ cell with Rigaku Miniflex 600 a) Installation of in situ cell inside Rigaku Miniflex 600 b) XRD diffraction of baseline in situ cell

Samples analyzed with the Rigaku are mounted to a goniometer and rotated to analyze all of the different scattering angles. To fit with the goniometer in the Rigaku XRD, an in situ cell holder was fabricated using lightweight acrylonitrile butadiene styrene (ABS). The in situ cell was placed inside of the in situ cell holder and the installation of both inside the Rigaku diffractometer can be seen in Figure 2.2a. Deviations in the placement of the height of the in situ cell can result in erroneous  $2\theta$  shifts of several reflections. As a result, the height of the in situ cell inside of the cell holder needs to be set to the same height for each scan and can be adjusted using a wheel that is under the cell holder. A full turn of the in situ cell wheel corresponds to a height correction of 0.0197 inches. The in situ cell also has a small protruding rod that keeps the in situ cell properly aligned as it is installed inside the in situ cell holder. Design files for all components of the in situ cell and in situ cell holder are outlined in the Supplemental Information (Figure SI 2.1 - SI 2.18)

The  $\text{LiCoO}_2$  was fabricated using the previously mentioned protocol for fabricating freestanding electrodes. The freestanding electrode, lithium metal and in situ cell were all assembled inside of an argon filled glovebox. Once assembled, a baseline scan of the  $\text{LiCoO}_2$  inside of the in situ cell

was taken and compared to the powder pattern of LiCoO<sub>2</sub>. The comparisons between LiCoO<sub>2</sub> powder and the in situ cell are outlined in Figure 2.3 Rietveld refinement<sup>[22-25]</sup> was performed on the LiCoO<sub>2</sub> and identified the sample with space group R-3m (mp-22526) and the following lattice parameters: a = 2.814878 Å, b = 2.814878 Å, and c = 14.044620 Å.

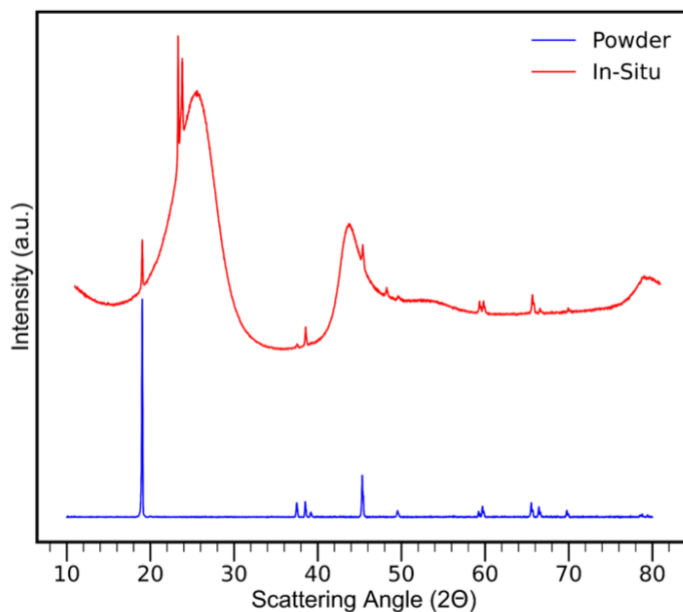


**Figure 2.3** - XRD diffraction of the LiCoO<sub>2</sub> powder and freestanding electrode as it is assembled inside of in situ cell

The highly amorphous nature of the glassy carbon makes direct analysis of the XRD peaks difficult. The in situ XRD spectra serves as a more qualitative means of tracking structural changes to the electrode. To provide a slightly more quantitative analysis into the behavior of the electrodes, a python script was developed for analyzing individual peaks. The python script itself would implement a background subtraction of the glassy carbon and subsequently deconvolute peaks using Gaussian functions. This analysis was used for tracking the peak splitting observed with the (003) lattice planes of the LiCoO<sub>2</sub>. More quantitative means of analyzing the lithium occupancy and lattice parameters would require the coordination of ex situ studies and generating theoretical

patterns of different occupancies of the LiCoO<sub>2</sub> to serve as a library of reflections to match the in situ patterns to. This level of analysis was beyond the scope of the LiCoO<sub>2</sub> cathode work for validating the in situ cell and instead relied on previously published literature for the LiCoO<sub>2</sub> behavior as it was cycled inside of the in situ cell.

### **2.3 Results and Discussion**

The results of cycling LiCoO<sub>2</sub> are summarized in Figure 2.4. The LiCoO<sub>2</sub> was cycled 10 times at a c-rate of C/40 with a reversible capacity of 32 mAh/g. The achieved capacity is approximately 11% of the total theoretical capacity capable of LiCoO<sub>2</sub> (274 mAh/g). The charging profile seen in Figure 2.4b identifies 1 charging plateau at 3.98 V (v. Li/Li<sup>+</sup>) that decreases over the lifetime of cycling. The discharge profile of LiCoO<sub>2</sub> has two plateaus of activity. One plateau approximately at 3.88 V (v. Li/Li<sup>+</sup>) and another at 3.82 V (v. Li/Li<sup>+</sup>), indicative of some phase change that occurs with the cathode over the course of cycling.<sup>[26]</sup> Numerous studies on LiCoO<sub>2</sub> have been able to reversibly cycle 50% of the lithium inside of the electrode which produces more substantial structural changes with the electrode that can be observed with XRD.<sup>[19,26,27]</sup> The gap in performance between the in situ cell and established literature values for LiCoO<sub>2</sub> is likely due to issues with the electrode fabrication.<sup>[27]</sup> Maximizing the achievable capacity of the LiCoO<sub>2</sub> depends strongly on the optimization of active material within the electrode. Future iterations of the work would require modifications between the amount of binder used and the total active material for the electrode.

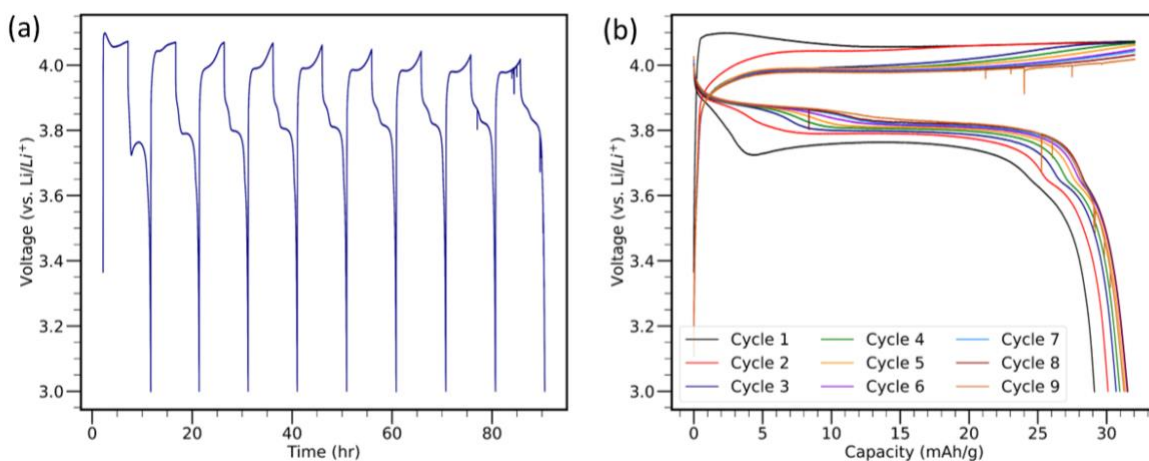


**Figure 2.4** - LiCoO<sub>2</sub> cycling inside of in situ cell a) Voltage-time curves with 10 cycles of testing b) Voltage-capacity curves for the LiCoO<sub>2</sub>

Between charge and discharge cycles of the LiCoO<sub>2</sub>, the in situ cell was analyzed with the Rigaku Miniflex 600 XRD. To track the structural changes of the LiCoO<sub>2</sub> between each half cycle, the in situ XRD was analyzed immediately at the conclusion of either charging or discharging. Ideal operation of the in situ cell would involve the combined cycling of the cathode and simultaneous XRD spectra to best capture the performance of the electrode. Due to the physical constraints of the benchtop XRD, the in situ cell was analyzed following the charging and discharging of the cell. An overview of all the structural changes that occur with LiCoO<sub>2</sub> as a function of cycling is outlined in Figure 2.5.

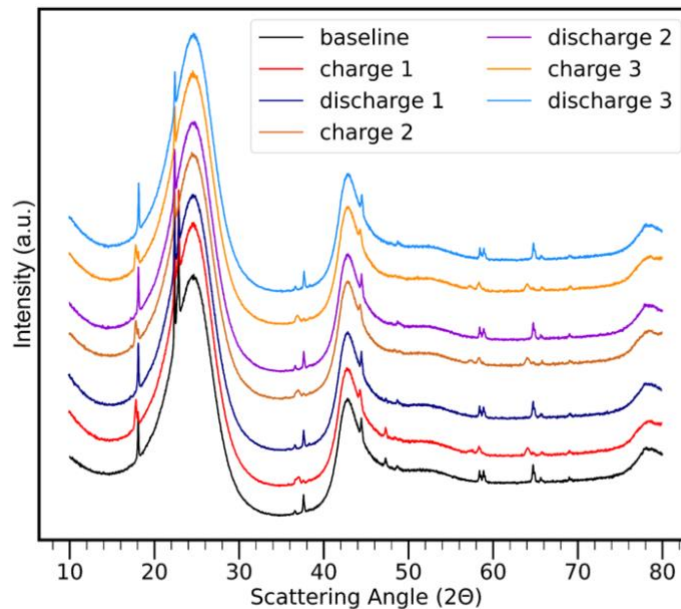


**Figure 2.5** - In situ XRD diffraction of LiCoO<sub>2</sub> cathode as it is charged and discharged

Focusing on one of the most prominent reflections of LiCoO<sub>2</sub>, the (003) lattice planes are recorded at approximately 18.1° (2θ). The results from the LiCoO<sub>2</sub> cycling and their effect on the peak position of the (003) lattice plane are outlined in Figure 2.6a. The baseline scan of the (003) plane resolves the reflection at approximately 18.1°. Upon charging of LiCoO<sub>2</sub>, the intensity of the 18.1° reflection decreases and a secondary peak forms at 17.8°. The python script for resolving the in situ XRD reflections was implemented for deconvoluting the twin peaks, removing the amorphous background of the glassy carbon, and identifying the positions of the (003) lattice plane. The results of the deconvoluted peaks can be seen in Figure 2.6b. The development of a second peak with the (003) lattice plane to a lower diffraction angle is indicative of an increase in the d-spacing and lattice parameters of the c-axis.<sup>[26,28-30]</sup> This behavior is consistent with delithiation of LiCoO<sub>2</sub> and has been reported in numerous studies.<sup>[26,28]</sup> The continued presence of the 18.1° reflection with the 17.9° reflection outlines the coexistence of two-phases with LiCoO<sub>2</sub> as it is charged. Previous reports on this structural development concluded a partial phase change as the lithium occupancy

decreases from 0.93 to 0.75.<sup>[26]</sup> Subsequent discharging of the LiCoO<sub>2</sub> to 3.0 V (v Li/Li<sup>+</sup>) eliminated the second peak at 17.8° and increased the intensity of the 18.1° reflection back to its original value, signaling the reversibility of the intercalation chemistry and decrease of the c-axis lattice parameters (Figure 2.6a).

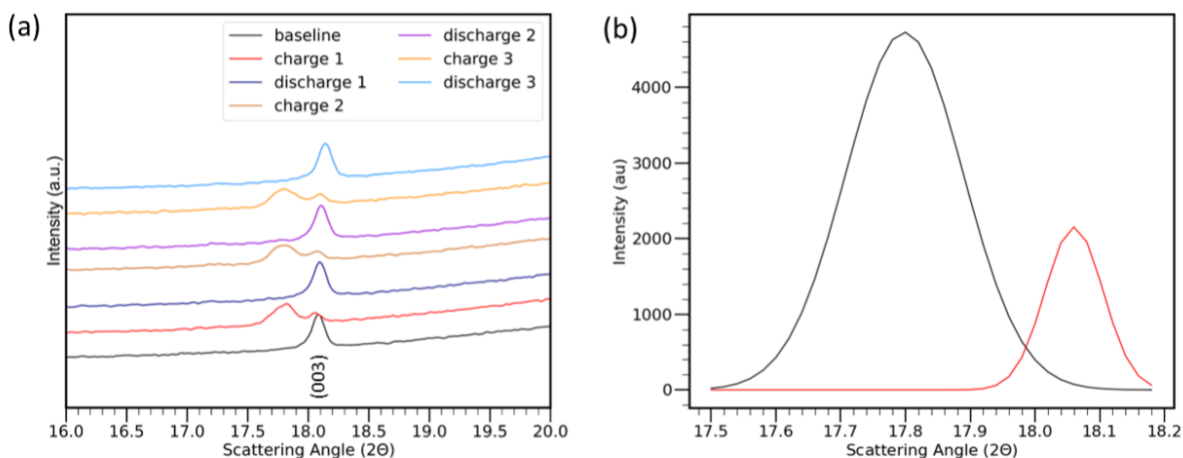


**Figure 2.6** - In situ XRD of LiCoO<sub>2</sub> during first 3 cycles of testing a) XRD evolution of the (003) lattice plane b) Deconvolution of XRD peaks after first charge of LiCoO<sub>2</sub>

Analysis of the (101) lattice planes (Figure 2.7a) did not produce a similar peak splitting that is observed with the (003) planes. This result indicates that the partial phase change of LiCoO<sub>2</sub> does not occur along the basal plane. Previous investigations into LiCoO<sub>2</sub> observed peak splitting of the (101) planes when 50% of the total lithium was removed and corresponding to the transition of LiCoO<sub>2</sub> from a rhombohedral to monoclinic crystal structure.<sup>[19,26,31]</sup> Similarly, peak splitting was not observed with the (109), (107) and (018) lattice planes and can be observed in Figure 2.7b.

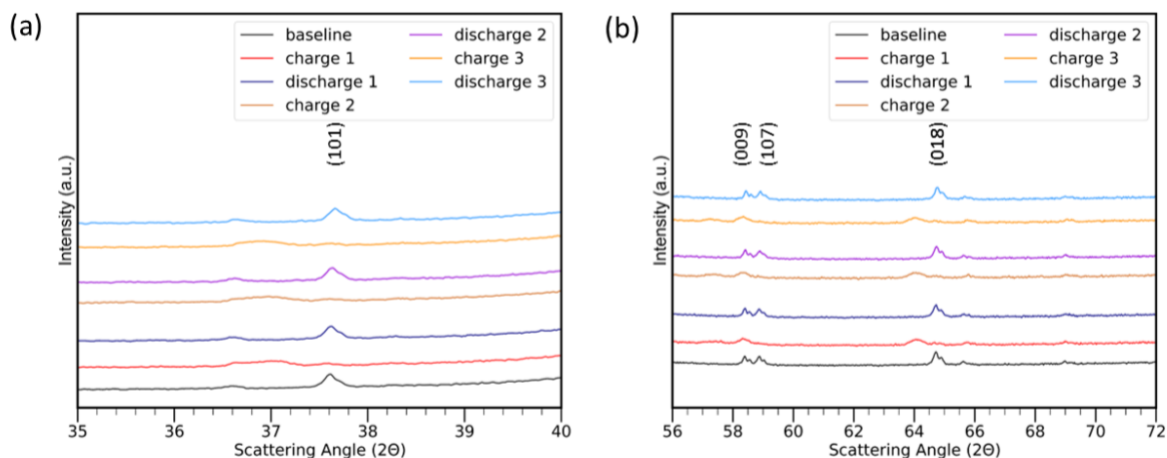


**Figure 2.7** - XRD of LiCoO<sub>2</sub> for first 3 cycles of testing a) XRD spectra of (101) lattice plane b) XRD spectra of (109), (107) and (108) planes

## 2.4 Conclusion

An in situ cell for operando X-ray diffraction studies is presented and its functionality is validated with an experimental study of a battery system with LiCoO<sub>2</sub> as the cathode and Li as the anode. Reversible capacities of 32 mAh/g with the LiCoO<sub>2</sub> are established with structural features at several diffraction angles corroborating the limited phase changes that occur with the cathode. Glassy carbon is successfully used as the transparent XRD window. The in situ cell and in situ cell holder prove to be a precise and cost-efficient means of tracking the structural changes of an electrode during cycling. Further optimizations of the electrode fabrication procedure are needed to increase the possible capacity out of the cathode and achieve capacities and c-rates that are on par with lithium battery literature.

**Supplemental Information**

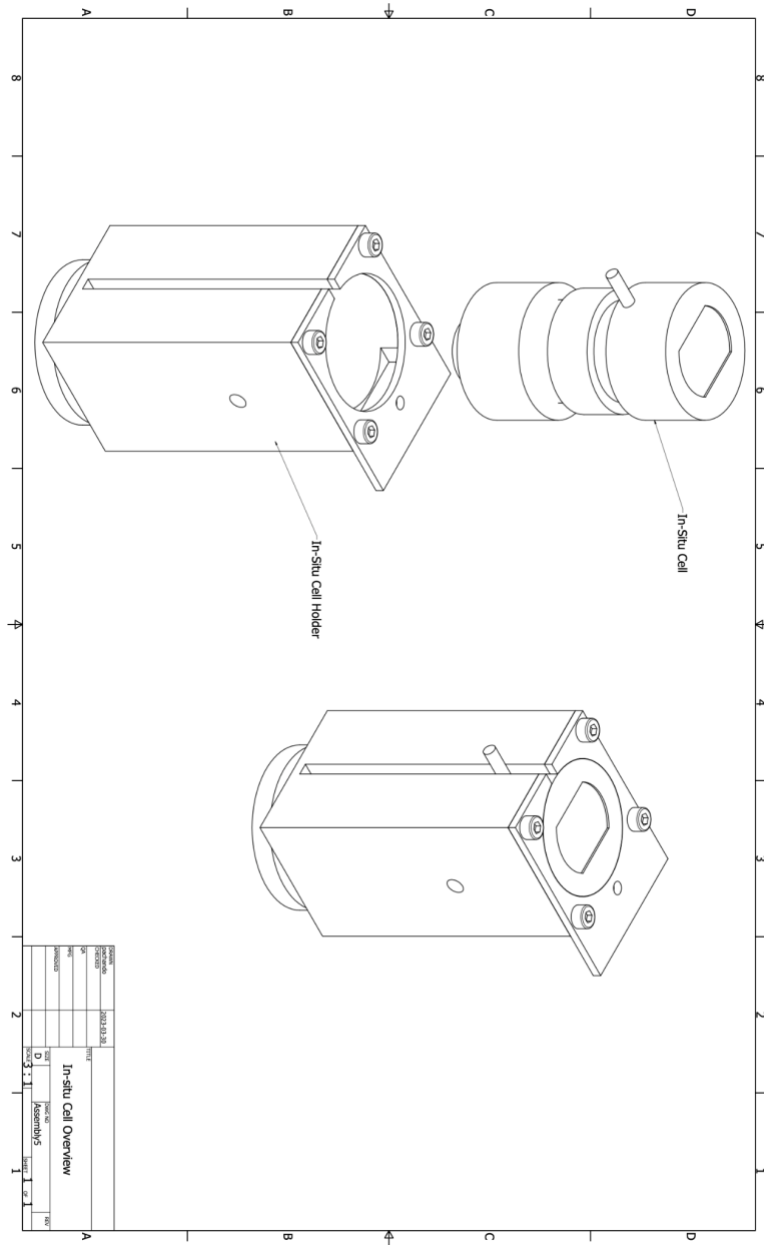


**Figure SI 2.1 - In situ cell assembly**

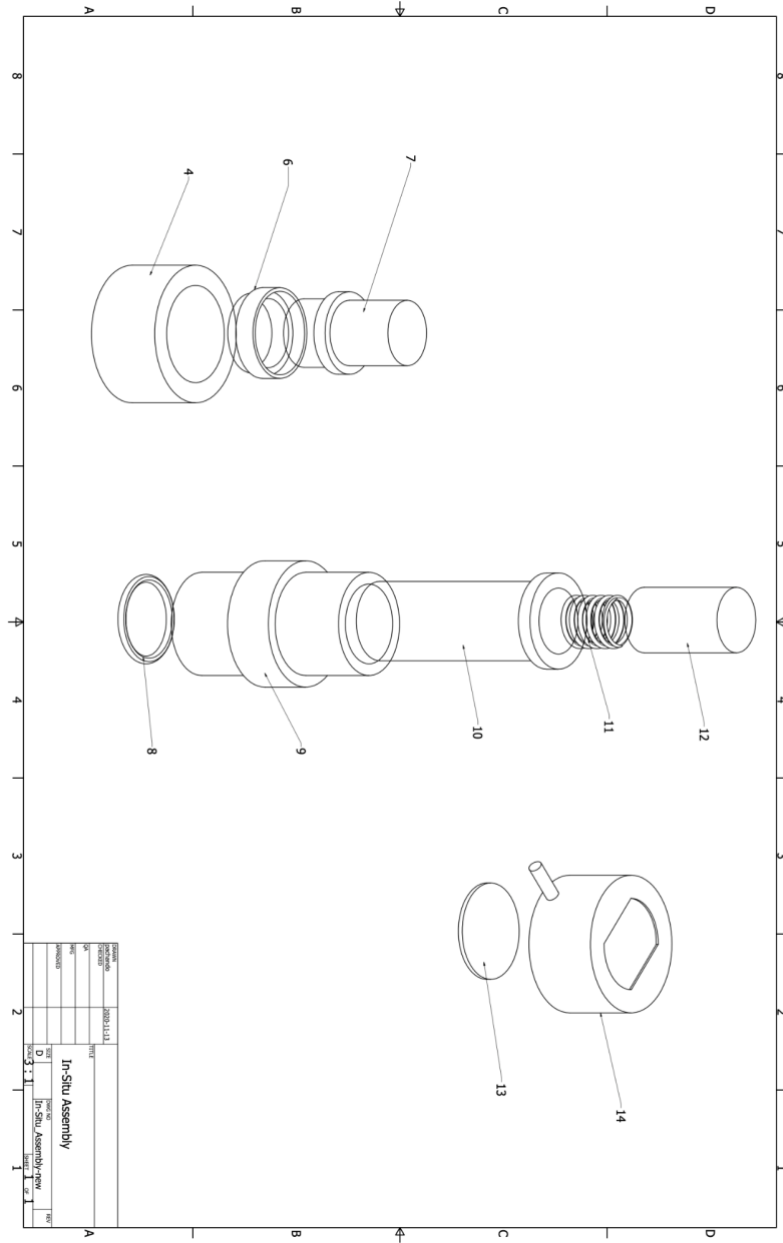


**Figure SI 2.2 - In situ cell sub-assembly**



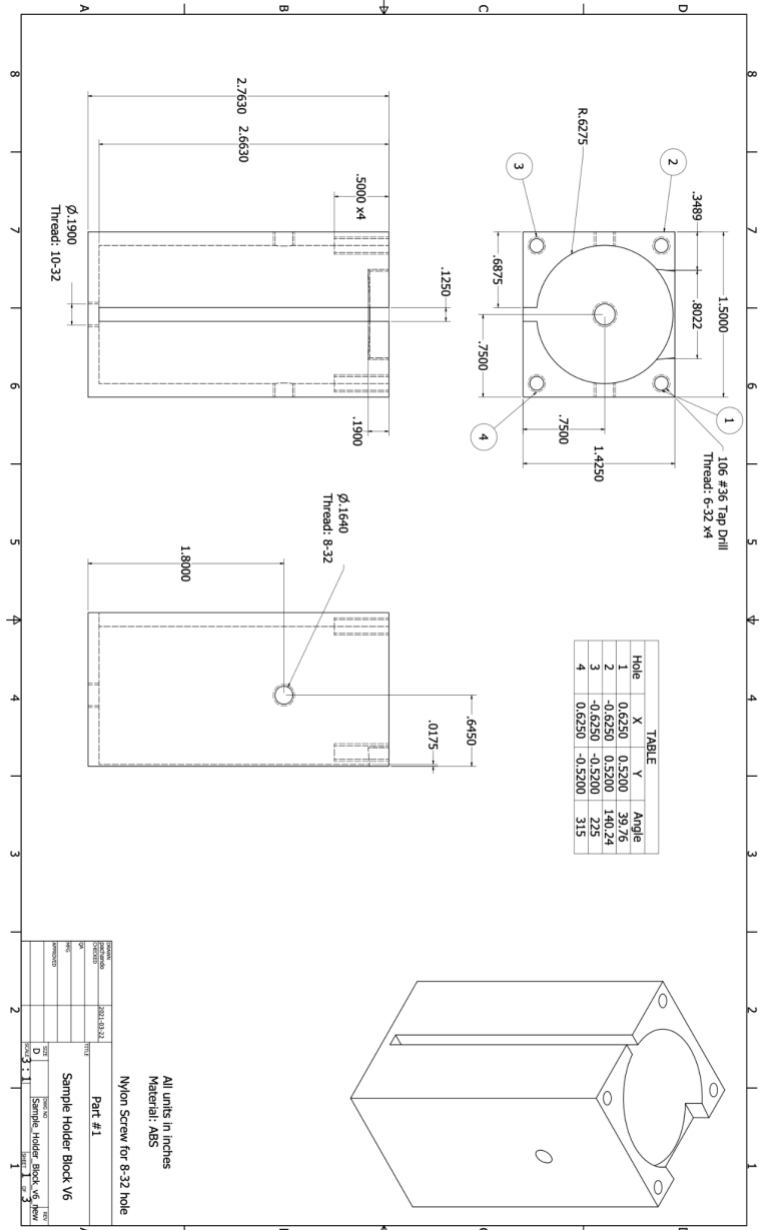


Figure SI 2.4 - Part 1 - Sample holder block

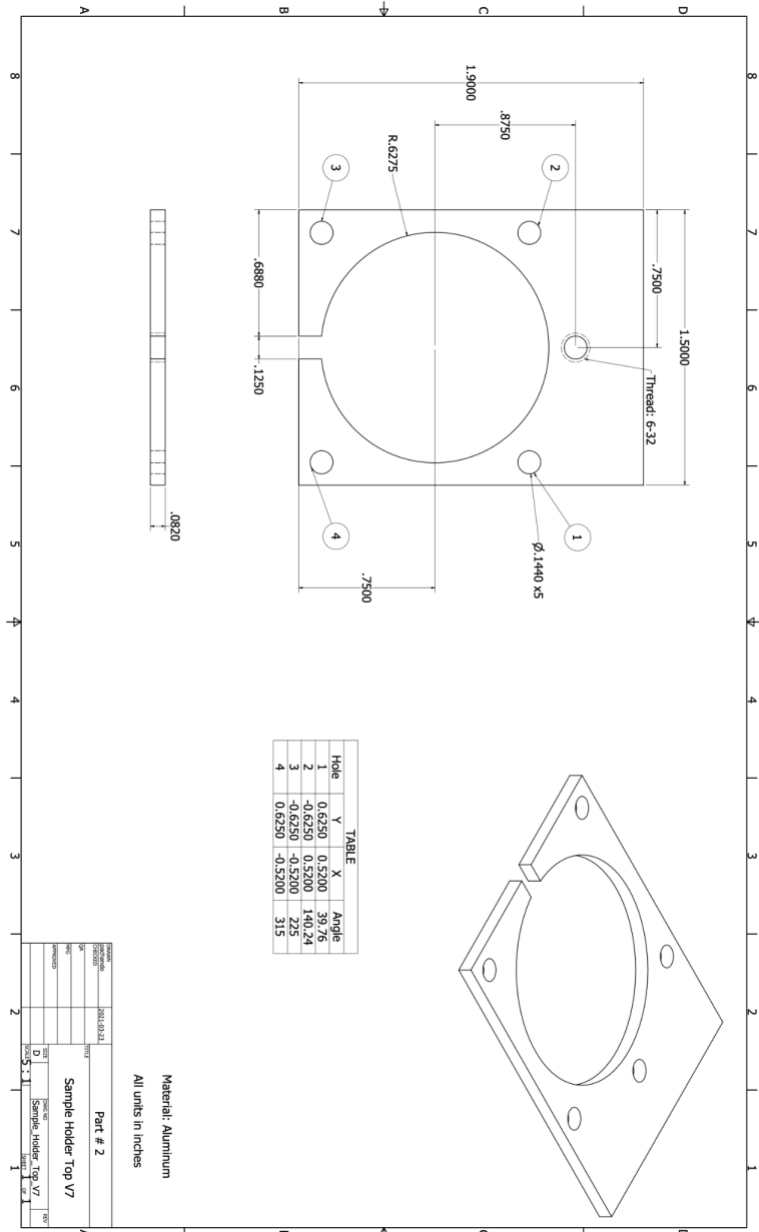
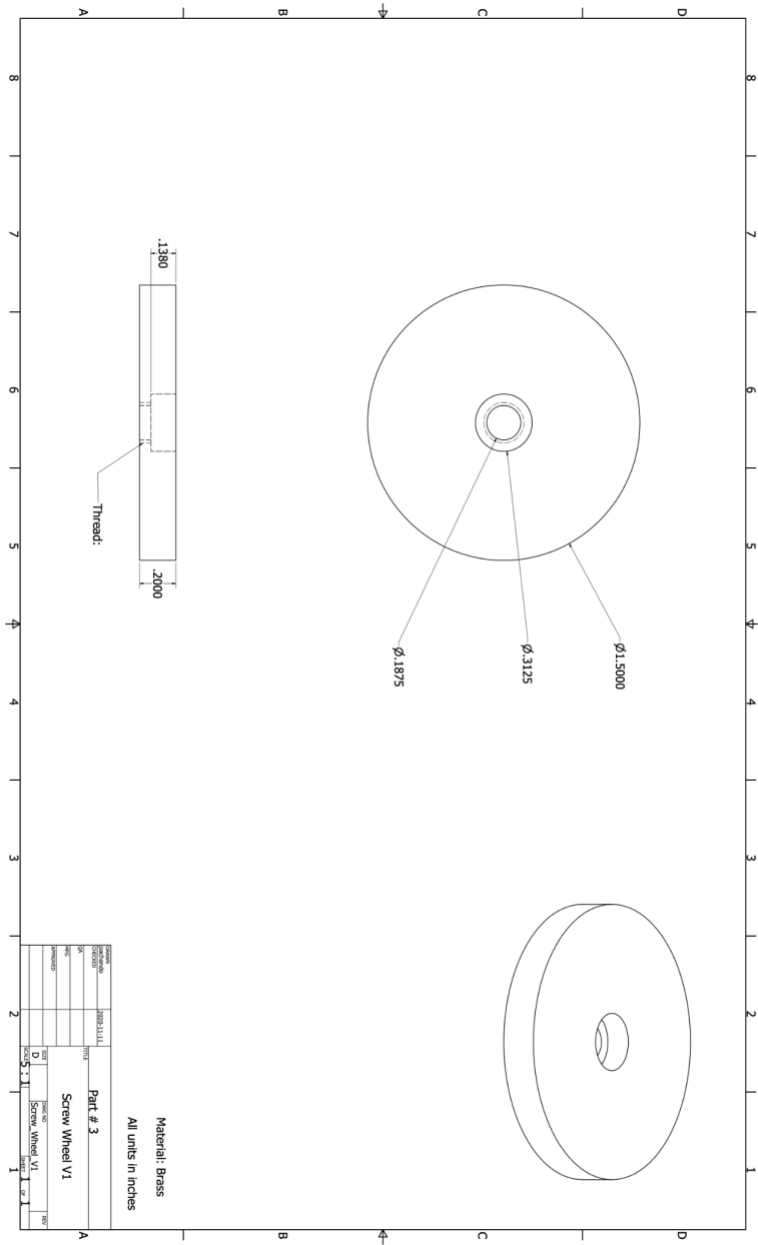


Figure SI 2.5 - Part 2 - Sample holder top



**Figure SI 2.6 - Part 3 - Screw wheel**

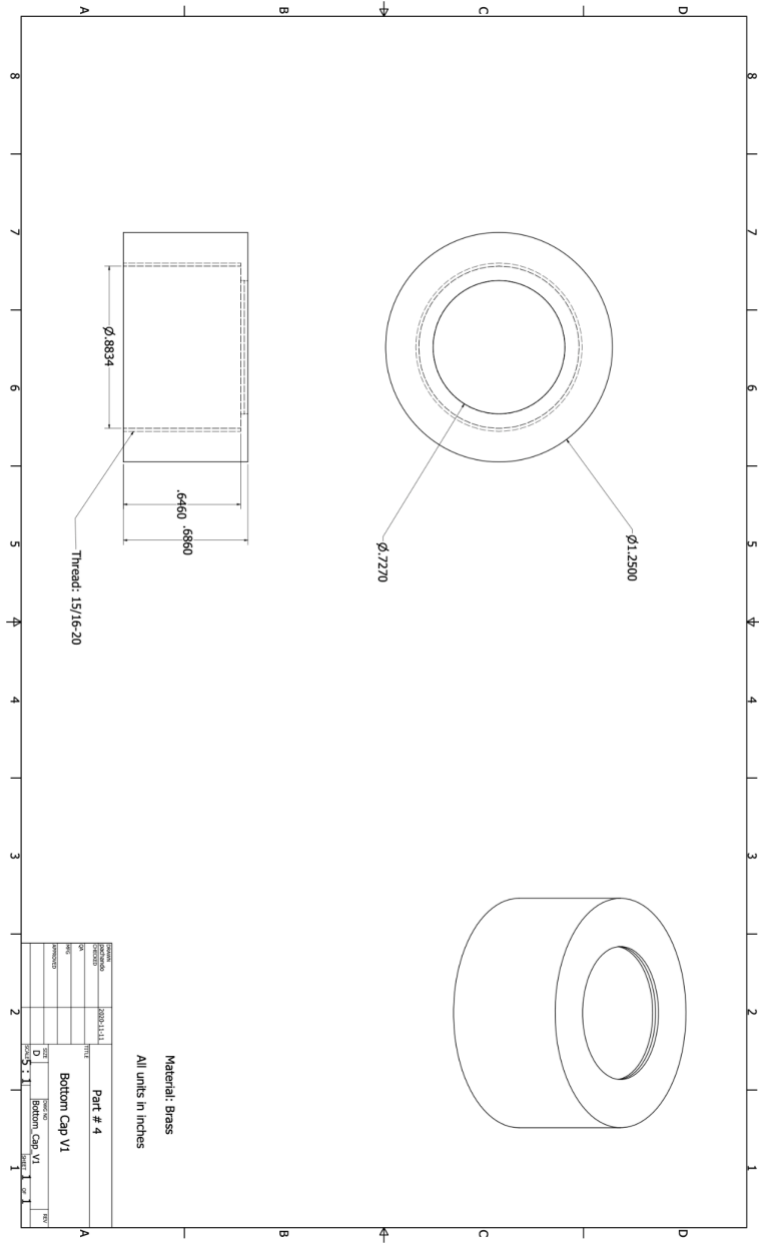


Figure SI 2.7 - Part 4 - Bottom cap



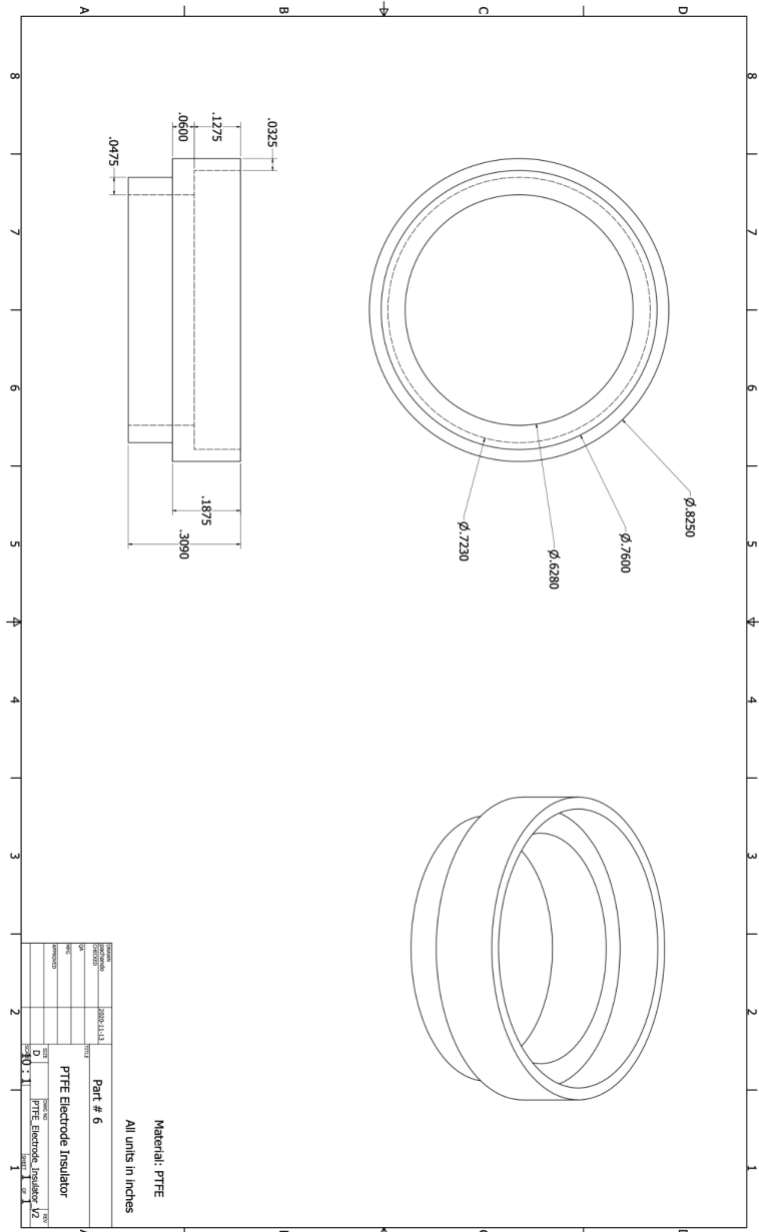


Figure SI 2.9 - Part 6 - PTFE electrode insulator

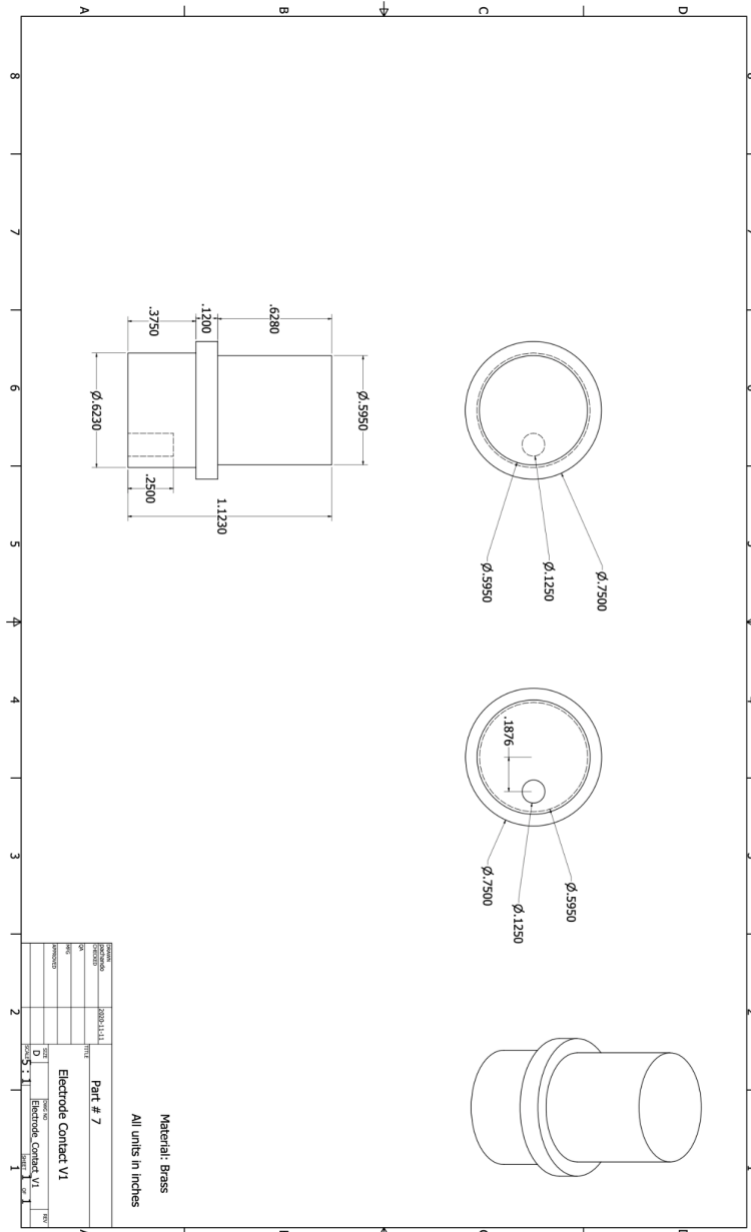


Figure SI 2.10 - Part 7 - Electrode contact

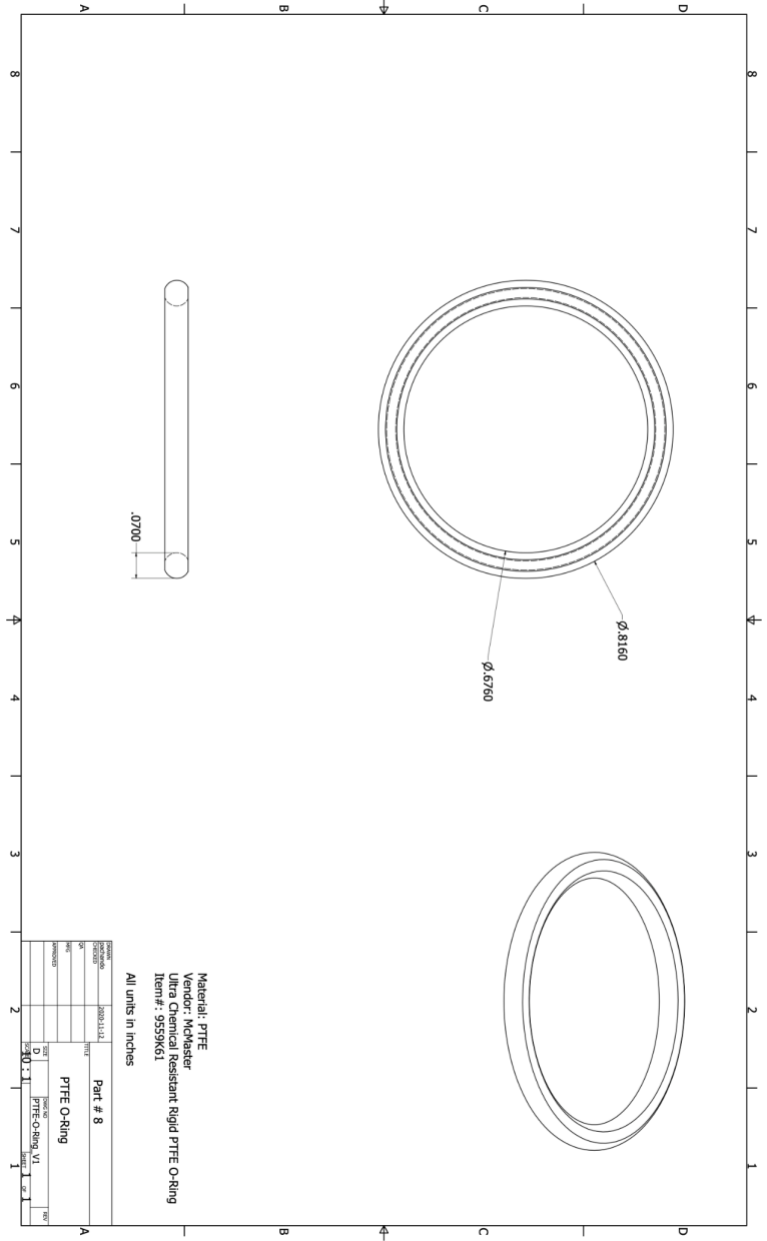


Figure SI 2.11 - Part 8 - In situ o-ring

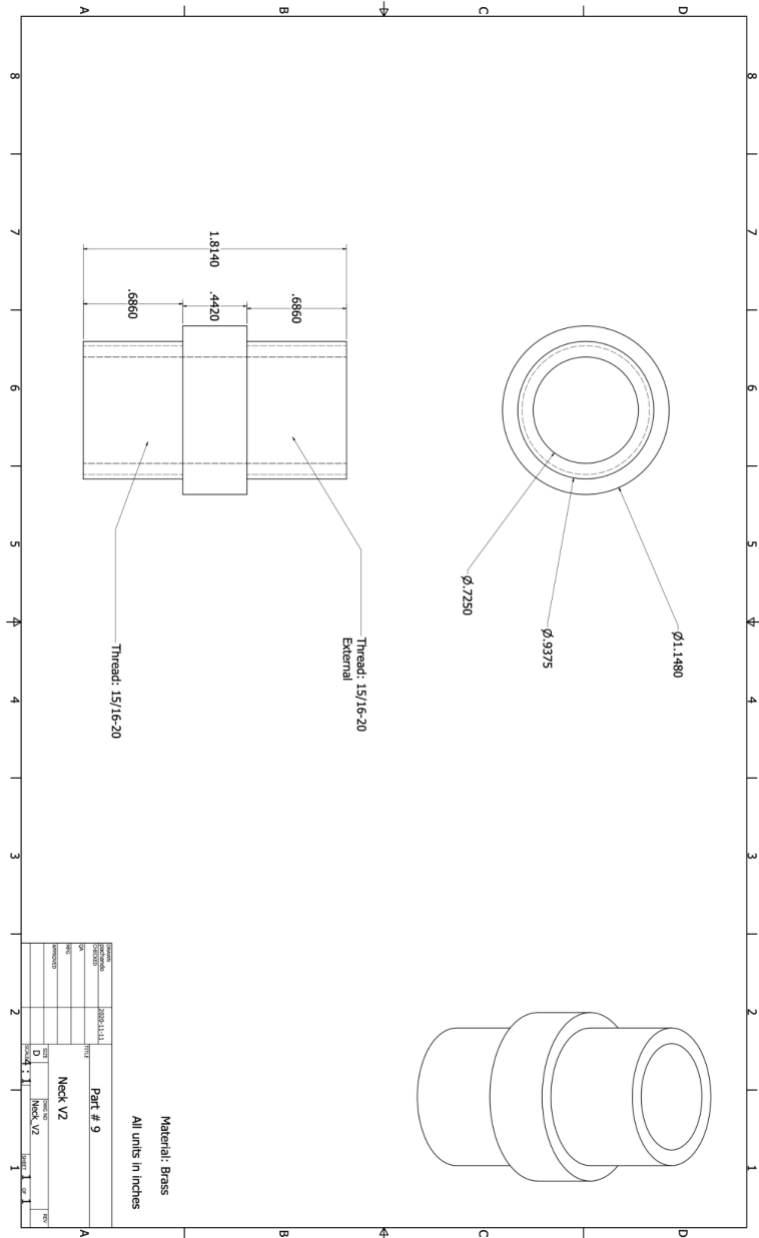


Figure SI 2.12 - Part 9 - In situ neck

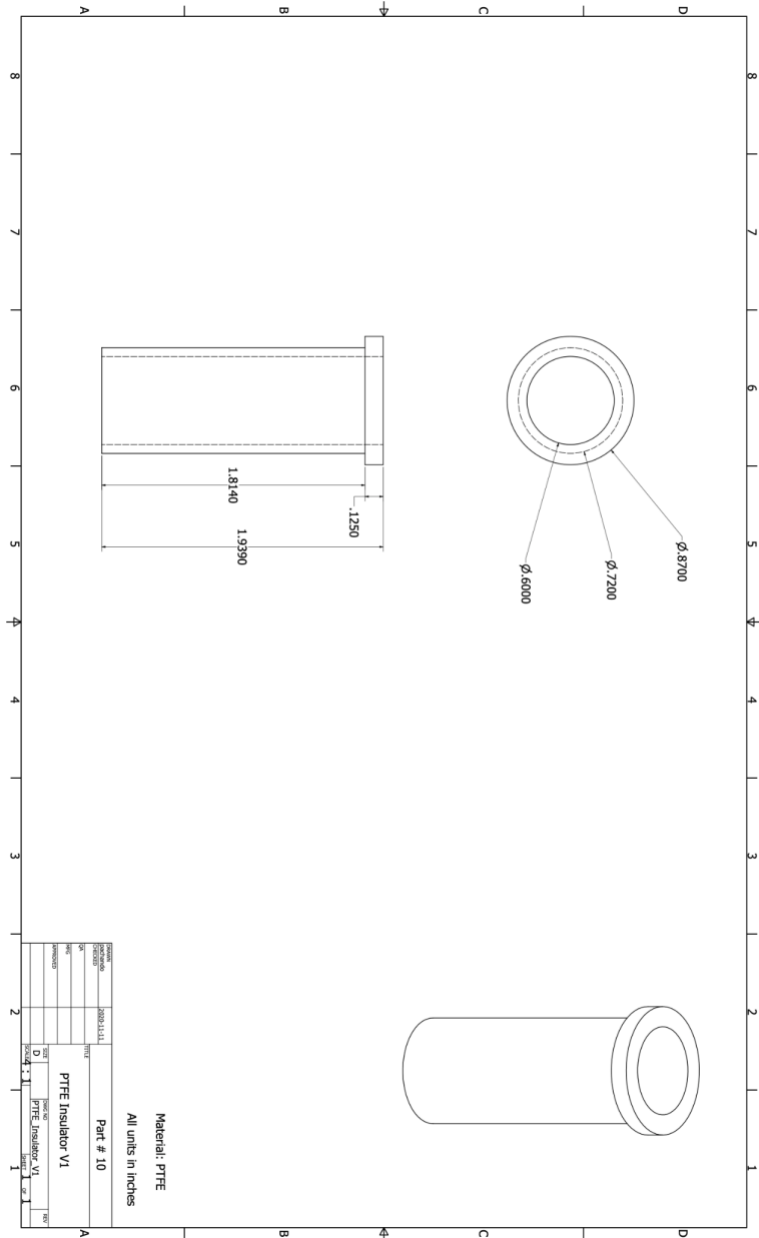


Figure SI 2.13 - Part 10 - PTFE insulation

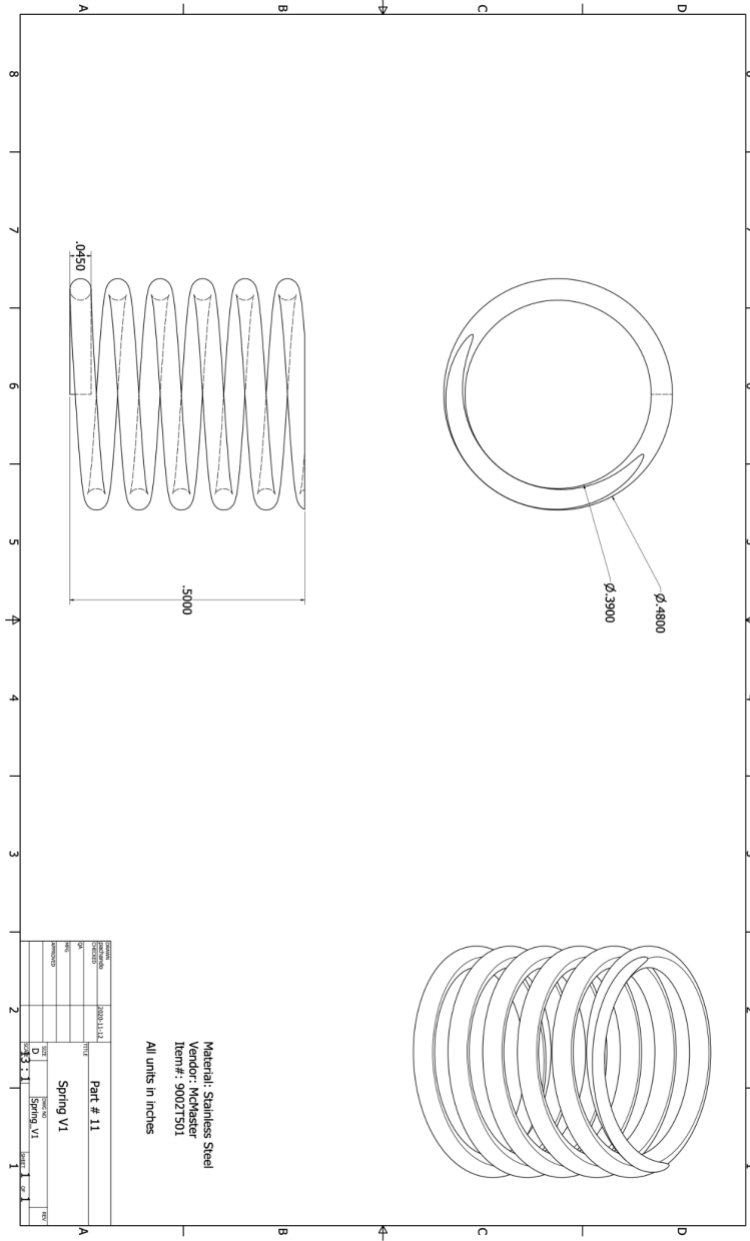


Figure SI 2.14 - Part 11 - Spring

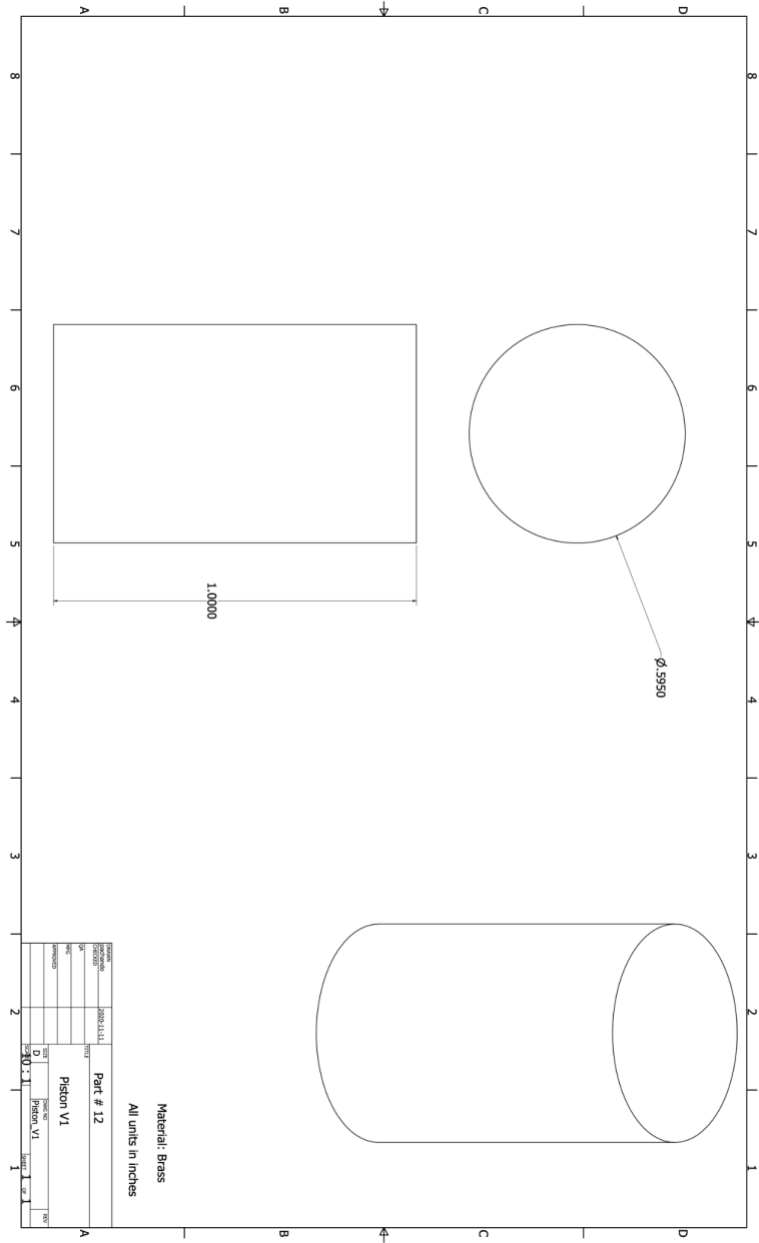


Figure SI 2.15 - Part 12 - Brass piston

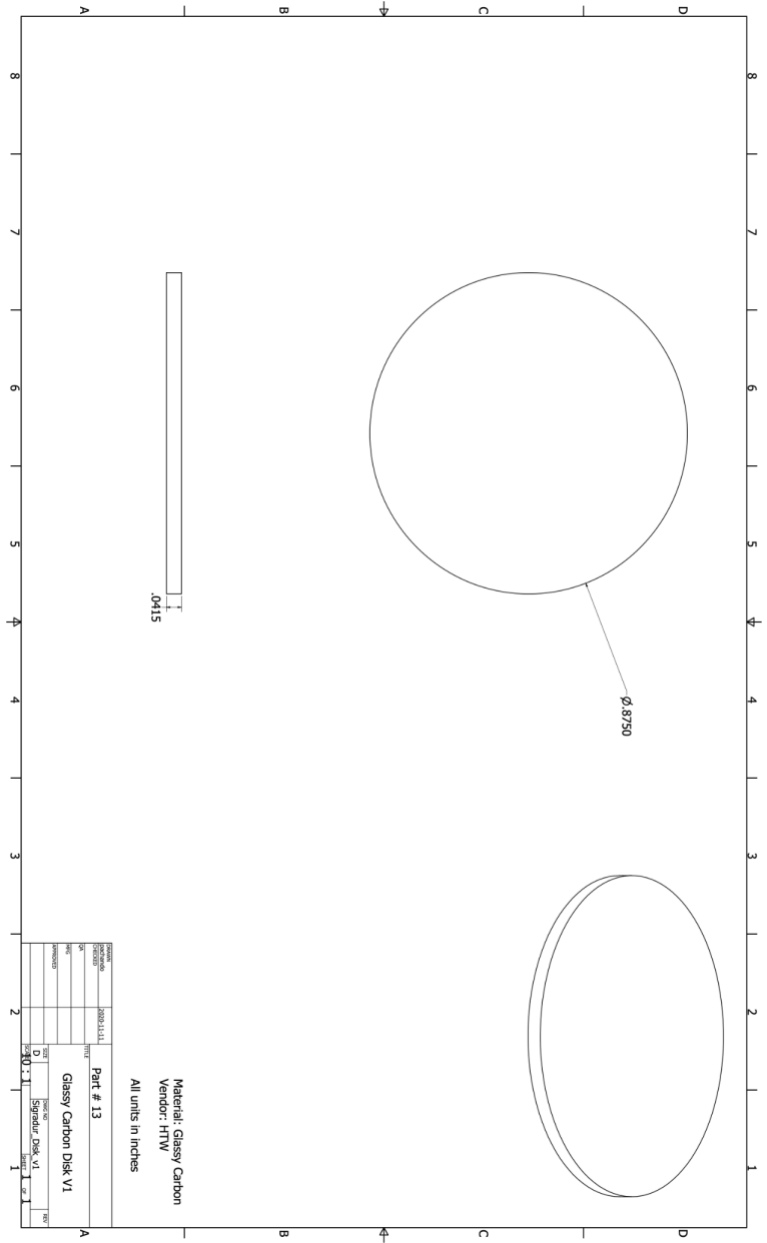


Figure SI 2.16 - Part 13 - Glassy carbon window

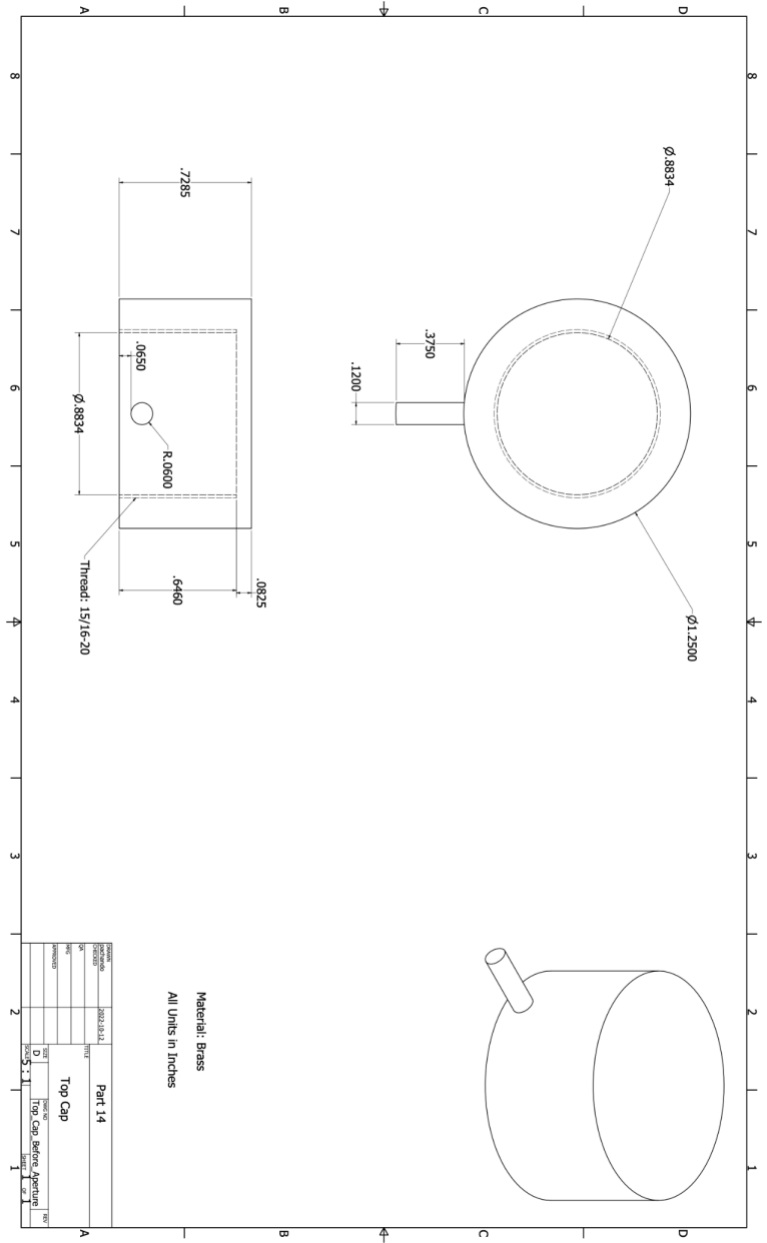


Figure SI 2.17 - Part 14 - Top cap (before machining aperture)

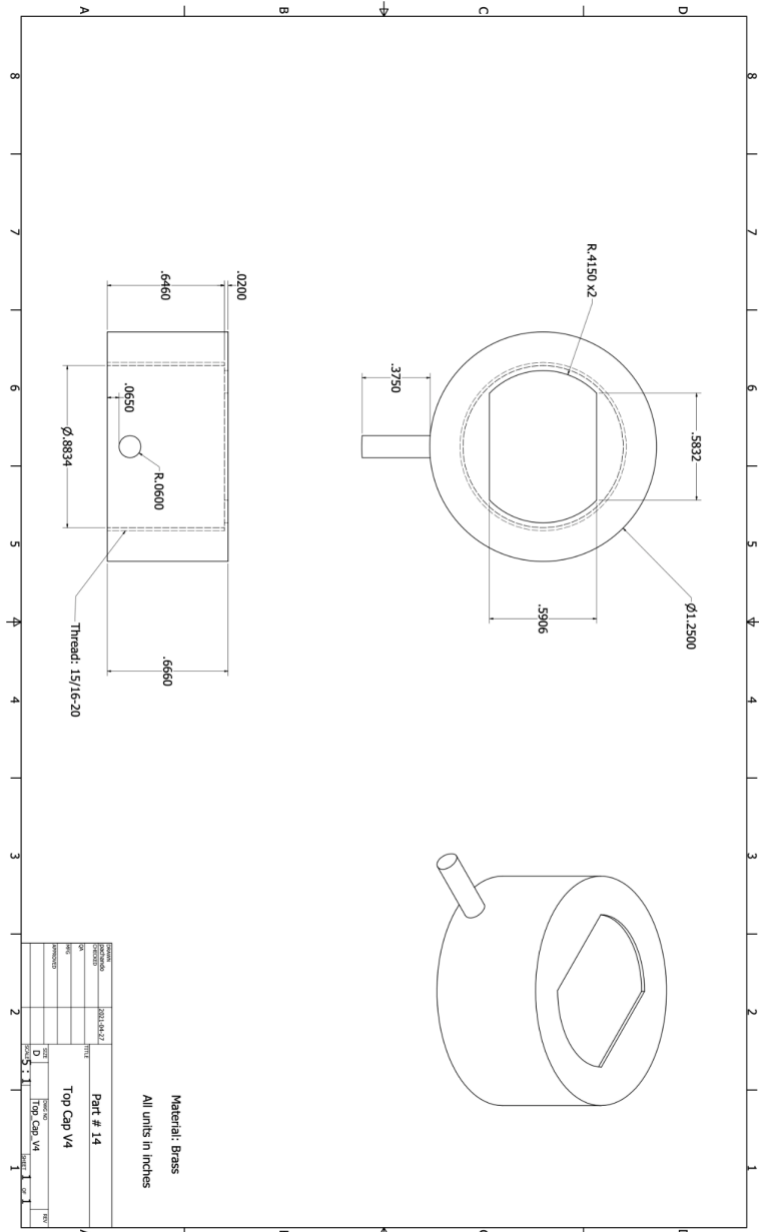


Figure SI 2.18 - Part 14 - Top cap (with machined aperture)

## References

1. Mizushima, K.; Jones, P. C.; Wiseman, P. J.; Goodenough, J. B.  $\text{Li}_x\text{CoO}$  ( $0 < x < 1$ ): A NEW CATHODE MATERIAL FOR BATTERIES OF HIGH ENERGY DENSITY. *Plan. Perspect.* **1980**, 783, 789.
2. Harks, P. P. R. M. L.; Mulder, F. M.; Notten, P. H. L. In Situ Methods for Li-Ion Battery Research: A Review of Recent Developments. *J. Power Sources* **2015**, 288, 92–105.
3. Van der Ven, A.; Bhattacharya, J.; Belak, A. A. Understanding Li Diffusion in Li-Intercalation Compounds. *Acc. Chem. Res.* **2013**, 46 (5), 1216–1225.
4. Vetter, J.; Novák, P.; Wagner, M. R.; Veit, C.; Möller, K.-C.; Besenhard, J. O.; Winter, M.; Wohlfahrt-Mehrens, M.; Vogler, C.; Hammouche, A. Ageing Mechanisms in Lithium-Ion Batteries. *J. Power Sources* **2005**, 147 (1), 269–281.
5. Wu, Y.; Liu, N. Visualizing Battery Reactions and Processes by Using In Situ and In Operando Microscopies. *CHEM* **2017**. <https://doi.org/10.1016/j.chempr.2017.12.022>.
6. Saurel, D.; Pendashteh, A.; Jáuregui, M.; Reynaud, M.; Fehse, M.; Galceran, M.; Casas-Cabanas, M. Experimental Considerations for Operando Metal-ion Battery Monitoring Using X-ray Techniques. *Chem. Methods* **2021**, 1 (6), 249–260.
7. Bak, S.-M.; Shadik, Z.; Lin, R.; Yu, X.; Yang, X.-Q. In Situ/operando Synchrotron-Based X-Ray Techniques for Lithium-Ion Battery Research. *NPG Asia Materials* **2018**, 10 (7), 563–580.
8. Koop, T.; Schindler, W.; Kazimirov, A.; Scherb, G.; Zegenhagen, J.; Schulz, T.; Feidenhans'l, R.; Kirschner, J. Electrochemical Cell for in Situ X-Ray Diffraction under Ultrapure Conditions. *Rev. Sci. Instrum.* **1998**, 69 (4), 1840–1843.
9. Borkiewicz, O. J.; Shyam, B.; Wiaderek, K. M.; Kurtz, C.; Chupas, P. J.; Chapman, K. W. The AMPIX Electrochemical Cell: A Versatile Apparatus for in Situ X-Ray Scattering and Spectroscopic Measurements. *J. Appl. Crystallogr.* **2012**, 45 (6), 1261–1269.
10. Goetz, D. 3D-Printed Electrochemical Cell for In Situ Analysis. Bachelor's of Science (with Honors Research Distinction), The Ohio State University, 2020.
11. Leriche, J. B.; Hamelet, S.; Shu, J.; Morcrette, M.; Masquelier, C.; Ouyard, G.; Zerrouki, M.; Soudan, P.; Belin, S.; Elkaïm, E.; Baudalet, F. An Electrochemical Cell for Operando Study of Lithium Batteries Using Synchrotron Radiation. *J. Electrochem. Soc.* **2010**, 157 (5), A606.
12. Bach, P.; Seemayer, A.; Rütt, U.; Gutowski, O.; Renner, F. U. Electrochemical Cells for In situ XRD Studies of Insertion and Extraction Mechanisms of Lithium in Anode

- Materials for Lithium Ion Batteries Tested at Aluminum Model Electrodes. *ECS Trans.* **2013**, *53* (29), 29.
13. Sottmann, J.; Homs-Regojo, R.; Wragg, D. S.; Fjellvåg, H.; Margadonna, S.; Emerich, H. Versatile Electrochemical Cell for Li/Na-Ion Batteries and High-Throughput Setup for Combined Operando X-Ray Diffraction and Absorption Spectroscopy. *J. Appl. Crystallogr.* **2016**, *49* (6), 1972–1981.
  14. Wilson, B. E.; Smyrl, W. H.; Stein, A. Design of a Low-Cost Electrochemical Cell for In Situ XRD Analysis of Electrode Materials. *J. Electrochem. Soc.* **2014**, *161* (5), A700.
  15. Zhang, L.; Guo, X.; Huang, J.; Qu, Y.; Niu, C.; Du, Z.; Li, D.; Chen, Y. Coin-Cell-Based In Situ Characterization Techniques for Li-Ion Batteries. *Frontiers in Energy Research* **2018**, *6*, 16.
  16. Sottmann, J.; Pralong, V.; Barrier, N.; Martin, C. An Electrochemical Cell for Operando Bench-Top X-Ray Diffraction. *J. Appl. Crystallogr.* **2019**, *52* (2), 485–490.
  17. Maarof, H. I.; Wan Daud, W. M. A.; Aroua, M. K. Effect of Varying the Amount of Binder on the Electrochemical Characteristics of Palm Shell Activated Carbon. *IOP Conf. Ser. Mater. Sci. Eng.* **2017**, *210*, 012011.
  18. Eguchi, T.; Kanamoto, Y.; Tomioka, M.; Tashima, D.; Kumagai, S. Effect of Ball Milling on the Electrochemical Performance of Activated Carbon with a Very High Specific Surface Area. *Batteries* **2020**, *6* (2), 22.
  19. Shu, J.; Shui, M.; Huang, F.; Ren, Y.; Wang, Q.; Xu, D.; Hou, L. A New Look at Lithium Cobalt Oxide in a Broad Voltage Range for Lithium-Ion Batteries. *J. Phys. Chem. C* **2010**, *114* (7), 3323–3328.
  20. Degen, T.; Sadki, M.; Bron, E.; König, U.; Nénert, G. The HighScore Suite. *Powder Diffr.* **2014**, *29* (S2), S13–S18.
  21. Jain, A.; Ong, S. P.; Hautier, G.; Chen, W.; Richards, W. D.; Dacek, S.; Cholia, S.; Gunter, D.; Skinner, D.; Ceder, G.; Persson, K. A. Commentary: The Materials Project: A Materials Genome Approach to Accelerating Materials Innovation. *APL Materials* **2013**, *1* (1), 011002.
  22. Young, R. A. *The Rietveld Method*; Oxford university press Oxford, 1993; Vol. 6.
  23. Pecharesky, V. K.; Zavalij, P. Y. *Fundamentals of Powder Diffraction and Structural Characterization of Materials*; Springer, 2005.
  24. McCusker, L. B.; Von Dreele, R. B.; Cox, D. E.; Louër, D.; Scardi, P. Rietveld Refinement Guidelines. *J. Appl. Crystallogr.* **1999**, *32* (1), 36–50.

25. Stinton, G. W.; Evans, J. S. O. Parametric Rietveld Refinement. *J. Appl. Crystallogr.* **2007**, *40* (Pt 1), 87–95.
26. Reimers, J. N.; Dahn, J. R. Electrochemical and In Situ X-Ray Diffraction Studies of Lithium Intercalation in Li X CoO<sub>2</sub>. *J. Electrochem. Soc.* **1992**, *139* (8), 2091.
27. Akhilash, M.; Salini, P. S.; John, B.; Mercy, T. D. A Journey through Layered Cathode Materials for Lithium Ion Cells – From Lithium Cobalt Oxide to Lithium-Rich Transition Metal Oxides. *J. Alloys Compd.* **2021**, *869*, 159239.
28. Gali, S.; Solans, X.; Altaba, M. F. Determination of Atomic Parameters from Powder Diffraction Intensity Ratios. *J. Solid State Chem.* **1983**, *46* (2), 172–179.
29. Tsubota, M.; Paik, B.; Kitagawa, J. Inter-Comparison of Lattice Parameters and Evaluation of Peak-Shift Obtained by Rietveld Refinements. *Results in Physics* **2019**, *15*, 102640.
30. Garrick, T. R.; Kanneganti, K.; Huang, X.; Weidner, J. W. Modeling Volume Change due to Intercalation into Porous Electrodes. *J. Electrochem. Soc.* **2014**, *161* (8), E3297.
31. Rodriguez, M. A.; Ingersoll, D.; Doughty, D. H. Quantitative Analysis of Li Contents in Li<sub>x</sub>CoO<sub>2</sub> Cathodes via Rietveld Refinement. *Powder Diffr.* **2003**, *18* (2), 135–139.

## **CHAPTER 3**

# **EXPLORING CALCIUM MANGANESE OXIDE AS A PROMISING CATHODE MATERIAL FOR CALCIUM-ION BATTERIES**

A version of this chapter has been published in ACS Chemistry of Materials 2023

Chando, P.A.; Chen, S.; Shellhamer, J.M.; Wall, E.; Wang, X.; Schuarca, R.; Smeu, M.; Hosein, I.D

Reprinted with Permission

### 3.1 Introduction

The increasing demand for new technologies that rely on lithium-ion batteries, coupled with the limited global supply of lithium, underscores the urgent need to explore alternative battery chemistries that offer a sustainable and economically viable solution to the growing energy demands of the world. Calcium (ion) batteries are a particularly promising alternative due to a high volumetric capacity of 2073 mAh/cm<sup>3</sup> and its low standard reduction potential of -2.87 (vs SHE). Additionally, calcium is the 5th most abundant element in the Earth's crust, with abundant domestic supply in the US and China (two major battery manufacturers), making the economics associated with its raw materials relatively inexpensive.<sup>[1-3]</sup> Compared to magnesium, calcium has a larger ionic radius causing calcium to have a lower charge density that is more amenable to intercalation chemistry.<sup>[4]</sup> Calcium-ion batteries would be suitable for the same technologies that employ Li-ion technology, including portable electronics, stationary storage, and even electric vehicles, owing to its combine high capacity, high voltage, and low cost.

The development of calcium-based batteries includes a set of challenges that must be addressed. One prominent issue is the identification of suitable cathodes. Cathodes for calcium batteries must possess certain properties including a high-capacity, ability to run at high-voltage, structural stability during cycling, and possessing stable transport pathways for calcium diffusion in and out of the structure.<sup>[1,5]</sup> To facilitate the search for such candidates, Density Functional Theory (DFT) calculations have been used as a screening tool, incorporating the previously described criteria in its search. Results from DFT screening have identified transition metal oxides as promising candidates for calcium batteries.<sup>[6-8]</sup> So far, however, only a select few of these compounds have been experimentally investigated.<sup>[9-12]</sup> Those that have been evaluated have shown promising

electrochemical activity with reversible insertion and deinsertion of calcium. These results have prompted investigation into similar compounds.

One transition metal oxide that has not been thoroughly studied is  $\text{CaMn}_2\text{O}_4$ . Early DFT investigations concluded that the spinel structure of  $\text{CaMn}_2\text{O}_4$ , with a cubic crystal structure, would be an attractive option as a cathode due to its low migration barrier of 600 meV since calcium would be tetrahedrally coordinated.<sup>[13,14]</sup> However, true spinels of  $\text{CaMn}_2\text{O}_4$  are difficult to synthesize, requiring high pressures to produce a true spinel structure.<sup>[15]</sup> The more naturally occurring alternative is the post-spinel of  $\text{CaMn}_2\text{O}_4$ . Post-spinels are crystal structures derived from spinels after being subjected to high temperature and pressure, causing the cubic crystal system to change and typically densify. DFT calculations performed on the post-spinel structure have concluded that while manganese itself is a transition metal capable of accessing different oxidation states, the diffusion barrier of 1.8 eV associated with calcium's migration between octahedral sites is problematic.<sup>[16,17]</sup> Preliminary experimental investigations of the post-spinel using an electrolyte of  $\text{Ca}(\text{BF}_4)_2$  in EC/PC at 75°C did not yield any structural changes via XRD and no other experimental work has been performed on the post-spinel  $\text{CaMn}_2\text{O}_4$ .<sup>[17]</sup>

Herein, we report an experimental evaluation of the post-spinel  $\text{CaMn}_2\text{O}_4$  for calcium-ion batteries. The calcium manganese oxide is prepared using a solid-state synthesis method and its phase is verified through Rietveld Refinement of XRD.<sup>[15,18]</sup> The synthesized  $\text{CaMn}_2\text{O}_4$  is processed into an electrode where its electrochemical activity is evaluated in an electrolyte of  $\text{Ca}(\text{TFSI})_2$  in DME using cyclic voltammetry, linear sweep voltammetry, and galvanostatic cycling. Redox activity of the manganese and cycling of the calcium are analyzed using XRD, XPS and Scanning Electron Microscopy (SEM), complemented with DFT calculations. The results

from these experiments and simulations outline that the post-spinel can successfully cycle calcium at room temperature.

## **3.2 Experimental Section**

### **3.2.1 Materials**

Manganese Oxide ( $\text{MnO}_2$ ), Calcium Carbonate ( $\text{CaCO}_3$ ), Diethylene Glycol Monobutyl Ether (DME), Ferrocene and 1-Methyl-2-Pyrrolidone (NMP) were purchased from Sigma-Aldrich, USA, and used as received. Calcium(II) Bis(trifluoromethanesulfonyl)imide ( $\text{Ca}(\text{TFSI})_2$ ) was purchased from Solvionic. Silver Nitrate ( $\text{AgNO}_3$ ) was purchased from Alfa Aesar.  $\text{Ca}(\text{TFSI})_2$  salt was vacuum-dried at 120 °C overnight before use. Polytetrafluoroethylene (PTFE) preparation (60% wt) was purchased from Sigma-Aldrich. Polyvinylidene Fluoride (PVDF) binder, Super P Carbon black, Activated Carbon, CR2032 316 stainless steel coin cells and Aluminum foil (~10  $\mu\text{m}$  thickness) were purchased from MTI Corporation, USA.

### **3.2.2 Synthesis of $\text{CaMn}_2\text{O}_4$**

A solid state synthesis method was used for post-spinel  $\text{CaMn}_2\text{O}_4$ .  $\text{MnO}_2$  and  $\text{CaCO}_3$  were combined in a 7:3 Mn:Ca molar ratio to produce a total mixture of 20g. The powders were mixed in a ball mill for 1 hour at 200 rpm. The mixture was then baked in a furnace for 20 hours at 1100°C. The calcined product was ground with a mortar and pestle and ball milled under the previous conditions. After ball milling, the powder was baked for 20 hours at 1200°C. Following the bake, the same grinding and ball milling process was repeated. The last three bakes were performed at 1250°C for 20 hours. After each bake, the grinding and ball milling procedure was followed.<sup>[15,18]</sup>

### 3.2.3 Electrode Preparation

The electrodes used in the study were formulated using two methods. Electrodes used with the in situ cell and cyclic voltammetry experiments were processed as freestanding electrodes while galvanostatic experiments using coin cells were assembled with slurry casted electrodes. To prepare a freestanding electrode, powders of  $\text{CaMn}_2\text{O}_4$  (65% wt) and carbon black (5% wt) were mixed with PTFE Binder (30% wt).<sup>[19,20]</sup> The active material was mixed with carbon black in a ball miller. The components were mixed at 19.67 Hz for 90 minutes.<sup>[21]</sup> After ball milling, the mixture was placed in a mortar and pestle where PTFE binder was added and suspended in excess ethanol. The materials were mixed until all excess ethanol evaporated. The freestanding electrode would then be processed in a hot roll press at 80°C. Freestanding electrodes were then vacuum dried overnight at 80°C for a final weight density of 3 mg/cm<sup>2</sup>. Activated Carbon freestanding electrodes were prepared using the same procedure. The composition of the activated carbon electrodes was activated carbon (80% wt) and PTFE binder (20% wt) with a mass loading density of 30 mg/cm<sup>2</sup>.<sup>[22]</sup>

The following procedure was used for the processing of casted electrodes in galvanostatic experiments. To prepare the working electrode, a slurry of 95%  $\text{CaMn}_2\text{O}_4$ , 2.5% Carbon Black and 2.5% PVDF binder was made. The solid content of the slurry is fixed at 65 wt%.<sup>[23,24]</sup> The active material and conductive additive were mixed in powder form for 60 minutes in the ball mill at 19.67 Hz. Separately, the PVDF and 2/5 of the total NMP were mixed in the ball mill for 30 minutes and then sonicated for another 30 minutes. The pre-mixed solids were added and mixed again in the ball mill and sonicator. 1/3 of the remaining NMP, or 1/5 of the overall volume, was added and the ball mill and sonication mixings were repeated. The remaining NMP was added in 1/5 increments with the ball milling and sonication mixings following each addition.<sup>[25]</sup> Once

mixed, the slurry was casted onto the carbon coated aluminum current collector with a thickness of 200 microns. After the slurry was casted onto the current collector, the casted electrode was dried at 80°C for 1 hour and subsequently vacuum dried at 110°C overnight.<sup>[26]</sup> The method for making the casted activated carbon was the same as the  $\text{CaMn}_2\text{O}_4$  with the exception that the activated carbon was casted onto a carbon coated copper collector. Mass loading of the  $\text{CaMn}_2\text{O}_4$  working electrode was recorded to be 5 mg/cm<sup>2</sup> while the activated carbon mass loading was recorded to be 30 mg/cm<sup>2</sup>.

### 3.2.4 Electrolyte Preparation

The electrolyte used in all electrochemistry experiments was 0.5 M  $\text{Ca}(\text{TFSI})_2$  in DME. A stock of the DME solvent was prepared by drying it for 48 hours over 3 Å molecular sieves. To remove any residual moisture from the salt, the  $\text{Ca}(\text{TFSI})_2$  salt was dried overnight at 120°C in a vacuum oven. Following the drying, the salt was then dissolved in the DME and magnetically stirred for 24 hours to allow homogenization of the salt in the DME. The electrolyte was then dried over 3 Å molecular sieves again to remove any remaining traces of water and the water content in the electrolyte was verified to be below 50 ppm using a Karl Fischer Titrator (899 Coulometer, Metrohm). Experiments involving the calibration of the  $\text{Ag}/\text{Ag}^+$  reference electrode included the addition of dried 50mM ferrocene to the  $\text{Ca}(\text{TFSI})_2$  DME electrolyte along with the addition of 0.01 M  $\text{AgNO}_3$  supporting salt in the reference electrode.<sup>[27]</sup> The use of two electrolytes for the reference electrode was designed to avoid development of junction potentials between the reference electrode and bulk electrolyte.

### 3.2.5 Electrochemistry

Cyclic voltammetry (CV) and linear sweep voltammetry (LSV) experiments were performed in beaker cell setups (Gamry Instruments). Cyclic Voltammetry experiments used a three-electrode configuration with Ag/Ag<sup>+</sup> reference electrode (Redox.me), CaMn<sub>2</sub>O<sub>4</sub> working electrode and activated carbon as the counter electrode. Working and counter electrodes were attached to the end of 316 stainless steel supports and immersed in electrolyte. The experiments were carried out for 20 cycles at a scan rate of 0.5 mV/s and performed with a Metrohm Autolab. Calibrations of the Ag/Ag<sup>+</sup> reference electrode and activated carbon with ferrocene were also carried out in a beaker cell with platinum wire as the working electrode (Figure SI 3.1a,b). The Ag/Ag<sup>+</sup> reference electrode consists of 0.5 M Ca(TFSI)<sub>2</sub> in DME along with 0.01 M AgNO<sub>3</sub>. Linear stability window measurements used a two-electrode cell with stainless steel as the blocking electrode and calcium as the non-blocking electrode. Linear scans were made at a sweep rate of 0.5 mV/s from 0 to 2.5 V (Figure SI 3.2). All experiments were carried out in an Argon filled glovebox with H<sub>2</sub>O and O<sub>2</sub> levels maintained below 0.5 ppm.

Galvanostatic and in situ EIS experiments were carried out in two-electrode coin cell configurations with CaMn<sub>2</sub>O<sub>4</sub> as the working electrode (5 mm diameter) and activated carbon as the counter electrode (15 mm diameter). 80 μL of Ca(TFSI)<sub>2</sub> in DME was used in each coin cell assembly and all coin cells were assembled in a glovebox. Testing of all coin cells began with a 2 hour open circuit voltage to allow components to equilibrate before testing. Galvanostatic cycling of coin cells was performed on an Arbin battery tester where the coin cells were cycled at room temperature at a rate of C/33. In situ EIS measurements were performed with a Solartron Energy Lab XM Instrument over a frequency range from 0.1 Hz to 1 MHz between each charge and

discharge of the coin cell. A 10 mV perturbation was used in all EIS measurements and the resulting Nyquist plot was analyzed using an equivalent circuit model.<sup>[28-31]</sup>

### 3.2.6 Electrode Characterization

A Rigaku Miniflex diffractometer was used for the collection of X-ray diffraction data. Copper (Cu)  $K\alpha$  radiation was used to collect data in the range of 10-80° at a scan rate of 5°/min. To eliminate the effect of residual electrolyte, all samples were rinsed with solvent and dried before measurements were taken. The XRD data collection was performed at room temperature. In situ XRD measurements were performed with a custom in situ cell (Figure SI 3.3 & SI 3.4). Figure SI 3.3a is a schematic of the in situ cell and Figure SI 3.3b is the assembled in situ cell. Figure SI 3.4a outlines the assembled in situ cell as it is installed inside of the Rigaku Miniflex diffractometer while Figure SI 3.4b is a baseline XRD scan of  $\text{CaMn}_2\text{O}_4$  within the in situ cell. Rietveld refinement of each material was performed using Highscore Plus software.<sup>[32]</sup> The Materials Project was used for the identification of phases.<sup>[33]</sup> Scanning electron microscopy (SEM) was performed using a JEOL 5600 and was equipped with an energy dispersive X-ray (EDX) detector. The accelerating voltage used on all samples was 15 kV. All samples were first sputter coated with gold before being placed inside the SEM chamber. XPS analysis of the  $\text{CaMn}_2\text{O}_4$  electrodes were performed at the Cornell Center for Materials Research (CCMR) with a Thermo Nexsa G2 XPS Surface Analysis System that employs a monochromatic Al  $K\alpha$  X-ray operating at 10 mA and 12 kV. Samples were mounted using conductive spring clips in contact with the top surfaces of the samples. High resolution scans of the Mn 2p, Mn 3s, O1s, and C1s lines were performed with an analysis spot 400  $\mu\text{m}$  in diameter, a step size of 0.1 eV, and a pass energy of 50 eV. Survey scans were performed with a pass energy of 200 eV and a step size of 0.4 eV.

### 3.2.7 Ab-Initio Calculations

The DFT calculation was performed using the Vienna Ab Initio Simulation Package,<sup>[34]</sup> which uses the projector augmented wave method.<sup>[35]</sup> The PBE+ $U$  <sup>[36]</sup> functional was chosen for electronic interactions with a  $U$  value of 3.9 eV. The cutoff energy for the plane-wave basis is 700 eV and the  $k$ -point grid is a  $15 \times 5 \times 5$  mesh with a  $\Gamma$ -centered scheme.  $k$ -Point and cutoff energy were tested, and results converge to 1 meV per atom difference. Antiferromagnetic configurations were chosen for all cases. This configuration is kept for all other calculations. Each structure was fully relaxed, including energies, cell parameters, and atomic positions. All de-intercalation of Ca ions was performed using the fully relaxed  $\text{CaMn}_2\text{O}_4$  structure and was then relaxed again to obtain correct energies, cell parameters, and atomic positions.

### 3.3 Results and Discussion

The synthesized calcium manganese oxide was identified with XRD. Figure 3.1a displays the XRD profiles of experimental and fitted results from Rietveld refinement performed on the synthesized  $\text{CaMn}_2\text{O}_4$  powder. The refinement on the sample concluded a pure post-spinel phase with high crystallinity and no remaining competing phases from the solid-state synthesis. The results from the refinement identifies an orthorhombic structure with a space group of  $\text{Pbcm}$  (mp-18844).<sup>[37]</sup> The resulting lattice parameters were  $a = 3.1575 \text{ \AA}$ ,  $b = 9.9916 \text{ \AA}$ , and  $c = 9.6738 \text{ \AA}$ . The Scherrer equation performed on the synthesized powder found a crystallite size that was approximately 600  $\text{\AA}$ .<sup>[38]</sup> SEM analysis of the synthesized powder (Figure 3.1b, c) found the morphology of the particles to have a polydisperse, irregular morphology.<sup>[39]</sup>

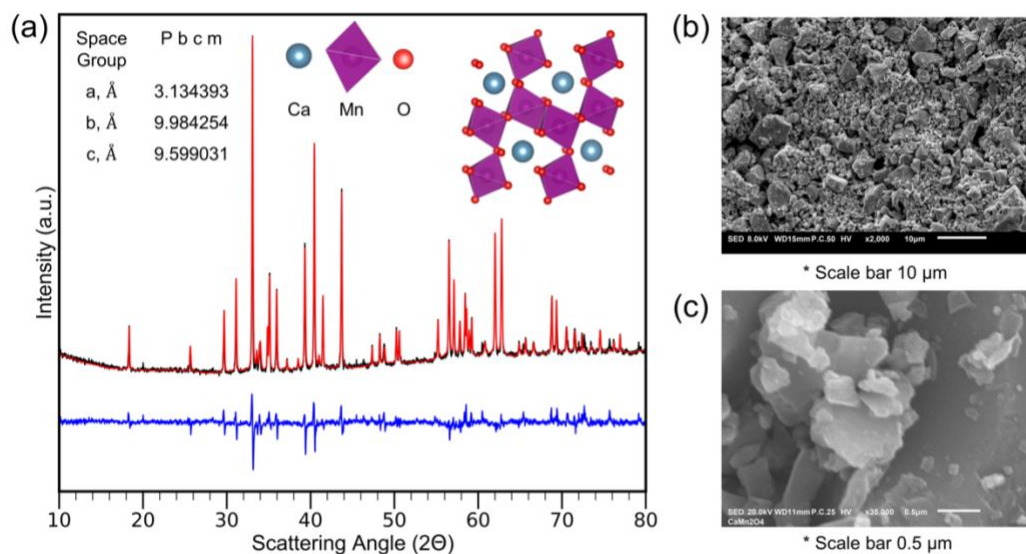


**Figure 3.1** - Synthesis of post-spinel  $\text{CaMn}_2\text{O}_4$ . a) XRD diffraction of  $\text{CaMn}_2\text{O}_4$  (inset of lattice parameters, space group and unit cell) b) SEM image of  $\text{CaMn}_2\text{O}_4$  powders (Scale bar of 10 microns) c) Close up SEM image of  $\text{CaMn}_2\text{O}_4$  particles (Scale bar of 0.5 microns).

Evaluation of the redox activity for the  $\text{CaMn}_2\text{O}_4$  began with cyclic voltammetry. A three-electrode cell was used for the analysis. The freestanding electrodes of  $\text{CaMn}_2\text{O}_4$  and activated carbon were assembled in a beaker cell with  $\text{Ag}/\text{Ag}^+$  being used as a reference electrode. Calibrations of both the  $\text{Ag}/\text{Ag}^+$  electrode and the activated carbon are summarized in Figure SI 3.1. Open circuit voltage (OCV) measurements of the cell were made before electrochemical testing and found the cell to have an OCV of 0.275 V vs.  $\text{Ag}/\text{Ag}^+$ . The results from cyclic voltammetry outline redox active processes with the  $\text{CaMn}_2\text{O}_4$  where an oxidative potential can be observed at 0.2 V (Figure 3.2a). Upon continued cycling, the oxidative potential shifts from 0.2 V to approximately 0.5 V, indicative of an irreversible process or partial phase change from the  $\text{CaMn}_2\text{O}_4$  undergoing a conversion reaction.<sup>[40,16]</sup> The oxidation potential does stabilize at 0.5 V by the end of cycling and is consistent with previously reported oxidation potentials of manganese.<sup>[31]</sup> There is also evidence of limited reinsertion of the calcium back into the  $\text{CaMn}_2\text{O}_4$  electrode. There is a broad reduction peak observed at -1.5 V.<sup>[31,41]</sup> The lack of a clear cathodic

peak indicates that the reinsertion of calcium into the cathode is slow.<sup>[42]</sup> With continued cycling of the electrode, the reduction peak at -1.5 V diminishes until the feature is absent by the 20th cycle and only a negative sloping line exists in the cathodic trace of the CV. This behavior outlines the limited success in reducing manganese from its +4 to +3 oxidation state with the intercalation of calcium.<sup>[43]</sup> The results from the CV also produce a secondary peak that drifts between 1.5 and 2 V and is observed on the first cycle at 2 V. However, this peak is not related to the redox activity of the manganese and is instead a product of the electrolyte interaction with the 316 stainless steel electrode supports. A linear stability window of the electrolyte was performed and found behaviors consistent with this peak in the cyclic voltammetry experiment (Figure SI 3.2).

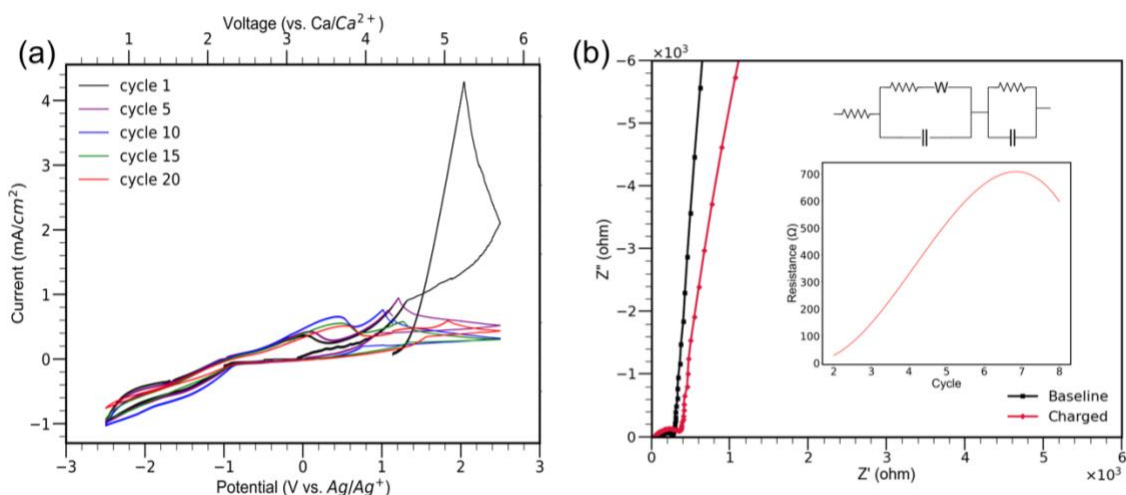


**Figure 3.2** - a) Cyclic voltammetry of CaMn<sub>2</sub>O<sub>4</sub>. b) In situ EIS measurements of the CaMn<sub>2</sub>O<sub>4</sub> (inset shows equivalent circuit used for impedance analysis and charge transfer resistance plot).

One of the major issues known to the post-spinel structure of CaMn<sub>2</sub>O<sub>4</sub> is the charge transfer resistance that develops from calcium attempting to diffuse through the crystal structure of the electrode. Previous DFT investigations into the post-spinel CaMn<sub>2</sub>O<sub>4</sub> have revealed that a substantial diffusion barrier exists for the electrode that suppresses large capacities of calcium from being cycled in and out of the electrode.<sup>[16,17]</sup> To establish the degree of the charge transfer resistance experienced by the CaMn<sub>2</sub>O<sub>4</sub>, in situ EIS studies were performed on the electrode in

coin cell configurations.<sup>[28-31]</sup> The Nyquist plots generated from the in situ EIS experiments can be seen in Figure 3.2b and Figure SI 3.5. The impedance data was fit to an equivalent circuit that can be seen in an inset of Figure 3.2b. The resulting resistances from cycling  $\text{CaMn}_2\text{O}_4$  are an inset as well with Figure 3.2b. The charge transfer resistance increases substantially over the course of cycling, reaching a maximum resistance of 700 ohm. The increase in resistance is consistent with the previously reported sluggish diffusion kinetics of the post-spinel structure and has been observed with a decreased charge capacity with initial cycles.<sup>[31]</sup> By cycle 8 though, a drop in the resistance can be seen with the value decreasing from 700 to 600 ohms. This decrease in resistance allows for better intercalation chemistry in  $\text{CaMn}_2\text{O}_4$ . Upon continued cycling, the charge transfer resistance continued to decrease and comparisons of cycling data can be seen in Figure SI 3.5. This decrease of charge transfer resistance in the  $\text{CaMn}_2\text{O}_4$  is suspected to be partly influenced by some irreversible process or change in the  $\text{CaMn}_2\text{O}_4$  that has already been identified with the CV experiment.

To determine the maximum capacity of calcium that could be extracted from the calcium manganese oxide, a maximum charge was performed on it. Freestanding electrodes of  $\text{CaMn}_2\text{O}_4$  and Activated Carbon were used in the analysis and charged at a rate of C/200. The results from the maximum charge revealed that a total of 100 mAh/g could be extracted from the  $\text{CaMn}_2\text{O}_4$  (Figure 3.3a). Similar experiments aimed at performing maximum charges on a spinel structure have yielded the same two-tiered charging profile that has been labeled as some partial phase transformation.<sup>[44]</sup> There are small fluctuations in the voltage of the second plateau at approximately 0.6 V. There are several possible causes for this including nonuniform electrolyte distribution and variations in electrode roughness causing nonuniform charging. The sharp rise in voltage after 100 mAh/g to 4 V identifies that the capacity of the cathode has been exhausted.

Based on DFT calculations and literature with magnesium-based spinel structures, the phase change observed in the charging profile would be a result from conversion reactions that form decalciated  $\text{CaMn}_2\text{O}_4$  and  $\text{Mn}_3\text{O}_4$  phases. The DFT calculations performed on the  $\text{CaMn}_2\text{O}_4$  are summarized in Figures SI 3.6-SI 3.8 and Tables SI 3.1-SI 3.8. Figure SI 3.6a outlines the voltage profile of the  $\text{CaMn}_2\text{O}_4$  while Figure SI 3.6b is the convex hull of the  $\text{CaMn}_2\text{O}_4$  as it undergoes intercalation chemistry. Based on the established convex hull of the  $\text{CaMn}_2\text{O}_4$ , much of the formation energies lie slightly above the hull, identifying a preference for the post-spinel cathode to undergo conversion reactions.<sup>[16]</sup> Based on magnesium battery literature, the lower voltages from the charging of the  $\text{CaMn}_2\text{O}_4$  would be identified as intercalation behavior involving the extraction of calcium from the post-spinel while the second plateau would focus more on conversion reactions of the post-spinel cathode.<sup>[16,17,42,45-52]</sup> XRD analysis was performed on the working electrode before and after charging. The refinement performed on the  $\text{CaMn}_2\text{O}_4$  tracked lattice parameter changes of the  $\text{CaMn}_2\text{O}_4$  and occupancies of the calcium. The pristine sample of  $\text{CaMn}_2\text{O}_4$  was refined with lattice parameters  $a = 3.156676 \text{ \AA}$ ,  $b = 9.988452 \text{ \AA}$  and  $c = 9.675391 \text{ \AA}$ . The charged sample was analyzed to have lattice parameters  $a = 3.154765 \text{ \AA}$ ,  $b = 9.978689 \text{ \AA}$  and  $c = 9.666233 \text{ \AA}$ . The occupancies of the calcium were also tracked before and after charging. The occupancy of the calcium in the  $\text{CaMn}_2\text{O}_4$  post-charging decreased from 1.0 to 0.785. In addition to the decalciated  $\text{CaMn}_2\text{O}_4$  phase,  $\text{Mn}_3\text{O}_4$  (mp-18759) and  $\text{MnO}$  (mp-19006) phases were also identified and refined.<sup>[53,54]</sup> The  $\text{Mn}_3\text{O}_4$  phase was refined with lattice parameters  $a = 5.761503 \text{ \AA}$ ,  $b = 5.761503 \text{ \AA}$  and  $c = 9.464502 \text{ \AA}$  while the  $\text{MnO}$  phase was refined with lattice parameters  $a = b = c = 4.48 \text{ \AA}$ . The  $\text{Mn}_3\text{O}_4$  phase was the product of a conversion reaction while the  $\text{MnO}$  phase occurred from a disproportionation reaction occurring on the surface of the  $\text{CaMn}_2\text{O}_4$  electrode.<sup>[16,17,45,55,56]</sup> Results from the Rietveld refinement performed on the  $\text{CaMn}_2\text{O}_4$  cathode

post-charging are summarized in Figure SI 3.9a and Tables SI 3.9-SI 3.11. Previous DFT calculations performed on the  $\text{CaMn}_2\text{O}_4$  post-spinel have reported that successful intercalation chemistry with the structure would require volume variations of the  $\text{CaMn}_2\text{O}_4$  to be less than 6%.<sup>[17,57]</sup> DFT calculations of the  $\text{CaMn}_2\text{O}_4$  yielded a volumetric reduction of 3% for removal of 25% of calcium. Comparisons of the experimental lattice parameters produce a volume variation of approximately 0.25%. The small volumetric variations of the  $\text{CaMn}_2\text{O}_4$  post-charging are a feature that has been observed with  $\text{MgMn}_2\text{O}_4$  spinels when two phases were present in the cathode as a result of conversion reactions.<sup>[46-48]</sup> In addition to performing Rietveld refinement of the charged  $\text{CaMn}_2\text{O}_4$  cathode, several XRD changes in the electrode were observed that align with DFT calculations. The scope of structural changes of the cathode and their comparisons to theoretical XRD patterns where 25% of calcium was removed are summarized in Figure SI 3.10. Figure SI 3.10a compares the experimental XRD patterns between the pristine and charged samples while Figure SI 3.10b compares theoretical XRD patterns generated from DFT calculations. Theoretical XRD patterns of decaordinated  $\text{CaMn}_2\text{O}_4$  are also outlined in Figure SI 3.8. One of the most prominent changes with the  $\text{CaMn}_2\text{O}_4$  was an increase in the intensity of the (020) reflection (Figure 3.3b). The (020) lattice plane intensity increase is a feature consistent with DFT calculations and is associated with activity occurring along the  $\text{MnO}_6$  edge sharing octahedra.<sup>[10,40]</sup> The intensity increase of the (020) lattice planes was attributed to the activity of calcium extraction and not a preferred orientation effect since similar effects were not observed with parallel planes.<sup>[58]</sup> Another structural development predicted from DFT calculations is the development of two peaks with the (132) reflection (Figure 3.3c). The emergence of a second peak for the (132) reflection is identified with dashed lines at  $\sim 44.5^\circ$  and its intensity increases by the end of charging. The development of two peaks in the  $\text{CaMn}_2\text{O}_4$  post-charging is likely caused by some decrease

of symmetry in the host structure or could be attributed to the formation of a secondary phase in the  $\text{CaMn}_2\text{O}_4$  as it undergoes a conversion reaction forming  $\text{Mn}_3\text{O}_4$ . [16,17,48,50,59,60] Evidence of partial phase changes is further supported by the activity of the (055) reflection. The pristine  $\text{CaMn}_2\text{O}_4$  (055) reflection (Figure SI 3.10) has twin peaks and upon charging, the reflections are consolidated where the second peak is observed as a shoulder rather than an individual peak, consistent with a phase change in the host structure. The structural changes previously outlined between pristine and charged samples of the  $\text{CaMn}_2\text{O}_4$  are outlined in Figure SI 3.10b with asterisks. Additionally, cyclic voltammetry of the  $\text{CaMn}_2\text{O}_4$  (Figure 3.2a) did produce a shift in the oxidation potential from 0.2 V to 0.5 V, consistent with the activity seen in the maximum charge of the  $\text{CaMn}_2\text{O}_4$  and would align with some irreversible process with the  $\text{CaMn}_2\text{O}_4$ . Based on the XRD from the maximum charge, probable developments within the  $\text{CaMn}_2\text{O}_4$  would be several domains of the post-spinel undergoing conversion reactions while others transition their symmetries due to Jahn-Teller distortions. Further testing of the electrode with TEM would be needed to confirm crystal structure changes within the  $\text{CaMn}_2\text{O}_4$ .

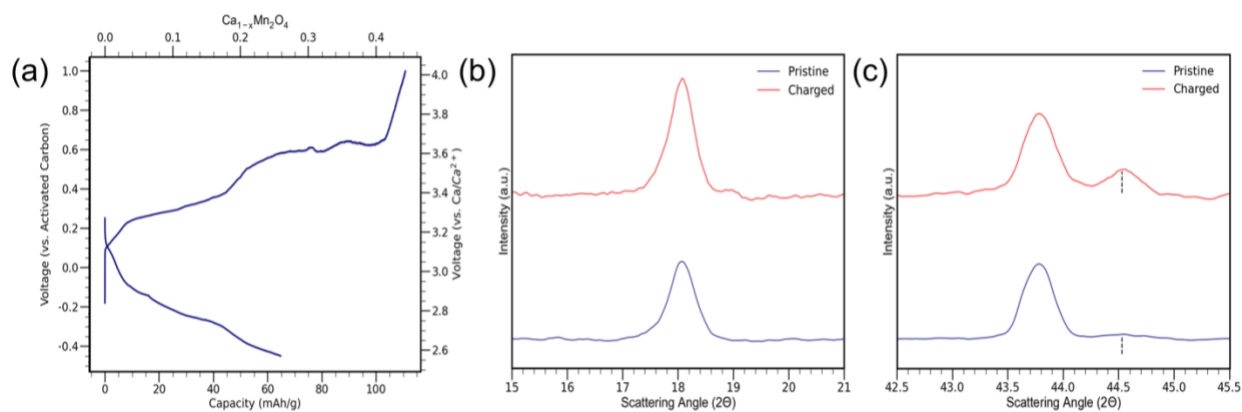


**Figure 3.3** - a) Maximum charge of the  $\text{CaMn}_2\text{O}_4$  (C/200) and discharge b) XRD of lattice plane (020). c) XRD of lattice plane (132) before and after charging (dashed lines denoting emergence of peak at  $44.5^\circ$ ).

In addition to the maximum charge performed on the  $\text{CaMn}_2\text{O}_4$  post-spinel, a discharge of 65 mAh/g (Figure 3.3a) was also performed and subsequently characterized with XRD and Rietveld refinement. A discharge plateau with  $\text{CaMn}_2\text{O}_4$  is observed between 2.9 and 2.75 V (vs  $\text{Ca}/\text{Ca}^{2+}$ ). The discharge plateau is consistent with the reduction of manganese from +4 to +3 oxidation states based on magnesium battery literature. [44,46,48] Following the discharge of the  $\text{CaMn}_2\text{O}_4$ , the cathode was characterized with XRD and analyzed with Rietveld refinement. The  $\text{CaMn}_2\text{O}_4$  phase was refined with lattice parameters  $a = 3.158088 \text{ \AA}$ ,  $b = 9.997047 \text{ \AA}$ ,  $c = 9.678633 \text{ \AA}$ . Occupancy of calcium within the  $\text{CaMn}_2\text{O}_4$  phase was also refined to a value of 0.864617, an increase from the 0.785 occupancy with the maximum charge and identifying a reinsertion of calcium into the post-spinel. The  $\text{Mn}_3\text{O}_4$  phase was also identified and refined with lattice parameters  $a = 5.753304 \text{ \AA}$ ,  $b = 5.753304 \text{ \AA}$  and  $c = 9.481883$ . The  $\text{MnO}$  phase was refined with lattice parameters  $a = b = c = 4.46448 \text{ \AA}$ . The results from the analysis performed on the discharged sample are summarized in Table SI 3.9b and Tables SI 3.9-SI 3.11. The Rietveld refinement performed on the cathode supports some intercalation chemistry occurring within the cathode as the calcium occupancy within the phase increases from 0.785 to 0.864617 at the end of discharge.

To further corroborate the redox activity associated with the decalciation of  $\text{CaMn}_2\text{O}_4$ , XPS analysis was performed to track the average oxidation state change of manganese between pristine and charged samples. To determine the average oxidation state of the manganese, high resolution scans of the  $\text{CaMn}_2\text{O}_4$  were performed on Mn 3s, Mn 2p and C 1s orbitals. Spectra were fitted after applying Shirley background subtractions using non-linear least squares (implemented in CasaXPS). The charging of the  $\text{CaMn}_2\text{O}_4$  was fixed with a C 1s binding energy of 285 eV. Analysis of the Mn 3s orbitals (Figure 3.4a) gave binding energy differences of 5.54 and 5.49 eV for baseline and charged samples of the  $\text{CaMn}_2\text{O}_4$ , respectively. Because the average oxidation state of the

manganese is established to vary linearly with the binding energies of the 3s orbitals,<sup>[61,62]</sup> the average oxidation state of the baseline manganese was found to be 2.94 and the charged sample was 3.01.<sup>[63,64]</sup> The average oxidation state of the baseline manganese would be lower than +3 from either oxygen vacancies within the cathode or manganese occupying interstitial sites.<sup>[65,66]</sup> To verify the accuracy of the average oxidation states of each sample, the Mn 2p orbitals were analyzed. Deconvolutions of the binding energies were made using a Voigt function with Gaussian/Lorentzian (G/L) contributions. Using established values for the Mn 2p orbital binding energies (Figure 3.4b, c), the ratios between the manganese oxidation states was found to be in close agreement with the measurement that was made using the Mn 3s orbitals.<sup>[61,67]</sup>

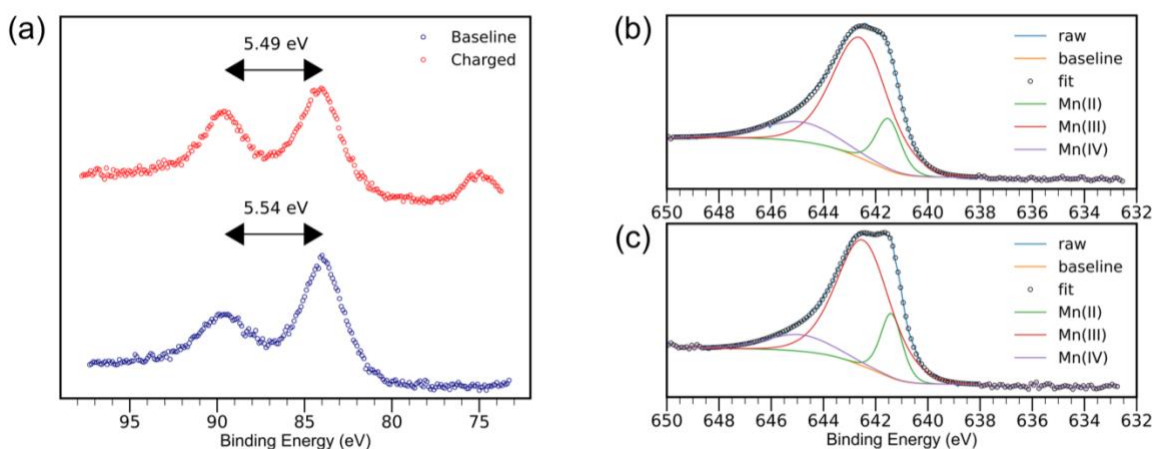


**Figure 3.4** - XPS of  $\text{CaMn}_2\text{O}_4$  for average oxidation of manganese a) Mn 3s binding energy b) Mn 2p binding energy of charged sample c) Mn 2p binding energy of baseline sample.

After establishing the redox activity of  $\text{CaMn}_2\text{O}_4$ , the cathode was then assembled into a coin cell for evaluating long term cycling behavior at a rate of C/33 for a capacity of 52 mAh/g. The results from the coin cell cycling are outlined in Figure 3.5a. Analysis of the coin cell cycling with a capacity voltage curve is outlined in Figure 3.5b. The oxidation of the  $\text{CaMn}_2\text{O}_4$  occurs in the voltage region from 0 - 0.5 V and includes a shoulder of redox activity at approximately 0.5 V ( $\sim 3.5$  V vs  $\text{Ca}/\text{Ca}^{2+}$ ), consistent with expectations made with cyclic voltammetry studies. The

capacity associated with this region of activity is approximately 15 mAh/g. The oxidation of  $\text{CaMn}_2\text{O}_4$  at 3.5 V (vs.  $\text{Ca}/\text{Ca}^{2+}$ ) is a promising first step towards this post-spinel system functioning as a high voltage cathode. The termination of  $\text{CaMn}_2\text{O}_4$  oxidation is identified by an additional increase in voltage from  $\sim 0.5$  V to 1.8 V ( $\sim 4.7$  V vs  $(\text{Ca}/\text{Ca}^{2+})$ ). There is a plateau approximately at 1.8 V and a large amount of the coin cell capacity occurs at this voltage. However, this electrochemical activity is not associated with intercalation chemistry of the  $\text{CaMn}_2\text{O}_4$  cathode and is instead a product of electrolyte oxidation.<sup>[40]</sup> The first cycle of galvanostatic data does exhibit voltage variations from several factors including temperature fluctuations within the coin cell and the C/33 charging rate. Other researchers have cycled cathodes at more modest rates below C/50.<sup>[17,41]</sup> The higher cycling rate, along with sluggish diffusion kinetics contributes to voltage spikes in the galvanostatic data. Additional galvanostatic studies using lower cycling rates have been performed and exhibited a decrease in voltage noise as the cathode was cycled. The results of lower cycling rates are outlined in Figure SI 3.11.

The first several discharges of  $\text{CaMn}_2\text{O}_4$  include some electrochemical activity observed at -1.5 V, corresponding to the reduction of manganese and can be observed in cycle 10. Beyond the first 10 cycles of testing, the reinsertion of the calcium back into the  $\text{CaMn}_2\text{O}_4$  follows a voltage curve that consistently trends downward. This behavior outlines the reinsertion of calcium back into the electrode but does not include reduction of manganese back into its lower oxidation state.<sup>[31,41]</sup>

Further confirmation of the calcium activity in the cathode is supported by postmortem EDS and XRD analysis run on the  $\text{CaMn}_2\text{O}_4$  at the conclusion of testing. The EDS analysis revealed that the end of cycling produced a decrease in the calcium signal from 12% to 9%. The decrease in the manganese signal can be attributed to the decrease of crystallite size that occurs in the cathode as a function of cycling. Decreased crystallite sizes can translate to a decrease in fluorescence of

elements and, as such, cause the elemental signal of manganese to decrease.<sup>[68]</sup> Results from EDS analysis are summarized in Figure 3.5c. Post-cycling XRD of the  $\text{CaMn}_2\text{O}_4$  verified activity of the  $\text{CaMn}_2\text{O}_4$  with a decrease in the reflection at 34 degrees (Figure SI 3.12). The decrease of this reflection is consistent with DFT calculations performed on the  $\text{CaMn}_2\text{O}_4$ . The 34 degree angle of the  $\text{CaMn}_2\text{O}_4$  is identified with the (120) lattice plane of the  $\text{CaMn}_2\text{O}_4$ . Calcium, with a Wyckoff factor of 4d, strongly contributes to the scattering intensity of the (120) lattice plane. The removal of calcium from the  $\text{CaMn}_2\text{O}_4$  can be observed with the decrease with the intensity of the (120) lattice plane. XRD analysis of the electrode, using the Scherrer equation, before and after cycling also concluded a decrease in the crystallite size of the  $\text{CaMn}_2\text{O}_4$  from 600 Å to 480 Å. Decreases in crystallite size are correlated to more favorable cycling behavior and its effect can be observed with the evolution of the voltage-capacity curves in Figure 3.5b.<sup>[69]</sup> The energy density from the  $\text{CaMn}_2\text{O}_4$  coin cell cycling behavior was calculated to be 205 Wh/kg and falls within the range of energy densities for nickel, manganese, and cobalt (NMC) cathodes for lithium-ion batteries.<sup>[70,71,72]</sup>

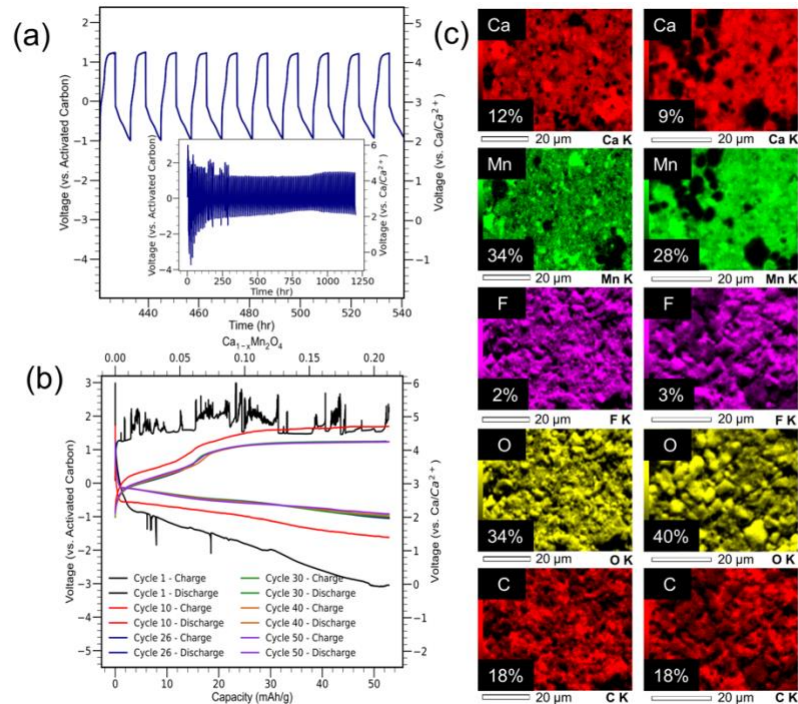


**Figure 3.5** - Galvanostatic cycling of the  $\text{CaMn}_2\text{O}_4$  a) Voltage-time curve of selected cycles (inset of full 100 cycle testing with  $\text{CaMn}_2\text{O}_4$ ) b) Capacity-voltage curves of selected cycles of  $\text{CaMn}_2\text{O}_4$  c) EDS of the  $\text{CaMn}_2\text{O}_4$  before and after galvanostatic cycling.

In situ XRD measurements made of the  $\text{CaMn}_2\text{O}_4$  were also performed on the  $\text{CaMn}_2\text{O}_4$ . Freestanding electrodes of  $\text{CaMn}_2\text{O}_4$  and Activated Carbon were assembled into the in situ XRD cell. Charge and discharge studies were performed on the  $\text{CaMn}_2\text{O}_4$  at a C-Rate of C/200 (Figure 3.6a). The charging of the  $\text{CaMn}_2\text{O}_4$  achieved approximately 25 mAh/g of capacity which would be 10% of calcium within the cathode. Discharge of the  $\text{CaMn}_2\text{O}_4$  exhibits a two tiered reinsertion of calcium into the cathode, consistent with phase transformations that would be expected in the host structure.<sup>[44,59,60]</sup> Based on magnesium literature, the first plateau of the discharge curve would be the reduction of manganese from +4 to +3 oxidation states. The second plateau would be attributed to the reduction of manganese from +3 to +2 oxidation states along with the Activated Carbon counter electrode forming a double layer capacitance.<sup>[46,48,49]</sup> Following the charge and discharge of the  $\text{CaMn}_2\text{O}_4$ , the XRD of the cell was measured. Structural changes of the (020)

plane in the  $\text{CaMn}_2\text{O}_4$  are the most notable development with the in situ XRD pattern (Figure 3.6b). A shift of the (020) peak from  $17.02^\circ$  to  $17.04^\circ$  is consistent with a decrease in the d-spacing of the  $\text{CaMn}_2\text{O}_4$  from  $5.01159 \text{ \AA}$  to  $4.99347 \text{ \AA}$  as it is charged. Factors such as sample displacement were accounted for in the XRD measurements by having an adjustable stand with the in situ cell and maintaining the same sample height for each measurement. Additionally, there is an increase with the (020) intensity, consistent with previous findings on a decalciated structure.<sup>[40]</sup> These findings are also consistent with DFT calculations performed on the  $\text{CaMn}_2\text{O}_4$ . DFT calculations project a shift of the (020) lattice plane from  $17.45^\circ$  to  $17.64^\circ$ . Differences of the  $2\theta$  angles between experimental and theoretical predictions would be influenced by the glassy carbon window of the in situ cell. The DFT predictions for the changes in the d-spacing are a bit more substantial with changes from  $5.07857 \text{ \AA}$  to  $5.0235 \text{ \AA}$  as the electrode is charged. While there is a slight shift in the  $\text{CaMn}_2\text{O}_4$  (020) reflection toward a lower angle, indicative of an increase in the interplanar spacing, there is no decrease in the intensity of the (020) signal, outlining limited effect on reinserting calcium back into the  $\text{CaMn}_2\text{O}_4$  cathode. A large portion of the capacity reported from the reinsertion is likely due to the Activated Carbon forming a double layer capacitance.<sup>[40, 48,49]</sup>

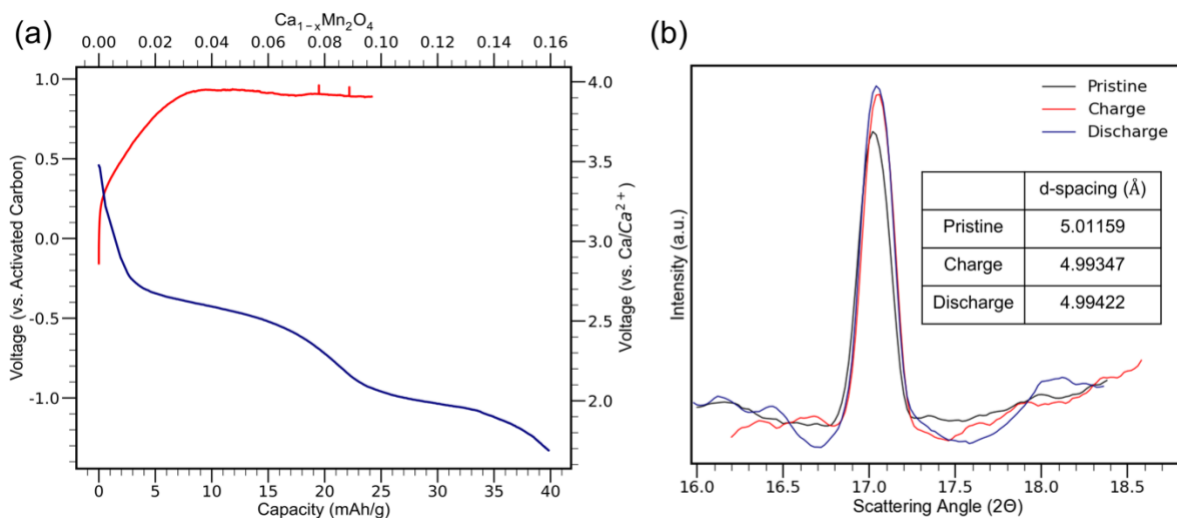


**Figure 3.6** - In situ cell cycling of  $\text{CaMn}_2\text{O}_4$  a) voltage-capacity curves of  $\text{CaMn}_2\text{O}_4$  b) XRD of  $\text{CaMn}_2\text{O}_4$  during charge and discharge within in situ cell (inset of interplanar spacing during charge and discharge).

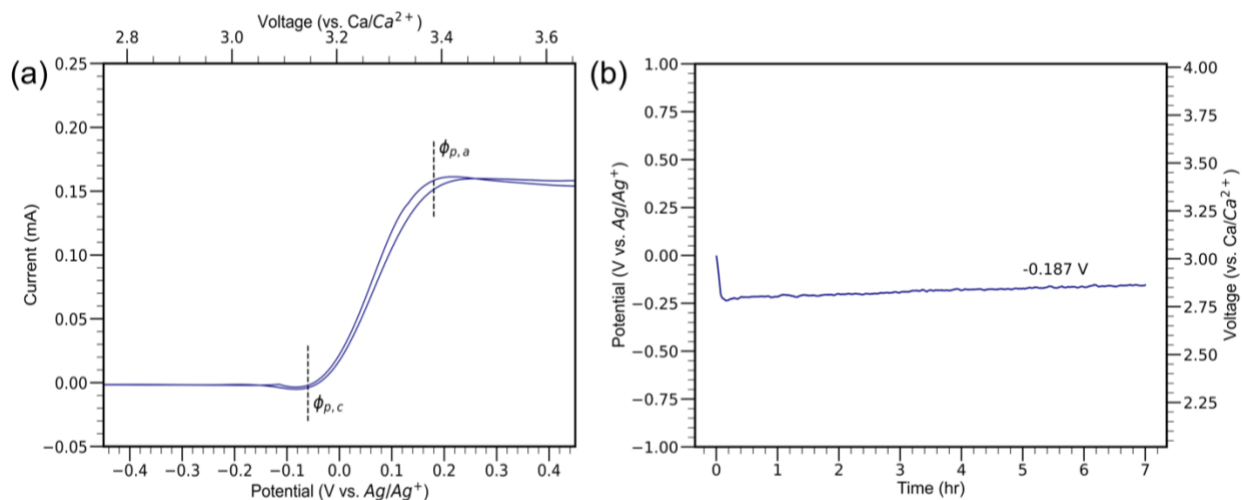
### 3.4 Conclusion

Our study provides important insights into the intercalation chemistry of calcium-ion batteries using post-spinel  $\text{CaMn}_2\text{O}_4$  as a cathode material, which can offer an alternative to lithium-ion batteries in the future. We have shown the successful synthesis and characterization of post-spinel  $\text{CaMn}_2\text{O}_4$ . Cyclic voltammetry measurements outlined the redox activity of the  $\text{CaMn}_2\text{O}_4$  electrodes. In situ EIS measurements revealed the rapid increase of charge transfer resistance that builds within the electrode and leads to limited capacities during cycling. A maximum charge of the  $\text{CaMn}_2\text{O}_4$  at a rate of  $C/200$  yielded a capacity of 100 mAh/g that could be extracted from the electrode. Structural changes of the  $\text{CaMn}_2\text{O}_4$  post-charging with XRD revealed several features that aligned with DFT calculations made of decalciated  $\text{CaMn}_2\text{O}_4$ . Additional techniques involving XPS confirmed an increase in the average oxidation state of manganese, further supporting the redox activity of the  $\text{CaMn}_2\text{O}_4$  electrode. Coin cell cycling demonstrated the capability of  $\text{CaMn}_2\text{O}_4$  to reversibly cycle calcium at higher rates of  $C/33$ . The electrochemical activity of the coin cell, along with its capacity to function as a high-voltage cathode when measured against

Ca/Ca<sup>2+</sup>, yielded an energy density of 205 Wh/kg. Results from in situ cell testing revealed a shift of the (020) reflection towards higher diffraction angles, outlining a decrease in the interplanar spacing that would occur from the removal of calcium and is consistent with theoretical calculations on CaMn<sub>2</sub>O<sub>4</sub>. Further evidence of the calcium extraction with the in situ experiment is the increase of the (020) reflection intensity which was also projected with DFT calculations. Future work with in situ cell testing would have to include strategies to increase the active material with the working electrode. The intensity of several CaMn<sub>2</sub>O<sub>4</sub> reflections were minimal due to the amount of active material within the electrode. Maximizing the amount of active material in the working electrode will not only increase the charge capacities but also improve signal intensity of the CaMn<sub>2</sub>O<sub>4</sub>, allowing for more detailed analysis of the structural changes to the electrode as it is cycled within the in situ cell.

The successful demonstration of CaMn<sub>2</sub>O<sub>4</sub> post-spinel as a viable cathode material for calcium-ion batteries represents a significant breakthrough in the search for alternatives to lithium-ion batteries. Our findings indicate that CaMn<sub>2</sub>O<sub>4</sub> post-spinel exhibits intercalation capacities and redox activity, with structural developments supporting its effectiveness as an electrode material. While the diffusion kinetics of calcium remain a limiting factor for achieving larger capacities, our study was able to accomplish all experiments at room temperature, providing a strong foundation for future optimization. These results establish a new baseline for the functionality of CaMn<sub>2</sub>O<sub>4</sub> post-spinel and pave the way for further exploration of its potential as a high-performance cathode material. Further studies could investigate the use of other transition metals in the CaMn<sub>2</sub>O<sub>4</sub> host to optimize the crystal structure and facilitate more substantial diffusion of calcium.

## Supplemental Information



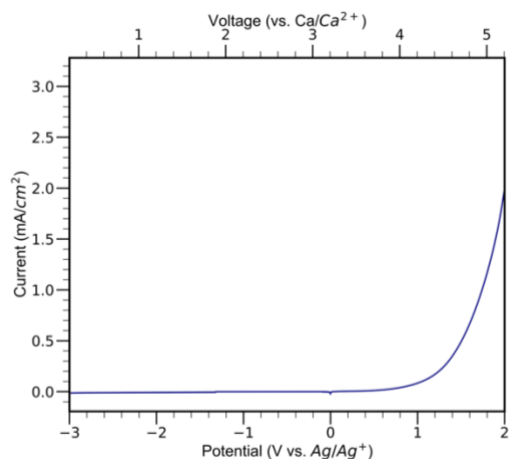
**Figure SI 3.1** - Calibration of reference electrodes a) CV test of Ag/Ag<sup>+</sup> reference electrode (0.01 M AgNO<sub>3</sub> in 0.5 M Ca(TFSI)<sub>2</sub> DME) with 50 mM ferrocene dissolved in 0.5 M Ca(TFSI)<sub>2</sub> in DME with Pt working electrode and AC counter electrode b) OCV of the activated carbon is -0.187 V vs. Ag/Ag<sup>+</sup>

Figure SI 3.1a shows the cyclic voltammetry (CV) of a three-electrode system with 50 mM ferrocene dissolved in Ca(TFSI)<sub>2</sub> in DME. The working electrode was platinum while the counter and reference electrodes were activated carbon and Ag/Ag<sup>+</sup>, respectively. The ferrocene potential was calculated using equation (S3.1)

$$\phi_{Fc/Fc^+} = \frac{\phi_{p,c} + \phi_{p,a}}{2} \quad (\text{S3.1})$$

with  $\phi_{Fc/Fc^+}$  being the measured potential of the ferrocene/ferrocenium reaction.  $\phi_{p,c}$  and  $\phi_{p,a}$  were the cathodic and anodic potentials, respectively. The results from the CV yielded a redox potential at 0.065 V. The value of the ferrocene reaction against the standard hydrogen electrode is 0.4 V. Using the results of the ferrocene CV and the established 0.4 V (vs. SHE) redox reaction, the potential of the Ag/Ag<sup>+</sup> reference electrode was adjusted from its standard reduction potential of 0.8 V to 1.135 V. The calibration also establishes that the Ca/Ca<sup>2+</sup> redox reaction would occur

at  $-3.205\text{ V vs Ag/Ag}^+$ . Following the calibration of the  $\text{Ag/Ag}^+$  reference electrode, an open circuit voltage (OCV) measurement of the activated carbon was performed and found the potential to be  $-0.187\text{ V (vs Ag/Ag}^+)$ . (Figure SI 3.1b) Using the OCV, the voltage of the activated carbon would be  $3.018\text{ V (vs Ca/Ca}^{2+})$ . Values from the ferrocene CV and activated carbon OCV are in close agreement with previous studies on reference electrode calibrations.<sup>[31,73]</sup>



**Figure SI 3.2** - Linear Stability Window of  $\text{Ca(TFSI)}_2$  in DME using 316 stainless steel blocking and calcium nonblocking electrode at  $0.5\text{ mV/s}$

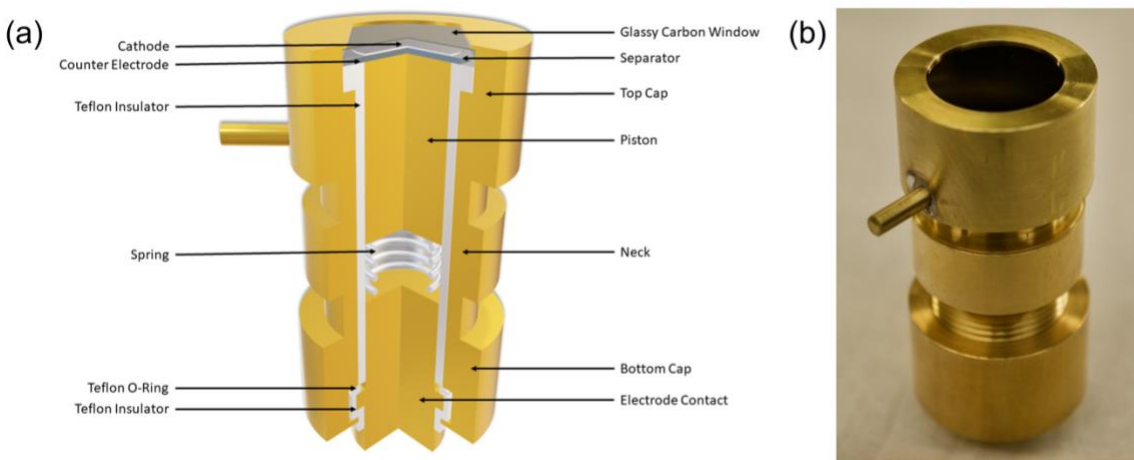


**Figure SI 3.3** - In situ cell a) Schematic of in situ cell used for  $\text{CaMn}_2\text{O}_4$  b) photo of the in situ cell assembled

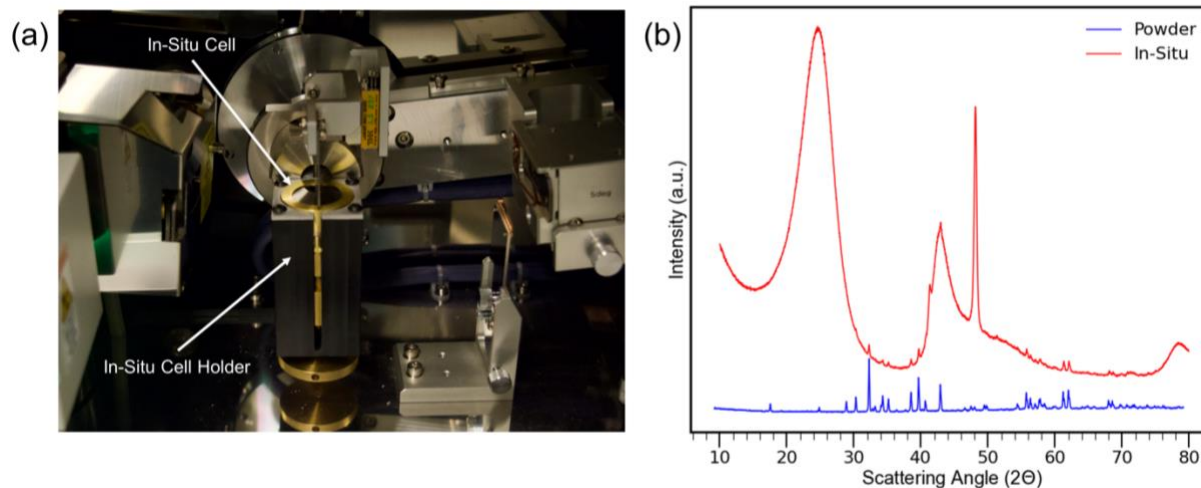


**Figure SI 3.4** - a) Installation of in situ cell inside of the Rigaku XRD b) baseline XRD scan of  $\text{CaMn}_2\text{O}_4$  inside of in situ cell.

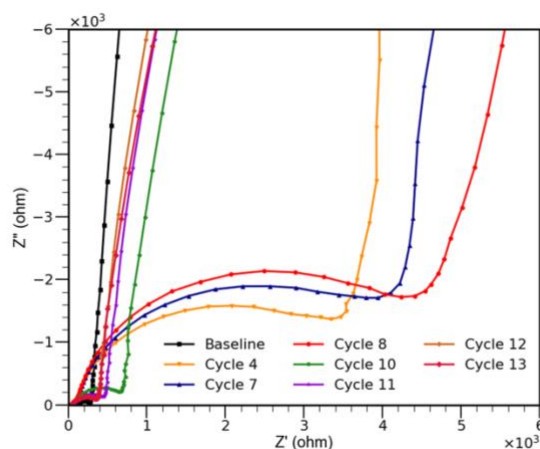


**Figure SI 3.5** - Nyquist plots of impedance for  $\text{CaMn}_2\text{O}_4$  after charge and discharge cycling

After the DFT calculations were completed, structure files were generated using VASP. These files were opened with VESTA<sup>[74]</sup> and XRD patterns were generated using powder diffraction pattern functionality. The simulation incident light has wavelength of 1.54059 Å (X-ray) and the XRD plot was generated based on atomic positions.

The method for simulating the XRD diffraction pattern required the use of eq. S3.2. After performing Fourier transformation of the structural information, the phase of incident light and the structure were combined. The intensity of reflected light can be calculated using structure factor,

$$I(q) = f^2 \sum_{i=1}^N e^{-iq \cdot R_i}, \quad (\text{S3.2})$$

where  $R_i$  is the atomic position,  $f$  is the atomic form factor, and  $q$  is the scattering vector. A plot of intensity with respect to angle  $2\theta$  was generated. The results for the theoretical XRD patterns from  $\text{CaMn}_2\text{O}_4$  at 0% and 25% decalciation are outlined in Figure SI 3.10b. The generated lattice parameters, coordinates and theoretical XRD patterns from DFT calculations are summarized in Figures SI 3.7 & SI 3.8 and Tables SI 3.1-SI 3.8. Structural information in Tables SI 3.2-SI 3.8 used P1 cell symmetry.

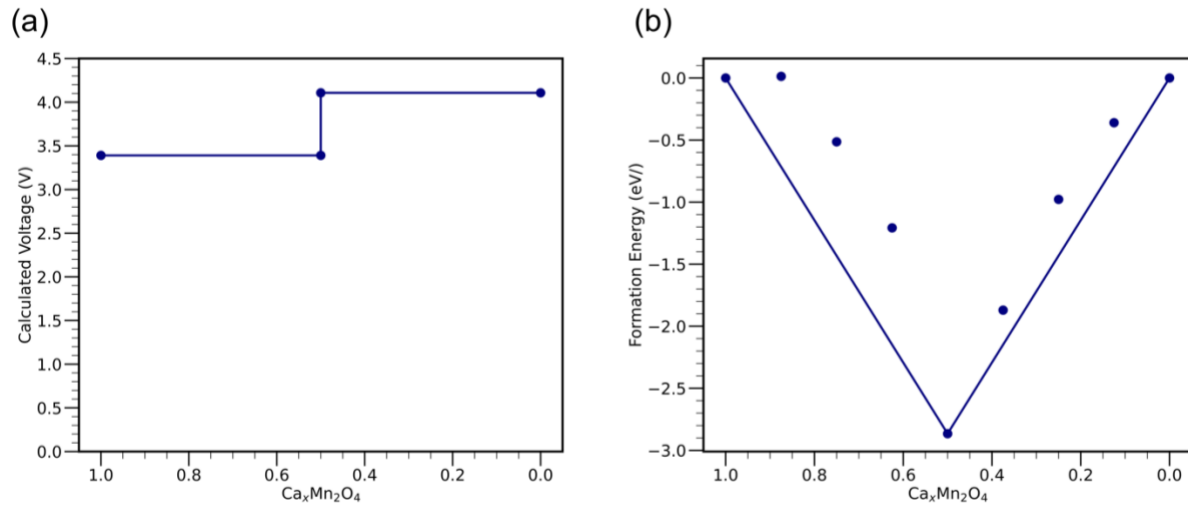


**Figure SI 3.6** - DFT Calculations of  $\text{CaMn}_2\text{O}_4$  a) Voltage profile of  $\text{CaMn}_2\text{O}_4$  as calcium is removed. Voltage values were calculated with stable concentrations of calcium in  $\text{CaMn}_2\text{O}_4$  with the convex hull. b) Convex hull of  $\text{CaMn}_2\text{O}_4$ . Three concentrations of calcium were on the hull and connected by the line.

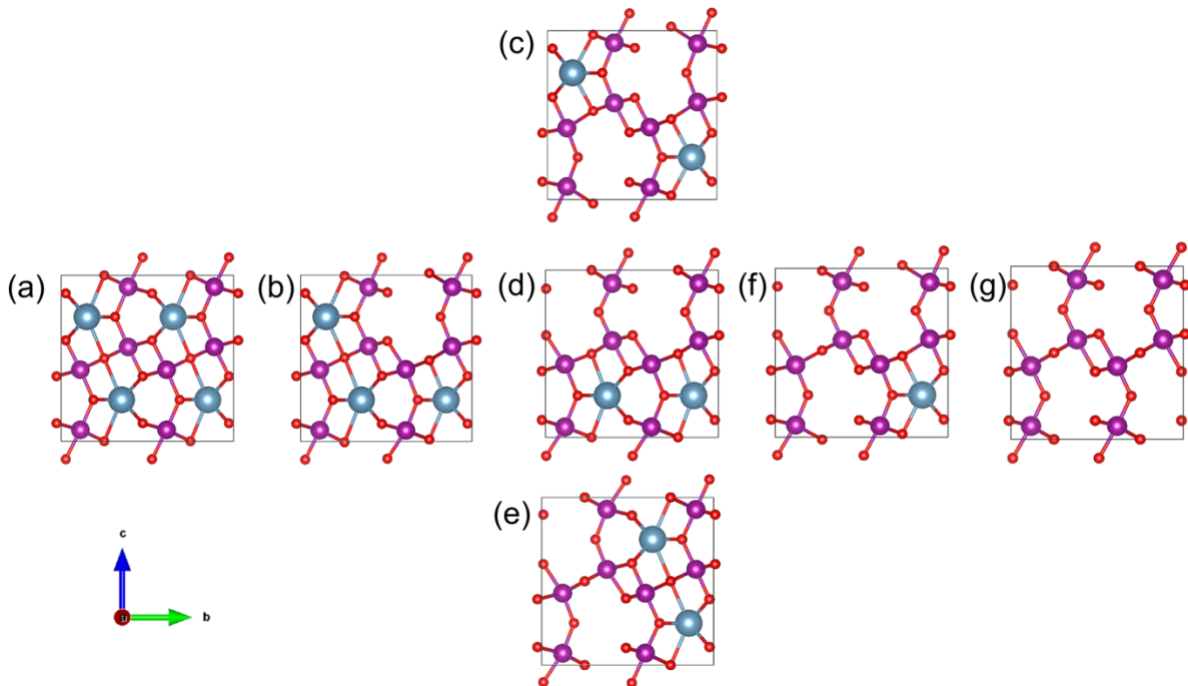


**Figure SI 3.7** - Structural models of  $\text{Ca}_{1-x}\text{Mn}_2\text{O}_4$  deinsertion a)  $x = 0$  b)  $x = 0.25$  c)  $x = 0.5$  d)  $x = 0.5$  e)  $x = 0.5$  f)  $x = 0.75$  g)  $x = 1.0$

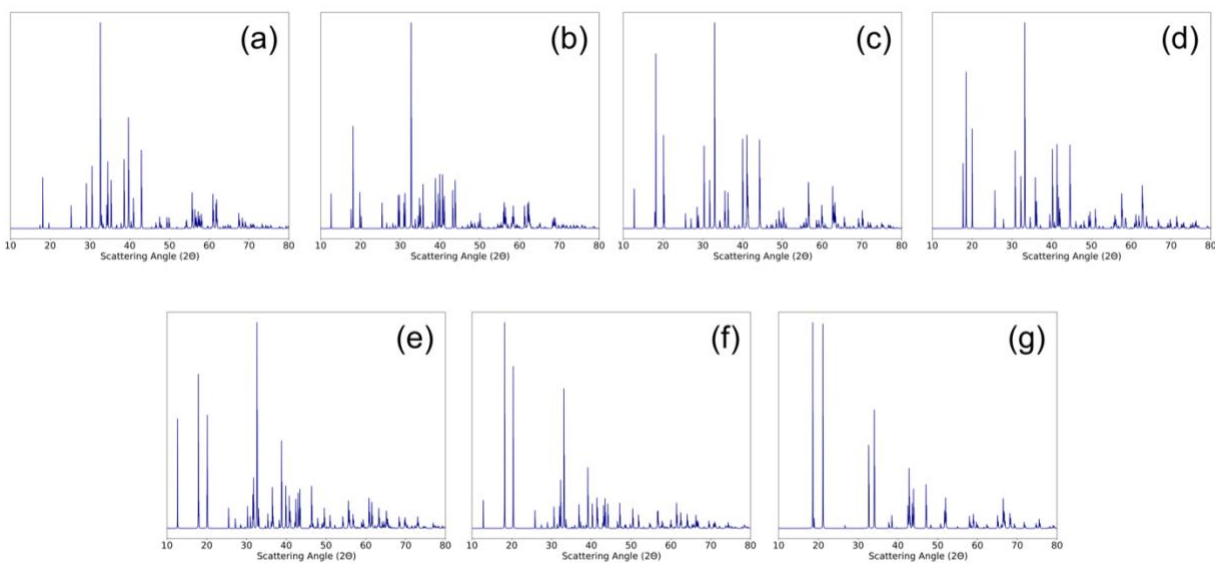


**Figure SI 3.8** - Theoretical XRD patterns of  $\text{Ca}_{1-x}\text{Mn}_2\text{O}_4$  deinsertion a)  $x = 0$  b)  $x = 0.25$  c)  $x = 0.5$  d)  $x = 0.5$  e)  $x = 0.5$  f)  $x = 0.75$  g)  $x = 1.0$

	(a)	(b)	(c)	(d)	(e)	(f)	(g)
<b>Space Group</b>	Pbcm	Pm	P2 <sub>1</sub> /m	Pmc2 <sub>1</sub>	Pma2	Pm	Cmcm
<b>a (Å)</b>	3.21696	3.15752	3.02402	3.02795	3.08506	2.98366	2.86492
<b>b (Å)</b>	10.15714	10.04844	9.87361	9.99746	9.88520	9.78194	9.35579
<b>c (Å)</b>	9.78279	9.77412	9.90640	9.58717	9.75041	9.74097	9.53471
<b>alpha</b>	90	90	90	90	90	90	90
<b>beta</b>	90	90	90	90	90	90	90
<b>gamma</b>	90	90.9703	94.9005	90	90	95.3300	90
<b>Volume (Å<sup>3</sup>)</b>	319.6542	310.0698	294.7035	290.2206	297.3530	283.0702	255.5645

**Table SI 3.1** - Calculated lattice parameters of Ca<sub>1-x</sub>Mn<sub>2</sub>O<sub>4</sub> deinsertion a) x = 0 b) x = 0.25 c) x = 0.5 d) x = 0.5 e) x = 0.5 f) x = 0.75 g) x = 1.0

<b>Element</b>	<b>x</b>	<b>y</b>	<b>z</b>	<b>Occupancy</b>	<b>Biso</b>	<b>Symmetry</b>
Mn1	0.20741	0.38861	0.56872	1	0	1a
Mn2	0.79259	0.61139	0.43128	1	0	1a
Mn3	0.79259	0.61139	0.06872	1	0	1a
Mn4	0.20741	0.38861	0.93128	1	0	1a
Mn5	0.79259	0.88861	0.93128	1	0	1a
Mn6	0.20741	0.11139	0.06872	1	0	1a
Mn7	0.20741	0.11139	0.43128	1	0	1a
Mn8	0.79259	0.88861	0.56872	1	0	1a
Ca1	0.31975	0.64956	0.75000	1	0	1a
Ca2	0.68025	0.35044	0.25000	1	0	1a
Ca3	0.68025	0.14956	0.75000	1	0	1a

Ca4	0.31975	0.85044	0.25000	1	0	1a
O1	0.81210	0.81293	0.75000	1	0	1a
O2	0.18790	0.18707	0.25000	1	0	1a
O3	0.18790	0.31293	0.75000	1	0	1a
O4	0.81210	0.68707	0.25000	1	0	1a
O5	0.79989	0.52693	0.60840	1	0	1a
O6	0.20011	0.47307	0.39160	1	0	1a
O7	0.20011	0.47307	0.10840	1	0	1a
O8	0.79989	0.52693	0.89160	1	0	1a
O9	0.20011	0.02693	0.89160	1	0	1a
O10	0.79989	0.97307	0.10840	1	0	1a
O11	0.79989	0.97307	0.39160	1	0	1a
O12	0.20011	0.02693	0.60840	1	0	1a
O13	0.41369	0.75000	0.50000	1	0	1a
O14	0.58631	0.25000	0.50000	1	0	1a
O15	0.58631	0.25000	0.00000	1	0	1a
O16	0.41369	0.75000	0.00000	1	0	1a

**Table SI 3.2** - Atomic x, y, z coordinates and occupancy of  $\text{Ca}_{1-x}\text{Mn}_2\text{O}_4$  deinsertion with  $x = 0$  (a)

<b>Element</b>	<b>x</b>	<b>y</b>	<b>z</b>	<b>Occupancy</b>	<b>Biso</b>	<b>Symmetry</b>
Mn1	0.22867	0.39685	0.57301	1	0	1a
Mn2	0.78981	0.61431	0.43390	1	0	1a
Mn3	0.78981	0.61431	0.06610	1	0	1a
Mn4	0.22867	0.39685	0.92699	1	0	1a
Mn5	0.78378	0.88411	0.92890	1	0	1a
Mn6	0.22606	0.11148	0.06818	1	0	1a

Mn7	0.22606	0.11148	0.43182	1	0	1a
Mn8	0.78378	0.88411	0.57110	1	0	1a
Ca1	0.69770	0.35446	0.25000	1	0	1a
Ca2	0.69131	0.14775	0.75000	1	0	1a
Ca3	0.32500	0.84975	0.25000	1	0	1a
O1	0.77912	0.81724	0.75000	1	0	1a
O2	0.20186	0.18852	0.25000	1	0	1a
O3	0.20109	0.31590	0.75000	1	0	1a
O4	0.81657	0.68402	0.25000	1	0	1a
O5	0.73681	0.50649	0.60359	1	0	1a
O6	0.20313	0.47443	0.39430	1	0	1a
O7	0.20313	0.47443	0.10571	1	0	1a
O8	0.73681	0.50649	0.89641	1	0	1a
O9	0.20586	0.02673	0.89109	1	0	1a
O10	0.80158	0.97480	0.10688	1	0	1a
O11	0.80158	0.97480	0.39312	1	0	1a
O12	0.20586	0.02673	0.60891	1	0	1a
O13	0.39520	0.75136	0.48795	1	0	1a
O14	0.61399	0.25621	0.50476	1	0	1a
O15	0.61399	0.25621	0.99524	1	0	1a
O16	0.39520	0.75136	0.01205	1	0	1a

**Table SI 3.3** - Atomic x, y, z coordinates and occupancy of  $\text{Ca}_{1-x}\text{Mn}_2\text{O}_4$  deinsertion with  $x = 0.25$   
(b)

Element	x	y	z	Occupancy	Biso	Symmetry
Mn1	0.22519	0.39463	0.57167	1	0	1a
Mn2	0.77481	0.60537	0.42833	1	0	1a

Mn3	0.77481	0.60537	0.07167	1	0	1a
Mn4	0.22519	0.39463	0.92833	1	0	1a
Mn5	0.73099	0.88570	0.92318	1	0	1a
Mn6	0.26901	0.11430	0.07682	1	0	1a
Mn7	0.26901	0.11430	0.42318	1	0	1a
Mn8	0.73099	0.88570	0.57682	1	0	1a
Ca1	0.69825	0.14808	0.75000	1	0	1a
Ca2	0.30175	0.85192	0.25000	1	0	1a
O1	0.65418	0.82085	0.75000	1	0	1a
O2	0.34582	0.17915	0.25000	1	0	1a
O3	0.22284	0.32377	0.75000	1	0	1a
O4	0.77716	0.67623	0.25000	1	0	1a
O5	0.75370	0.51567	0.60221	1	0	1a
O6	0.24630	0.48433	0.39779	1	0	1a
O7	0.24630	0.48433	0.10221	1	0	1a
O8	0.75370	0.51567	0.89779	1	0	1a
O9	0.20665	0.02964	0.89409	1	0	1a
O10	0.79335	0.97036	0.10591	1	0	1a
O11	0.79335	0.97036	0.39409	1	0	1a
O12	0.20665	0.02964	0.60591	1	0	1a
O13	0.32231	0.73033	0.47593	1	0	1a
O14	0.67769	0.26967	0.52407	1	0	1a
O15	0.67769	0.26967	0.97593	1	0	1a
O16	0.32231	0.73033	0.02407	1	0	1a

**Table SI 3.4** - Atomic x, y, z coordinates and occupancy of  $\text{Ca}_{1-x}\text{Mn}_2\text{O}_4$  deinsertion with  $x = 0.5$   
(c)

<b>Element</b>	<b>x</b>	<b>y</b>	<b>z</b>	<b>Occupancy</b>	<b>Biso</b>	<b>Symmetry</b>
Mn1	0.18099	0.38648	0.57847	1	0	1a
Mn2	0.72385	0.61251	0.43775	1	0	1a
Mn3	0.72385	0.61251	0.06225	1	0	1a
Mn4	0.18099	0.38648	0.92153	1	0	1a
Mn5	0.81901	0.88648	0.92153	1	0	1a
Mn6	0.27615	0.11252	0.06225	1	0	1a
Mn7	0.27615	0.11252	0.43775	1	0	1a
Mn8	0.81901	0.88648	0.57847	1	0	1a
Ca1	0.69049	0.35705	0.25000	1	0	1a
Ca2	0.30951	0.85705	0.25000	1	0	1a
O1	0.82356	0.80820	0.75000	1	0	1a
O2	0.21395	0.18646	0.25000	1	0	1a
O3	0.17644	0.30820	0.75000	1	0	1a
O4	0.78605	0.68646	0.25000	1	0	1a
O5	0.67964	0.50442	0.61043	1	0	1a
O6	0.16910	0.47928	0.39630	1	0	1a
O7	0.16910	0.47928	0.10370	1	0	1a
O8	0.67964	0.50442	0.88957	1	0	1a
O9	0.32036	0.00442	0.88957	1	0	1a
O10	0.83090	0.97928	0.10370	1	0	1a
O11	0.83090	0.97928	0.39630	1	0	1a
O12	0.32036	0.00442	0.61043	1	0	1a
O13	0.34901	0.76704	0.49946	1	0	1a
O14	0.65099	0.26704	0.49946	1	0	1a
O15	0.65099	0.26704	0.00054	1	0	1a

O16	0.34901	0.76704	0.00054	1	0	1a
-----	---------	---------	---------	---	---	----

**Table SI 3.5** - Atomic x, y, z coordinates and occupancy of  $\text{Ca}_{1-x}\text{Mn}_2\text{O}_4$  deinsertion with  $x = 0.5$   
(d)

Element	x	y	z	Occupancy	Biso	Symmetry
Mn1	0.21500	0.37853	0.57067	1	0	1a
Mn2	0.76363	0.60297	0.42849	1	0	1a
Mn3	0.76363	0.60297	0.07152	1	0	1a
Mn4	0.21500	0.37853	0.92933	1	0	1a
Mn5	0.76363	0.89703	0.92848	1	0	1a
Mn6	0.21500	0.12147	0.07067	1	0	1a
Mn7	0.21500	0.12147	0.42933	1	0	1a
Mn8	0.76363	0.89703	0.57152	1	0	1a
Ca1	0.29500	0.64494	0.75000	1	0	1a
Ca2	0.29500	0.85506	0.25000	1	0	1a
O1	0.78649	0.81599	0.75000	1	0	1a
O2	0.20512	0.18771	0.25000	1	0	1a
O3	0.20512	0.31229	0.75000	1	0	1a
O4	0.78649	0.68401	0.25000	1	0	1a
O5	0.79038	0.52429	0.60737	1	0	1a
O6	0.25860	0.49084	0.39764	1	0	1a
O7	0.25860	0.49084	0.10236	1	0	1a
O8	0.79038	0.52429	0.89263	1	0	1a
O9	0.25860	0.00916	0.89764	1	0	1a
O10	0.79038	0.97571	0.10737	1	0	1a
O11	0.79038	0.97571	0.39263	1	0	1a
O12	0.25860	0.00916	0.60236	1	0	1a

O13	0.34353	0.75000	0.50000	1	0	1a
O14	0.63219	0.25000	0.50000	1	0	1a
O15	0.63219	0.25000	0.00000	1	0	1a
O16	0.34353	0.75000	0.00000	1	0	1a

**Table SI 3.6** - Atomic x, y, z coordinates and occupancy of  $\text{Ca}_{1-x}\text{Mn}_2\text{O}_4$  deinsertion with  $x = 0.5$   
(e)

Element	x	y	z	Occupancy	Biso	Symmetry
Mn1	0.20158	0.38870	0.57660	1	0	1a
Mn2	0.76135	0.60601	0.43231	1	0	1a
Mn3	0.76135	0.60601	0.06769	1	0	1a
Mn4	0.20158	0.38870	0.92340	1	0	1a
Mn5	0.74277	0.89470	0.91827	1	0	1a
Mn6	0.29525	0.11841	0.07202	1	0	1a
Mn7	0.29525	0.11841	0.42798	1	0	1a
Mn8	0.74277	0.89470	0.58173	1	0	1a
Ca1	0.30680	0.85120	0.25000	1	0	1a
O1	0.72435	0.81364	0.75000	1	0	1a
O2	0.29349	0.18962	0.25000	1	0	1a
O3	0.17474	0.31232	0.75000	1	0	1a
O4	0.77044	0.67759	0.25000	1	0	1a
O5	0.73506	0.51271	0.60860	1	0	1a
O6	0.22913	0.48584	0.39946	1	0	1a
O7	0.22913	0.48584	0.10054	1	0	1a
O8	0.73506	0.51271	0.89140	1	0	1a
O9	0.27415	0.01325	0.89353	1	0	1a
O10	0.81030	0.97619	0.10443	1	0	1a

O11	0.81030	0.97619	0.39557	1	0	1a
O12	0.27415	0.01325	0.60647	1	0	1a
O13	0.31212	0.73571	0.48077	1	0	1a
O14	0.66214	0.27189	0.51390	1	0	1a
O15	0.66214	0.27189	0.98610	1	0	1a
O16	0.31212	0.73571	0.01923	1	0	1a

**Table SI 3.7** - Atomic x, y, z coordinates and occupancy of  $\text{Ca}_{1-x}\text{Mn}_2\text{O}_4$  deinsertion with  $x = 0.75$   
(f)

Element	x	y	z	Occupancy	Biso	Symmetry
Mn1	0.24956	0.38384	0.57700	1	0	1a
Mn2	0.75044	0.61616	0.42300	1	0	1a
Mn3	0.75044	0.61616	0.07700	1	0	1a
Mn4	0.24956	0.38384	0.92300	1	0	1a
Mn5	0.75044	0.88384	0.92300	1	0	1a
Mn6	0.24956	0.11616	0.07700	1	0	1a
Mn7	0.24956	0.11616	0.42300	1	0	1a
Mn8	0.75044	0.88384	0.57700	1	0	1a
O1	0.75182	0.80217	0.75000	1	0	1a
O2	0.24818	0.19782	0.25000	1	0	1a
O3	0.24818	0.30217	0.75000	1	0	1a
O4	0.75182	0.69783	0.25000	1	0	1a
O5	0.74965	0.51078	0.60865	1	0	1a
O6	0.25035	0.48922	0.39135	1	0	1a
O7	0.25035	0.48922	0.10865	1	0	1a
O8	0.74965	0.51078	0.89135	1	0	1a
O9	0.25035	0.01078	0.89135	1	0	1a

O10	0.74965	0.98922	0.10865	1	0	1a
O11	0.74965	0.98922	0.39135	1	0	1a
O12	0.25035	0.01078	0.60865	1	0	1a
O13	0.25035	0.75000	0.50000	1	0	1a
O14	0.74965	0.25000	0.50000	1	0	1a
O15	0.74965	0.25000	0.00000	1	0	1a
O16	0.25035	0.75000	0.00000	1	0	1a

**Table SI 3.8** - Atomic x, y, z coordinates and occupancy of  $\text{Ca}_{1-x}\text{Mn}_2\text{O}_4$  deinsertion with  $x = 1.0$  (g)

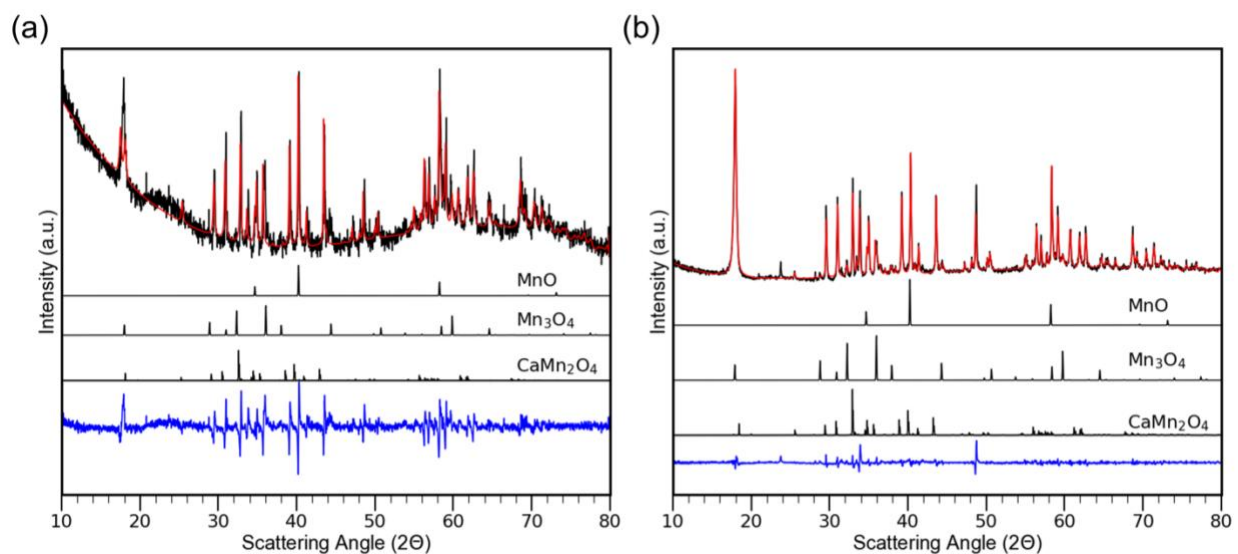


**Figure SI 3.9** - Rietveld refinement of  $\text{CaMn}_2\text{O}_4$  cathode a) post-maximum charge b) post-discharge

	<b>a</b> (Å)	<b>Deviation</b> (Å)	<b>b</b> (Å)	<b>Deviation</b> (Å)	<b>c</b> (Å)	<b>Deviation</b> (Å)
<b>Pristine</b>	3.156676	0.000119	9.988452	0.000457	9.675391	0.000396
<b>Charged</b>	3.154765	0.000302	9.978689	0.001508	9.666233	0.00109
<b>Discharged</b>	3.158088	0.000311	9.997047	0.001092	9.678633	0.000979

**Table SI 3.9** - Refined parameters for  $\text{CaMn}_2\text{O}_4$

	<b>a</b> (Å)	<b>Deviation</b> (Å)	<b>b</b> (Å)	<b>Deviation</b> (Å)	<b>c</b> (Å)	<b>Deviation</b> (Å)
<b>Charged</b>	5.761503	0.000405	5.761503	0	9.464502	0.002912
<b>Discharged</b>	5.753304	0.001810	5.753304	0	9.481883	0.003148

**Table SI 3.10** - Refined parameters for Mn<sub>3</sub>O<sub>4</sub>

	<b>a</b> (Å)	<b>Deviation</b> (Å)	<b>b</b> (Å)	<b>Deviation</b> (Å)	<b>c</b> (Å)	<b>Deviation</b> (Å)
<b>Charged</b>	4.48863	0.001023	4.48863	0	4.48863	0
<b>Discharged</b>	4.46448	0.001569	4.46448	0	4.46448	0

**Table SI 3.11** - Refined parameters for MnO

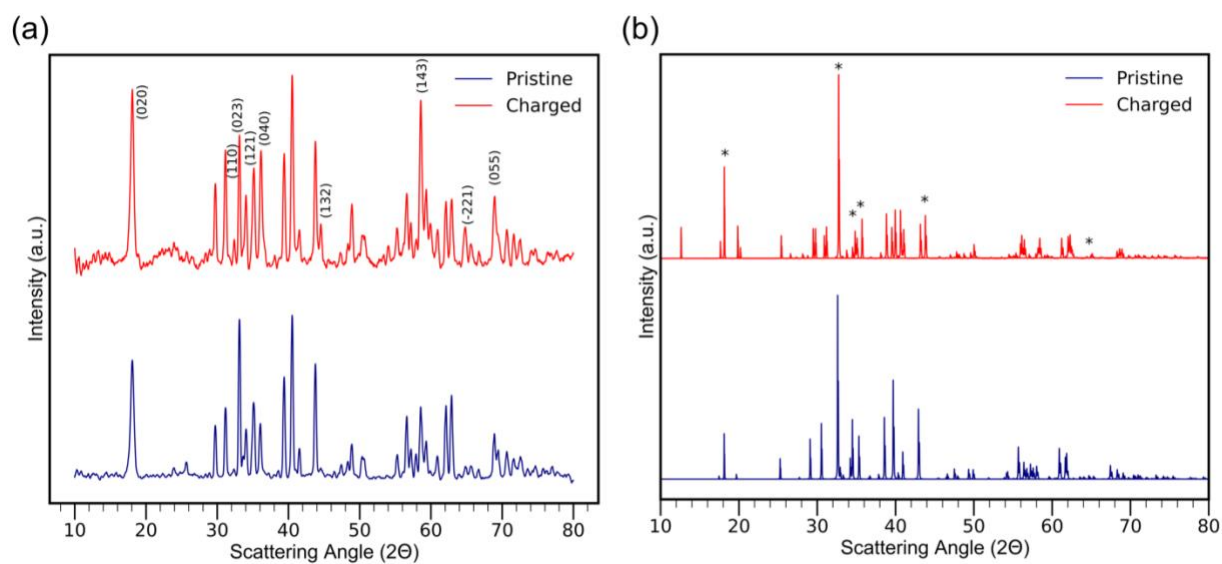


**Figure SI 3.10** - XRD changes with CaMn<sub>2</sub>O<sub>4</sub> from maximum charge a) Full experimental XRD of CaMn<sub>2</sub>O<sub>4</sub> from its pristine electrode and after maximum charge of the CaMn<sub>2</sub>O<sub>4</sub> b) Theoretical XRD of the CaMn<sub>2</sub>O<sub>4</sub> with 25% vacancies from the pristine electrode

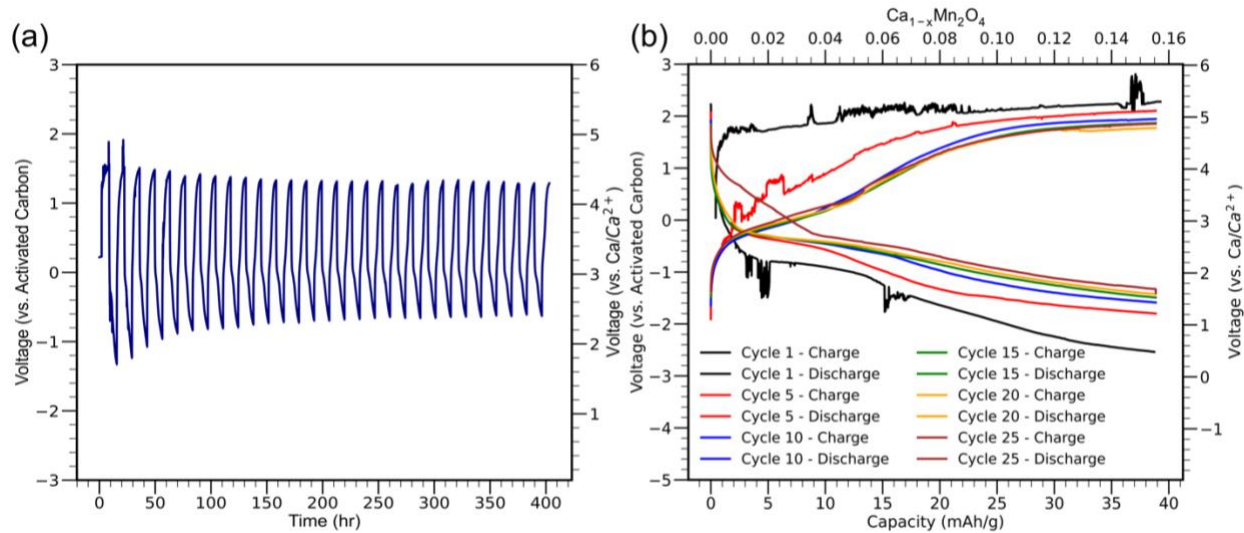


**Figure SI 3.11** - Galvanostatic cycling of the  $\text{CaMn}_2\text{O}_4$  at C/39 a) Voltage-time curve of 30 cycles of testing b) Capacity-voltage curves of selected cycles of  $\text{CaMn}_2\text{O}_4$

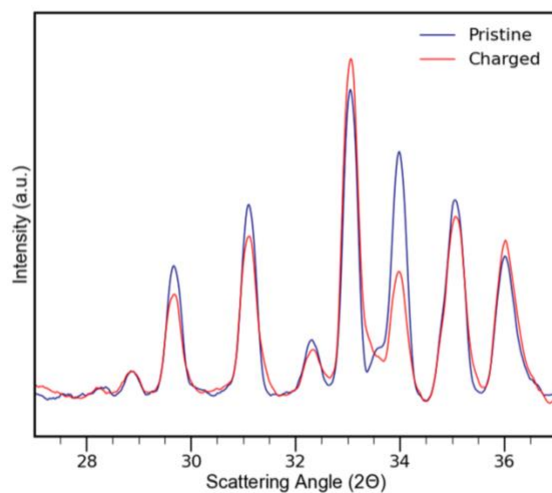


**Figure SI 3.12** - XRD of the  $\text{CaMn}_2\text{O}_4$  before after galvanostatic cycling of the  $\text{CaMn}_2\text{O}_4$

## References

1. Arroyo-de Dompablo, M. E.; Ponrouch, A.; Johansson, P.; Palacín, M. R. Achievements, Challenges, and Prospects of Calcium Batteries. *Chem. Rev.* **2019**. <https://doi.org/10.1021/acs.chemrev.9b00339>.
2. Canepa, P.; Sai Gautam, G.; Hannah, D. C.; Malik, R.; Liu, M.; Gallagher, K. G.; Persson, K. A.; Ceder, G. Odyssey of Multivalent Cathode Materials: Open Questions and Future Challenges. *Chem. Rev.* **2017**, *117* (5), 4287–4341.
3. Hosein, I. D. The Promise of Calcium Batteries: Open Perspectives and Fair Comparisons. *ACS Energy Lett.* **2021**, 1560–1565.
4. Zhang, S.; Zhu, Y.; Wang, D.; Li, C.; Han, Y.; Shi, Z.; Feng, S. Poly(Anthraquinonyl Sulfide)/CNT Composites as High-Rate-Performance Cathodes for Nonaqueous Rechargeable Calcium-Ion Batteries. *Adv. Sci.* **2022**, e2200397.
5. Rong, Z.; Malik, R.; Canepa, P.; Sai Gautam, G.; Liu, M.; Jain, A.; Persson, K.; Ceder, G. Materials Design Rules for Multivalent Ion Mobility in Intercalation Structures. *Chem. Mater.* **2015**, *27* (17), 6016–6021.
6. Rutt, A.; Shen, J.-X.; Horton, M.; Kim, J.; Lin, J.; Persson, K. A. Expanding the Material Search Space for Multivalent Cathodes. *ACS Appl. Mater. Interfaces* **2022**, *14* (39), 44367–44376.
7. Zhang, Z.; Zhang, X.; Zhao, X.; Yao, S.; Chen, A.; Zhou, Z. Computational Screening of Layered Materials for Multivalent Ion Batteries. *ACS Omega* **2019**, *4* (4), 7822–7828.
8. Park, H.; Bartel, C. J.; Ceder, G.; Zapol, P. Layered Transition Metal Oxides as ca Intercalation Cathodes: A Systematic First-principles Evaluation. *Adv. Energy Mater.* **2021**, 2101698.
9. Pathreker, S.; Reed, S.; Chando, P.; Hosein, I. D. A Study of Calcium Ion Intercalation in Perovskite Calcium Manganese Oxide. *J. Electroanal. Chem.* **2020**, *874*, 114453.
10. Cabello, M.; Nacimiento, F.; Alcántara, R.; Lavela, P.; Pérez Vicente, C.; Tirado, J. L. Applicability of Molybdate as an Electrode Material in Calcium Batteries: A Structural Study of Layer-Type  $\text{Ca}_x\text{MoO}_3$ . *Chem. Mater.* **2018**, *30* (17), 5853–5861.
11. Cabello, M.; Nacimiento, F.; González, J. R.; Ortiz, G.; Alcántara, R.; Lavela, P.; Pérez-Vicente, C.; Tirado, J. L. Advancing towards a Veritable Calcium-Ion Battery:  $\text{CaCo}_2\text{O}_4$  Positive Electrode Material. *Electrochem. commun.* **2016**, *67*, 59–64.

12. Biria, S.; Pathreker, S.; Genier, F. S.; Hosein, I. D. A Highly Conductive and Thermally Stable Ionic Liquid Gel Electrolyte for Calcium Ion Batteries. *ACS Appl. Polym. Mater.* **2020**. <https://doi.org/10.1021/acsapm.9b01223>.
13. Liu, M.; Rong, Z.; Malik, R.; Canepa, P.; Jain, A.; Ceder, G.; Persson, K. A. Spinel Compounds as Multivalent Battery Cathodes: A Systematic Evaluation Based on Ab Initio Calculations. *Energy Environ. Sci.* **2015**, *8* (3), 964–974.
14. Sickafus, K. E.; Wills, J. M.; Grimes, N. W. Structure of Spinel. *J. Am. Ceram. Soc.* **2004**, *82* (12), 3279–3292.
15. Yamanaka, T.; Uchida, A.; Nakamoto, Y. Structural Transition of Post-Spinel Phases CaMn<sub>2</sub>O<sub>4</sub>, CaFe<sub>2</sub>O<sub>4</sub>, and CaTi<sub>2</sub>O<sub>4</sub> under High Pressures up to 80 GPa. *Am. Mineral.* **2008**, *93* (11-12), 1874–1881.
16. Ling, C.; Mizuno, F. Phase Stability of Post-Spinel Compound AMn<sub>2</sub>O<sub>4</sub> (A = Li, Na, or Mg) and Its Application as a Rechargeable Battery Cathode. *Chem. Mater.* **2013**, *25* (15), 3062–3071.
17. Dompablo, M. E. A.; Krich, C.; Nava-Avenidaño, J.; Biškup, N.; Palacín, M. R.; Bardé, F. A Joint Computational and Experimental Evaluation of CaMn<sub>2</sub>O<sub>4</sub> Polymorphs as Cathode Materials for Ca Ion Batteries. *Chem. Mater.* **2016**, *28* (19), 6886–6893.
18. White, B. D.; dos Santos, C. A. M.; Souza, J. A.; McClellan, K. J.; Neumeier, J. J. Crystal Growth and Characterization of Marokite CaMn<sub>2</sub>O<sub>4</sub>+ $\delta$ . *J. Cryst. Growth* **2008**, *310* (14), 3325–3330.
19. Maarof, H. I.; Wan Daud, W. M. A.; Aroua, M. K. Effect of Varying the Amount of Binder on the Electrochemical Characteristics of Palm Shell Activated Carbon. *IOP Conf. Ser. Mater. Sci. Eng.* **2017**, *210*, 012011.
20. Sottmann, J.; Pralong, V.; Barrier, N.; Martin, C. An Electrochemical Cell for Operando Bench-Top X-Ray Diffraction. *J. Appl. Crystallogr.* **2019**, *52* (2), 485–490.
21. Eguchi, T.; Kanamoto, Y.; Tomioka, M.; Tashima, D.; Kumagai, S. Effect of Ball Milling on the Electrochemical Performance of Activated Carbon with a Very High Specific Surface Area. *Batteries* **2020**, *6* (2), 22.
22. Zhang, Y.; Huld, F.; Lu, S.; Jektvik, C.; Lou, F.; Yu, Z. Revisiting Polytetrafluorethylene Binder for Solvent-Free Lithium-Ion Battery Anode Fabrication. *Batteries* **2022**, *8* (6), 57.
23. Bryntesen, S. N.; Strømman, A. H.; Tolstorebrov, I.; Shearing, P. R.; Lamb, J. J.; Stokke Burheim, O. Opportunities for the State-of-the-Art Production of LIB electrodes—A Review. *Energies* **2021**, *14* (5), 1406.

24. Kraytsberg, A.; Ein-Eli, Y. Conveying Advanced Li-Ion Battery Materials into Practice the Impact of Electrode Slurry Preparation Skills. *Adv. Energy Mater.* **2016**, *6* (21), 1600655.
25. Lee, G.-W.; Ryu, J. H.; Han, W.; Ahn, K. H.; Oh, S. M. Effect of Slurry Preparation Process on Electrochemical Performances of LiCoO<sub>2</sub> Composite Electrode. *J. Power Sources* **2010**, *195* (18), 6049–6054.
26. Ram, P.; Patel, H.; Singhal, R.; Choudhary, G.; Sharma, R. K. On the Study of Mixing and Drying on Electrochemical Performance of Spinel LiMn<sub>2</sub>O<sub>4</sub> Cathodes. *J. Renewable Sustainable Energy* **2019**, *11* (1), 014104.
27. Bond, A. M.; Oldham, K. B.; Snook, G. A. Use of the Ferrocene Oxidation Process to Provide Both Reference Electrode Potential Calibration and a Simple Measurement (via Semiintegration) of the Uncompensated Resistance in Cyclic Voltammetric Studies in High-Resistance Organic Solvents. *Anal. Chem.* **2000**, *72* (15), 3492–3496.
28. Biria, S.; Pathreker, S.; Genier, F. S.; Li, H.; Hosein, I. D. Plating and Stripping Calcium at Room Temperature in an Ionic-Liquid Electrolyte. *ACS Appl. Energy Mater.* **2020**, *3* (3), 2310–2314.
29. Biria, S.; Pathreker, S.; Li, H.; Hosein, I. D. Plating and Stripping of Calcium in an Alkyl Carbonate Electrolyte at Room Temperature. *ACS Appl. Energy Mater.* **2019**, *2* (11), 7738–7743.
30. Chen, C.; Shi, F.; Zhang, S.; Su, Y.; Xu, Z.-L. Ultrastable and High Energy Calcium Rechargeable Batteries Enabled by Calcium Intercalation in a NASICON Cathode. *Small* **2022**, 2107853.
31. Zuo, C.; Xiong, F.; Wang, J.; An, Y.; Zhang, L.; An, Q. MnO<sub>2</sub> Polymorphs as Cathode Materials for Rechargeable Ca-ion Batteries. *Adv. Funct. Mater.* **2022**, 2202975.
32. Degen, T.; Sadki, M.; Bron, E.; König, U.; Nénert, G. The HighScore Suite. *Powder Diffr.* **2014**, *29* (S2), S13–S18.
33. Jain, A.; Ong, S. P.; Hautier, G.; Chen, W.; Richards, W. D.; Dacek, S.; Cholia, S.; Gunter, D.; Skinner, D.; Ceder, G.; Persson, K. A. Commentary: The Materials Project: A Materials Genome Approach to Accelerating Materials Innovation. *APL Materials* **2013**, *1* (1), 011002.
34. Kresse, G.; Furthmüller, J. Efficient Iterative Schemes for Ab Initio Total-Energy Calculations Using a Plane-Wave Basis Set. *Phys. Rev. B Condens. Matter* **1996**, *54* (16), 11169–11186.
35. Blöchl, P. E. Projector Augmented-Wave Method. *Phys. Rev. B Condens. Matter* **1994**, *50* (24), 17953–17979.

36. Perdew, J. P.; Burke, K.; Ernzerhof, M. Generalized Gradient Approximation Made Simple. *Phys. Rev. Lett.* **1996**, *77* (18), 3865–3868.
37. The Materials Project. *Materials Data on CaMn<sub>2</sub>O<sub>4</sub> by Materials Project*. United States: N. p., 2020. Web. doi:10.17188/1193549.
38. He, K.; Chen, N.; Wang, C.; Wei, L.; Chen, J. Method for Determining Crystal Grain Size by X-Ray Diffraction. *Cryst. Res. Technol.* **2018**, *53* (2), 1700157.
39. Yu, N.; Nair, M. M.; Mahinpey, N. Structure and Phase Evolution of CaMnO<sub>3</sub> Perovskite during Isothermal Redox Cycles. *Can. J. Chem. Eng.* **2019**, *97* (7), 2131–2136.
40. Black, A. P.; Frontera, C.; Torres, A.; Recio-Poo, M.; Rozier, P.; Forero-Saboya, J. D.; Fauth, F.; Urones-Garrote, E.; Arroyo-de Dompablo, M. E.; Palacín, M. R. Elucidation of the Redox Activity of Ca<sub>2</sub>MnO<sub>3.5</sub> and CaV<sub>2</sub>O<sub>4</sub> in Calcium Batteries Using Operando XRD: Charge Compensation Mechanism and Reversibility. *Energy Storage Materials* **2022**, *47*, 354–364.
41. Kwon, B. J.; Yin, L.; Bartel, C. J.; Kumar, K.; Parajuli, P.; Gim, J.; Kim, S.; Wu, Y. A.; Klie, R. F.; Lapidus, S. H.; Key, B.; Ceder, G.; Cabana, J. Intercalation of Ca into a Highly Defective Manganese Oxide at Room Temperature. *Chem. Mater.* **2022**, *34* (2), 836–846.
42. Han, J.; Yagi, S.; Ichitsubo, T. Suppressive Effect of Fe Cations in Mg(Mn<sub>1-x</sub>Fe<sub>x</sub>)<sub>2</sub>O<sub>4</sub> Positive Electrodes on Oxidative Electrolyte Decomposition for Mg Rechargeable Batteries. *J. Power Sources* **2019**, *435*, 226822.
43. Zhang, X.; Xu, X.; Song, B.; Duan, M.; Meng, J.; Wang, X.; Xiao, Z.; Xu, L.; Mai, L. Towards a Stable Layered Vanadium Oxide Cathode for High-Capacity Calcium Batteries. *Small* **2022**, e2107174.
44. Nolis, G. M.; Adil, A.; Yoo, H. D.; Hu, L.; Bayliss, R. D.; Lapidus, S. H.; Berkland, L.; Phillips, P. J.; Freeland, J. W.; Kim, C.; Klie, R. F.; Cabana, J. Electrochemical Reduction of a Spinel-Type Manganese Oxide Cathode in Aqueous Electrolytes with Ca<sup>2+</sup> or Zn<sup>2+</sup>. *J. Phys. Chem. C* **2018**, *122* (8), 4182–4188.
45. Ling, C.; Zhang, R.; Arthur, T. S.; Mizuno, F. How General Is the Conversion Reaction in Mg Battery Cathode: A Case Study of the Magnesium of  $\alpha$ -MnO<sub>2</sub>. *Chem. Mater.* **2015**, *27* (16), 5799–5807.
46. Michail, A.; Silván, B.; Tapia-Ruiz, N. Progress in High-Voltage MgMn<sub>2</sub>O<sub>4</sub> Oxyspinel Cathode Materials for Mg Batteries. *Current Opinion in Electrochemistry* **2022**, *31*, 100817.
47. Cabello, M.; Alcántara, R.; Nacimiento, F.; Ortiz, G.; Lavela, P.; Tirado, J. L. Electrochemical and Chemical Insertion/deinsertion of Magnesium in Spinel-Type

- MgMn<sub>2</sub>O<sub>4</sub> and Lambda-MnO<sub>2</sub> for Both Aqueous and Non-Aqueous Magnesium-Ion Batteries. *CrystEngComm* **2015**, *17* (45), 8728–8735.
48. Hatakeyama, T.; Okamoto, N. L.; Shimokawa, K.; Li, H.; Nakao, A.; Uchimoto, Y.; Tanimura, H.; Kawaguchi, T.; Ichitsubo, T. Electrochemical Phase Transformation Accompanied with Mg Extraction and Insertion in a Spinel MgMn<sub>2</sub>O<sub>4</sub> Cathode Material. *Phys. Chem. Chem. Phys.* **2019**, *21* (42), 23749–23757.
49. Robba, A.; Tchernychova, E.; Bitenc, J.; Randon-Vitanova, A.; Dominko, R. Magnesium Insertion and Related Structural Changes in Spinel-Type Manganese Oxides. *Crystals (Basel)* **2021**, *11* (8), 984.
50. Tuerxun, F.; Otani, S.; Yamamoto, K.; Matsunaga, T.; Imai, H.; Mandai, T.; Watanabe, T.; Uchiyama, T.; Kanamura, K.; Uchimoto, Y. Phase Transition Behavior of MgMn<sub>2</sub>O<sub>4</sub> Spinel Oxide Cathode during Magnesium Ion Insertion. *Chem. Mater.* **2021**, *33* (3), 1006–1012.
51. Okamoto, S.; Ichitsubo, T.; Kawaguchi, T.; Kumagai, Y.; Oba, F.; Yagi, S.; Shimokawa, K.; Goto, N.; Doi, T.; Matsubara, E. Intercalation and Push-Out Process with Spinel-to-Rocksalt Transition on Mg Insertion into Spinel Oxides in Magnesium Batteries. *Adv. Sci.* **2015**, *2* (8), 1500072.
52. Ling, C.; Zhang, R. Manganese Dioxide As Rechargeable Magnesium Battery Cathode. *Frontiers in Energy Research* **2017**, *5*. <https://doi.org/10.3389/fenrg.2017.00030>.
53. The Materials Project. *Materials Data on Mn<sub>3</sub>O<sub>4</sub> by Materials Project*. United States: N. p., 2020. Web. doi:10.17188/1183671.
54. The Materials Project. *Materials Data on MnO by Materials Project*. United States: N. p., 2020. Web. doi:10.17188/1193794.
55. Truong, Q. D.; Kempaiah Devaraju, M.; Tran, P. D.; Gambe, Y.; Nayuki, K.; Sasaki, Y.; Honma, I. Unravelling the Surface Structure of MgMn<sub>2</sub>O<sub>4</sub> Cathode Materials for Rechargeable Magnesium-Ion Battery. *Chem. Mater.* **2017**, *29* (15), 6245–6251.
56. Liu, L.-G. Disproportionation of Marokite at High Pressures and Temperatures with Geophysical Implications. *Earth Planet. Sci. Lett.* **1983**, *64* (1), 139–144.
57. Torres, A.; Luque, F. J.; Tortajada, J.; Arroyo-de Dompablo, M. E. DFT Investigation of Ca Mobility in Reduced-Perovskite and Oxidized-Marokite Oxides. *Energy Storage Materials* **2019**, *21*, 354–360.
58. Holder, C. F.; Schaak, R. E. Tutorial on Powder X-Ray Diffraction for Characterizing Nanoscale Materials. *ACS Nano* **2019**, *13* (7), 7359–7365.

59. Chauhan, A.; Chauhan, P. Powder XRD Technique and Its Applications in Science and Technology. *J. Anal. Bioanal. Tech.* **2014**, *5* (5), 1–5.
60. Tojo, T.; Tawa, H.; Oshida, N.; Inada, R.; Sakurai, Y. Electrochemical Characterization of a Layered  $\alpha$ -MoO<sub>3</sub> as a New Cathode Material for Calcium Ion Batteries. *J. Electroanal. Chem.* **2018**, *825*, 51–56.
61. Ilton, E. S.; Post, J. E.; Heaney, P. J.; Ling, F. T.; Kerisit, S. N. XPS Determination of Mn Oxidation States in Mn (hydr)oxides. *Appl. Surf. Sci.* **2016**, *366*, 475–485.
62. Yang, J.; Yu, H.; Wang, Y.; Qi, F.; Liu, H.; Lou, L.-L.; Yu, K.; Zhou, W.; Liu, S. Effect of Oxygen Coordination Environment of Ca-Mn Oxides on Catalytic Performance of Pd Supported Catalysts for Aerobic Oxidation of 5-Hydroxymethyl-2-Furfural. <https://doi.org/10.1039/x0xx00000x>.
63. Toupin, M.; Brousse, T.; Bélanger, D. Charge Storage Mechanism of MnO<sub>2</sub> Electrode Used in Aqueous Electrochemical Capacitor. *Chem. Mater.* **2004**, *16* (16), 3184–3190.
64. Cerrato, J. M.; Hochella, M. F., Jr; Knocke, W. R.; Dietrich, A. M.; Cromer, T. F. Use of XPS to Identify the Oxidation State of Mn in Solid Surfaces of Filtration Media Oxide Samples from Drinking Water Treatment Plants. *Environ. Sci. Technol.* **2010**, *44* (15), 5881–5886.
65. Zhuang, G.; Chen, Y.; Zhuang, Z.; Yu, Y.; Yu, J. Oxygen Vacancies in Metal Oxides: Recent Progress towards Advanced Catalyst Design. *Science China Materials* **2020**, *63* (11), 2089–2118.
66. Gouda, G. M.; Nagendra, C. L. Preparation and Characterization of Thin Film Thermistors of Metal Oxides of Manganese and Vanadium (Mn-V-O). *Sens. Actuators A Phys.* **2013**, *190*, 181–190.
67. Biesinger, M. C.; Payne, B. P.; Grosvenor, A. P.; Lau, L. W. M.; Gerson, A. R.; Smart, R. S. C. Resolving Surface Chemical States in XPS Analysis of First Row Transition Metals, Oxides and Hydroxides: Cr, Mn, Fe, Co and Ni. *Appl. Surf. Sci.* **2011**, *257* (7), 2717–2730.
68. Głuchowski, P.; Tomala, R.; Kujawa, D.; Boiko, V.; Murauskas, T.; Solarz, P. Insights into the Relationship between Crystallite Size, Sintering Pressure, Temperature Sensitivity, and Persistent Luminescence Color of Gd<sub>2.97</sub>Pr<sub>0.03</sub>Ga<sub>3</sub>Al<sub>2</sub>O<sub>12</sub> Powders and Ceramics. *J. Phys. Chem. C* **2022**, *126* (16), 7127–7142.
69. Keller, C.; Desrues, A.; Karuppiah, S.; Martin, E.; Alper, J. P.; Boismain, F.; Villevieille, C.; Herlin-Boime, N.; Haon, C.; Chenevier, P. Effect of Size and Shape on Electrochemical Performance of Nano-Silicon-Based Lithium Battery. *Nanomaterials (Basel)* **2021**, *11* (2). <https://doi.org/10.3390/nano11020307>.

70. Landi, B. J.; Ganter, M. J.; Cress, C. D.; DiLeo, R. A.; Raffaele, R. P. Carbon Nanotubes for Lithium Ion Batteries. *Energy Environ. Sci.* **2009**, *2* (6), 638–654.
71. Xia, Y.; Zheng, J.; Wang, C.; Gu, M. Designing Principle for Ni-Rich Cathode Materials with High Energy Density for Practical Applications. *Nano Energy* **2018**, *49*, 434–452.
72. Myung, S.-T.; Maglia, F.; Park, K.-J.; Yoon, C. S.; Lamp, P.; Kim, S.-J.; Sun, Y.-K. Nickel-Rich Layered Cathode Materials for Automotive Lithium-Ion Batteries: Achievements and Perspectives. *ACS Energy Lett.* **2017**, *2* (1), 196–223.
73. Xu, Z.-L.; Park, J.; Wang, J.; Moon, H.; Yoon, G.; Lim, J.; Ko, Y.-J.; Cho, S.-P.; Lee, S.-Y.; Kang, K. A New High-Voltage Calcium Intercalation Host for Ultra-Stable and High-Power Calcium Rechargeable Batteries. *Nat. Commun.* **2021**, *12* (1), 3369.
74. Momma, K. and Izumi, F. (2008) VESTA: A Three-Dimensional Visualization System for Electronic and Structural Analysis. *Journal of Applied Crystallography*, *41*, 653-658. <http://dx.doi.org/10.1107/S0021889808012016>

## **CHAPTER 4**

# **A STUDY OF CALCIUM ION INTERCALATION IN POST-SPINEL CALCIUM IRON OXIDE**

## 4.1 Introduction

The continuous expansion of new technologies that rely on lithium-ion batteries to power them, along with lithium's limited supply, has prompted the exploration of alternative battery chemistries including calcium and magnesium based batteries.<sup>[1]</sup> Calcium holds particular appeal as an alternative battery chemistry due to its high gravimetric capacity of 2205 mAh/g and a standard reduction potential of -2.87 V (vs. SHE), which is similar to that of lithium.<sup>[2-4]</sup> Calcium is also the 5th most abundant element on the planet, making the raw materials needed for processing it relatively inexpensive. The United States has the greatest annual Ca production which alleviates the problem of geographical material distribution that is felt with other metals such as lithium.<sup>[2]</sup> The multivalency of calcium-ion batteries has the potential to achieve energy densities that would make them applicable for technologies that use lithium-ion batteries including portable electronics and stationary storage solutions.

There are several challenges to the development of calcium-based batteries including the identification of suitable cathodes for intercalation chemistry. A successful calcium cathode must be able to intercalate and deintercalate cations at high current densities, operate at high voltages, and retain structural stability that allow for high capacities and cycling life.<sup>[4,5]</sup> Because of the multivalent nature of calcium cations, they have more interactions with the intercalation host through stronger attraction to anions and greater repulsion with cations.<sup>[4,6]</sup> These stronger interactions cause slower diffusion kinetics and limit the performance of calcium-ion batteries.

Density Functional Theory (DFT) is a quantum mechanical modeling method that has been used as a screening tool for identifying suitable cathodes for calcium-ion batteries. Based on the criteria set for successful intercalation chemistry with electrodes, DFT calculations have been able to identify transition metal oxides as promising cathodes for calcium batteries.<sup>[7-9]</sup> While numerous

studies have focused on modeling the intercalation behavior between calcium and transition metal oxides, only a few of the modeled systems have been experimentally investigated.<sup>[10-12]</sup> Transition metal oxides that have been evaluated have shown promising electrochemical activity and reversible capacities.

One such transition metal oxide that has been theoretically investigated but does not have experimental validation is calcium iron oxide ( $\text{CaFe}_2\text{O}_4$ ). Theoretical work done on the transition metal oxide has concluded phase stability with the transition metal oxide as it is decalciated and has also reported a diffusion barrier of 1.2 eV.<sup>[13]</sup> Conclusions drawn from the theoretical investigations reported that the diffusion barrier for the  $\text{CaFe}_2\text{O}_4$  would be too high for any calcium ion mobility and that other ferrites would be more suitable for achieving the desired 600 meV diffusion barrier.<sup>[14]</sup> However, these theoretical predictions have not been experimentally verified.

Here, we report an experimental evaluation of post-spinel  $\text{CaFe}_2\text{O}_4$  for calcium-ion batteries. The calcium iron oxide is synthesized using an autocombustion synthesis method and the phase of the resulting post-spinel is verified through Rietveld Refinement.<sup>[15,16]</sup> The  $\text{CaFe}_2\text{O}_4$  is processed into an electrode where its electrochemical activity is evaluated with  $\text{Ca}(\text{TFSI})_2$  in DME as the electrolyte and Activated Carbon as a counter electrode. The activity of the calcium iron oxide is evaluated using cyclic voltammetry and galvanostatic cycling and the activity of the  $\text{CaFe}_2\text{O}_4$  is characterized using XRD and Scanning Electron Microscopy (SEM). The results from the experimental evaluation reveal that  $\text{CaFe}_2\text{O}_4$  does not have significant electrochemical activity and would not be a prime candidate for calcium-ion batteries.

## 4.2 Materials and Methods

### 4.2.1 Materials

Calcium Nitrate Tetrahydrate ( $\text{Ca}(\text{NO}_3)_2 \cdot 4\text{H}_2\text{O}$ ), Iron (III) Nitrate Nonahydrate ( $\text{Fe}(\text{NO}_3)_3 \cdot 9\text{H}_2\text{O}$ ), Diethylene Glycol Monobutyl Ether (DME), Glycine and 1-Methyl-2-Pyrrolidone (NMP) were purchased from Sigma-Aldrich, USA, and used as received. Calcium(II) Bis(trifluoromethanesulfonyl)imide ( $\text{Ca}(\text{TFSI})_2$ ) was purchased from Solvionic. The  $\text{Ca}(\text{TFSI})_2$  salt was vacuum-dried at 120 °C overnight before use. Polytetrafluoroethylene (PTFE) preparation (60% wt) was purchased from Sigma-Aldrich. Polyvinylidene Fluoride (PVDF) binder, Super P Carbon black, Activated Carbon, CR2032 316 stainless steel coin cells and Aluminum foil (~10  $\mu\text{m}$  thickness) were purchased from MTI Corporation, USA.

### 4.2.2 Synthesis of $\text{CaFe}_2\text{O}_4$

$\text{CaFe}_2\text{O}_4$  post-spinels were synthesized using an auto-combustion synthesis.<sup>[15]</sup> The synthesis begins with mixing 1 mmol  $\text{Ca}(\text{NO}_3)_2 \cdot 4\text{H}_2\text{O}$  with 2 mmol  $\text{Fe}(\text{NO}_3)_2$  in deionized water for 3 hours. Once thoroughly mixed, 3 mmol of glycine is added to the mixture and allowed to stir for another 3 hours. Following the mixture of the glycine, the solution is transferred to a petri dish and subsequently placed on a hot plate set to 100°C. The solution begins to evaporate, and a viscous material begins to form in the petri dish. Once the mixture forms a gel, the temperature of the petri dish is incrementally increased to 300°C where the auto-combustion reaction is triggered. The result from the autocombustion synthesis is the formation of a brick red powder. The powder is subsequently ball milled and calcined for 2 hours at 800°C in a furnace.

### 4.2.3 Electrode Preparation

The electrodes used in the study were formulated using two methods. Electrodes used with the in situ cell and cyclic voltammetry experiments were processed as freestanding electrodes. Galvanostatic experiments that involved the assembly of coin cells used slurry casted electrodes. To prepare a freestanding electrode, powders of  $\text{CaFe}_2\text{O}_4$  (65% wt) and carbon black (5% wt) were mixed with PTFE Binder (30% wt).<sup>[17,18]</sup>  $\text{CaFe}_2\text{O}_4$  and carbon black were mixed together in a ball miller at 19.67 Hz for 90 minutes.<sup>[19]</sup> After ball milling, the resulting mixture was transferred to a mortar and pestle where PTFE binder and ethanol were added to it. The materials were continuously mixed in the ethanol until the electrode congealed from ethanol evaporation. The electrode was processed through a hot roll press at 80°C. Following the hot roll press, the electrodes were vacuum dried overnight at 80°C for a final weight density of 3 mg/cm<sup>2</sup>. Activated Carbon freestanding electrodes were prepared using the same procedure. The composition of the activated carbon electrodes was activated carbon (80% wt) and PTFE binder (20% wt) with a mass loading density of 30 mg/cm<sup>2</sup>.<sup>[20]</sup>

The following procedure was used for the processing of casted electrodes in galvanostatic experiments. The preparation of slurry casted electrodes required the vacuum drying of the current collectors. Carbon coated copper foil was used for the counter electrode while carbon coated aluminum foil was used for the working electrode and each foil was vacuum dried at 120°C overnight before slurry casting. To prepare the working electrode, a slurry of 95%  $\text{CaFe}_2\text{O}_4$ , 2.5% Carbon Black and 2.5% PVDF binder was made. The solid content of the slurry is fixed at 65 wt%.<sup>[21,22]</sup> The  $\text{CaFe}_2\text{O}_4$  and carbon black were mixed in powder form for 60 minutes in the ball mill at 19.67 Hz. Separately, the PVDF and 2/5 of the total NMP were mixed in the ball miller for 30 minutes and then sonicated for another 30 minutes. The pre-mixed  $\text{CaFe}_2\text{O}_4$  and carbon black

were added to the PVDF and NMP mixture and mixed again in the ball miller and sonicator. 1/3 of the remaining NMP was added to the suspension and the ball milling and sonication steps were repeated. The remaining NMP was added in 1/5 increments with ball milling and sonication following each addition.<sup>[23]</sup> Once mixed, the slurry for the working electrode was casted onto the carbon coated aluminum current collector with a thickness of 200 microns. After the slurry was casted, the electrode was dried on a hot plate at 80°C for 1 hour and subsequently vacuum dried at 110°C overnight.<sup>[24]</sup> The method for making activated carbon electrodes was the same as the CaFe<sub>2</sub>O<sub>4</sub> with the exception that the activated carbon was casted onto a carbon coated copper collector.

#### **4.2.4 Electrolyte Preparation**

The electrolyte used was 0.5 M Ca(TFSI)<sub>2</sub> in DME. A stock of the DME solvent was prepared by drying the solvent for 48 hours over 3 Å molecular sieves. To remove any trace moisture from the salt, Ca(TFSI)<sub>2</sub> salt was dried overnight at 120°C in a vacuum oven. Following the vacuum drying, the salt was dissolved in DME and magnetically stirred for 24 hours to allow full dissolution of the salt in the DME. The resulting electrolyte was again dried over 3 Å molecular sieves again to remove any residual water. Water content of the solvent and electrolytes was verified to be below 50 ppm using a Karl Fischer Titrator (899 Coulometer, Metrohm).

#### **4.2.5 Electrochemistry**

Cyclic voltammetry (CV) experiments were performed in beaker cells (Gamry Instruments) using three-electrode configurations with Ag/Ag<sup>+</sup> reference electrode (Redox.me), CaFe<sub>2</sub>O<sub>4</sub> working electrode and activated carbon as the counter electrode. Working and counter electrodes were suspended in the electrolyte with 316 stainless steel supports. Cyclic voltammetry experiments

were performed for 20 cycles at a scan rate of 0.5 mV/s. A Metrohm Autolab was used for running CV experiments. All experiments were carried out in an Argon filled glovebox with H<sub>2</sub>O and O<sub>2</sub> levels maintained below 0.5 ppm.

Galvanostatic experiments were performed in coin cell configurations with CaFe<sub>2</sub>O<sub>4</sub> as the working electrode (5 mm diameter) and activated carbon as the counter electrode (15 mm diameter). All coin cell assemblies were performed in an argon filled glovebox. Each coin cell assembly consisted of a working electrode, counter electrode, separator and 80 μL of Ca(TFSI)<sub>2</sub> in DME. Each galvanostatic experiment began with a 2 hour open circuit voltage to allow components to equilibrate. Galvanostatic experiments were performed on an Arbin battery tester where the coin cells were cycled at room temperature at a rate of C/100.

#### **4.2.6 Electrode Characterization**

X-ray diffraction data was collected with a Rigaku Miniflex 600 diffractometer. Scattering angles between 10-80° were collected at a scan rate of 5°/min using Copper (Cu) K $\alpha$  radiation. To eliminate erroneous XRD reflections from residual electrolyte, all samples were rinsed with DME solvent and dried before measurements were taken. XRD scans of the cathode were all performed at room temperature. In situ XRD measurements were performed with an in situ cell that has been previously described. (Figure SI 3.3 & SI 3.4) Rietveld refinement of the cathode was performed using Highscore Plus software.<sup>[25]</sup> The Materials Project was used for the identification of phases.<sup>[26]</sup> Scanning electron microscopy (SEM) was performed using a JEOL 5600 and was equipped with an energy dispersive X-ray (EDX) detector. The accelerating voltage used on all samples was 15 kV. All samples were first sputter coated with gold before being placed inside the SEM chamber. N<sub>2</sub> adsorption/ desorption measurements were performed using a surface analyzer

(Micrometrics ASAP 2020). Brunauer-Emmett-Teller (BET) and Barrett-Joyner-Halenda (BJH) methods were used to determine the specific surface area.<sup>[27,28]</sup>

#### **4.2.7 Ab-Initio Calculations**

Structure optimization of a  $\text{CaFe}_2\text{O}_4$  unit cell was performed using the ab-initio program VASP (Vienna Ab-Initio Simulation Program).<sup>[29]</sup> Total energy calculations based on Density Functional Theory (DFT) were performed within the General Gradient Approximation (GGA), with the exchange and correlation functional form developed by Perdew, Burke, and Ernzerhof (PBE).<sup>[30]</sup> The interaction of the core electrons with the nuclei was described by the Projector Augmented Wave (PAW) method.<sup>[31]</sup> Spin polarized calculations were performed with a U value of 4.0 for manganese. The energy cut off for the plane wave basis set was fixed to 700 eV. The structure was fully relaxed (atomic positions, cell parameters, and volume) with a force convergence criterion of 1 meV/atom.

#### **4.3 Results and Discussion**

The phase of the synthesized calcium iron oxide from the autocombustion reaction was analyzed with x-ray diffraction. Figure 4.1 shows experimental and fitted XRD profiles for  $\text{CaFe}_2\text{O}_4$  powder. The results from the analysis confirm the post-spinel phase of  $\text{CaFe}_2\text{O}_4$  with a high degree of crystallinity. The Rietveld refinement of the  $\text{CaFe}_2\text{O}_4$  identifies an orthorhombic structure with a Pnma space group. The lattice parameters for the post-spinel phase were reported to be  $a = 9.2195 \text{ \AA}$ ,  $b = 3.0176 \text{ \AA}$ , and  $c = 10.6938 \text{ \AA}$ . The diffraction pattern did not produce any other peaks other than those indexed to  $\text{CaFe}_2\text{O}_4$ , indicative of the phase purity from the autocombustion synthesis.<sup>[32]</sup>

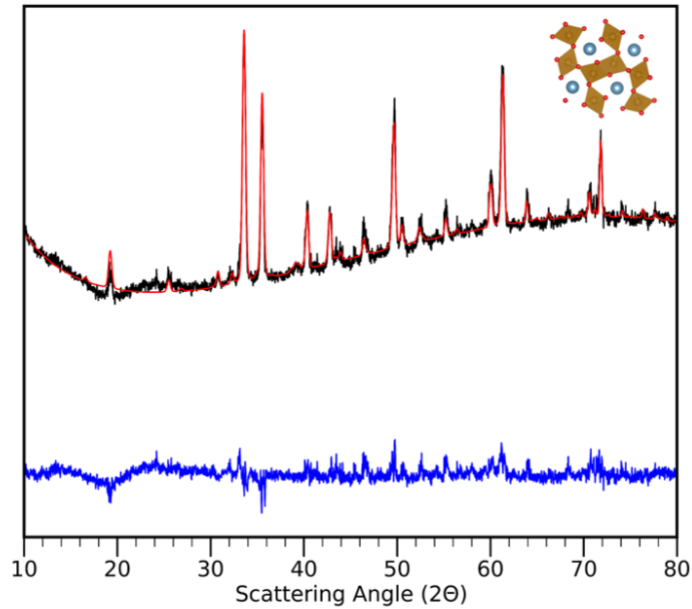


**Figure 4.1** - Synthesis of post-spinel CaFe<sub>2</sub>O<sub>4</sub>

SEM imaging of the synthesized powders are outlined in Figure 4.2 a,b. The CaFe<sub>2</sub>O<sub>4</sub> in Figure 4.2b shows spongy and interconnected, porous agglomerates. The porosity of the CaFe<sub>2</sub>O<sub>4</sub> is a product of the autocombustion process where gases such as N<sub>2</sub> and CO<sub>2</sub> were instantly released forming the highly porous network in the CaFe<sub>2</sub>O<sub>4</sub>.<sup>[32]</sup> The highly porous nature of the CaFe<sub>2</sub>O<sub>4</sub> would allow for better electrolyte percolation into the electrode, which could be beneficial to electrochemical performance. N<sub>2</sub> isotherms performed on the CaFe<sub>2</sub>O<sub>4</sub> powder reported a surface area of 30.256 m<sup>2</sup>/g and an average pore size of 387.259 Å. (Figure SI 4.1)

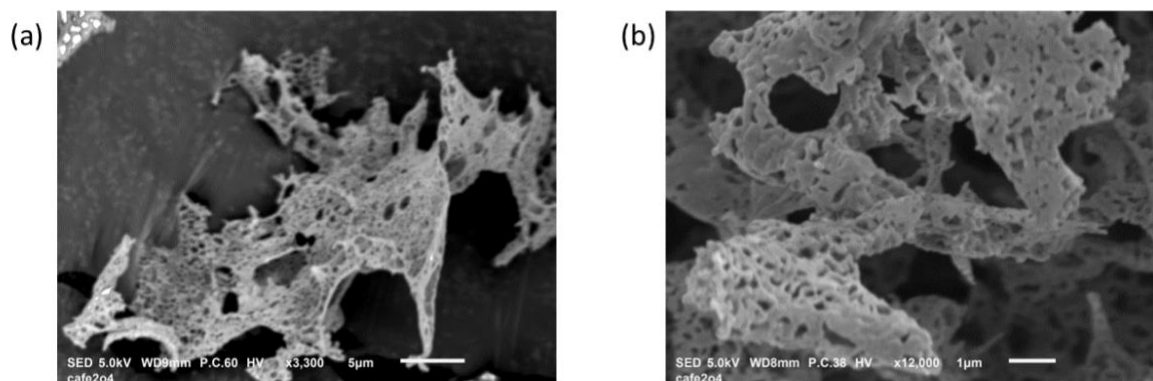


**Figure 4.2** - SEM images of  $\text{CaFe}_2\text{O}_4$  powders a) Overview image of  $\text{CaFe}_2\text{O}_4$  (Scale bar of 5 microns) b) Close up SEM image of  $\text{CaFe}_2\text{O}_4$  (Scale bar of 1 microns)

The redox activity of the  $\text{CaFe}_2\text{O}_4$  was first evaluated with cyclic voltammetry. (Figure 4.3) A three-electrode cell with  $\text{CaFe}_2\text{O}_4$  as the working electrode, activated carbon as the counter electrode and  $\text{Ag}/\text{Ag}^+$  as a reference electrode. Calibrations of the  $\text{Ag}/\text{Ag}^+$  reference electrode and activated carbon were previously established in Chapter 3. The results from cyclic voltammetry of the  $\text{CaFe}_2\text{O}_4$  identify a cathode with limited redox activity. The first scan of the  $\text{CaFe}_2\text{O}_4$  identifies some oxidative behavior that begins to appear at approximately  $-0.1\text{ V}$  and is more prominent at  $0.3\text{ V}$  (vs  $\text{Ag}/\text{Ag}^+$ ). The oxidative voltage is consistent with other experimental voltages that have been observed for calcium extraction from ferrites.<sup>[13]</sup> Beyond  $0.3\text{ V}$ , there is a substantial increase in the current response as the CV continues to scan up to  $1\text{ V}$  (vs.  $\text{Ag}/\text{Ag}^+$ ), which is assigned to the formation of an SEI on the cathode and anodic stability limits of the electrolyte. Additional experiments have been performed to expand the voltage range of the CV. When the voltage range was increased to  $1.2\text{ V}$ , there was a continued increase in the current response and would be assigned to the anodic stability limits of the electrolyte that have been previously established in Chapter 3. (Figure SI 3.2) Upon continued cycling of the cell, the oxidative features that were observed in the first cycle are no longer present and do not appear again in subsequent cycling.

CV scans of the  $\text{CaFe}_2\text{O}_4$  do not identify any reduction peak of the cathode. During cathodic traces of the CV, only a small, negative sloping line can be observed after the  $-1.5\text{ V}$  (vs.  $\text{Ag}/\text{Ag}^+$ ) potential, identifying an effort to insert calcium into the cathode.<sup>[33]</sup>

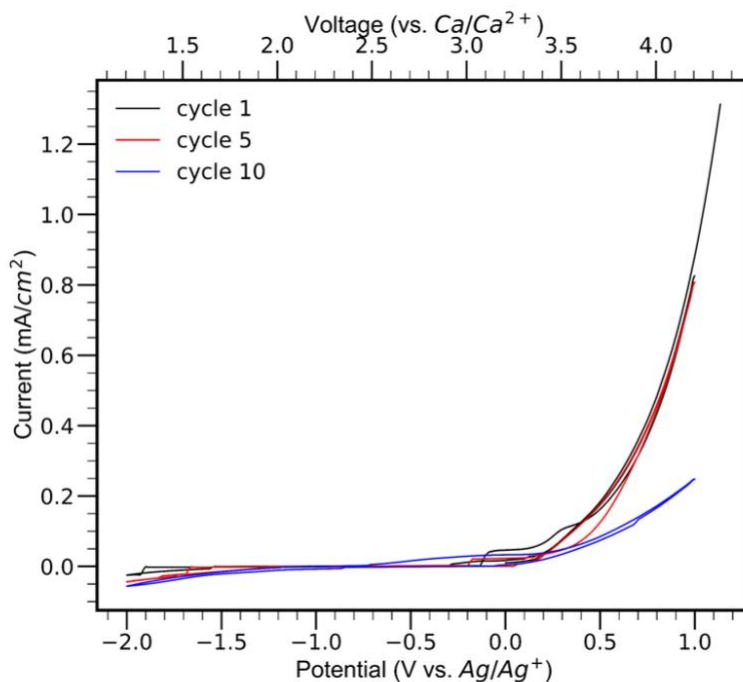


**Figure 4.3** - Cyclic voltammetry of  $\text{CaFe}_2\text{O}_4$  working electrode, activated carbon counter electrode and  $\text{Ag}/\text{Ag}^+$  reference electrode at  $0.5\text{ mV/s}$  scan rate

Following the cyclic voltammetry work performed on calcium iron oxide, the next goal was to determine the maximum capacity of calcium that could be removed from the cathode. Freestanding electrodes of  $\text{CaFe}_2\text{O}_4$  and activated carbon were fabricated and assembled inside of the in situ cell. To track structural changes to the  $\text{CaFe}_2\text{O}_4$ , a baseline scan of the assembled cell was indexed to the powder pattern of  $\text{CaFe}_2\text{O}_4$ . (Figure 4.4) Rietveld refinements performed of the freestanding electrode reported the lattice parameters of  $\text{CaFe}_2\text{O}_4$  being  $a = 9.223253\text{ \AA}$ ,  $b = 3.018984\text{ \AA}$ ,  $c = 10.695890\text{ \AA}$ . The reflections of the  $\text{CaFe}_2\text{O}_4$  inside the in situ cell (Figure 4.4) are not as prominent as previous spectra taken for  $\text{LiCoO}_2$  and  $\text{CaMn}_2\text{O}_4$ . This is partly due to the scale of intensities

between the  $\text{CaFe}_2\text{O}_4$  powder and in situ cell reflections along with a need to further optimize the active material of freestanding electrodes for stronger signal intensity in future work.<sup>[35]</sup>

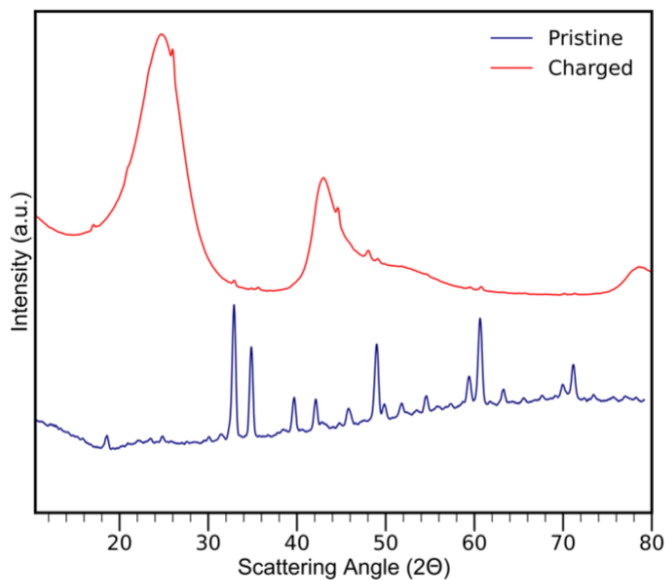


**Figure 4.4** - XRD of  $\text{CaFe}_2\text{O}_4$  synthesized powder and in situ XRD of  $\text{CaFe}_2\text{O}_4$

The in situ cell was charged at a c-rate of C/50 with XRD measurements being taken at every 10% depth of charge. The result of the maximum charge and in situ measurements taken of the  $\text{CaFe}_2\text{O}_4$  are summarized in Figure 4.5 and 4.6. Figure 4.5 outlines a maximum capacity of 180 mAh/g. The charging voltage of the  $\text{CaFe}_2\text{O}_4$  exceeds well beyond the oxidation activity observed in the cyclic voltammetry experiment of 0.3 V (vs.  $\text{Ag}/\text{Ag}^+$ ). Figure 4.5 identifies a voltage plateau that begins to appear at approximately 1.5 V (vs. Activated Carbon) and gradually increases over the course of charging to 1.9 V (vs. Activated Carbon). Exceeding well beyond the linear stability window of the electrolyte, the capacity observed from the in situ cell charging was a product of electrolyte oxidation and not from activity of the cathode.<sup>[13,35]</sup> XRD measurements taken reveal no structural variations in the cathode over the course of charging. (Figure 4.6a) Further inspection of the  $\text{CaFe}_2\text{O}_4$  reflections from the in situ XRD data confirm this. Figure 4.6b is focused on a (200)

lattice plane reflection. Under normal XRD conditions, this reflection would be located at  $19^\circ$  ( $2\theta$ ). However, due to the distortion created by the glassy carbon window, this reflection with the in situ cell is located at  $17^\circ$  ( $2\theta$ ). Comparisons between baseline scans, 20% charge and 50% charge reveal no variation in the intensity or position of the reflection. These experimental results are indicative of little to no redox activity with the  $\text{CaFe}_2\text{O}_4$  and this conclusion is further supported by how the experimental results contrast with theoretical XRD patterns generated from decalciated  $\text{CaFe}_2\text{O}_4$ .

DFT calculations performed on  $\text{CaFe}_2\text{O}_4$  with 25% decalciation project that the intensity of the (200) lattice plane reflection would increase. Results from the theoretical predictions of  $\text{CaFe}_2\text{O}_4$  are outlined in Figure SI 4.2. Figure SI 4.2a is the theoretical XRD pattern generated for pristine  $\text{CaFe}_2\text{O}_4$  while Figure SI 4.2b is the theoretical pattern when the occupancy of calcium has been reduced to 75%. The (200) lattice plane reflection change is denoted by an asterisk in Figure SI 4.2. In addition to differences in the intensity of the (200) lattice plane reflection, DFT calculations also project a decrease in the d-spacing value from  $4.6407 \text{ \AA}$  to  $4.5797 \text{ \AA}$  as the  $2\theta$  position of the (200) lattice planes shifts from  $19.1089^\circ$  to  $19.3660^\circ$ . The calculations performed on  $\text{CaFe}_2\text{O}_4$  also project changes from baseline lattice parameters  $a = 9.282 \text{ \AA}$ ,  $b = 3.037 \text{ \AA}$ ,  $c = 10.784 \text{ \AA}$  to  $a = 9.160 \text{ \AA}$ ,  $b = 3.042 \text{ \AA}$ , and  $c = 10.737 \text{ \AA}$  upon decalciation of the post-spinel. The DFT calculations performed on  $\text{CaFe}_2\text{O}_4$  predict XRD developments that the experimental data does not reflect, further supporting the lack of redox activity with this cathode.

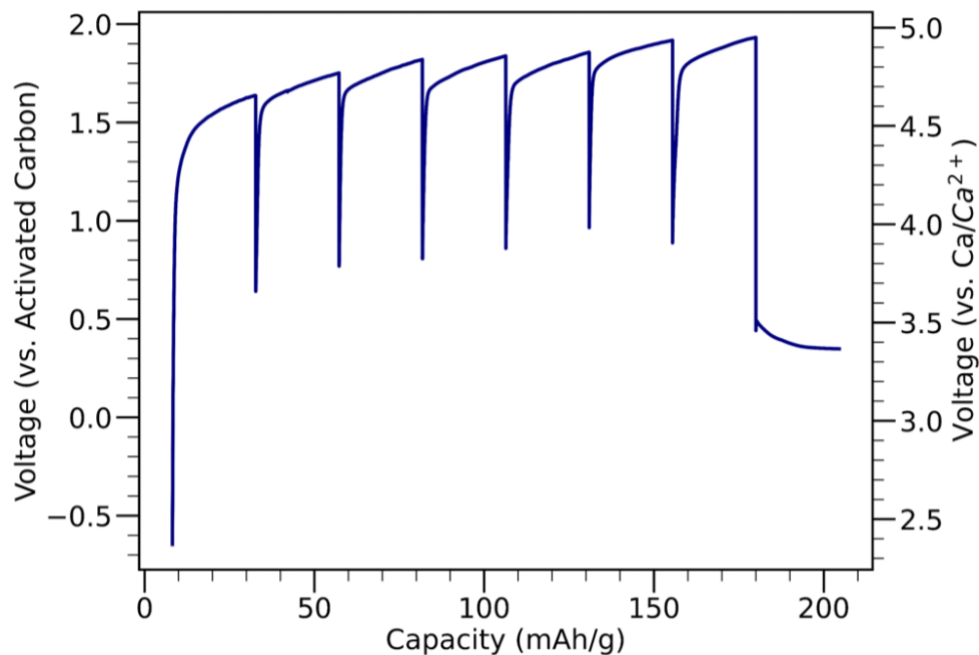


**Figure 4.5** - Maximum charge of the  $\text{CaFe}_2\text{O}_4$  inside of the in situ cell at C/50

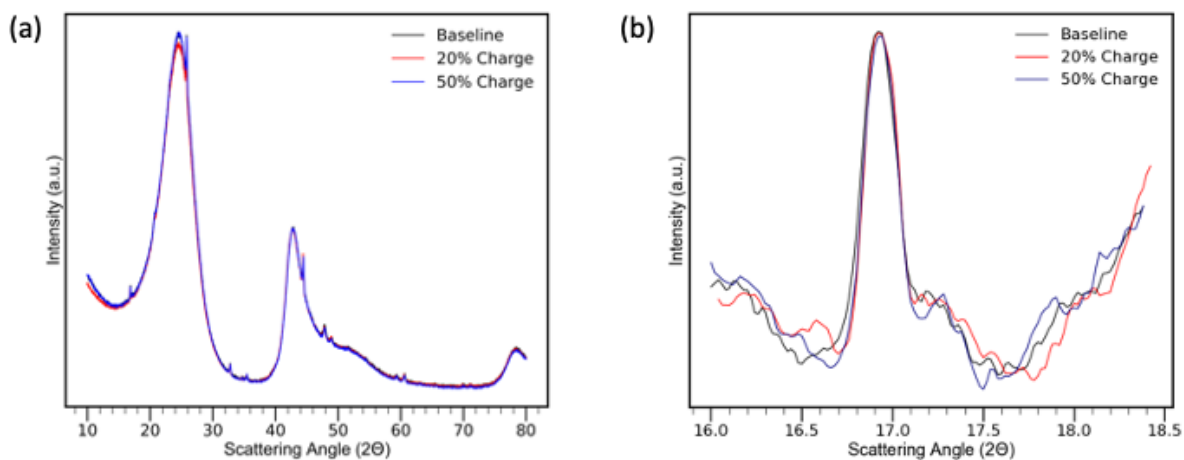


**Figure 4.6** - In situ XRD of the  $\text{CaFe}_2\text{O}_4$  a) in situ XRD overview of  $\text{CaFe}_2\text{O}_4$  from maximum charge b) In situ XRD of the (200) lattice planes over course of charging

The results from the in situ cell experiments produced no evidence of redox activity with the  $\text{CaFe}_2\text{O}_4$  and all capacity associated with the maximum charge is expected to be a product of electrolyte oxidation. However, part of the inactivity of the  $\text{CaFe}_2\text{O}_4$  is also attributed to its

sluggish diffusion kinetics since the  $\text{CaFe}_2\text{O}_4$  has a diffusion barrier of 1.2 eV. An additional experiment focused on a slower charging of the cathode was done to accommodate this diffusion barrier and was performed with a c-rate of C/100. Slurry casted electrodes of  $\text{CaFe}_2\text{O}_4$  and activated carbon were prepared and assembled inside of a coin cell. The coin cell was then cycled at a c-rate of C/100 with a capacity of 50 mAh/g for each charge and discharge. The results from the coin cell cycling are outlined in Figure 4.7. Figure 4.7a is the coin cell cycling over time. The initial cycles account for some electrolyte oxidation and formation of an SEI on the electrodes and can also be seen in Figure 4.7b. Subsequent cycling of the cathode results in a lower oxidation potential,  $\sim 0.4$  V (vs. Activated Carbon), and is more consistent with previously reported CV results (Figure 4.3). Subsequent cycles of testing outline a gradual increase in the charging voltage that would be assigned to side reactions occurring with the electrolyte.<sup>[13]</sup>

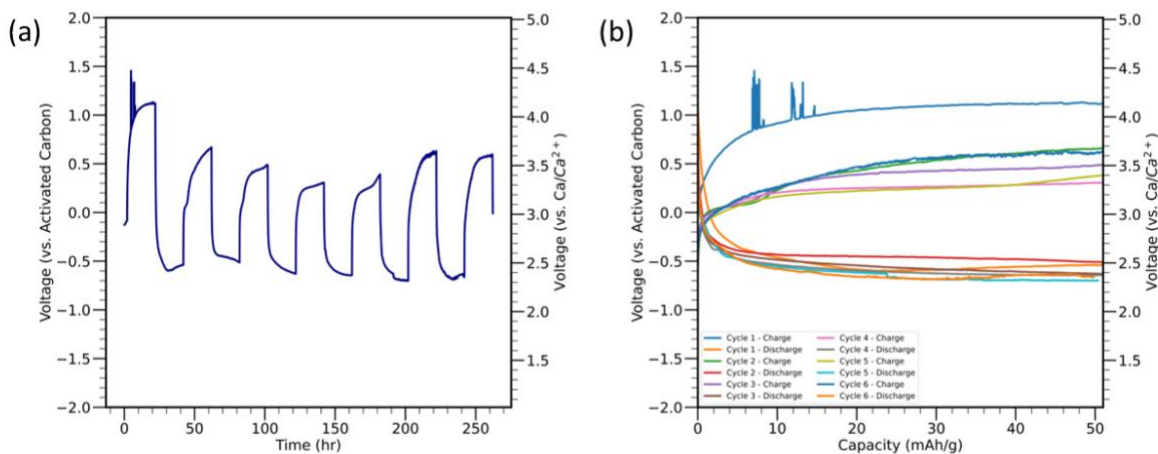


**Figure 4.7** - Galvanostatic cycling of  $\text{CaFe}_2\text{O}_4$  a) Voltage-time curve of cycling b) Capacity-voltage curves of cycled  $\text{CaFe}_2\text{O}_4$

At the conclusion of coin cell testing, the coin cells of  $\text{CaFe}_2\text{O}_4$  were opened and ex situ characterization of the  $\text{CaFe}_2\text{O}_4$  was performed. XRD of the  $\text{CaFe}_2\text{O}_4$  electrode before and after testing is summarized in Figure 4.8. Comparisons between the pristine and cycled electrodes of

CaFe<sub>2</sub>O<sub>4</sub> show no structural differences between the cycled and pristine electrodes of CaFe<sub>2</sub>O<sub>4</sub> with the exception of a new reflection at 26.75°, corresponding to (103) lattice plane reflections. Figure 4.9 is XRD spectra of the new (103) lattice plane post cycling. The (103) lattice planes intersect the edge sharing FeO<sub>6</sub> octahedra. (Figure SI 4.3) Theoretical calculations from the 25% decalciated CaFe<sub>2</sub>O<sub>4</sub> predict a shift in the placement of the oxygen and iron atoms that lie more directly on the (103) lattice plane, increasing the atomic density of the plane and contributing to the increased XRD intensity of the plane post cycling. While this feature is an indicator of some decalciation of the CaFe<sub>2</sub>O<sub>4</sub>, it is present in a limited capacity. Before testing began, baseline analysis of the CaFe<sub>2</sub>O<sub>4</sub> electrode was performed and reported lattice parameters of a = 9.225781 Å, b = 3.017116 Å, c = 10.694950 Å. The new lattice parameters of the CaFe<sub>2</sub>O<sub>4</sub> following Pawley fitting<sup>[36]</sup> of the electrode are a = 9.220151 Å, b = 3.014550 Å, c = 10.695260 Å. Occupancy of the calcium in the CaFe<sub>2</sub>O<sub>4</sub> electrode was analyzed with Rietveld refinement. However, no changes to the calcium occupancy were detected from the analysis. Additional analysis of crystallite size over the course of cycling was performed using the Scherrer equation.<sup>[37]</sup> Baseline crystallite size was recorded to be 300.9 Å while post cycling measurements reported 304.9 Å. These additional parameters offer more evidence regarding the limited redox activity of the CaFe<sub>2</sub>O<sub>4</sub>.

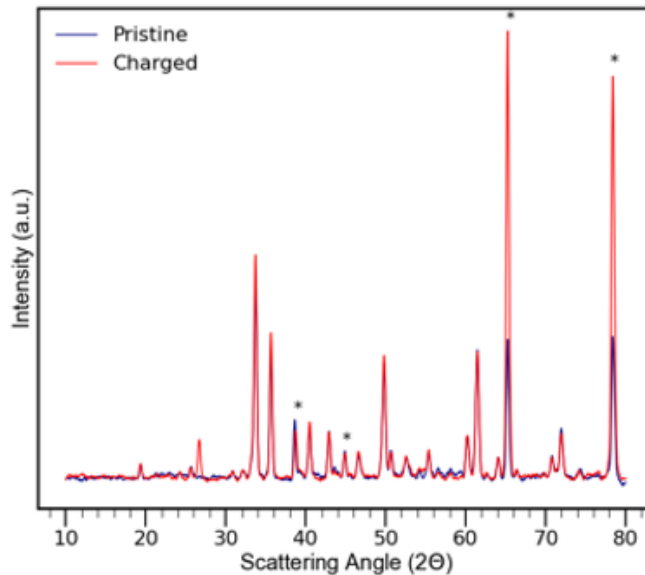


**Figure 4.8** - Overview XRD of CaFe<sub>2</sub>O<sub>4</sub> from galvanostatic cycling (asterisk in figure are reflections from aluminum current collector)

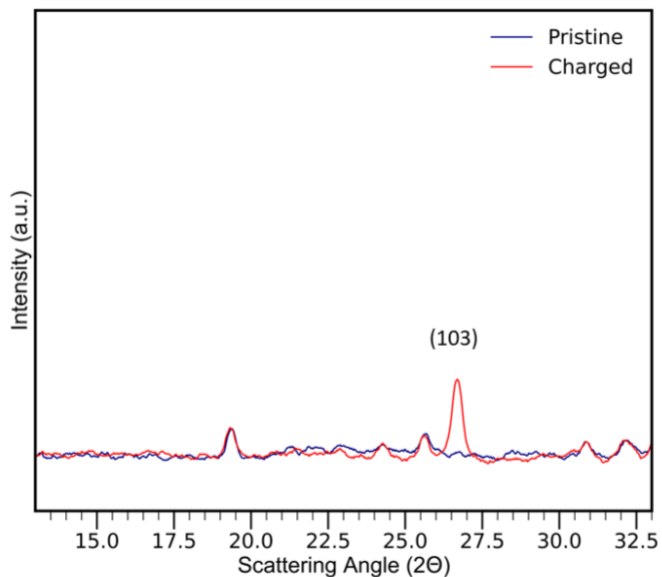


**Figure 4.9** - XRD of the CaFe<sub>2</sub>O<sub>4</sub> before and after galvanostatic cycling with (103) lattice planes

The last ex situ characterization of the CaFe<sub>2</sub>O<sub>4</sub> performed was SEM/EDS analysis of the electrodes as a product of cycling. Figure 4.10 outlines the elemental mapping of the calcium iron oxide electrodes before and after cycling. The results of the analysis reveal that there is a small

decrease in the calcium signal at the conclusion of galvanostatic cycling as it decreases from 10.6% to 9.8%. This small decrease in the calcium signal does highlight some electrochemical activity that would be consistent with previous results from CV and ex situ XRD.

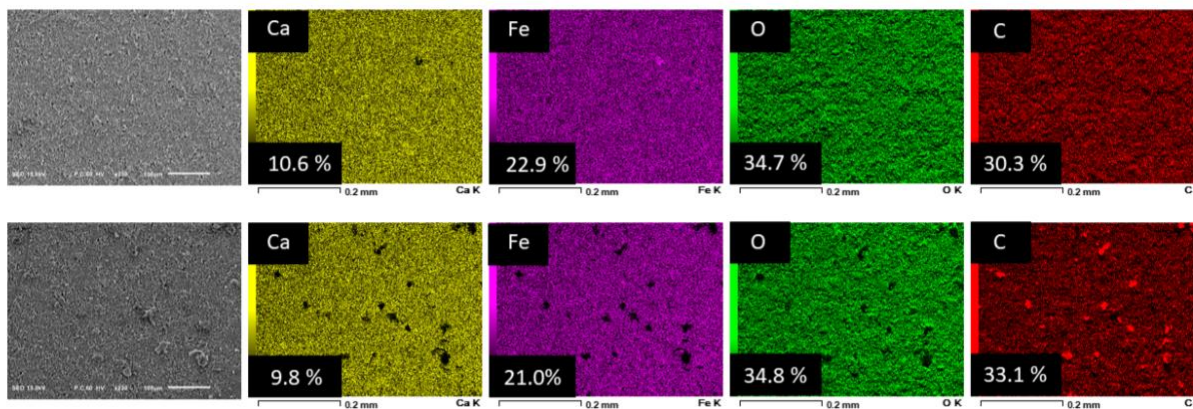


**Figure 4.10** - EDS of the CaFe<sub>2</sub>O<sub>4</sub> before and after galvanostatic cycling.

#### 4.4 Conclusion

Our study of CaFe<sub>2</sub>O<sub>4</sub> post-spinel provides important insights into its intercalation chemistry as it is used as a cathode for calcium-ion batteries. CaFe<sub>2</sub>O<sub>4</sub> has been successfully synthesized via auto-combustion and its phase verified with XRD. Cyclic voltammetry studies on the CaFe<sub>2</sub>O<sub>4</sub> revealed a limited redox activity of the cathode and began to articulate issues that would be encountered with this transition metal oxide. The diffusion barrier of 1.2 eV for CaFe<sub>2</sub>O<sub>4</sub> translates to a c-rate that needs to be lower than C/50, which was demonstrated with the maximum charge of the cathode with the in situ cell setup and its lack of structural changes upon charging. Galvanostatic testing of the CaFe<sub>2</sub>O<sub>4</sub> in a coin cell configuration using a slower c-rate of C/100 produced a structural variation that was recorded with XRD. The intensity increase of the (103) lattice planes at the end of cycling does corroborate some DFT expectations of decalciation with CaFe<sub>2</sub>O<sub>4</sub>. Further evidence of decalciation is supported by ex situ EDS analysis performed on the cathode, outlining a decrease in the calcium signal post-cycling. While there is evidence of some decalciation, there

isn't significant removal of calcium from the post-spinel. The lack of additional structural changes to the XRD profiles, including the lack of occupancy changes to the calcium in the cathode and no significant development of crystallites, reveals a limited electrochemical activity of the  $\text{CaFe}_2\text{O}_4$ .

The exploration of  $\text{CaFe}_2\text{O}_4$  post-spinel as a cathode for calcium-ion batteries outlines important experimental evaluation of transition metal oxides for these battery chemistries. While there is a limited amount of redox activity in the cathode, there isn't a substantial capacity cycled from the electrode to justify use in a calcium-ion battery. While  $\text{CaFe}_2\text{O}_4$  may not be the ideal cathode for calcium-ion batteries, it does validate limitations outlined by theoretical models and prompts exploration of other transition metal oxides.

## Supplemental Information

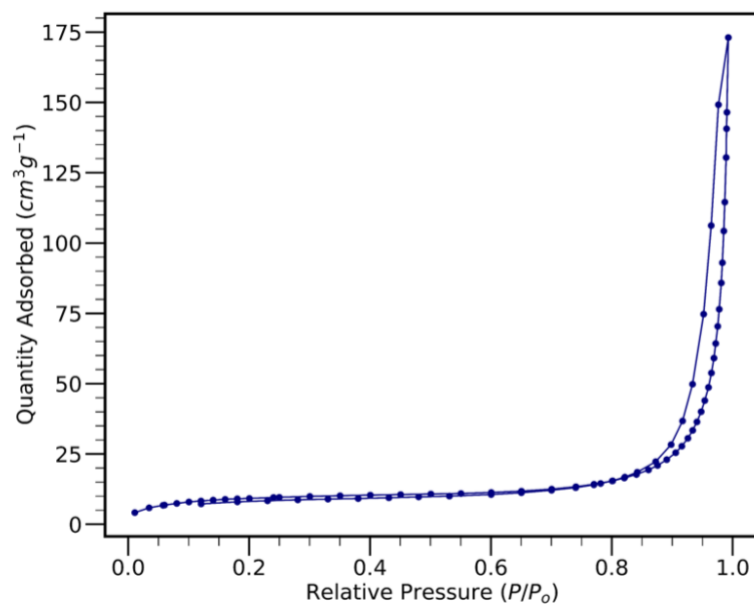


**Figure SI 4.1** - N<sub>2</sub> isotherm CaFe<sub>2</sub>O<sub>4</sub>

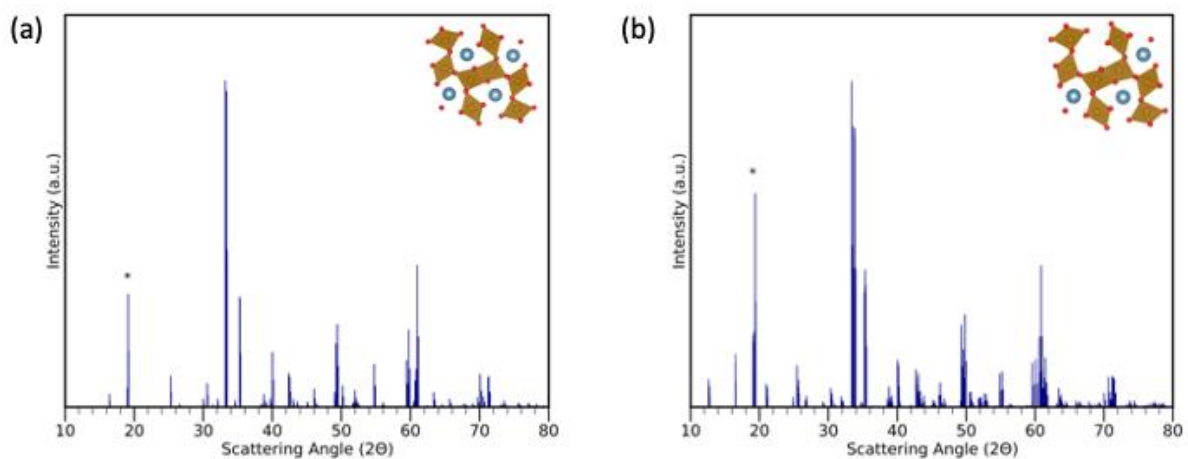


**Figure SI 4.2** - Theoretical XRD Patterns of CaFe<sub>2</sub>O<sub>4</sub> a) XRD with 100% calcium occupancy b) XRD with 75% calcium occupancy

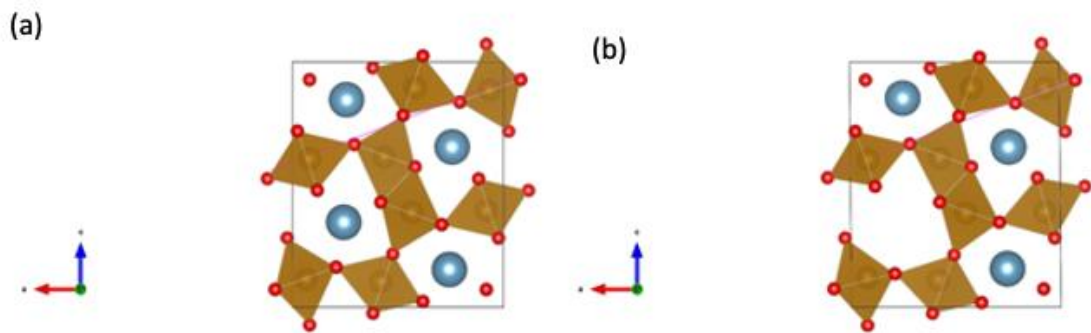


**Figure SI 4.3** - Crystal structure of  $\text{CaFe}_2\text{O}_4$  a) 100% calcium occupancy b) 75% calcium occupancy

## References

1. Wanger, T. C. The Lithium Future-Resources, Recycling, and the Environment. *Conserv. Lett.* **2011**, *4* (3), 202–206.
2. Hosein, I. D. The Promise of Calcium Batteries: Open Perspectives and Fair Comparisons. *ACS Energy Lett.* **2021**, 1560–1565.
3. Canepa, P.; Sai Gautam, G.; Hannah, D. C.; Malik, R.; Liu, M.; Gallagher, K. G.; Persson, K. A.; Ceder, G. Odyssey of Multivalent Cathode Materials: Open Questions and Future Challenges. *Chem. Rev.* **2017**, *117* (5), 4287–4341.
4. Arroyo-de Dompablo, M. E.; Ponrouch, A.; Johansson, P.; Palacín, M. R. Achievements, Challenges, and Prospects of Calcium Batteries. *Chem. Rev.* **2019**. <https://doi.org/10.1021/acs.chemrev.9b00339>.
5. Rong, Z.; Malik, R.; Canepa, P.; Sai Gautam, G.; Liu, M.; Jain, A.; Persson, K.; Ceder, G. Materials Design Rules for Multivalent Ion Mobility in Intercalation Structures. *Chem. Mater.* **2015**, *27* (17), 6016–6021.
6. Maroni, F.; Dongmo, S.; Gauckler, C.; Marinaro, M.; Wohlfahrt-Mehrens, M. Through the Maze of Multivalent-ion Batteries: A Critical Review on the Status of the Research on Cathode Materials for Mg  $2+$  and Ca  $2+$  Ions Insertion. *Batter. Supercaps* **2021**, *4* (8), 1221–1251.
7. Rutt, A.; Shen, J.-X.; Horton, M.; Kim, J.; Lin, J.; Persson, K. A. Expanding the Material Search Space for Multivalent Cathodes. *ACS Appl. Mater. Interfaces* **2022**, *14* (39), 44367–44376.
8. Zhang, Z.; Zhang, X.; Zhao, X.; Yao, S.; Chen, A.; Zhou, Z. Computational Screening of Layered Materials for Multivalent Ion Batteries. *ACS Omega* **2019**, *4* (4), 7822–7828.
9. Park, H.; Bartel, C. J.; Ceder, G.; Zapol, P. Layered Transition Metal Oxides as Ca Intercalation Cathodes: A Systematic First-principles Evaluation. *Adv. Energy Mater.* **2021**, 2101698.
10. Pathreker, S.; Reed, S.; Chando, P.; Hosein, I. D. A Study of Calcium Ion Intercalation in Perovskite Calcium Manganese Oxide. *J. Electroanal. Chem.* **2020**, *874*, 114453.
11. Cabello, M.; Nacimiento, F.; Alcántara, R.; Lavela, P.; Pérez Vicente, C.; Tirado, J. L. Applicability of Molybdenite as an Electrode Material in Calcium Batteries: A Structural Study of Layer-Type  $\text{Ca}_x\text{MoO}_3$ . *Chem. Mater.* **2018**, *30* (17), 5853–5861.

12. Cabello, M.; Nacimiento, F.; González, J. R.; Ortiz, G.; Alcántara, R.; Lavela, P.; Pérez-Vicente, C.; Tirado, J. L. Advancing towards a Veritable Calcium-Ion Battery: CaCo<sub>2</sub>O<sub>4</sub> Positive Electrode Material. *Electrochem. commun.* **2016**, *67*, 59–64.
13. Black, A. P.; Torres, A.; Frontera, C.; Palacín, M. R.; Arroyo-de Dompablo, M. E. Appraisal of Calcium Ferrites as Cathodes for Calcium Rechargeable Batteries: DFT, Synthesis, Characterization and Electrochemistry of Ca<sub>4</sub>Fe<sub>9</sub>O<sub>17</sub>. *Dalton Trans.* **2020**, *49* (8), 2671–2679.
14. Liu, M.; Rong, Z.; Malik, R.; Canepa, P.; Jain, A.; Ceder, G.; Persson, K. A. Spinel Compounds as Multivalent Battery Cathodes: A Systematic Evaluation Based on Ab Initio Calculations. *Energy Environ. Sci.* **2015**, *8* (3), 964–974.
15. Zhang, Z.; Wang, W. Solution Combustion Synthesis of CaFe<sub>2</sub>O<sub>4</sub> Nanocrystal as a Magnetically Separable Photocatalyst. *Mater. Lett.* **2014**, *133*, 212–215.
16. McCusker, L. B.; Von Dreele, R. B.; Cox, D. E.; Louër, D.; Scardi, P. Rietveld Refinement Guidelines. *J. Appl. Crystallogr.* **1999**, *32* (1), 36–50.
17. Maarof, H. I.; Wan Daud, W. M. A.; Aroua, M. K. Effect of Varying the Amount of Binder on the Electrochemical Characteristics of Palm Shell Activated Carbon. *IOP Conf. Ser. Mater. Sci. Eng.* **2017**, *210*, 012011.
18. Sottmann, J.; Pralong, V.; Barrier, N.; Martin, C. An Electrochemical Cell for Operando Bench-Top X-Ray Diffraction. *J. Appl. Crystallogr.* **2019**, *52* (2), 485–490.
19. Eguchi, T.; Kanamoto, Y.; Tomioka, M.; Tashima, D.; Kumagai, S. Effect of Ball Milling on the Electrochemical Performance of Activated Carbon with a Very High Specific Surface Area. *Batteries* **2020**, *6* (2), 22.
20. Zhang, Y.; Huld, F.; Lu, S.; Jektvik, C.; Lou, F.; Yu, Z. Revisiting Polytetrafluorethylene Binder for Solvent-Free Lithium-Ion Battery Anode Fabrication. *Batteries* **2022**, *8* (6), 57.
21. Bryntesen, S. N.; Strømman, A. H.; Tolstorebrov, I.; Shearing, P. R.; Lamb, J. J.; Stokke Burheim, O. Opportunities for the State-of-the-Art Production of LIB electrodes—A Review. *Energies* **2021**, *14* (5), 1406.
22. Kraytsberg, A.; Ein-Eli, Y. Conveying Advanced Li-Ion Battery Materials into Practice the Impact of Electrode Slurry Preparation Skills. *Adv. Energy Mater.* **2016**, *6* (21), 1600655.
23. Lee, G.-W.; Ryu, J. H.; Han, W.; Ahn, K. H.; Oh, S. M. Effect of Slurry Preparation Process on Electrochemical Performances of LiCoO<sub>2</sub> Composite Electrode. *J. Power Sources* **2010**, *195* (18), 6049–6054.

24. Ram, P.; Patel, H.; Singhal, R.; Choudhary, G.; Sharma, R. K. On the Study of Mixing and Drying on Electrochemical Performance of Spinel LiMn<sub>2</sub>O<sub>4</sub> Cathodes. *J. Renewable Sustainable Energy* **2019**, *11* (1), 014104.
25. Degen, T.; Sadki, M.; Bron, E.; König, U.; Nénert, G. The HighScore Suite. *Powder Diffraction* **2014**, *29* (S2), S13–S18.
26. Jain, A.; Ong, S. P.; Hautier, G.; Chen, W.; Richards, W. D.; Dacek, S.; Cholia, S.; Gunter, D.; Skinner, D.; Ceder, G.; Persson, K. A. Commentary: The Materials Project: A Materials Genome Approach to Accelerating Materials Innovation. *APL Materials* **2013**, *1* (1), 011002.
27. Brunauer, S.; Emmett, P. H.; Teller, E. Adsorption of Gases in Multimolecular Layers. *J. Am. Chem. Soc.* **1938**, *60* (2), 309–319.
28. Barrett, E. P.; Joyner, L. G.; Halenda, P. P. The Determination of Pore Volume and Area Distributions in Porous Substances. I. Computations from Nitrogen Isotherms. *J. Am. Chem. Soc.* **1951**, *73* (1), 373–380.
29. Kresse, G.; Furthmüller, J. Efficient Iterative Schemes for Ab Initio Total-Energy Calculations Using a Plane-Wave Basis Set. *Phys. Rev. B Condens. Matter* **1996**, *54* (16), 11169–11186.
30. Blöchl, P. E. Projector Augmented-Wave Method. *Phys. Rev. B Condens. Matter* **1994**, *50* (24), 17953–17979.
31. Perdew, J. P.; Burke, K.; Ernzerhof, M. Generalized Gradient Approximation Made Simple. *Phys. Rev. Lett.* **1996**, *77* (18), 3865–3868.
32. Shaji, N.; Santhoshkumar, P.; Nanthagopal, M.; Senthil, C.; Lee, C. W. Electrochemical Performance of Porous CaFe<sub>2</sub>O<sub>4</sub> as a Promising Anode Material for Lithium-Ion Batteries. *Appl. Surf. Sci.* **2019**, *491*, 757–764.
33. Zhang, X.; Xu, X.; Song, B.; Duan, M.; Meng, J.; Wang, X.; Xiao, Z.; Xu, L.; Mai, L. Towards a Stable Layered Vanadium Oxide Cathode for High-Capacity Calcium Batteries. *Small* **2022**, e2107174.
34. Sottmann, J.; Pralong, V.; Barrier, N.; Martin, C. An Electrochemical Cell for Operando Bench-Top X-Ray Diffraction. *J. Appl. Crystallogr.* **2019**, *52* (2), 485–490.
35. Dompablo, M. E. A.; Krich, C.; Nava-Avenidaño, J.; Biškup, N.; Palacín, M. R.; Bardé, F. A Joint Computational and Experimental Evaluation of CaMn<sub>2</sub>O<sub>4</sub> Polymorphs as Cathode Materials for Ca Ion Batteries. *Chem. Mater.* **2016**, *28* (19), 6886–6893.

36. Stinton, G. W.; Evans, J. S. O. Parametric Rietveld Refinement. *J. Appl. Crystallogr.* **2007**, *40* (Pt 1), 87–95.
37. He, K.; Chen, N.; Wang, C.; Wei, L.; Chen, J. Method for Determining Crystal Grain Size by X-Ray Diffraction. *Cryst. Res. Technol.* **2018**, *53* (2), 1700157.

## **CHAPTER 5**

# **PLATING AND STRIPPING CALCIUM METAL IN POTASSIUM HEXAFLUOROPHOSPHATE ELECTROLYTE TOWARDS A STABLE HYBRID SOLID ELECTROLYTE INTERPHASE**

A version of this chapter has been published in ACS Applied Energy Materials 2023

Chando, P.A.; Shellhamer, J.M.; Wall, E.; He, W.; Hosein, I.D

Reprinted with Permission

## 5.1 Introduction

The ever-increasing energy demands from developing technologies, along with the limited supply of lithium to meet them, has necessitated the need to explore post lithium-ion battery solutions.<sup>1</sup> Divalent ions such as calcium are particularly attractive due to their similar reduction potentials to lithium and wide availability making the economics associated with its use feasible. While there are such benefits to the use of calcium, there are challenges that need to be addressed such as the identification of appropriate electrolytes to use with calcium metal. Electrolytes for calcium metal batteries have been limited by successful plating and stripping. The cause of such bottlenecks has been the passivation layer that forms on the calcium metal surface as plating continues with native calcium electrolytes (i.e., employing only calcium salts). The SEI is formed from the degradation of the electrolyte onto the surface of the calcium, functioning as an electrically insulating material while still being ionically conductive. The use of fluorinated electrolytes produces a continuous deposition of calcium fluoride ( $\text{CaF}_2$ ) onto the SEI of the calcium which acts as highly insulating materials, decreasing ionic conductivity of the SEI and ultimately reducing the capacity on subsequent cycles.<sup>2</sup> This issue was first addressed by running plating and stripping of calcium at elevated temperatures.<sup>3</sup> The use of elevated temperatures increased the ionic conductivity of the SEI and slowed the development of the passivation layer. The successful plating and stripping of calcium from such efforts renewed interest in exploring alternative solutions with electrolyte formulations.<sup>4-8</sup>

An alternate strategy that bypasses the need for elevated temperatures and high overpotentials is the use of a hybrid SEI. The use of mixed cations in the SEI has proven effective at cycling with lithium anodes.<sup>9</sup> Expanding the use of the hybrid SEIs to calcium has focused on using cations with similar atomic radii such as sodium (Na) and continuing the use of hexafluorophosphate

anions due to their weakly coordinating nature.<sup>10</sup> Sodium hexafluorophosphate (NaPF<sub>6</sub>) was used as the salt in an electrolyte with calcium metal to create a sodium oxide (Na<sub>2</sub>O) phase in the SEI that allowed the deposition of calcium while mitigating the continuous formation of CaF<sub>2</sub> that would occur with a native calcium based electrolyte.<sup>4</sup> The efficacy of such an approach with sodium has prompted additional efforts at tailoring the SEI for improved cycling efficiencies.<sup>11-12</sup> An additional possibility for hybrid SEIs with calcium metal is the use of potassium owing to its larger ionic radius to calcium. Currently, potassium is a largely unexplored option for hybrid SEIs with calcium. The existing work on it has focused on having potassium partake in composite SEI along with sodium and calcium.<sup>13</sup> While successful, an evaluation of the standalone hybrid SEI between potassium and calcium remains unexplored.

Here, we report the development of such a hybrid SEI using potassium hexafluorophosphate (KPF<sub>6</sub>) salt in a composite solvent of ethylene carbonate (EC), dimethyl carbonate (DMC) and Ethyl methyl carbonate (EMC) as it is cycled between calcium metal electrodes. The plating and stripping behavior observed maintained overpotentials below 2 V throughout the course of cycling, while also exhibiting discrete events of potassium and calcium deposition onto the electrodes. XRD characterization of the SEI that formed on the electrodes revealed a composite of phases that allow the plating and stripping of calcium. Phase composition of plated materials was further supported by FTIR and SEM/EDX analysis on the deposited materials.

## **5.2 Experimental Section**

### **5.2.1 Materials**

Potassium Hexafluorophosphate (KPF<sub>6</sub>, ≥ 99%), Calcium (Ca, 99%) granules and molecular sieves (3 Å, 4-8 mesh) were purchased from Sigma-Aldrich. Calcium granules were first flattened

to an 8 mm diameter and 0.5 mm thickness with a mechanical press. The calcium pieces were subsequently polished with a dremel (4300, Dremel). Gold electrodes (99.95%) were purchased from Goodfellow Cambridge Limited. Additionally, Ethylene Carbonate (anhydrous, 99%), Dimethyl Carbonate (anhydrous,  $\geq 99\%$ ) and Ethyl Methyl Carbonate (99%) were purchased from Sigma-Aldrich.

### **5.2.2 Electrolyte Preparation**

All electrochemistry experiments used a 1 M solution of  $\text{KPF}_6$  in EC/DMC/EMC. The solvents were first mixed in a 1:1:1 volume ratio for 24 hours before being dried for 48 hours over molecular sieves. The  $\text{KPF}_6$  was dried overnight in a vacuum oven at  $120^\circ\text{C}$  before being added to the solvent mixture. The  $\text{KPF}_6$  solution was stirred for 24 hours to allow full dissolution of the salt and was again dried over molecular sieves. Water content of the electrolyte was verified by a Karl Fisher Titrator (899 Coulometer, Metrohm) to be below 50 ppm. All experiments were carried out in a glovebox where  $\text{H}_2\text{O}$  and  $\text{O}_2$  levels were below 0.5 ppm.

### **5.2.3 Electrode Preparation**

The calcium pellets were first flattened to a diameter of 8 mm and thickness of 1 mm using a mechanical press. The calcium electrodes were then polished with a Dremel 4300 using a procedure found elsewhere.<sup>8</sup> All polishing procedures were carried out in a glovebox with  $\text{O}_2$  and  $\text{H}_2\text{O}$  levels below 0.5 ppm. Briefly, a wire brush was first used to remove the oxide layer on the calcium disc. Once the initial oxide layer was removed, a dremel (Dremel 4300) with a silicon carbide (SiC) tip was used to polish the calcium to achieve a mirror finish. The dremel was operated between 5k-15k rpm to achieve the high polished finish on the Ca electrodes. For electrochemical experiments using a gold (Au) electrode, the electrode was electrochemically

cleaned in a sulfuric acid bath before being rinsed with methanol and dried under ambient conditions.<sup>14</sup>

#### **5.2.4 Electrochemistry**

A beaker cell was used in all experiments. Calcium electrodes were attached to the end of 316 stainless steel supports and immersed in the electrolyte. Two-electrode configurations were used for plating and stripping. Calcium or gold were used as the working electrodes (WE) and calcium as the counter (CE) and reference (RE) electrodes. Following the immersion of the electrodes into the electrolyte, the plating and stripping experiments were performed with a Metrohm Autolab at a current density of  $0.025 \text{ mA/cm}^2$  and an areal capacity of  $0.15 \text{ mAh/cm}^2$ . Linear stability window measurements were made using a two-electrode cell with gold as the blocking electrode and calcium as the nonblocking electrode. Measurements were made at a sweep rate of  $0.5 \text{ mV/s}$  with a voltage window from 0 to 5 V. Cyclic voltammetry was performed after 10 plating and stripping cycles ( $0.025 \text{ mA/cm}^2$ ,  $0.15 \text{ mAh/cm}^2$ ) with a calcium symmetric cell configuration. The 10 cycles of plating and stripping were used to form the hybrid SEI on the calcium electrodes. The scan rate used was  $0.5 \text{ mV/s}$  with a voltage range from -3 to 3 V. The evolution of the hybrid SEI on calcium electrodes was recorded using in situ electrochemical impedance spectroscopy (EIS). The measurements were performed with a Solartron Energy Lab XM Instrument over a frequency range from 0.1 Hz to 1 MHz between each plating and stripping step. A 10 mV perturbation was used in all EIS measurements and the resulting Nyquist plot was analyzed using an equivalent circuit model.<sup>5,6,15-16</sup> Transference number measurements were performed using the Bruce and Vincent method.<sup>17,18</sup> A 10 mV potential was applied to a calcium symmetric cell and the current response over time was recorded. The contact resistance of the calcium electrodes was recorded with impedance measurements and determined using an equivalent circuit model. The transference

number of the potassium hexafluorophosphate electrolyte was calculated with the following formula (5.1):

$$t_+ = \frac{I_{ss}(\Delta V - I_0 R_0)}{I_0(\Delta V - I_{ss} R_{ss})} \quad (5.1)$$

where  $I_{ss}$  is the steady-state current,  $I_0$  is the initial current,  $\Delta V$  is the applied potential,  $R_{ss}$  is the steady-state resistance and  $R_0$  is the initial resistance.<sup>17-20</sup>

### 5.2.5 Electrode Characterization

A Rigaku Miniflex diffractometer was used for the collection of X-ray diffraction data. All samples analyzed under XRD were washed with solvent following experiments. Cu K $\alpha$  radiation was used to collect diffraction data in the range of 10°-80° at a scan rate of 5°/min. All XRD measurements were performed at room temperature. XRD analysis of each material was performed using Highscore Plus software.<sup>21</sup> The Materials Project was used as well for identification of phases.<sup>22</sup> Scanning electron microscopy (SEM) was performed with a JEOL 5600 and was equipped with an energy dispersive X-ray (EDX) detector. The accelerating voltage used on the samples was 15 kV. All samples analyzed with the SEM were sputter coated with gold. FTIR analysis of the samples was performed in transmission mode at 4 cm<sup>-1</sup> resolution with an ATIR-FTIR spectrometer (Bruker, Alpha). Raman spectroscopy was used for evaluating the compositional changes of the electrolyte during plating and stripping between the calcium symmetric cell experiments. All measurements were performed with a confocal microscope connected to a Raman spectrometer (Renishaw InVia).

### 5.3 Results and Discussion

Figure 5.1a details the plating and stripping behavior of the calcium symmetrical cell in 1 M KPF<sub>6</sub> EC/DMC/EMC electrolyte. The overpotentials from plating and stripping remain at 1.8 V (vs Ca/Ca<sup>2+</sup>) for over 20 cycles. Unlike plating and stripping experiments that use Ca(PF<sub>6</sub>)<sub>2</sub> where the overpotentials quickly rise to 5 V,<sup>4</sup> cycling with KPF<sub>6</sub> is far more stable. Plateaus at -0.2 V and -1.8 V can be observed in the experiments, consistent with behavior that has been seen previously with hybrid SEI plating and stripping.<sup>13</sup> The galvanostatic cycling for the symmetric cell was set to an areal capacity of 0.15 mAh/cm<sup>2</sup>. The capacities are summarized in Figure 5.1b with the -0.2 V potential plating with an areal capacity of 0.0085 mAh/cm<sup>2</sup> and the -1.8 V potential plating with an areal capacity of 0.1415 mAh/cm<sup>2</sup>. The capacities from the plating and stripping at 0.2 V overpotentials increased over the course of cycling and ultimately reached a capacity of 0.05 mAh/cm<sup>2</sup> at 0.3 V overpotentials. Additional plating and stripping studies using a separate reference electrode were found to decrease overpotentials from 1.8 V to 1.7 V (vs. Ca/Ca<sup>2+</sup>). Measurements taken of the symmetric cell working electrode during stripping were recorded to be 1.6 V (vs. Ca/Ca<sup>2+</sup>) while the counter electrode was measured with a potential of -0.07 V (vs. Ca/Ca<sup>2+</sup>). Additionally, the working electrode potential is -0.07 V (vs. Ca/Ca<sup>2+</sup>) and the counter electrode potential is 1.6 V (vs. Ca/Ca<sup>2+</sup>) during plating. The results from the three-electrode are summarized in Figure SI 5.1. Cyclic voltammetry studies were performed to correlate faradaic reactions with the observed plating and stripping behavior. The results from the cyclic voltammetry study are outlined in Figure 5.1c. The voltage scans identify a redox active process on the calcium electrodes with an onset potential of -0.2 V and a maximum current response at -0.5 V. A cross-section of the SEI formed on the calcium metal electrodes was analyzed under SEM imaging and was found to have formed an SEI thickness of 9 μm. (Figure 5.1d)

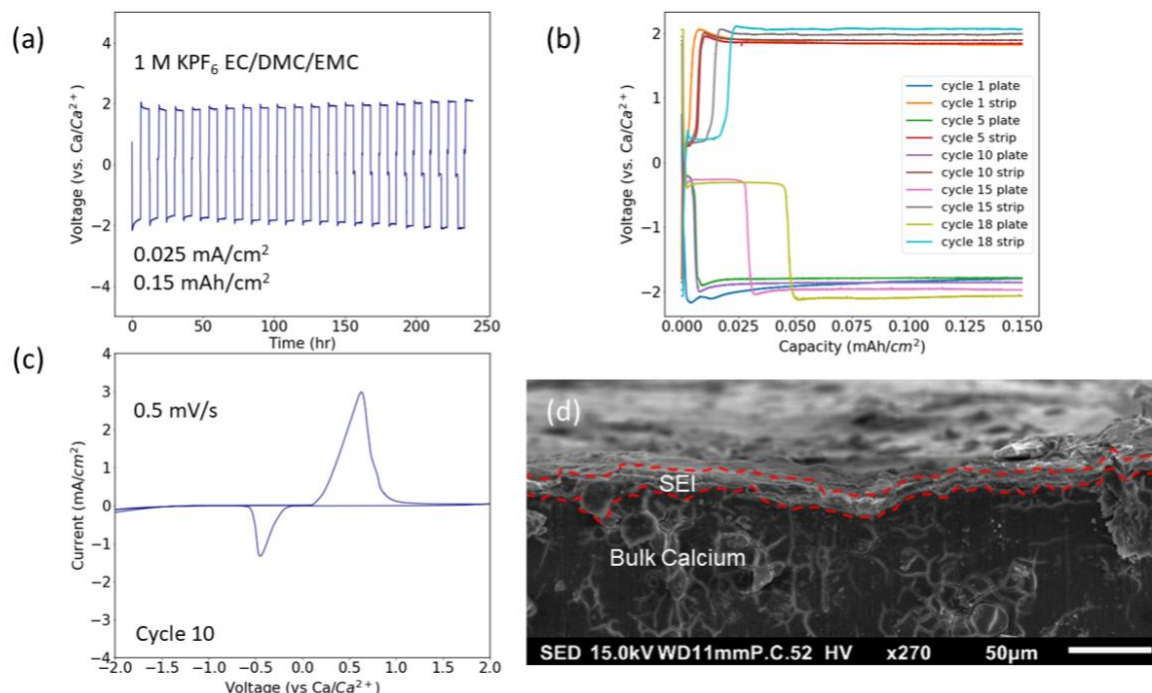


**Figure 5.1** - Galvanostatic cycling a) Plating and stripping of the Ca//Ca symmetric cell b) Voltage vs. capacity curves c) CV of the Ca//Ca symmetric cell d) Cross-sectional of SEI on calcium electrode after 10 cycles of galvanostatic cycling.

To characterize the plating and stripping behavior observed in Figure 5.1a, ex situ XRD studies were performed on the calcium electrodes. Potentiostatic holds at the previously observed voltages were performed to run controlled plating and stripping experiments on the calcium electrodes. Once completed, the electrodes were placed inside the Rigaku MiniFlex Diffractometer and analyzed over the specified range of diffraction angles. The results from the XRD analysis are summarized in Figure 5.2 a,b. Initial reflections of the calcium metal (mp-45) are recorded at  $28^\circ$ ,  $32^\circ$  and  $46^\circ$ . Additional reflections of calcium did not appear in the baseline scan due to the processing conditions of the electrode. Comparisons between processed and unprocessed calcium electrodes can be found in Figure SI 5.2. Following the plating potential at  $-0.5$  V, new calcium (mp-45) reflections are observed at  $54.5^\circ$ ,  $57.2^\circ$  and  $74^\circ$ , revealing that the  $-0.5$  V plating potential deposits calcium metal onto the SEI surface. The plating of calcium at  $-0.5$  V is consistent with

the cyclic voltammetry data and reveals that the redox reaction observed in Figure 5.1c was the plating and stripping of calcium. In addition to the new calcium reflections observed, phases of calcium fluoride ( $\text{CaF}_2$ , mp-2741) and phosphorus pentoxide ( $\text{P}_2\text{O}_5$ , mp-562613) were detected on the calcium surface and are identified in Figure 5.2 a, and b. Phosphorus pentoxide reflections were observed at  $17.5^\circ$ ,  $35.5^\circ$ ,  $44.5^\circ$ ,  $52.9^\circ$ ,  $58.8^\circ$ ,  $65.5^\circ$  and  $67^\circ$ . The presence of the  $\text{CaF}_2$  phase in the plated material is an inevitable product of electrolyte decomposition onto the surface of the calcium metal electrode.<sup>3</sup> The appearance of potassium (mp-58) as a plated material is observed after plating at the -1.8 V potential. Potassium plating reflections are identified at  $26.7^\circ$ ,  $47.1^\circ$ ,  $54.4^\circ$  and  $69.2^\circ$ . While the reflections at  $47.1^\circ$ ,  $54.4^\circ$ ,  $69.2^\circ$  overlap with calcium and calcium fluoride phases, the  $26.7^\circ$  reflection is unique to potassium and identifies it as a plated material onto the hybrid SEI surface. In addition to the previously defined phases, potassium difluorodiphosphate ( $\text{K}_2\text{P}_2\text{O}_5\text{F}_2$ , mp-558480) is also detected as a deposited material onto the hybrid SEI and its reflections are observed at  $17.1^\circ$ ,  $22.9^\circ$ ,  $26.7^\circ$ ,  $57.1^\circ$ ,  $61.4^\circ$  and  $62.9^\circ$ . The final component of the ex situ XRD study was performing a stripping step to the calcium electrodes. After stripping the calcium electrodes, reflections associated with potassium and potassium difluorodiphosphate were removed. Reflections of calcium metal decreased after stripping. The reflections of  $\text{P}_2\text{O}_5$  at  $65.5^\circ$  and  $67^\circ$ , while reduced in intensity, remained after stripping.

FTIR ex situ studies were performed to complement the findings from XRD analysis. Focusing on the -0.5 V plating potential, the presence of calcium and calcium fluoride in the hybrid SEI surface is outlined from the Ca-F bond observed at  $770\text{ cm}^{-1}$ .<sup>23</sup> Following the same behavior as the ex situ XRD study, the  $\text{P}_2\text{O}_5$  phase is also observed at the -0.5 V plating potential and is identified by the P-O-P bond at  $970\text{ cm}^{-1}$ .<sup>24</sup> The P=O bond at  $1210\text{ cm}^{-1}$  forms from the decomposition of the  $\text{KPF}_6$  electrolyte during the SEI formation.<sup>25,26</sup> The degradation of the carbonate solvents in the

electrolyte produce C-O-C bonds at 1067 and 1154  $\text{cm}^{-1}$  along with C=O bonds at 1300, 1769 and 1800  $\text{cm}^{-1}$ .<sup>25-28</sup> Additionally, carbonate degradation on the calcium electrode produces C-H bonds at 1475, 2900 and 3000  $\text{cm}^{-1}$ .<sup>25,27</sup> Minimal water is observed through an O-H bond at the broad peak centered around 3350  $\text{cm}^{-1}$ .<sup>25</sup> The plating potential at -1.8 V includes the previously determined bond assignments. The intensity of Ca-F, K-F and C-F bonds all increase after plating at -1.8 V, indicating an increased deposition of materials consistent with the ex situ XRD study performed on the calcium cycled in the symmetric cell. Plating of the potassium onto the calcium surface is identified with increased peak intensities at 717 and 892  $\text{cm}^{-1}$ .<sup>29,30</sup> The increase of the Ca-F bond, based on its increase in intensity at -1.8 V, would have some overlap with the K-F bond as well. Lastly, the stripping at 1.8 V results in a decrease of the fluoride based bond length intensities. The decrease of the fluorinated bonds, based on the ex situ XRD, would coincide with the stripping of the  $\text{K}_2\text{P}_2\text{O}_5\text{F}_2$ . The primary peaks remaining on the calcium electrode post-stripping are C-O-C bonds that were formed from the decomposition of the solvent onto the calcium surface along with small amounts of the P-O-P bonds from the  $\text{P}_2\text{O}_5$  and Ca-F from  $\text{CaF}_2$ . This is corroborated from the FTIR and XRD analyses that have been performed on the SEI.

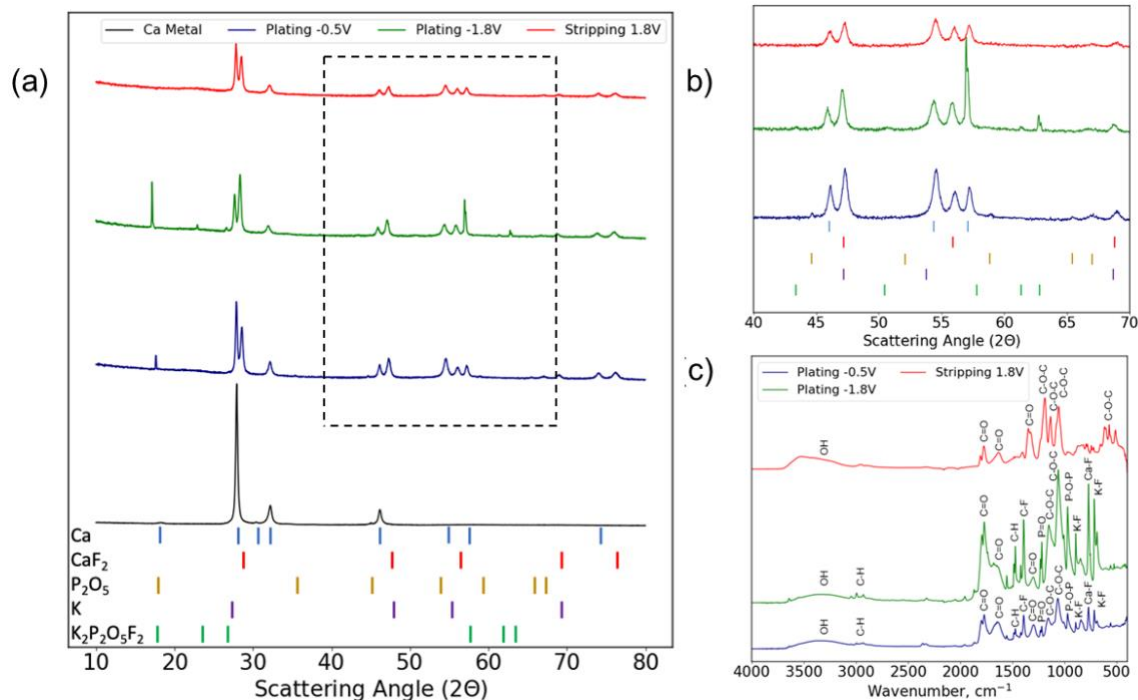


**Figure 5.2** - XRD of galvanostatic cycling with calcium electrodes a) XRD profiles of plating at -0.5 V and -1.8 V along with XRD of stripping at 1.8 V in a calcium symmetric cell. b) XRD profiles of plating and stripping between the diffraction angles of 40°-70° c) FTIR on the calcium plated and stripped materials

The plating and stripping behavior were also analyzed by EDX mapping of a cycled Ca electrode. Figure 5.3 details the EDX map spectra observed for the two plating and stripping potentials examined. Figure 5.3a-g maps plating at -0.5 V. Focusing on the phases of the plated materials, the atomic signals for calcium, oxygen, phosphorus, and fluorine were 8.83%, 32.22%, 0.61%, and 13.45%, respectively. Beyond the plating at -0.5 V, the deposition of potassium onto the calcium electrode increases. (Figure 5.3h-n) EDX of the potassium shows a strong increase in its fluorescence at this potential. While the atomic % signal of potassium remains below 1% at -1.8 V, this is influenced by the strong calcium signal (7.02%) from the bulk electrode and carbon (46.34%), minimizing compositional changes from the surface of the SEI. The phosphorus, oxygen and fluorine signals from the -1.8 V plating were 0.52%, 36.52%, and 7.8%. The stripping from 1.8 V (Figure 5.3o-u) shows a decrease in fluorescence with the plated elements. The

compositional changes in the calcium, oxygen, fluorine, phosphorus, and potassium signals were 17.05%, 44.8%, 11.34%, 0.09%, and 0.37%, respectively. From the analysis performed with EDX, all plated materials observed consist entirely of inorganic materials since no change in the carbon signal is observed throughout cycling. (Figure 5.3g,n,u) To determine the thickness of deposition from each plating cycle, the  $K_2P_2O_5F_2$  phase from the XRD was chosen since it is one of the phases fully stripped after applying the 1.8 V stripping potential. Focusing on the potassium EDX, it can be inferred, based on the atomic radius of potassium, that the deposition of each plating cycle is at least approximately 280-400 picometers.

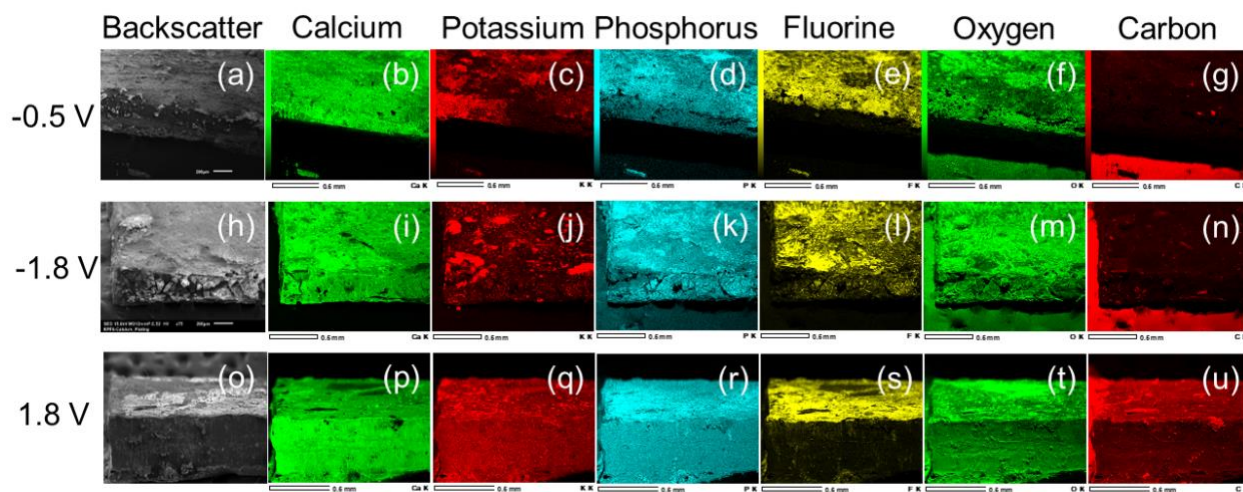


**Figure 5.3** - SEM/EDX from plating and stripping (a-g) EDX of calcium electrode from -0.5 V plating. (h-n) EDX of calcium electrode from -1.8 V. (o-u) EDX analysis after stripping at 1.8 V.

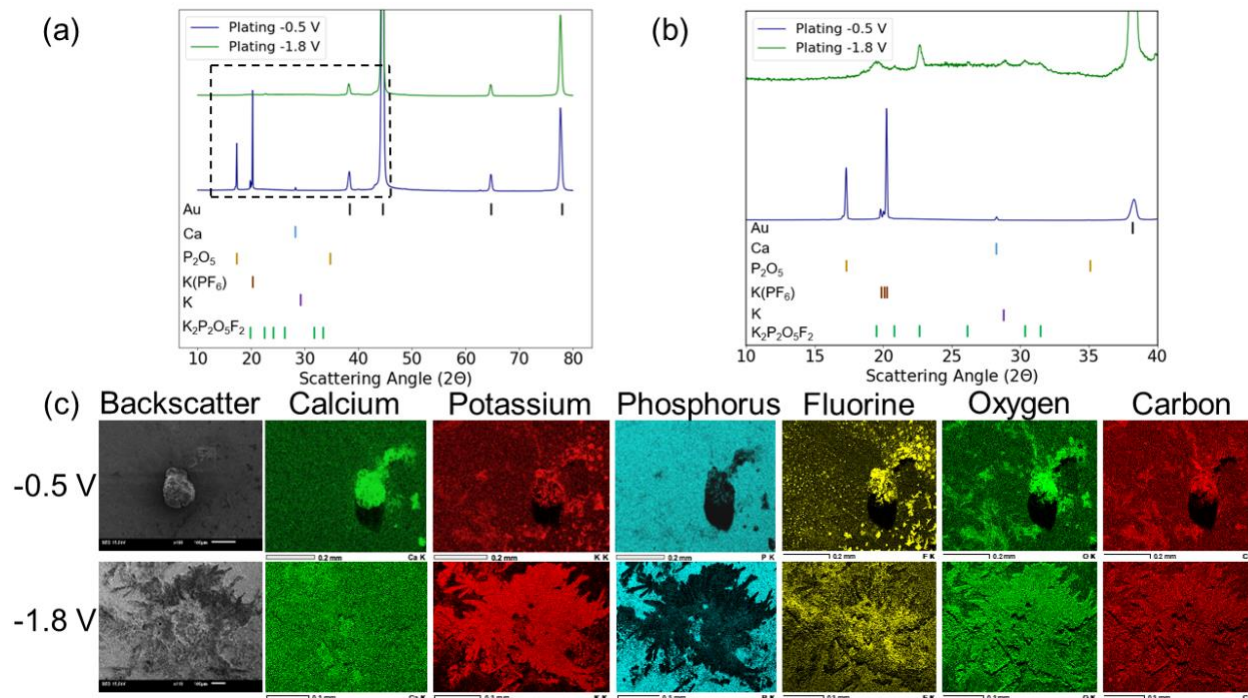


**Figure 5.4** - Plating onto gold electrode a) XRD profiles from plating onto a gold working electrode at -0.5 V and -1.8 V. b) XRD profiles from plating onto gold between diffraction angles of 10°-40° c) EDX of plated gold electrode at -0.5 V and -1.8 V.

To further understand the plating behavior with the KPF<sub>6</sub> EC/DMC/EMC electrolyte, a secondary cell was set up that used gold as a working electrode and calcium as a counter electrode (Au//Ca). The cell was subjected to the same potentiostatic holds (-0.5 V and -1.8 V) that were used for analyzing the plating potentials of the calcium symmetric cell. Following the potentiostatic holds, the gold electrodes were analyzed with XRD and SEM/EDX. Figure 5.4a,b shows the ex situ XRD study performed on the gold working electrodes. The established reflections for gold are 38°, 44.4°, 64.7° and 77.8°. All other reflections are from the deposition of materials onto the surface from plating with KPF<sub>6</sub> electrolyte. Three phases were observed from the plating potential at -0.5 V including Ca, P<sub>2</sub>O<sub>5</sub> and residual KPF<sub>6</sub>. The calcium reflection is observed at 28.27°. The P<sub>2</sub>O<sub>5</sub> phase reflections are at 17.27° and 35°. The residual KPF<sub>6</sub> on the gold electrode surface is indicated by the reflections at 19.8°, 20° and 20.2°. The plating at -1.8 V produced the same potassium and

potassium difluorodiphosphate phases that were observed with the calcium symmetric cell. A potassium phase reflection is observed at  $28.8^\circ$  while the  $\text{K}_2\text{P}_2\text{O}_5\text{F}_2$  phase is outlined by reflections at  $19.6^\circ$ ,  $20.9^\circ$ ,  $26.1^\circ$ ,  $30.3^\circ$  and  $31.4^\circ$ . To verify that all activity from the potentiostatic holds were strictly plating behavior, a linear stability window experiment was performed. (Figure SI 5.3) The  $\text{KPF}_6$  electrolyte remained stable with the gold electrode up to 4V, confirming that no side reactions are occurring on the gold electrode.

Figure 4c is the SEM/EDX analysis performed on the gold working electrodes post-plating. The calcium, oxygen, fluorine, phosphorus, and potassium atomic signals were recorded to be 2.2%, 15.59%, 15.45%, 1.09% and 3.2%, respectively. The phosphorus, potassium and fluorine signals would account for the residual  $\text{KPF}_6$  on the electrode. The remaining calcium signal would be due to the plating of calcium metal onto the gold electrode. The morphology of the deposited materials at -0.5 V is characterized as small globules. When analyzed with an EDX point spectra, the globule was found to have a calcium atomic signal of 42%, confirming that the composition of the plated calcium is calcium metal. When the plating potential of the  $\text{KPF}_6$  system was increased to -1.8 V, the SEM/EDX analysis revealed a potassium atomic signal increase from 3.2% at -0.5 V to 15.97% at -1.8 V. The signals for calcium, oxygen, fluorine, and phosphorus were reported to be 0.41%, 38.59%, 8.3%, and 1.38%, respectively. Additionally, the deposition of potassium on the gold working electrode surface also had more of a fractal pattern to it. When comparing the current densities from the two plating potentials, the -0.5 V plating achieved a steady current density of  $0.00015 \text{ mA/cm}^2$  while the -1.8 V plating had a current density of  $0.112 \text{ mA/cm}^2$ . The difference between current densities are orders of magnitude apart from one another and consequently produce plated materials with drastically different morphologies.<sup>31</sup>

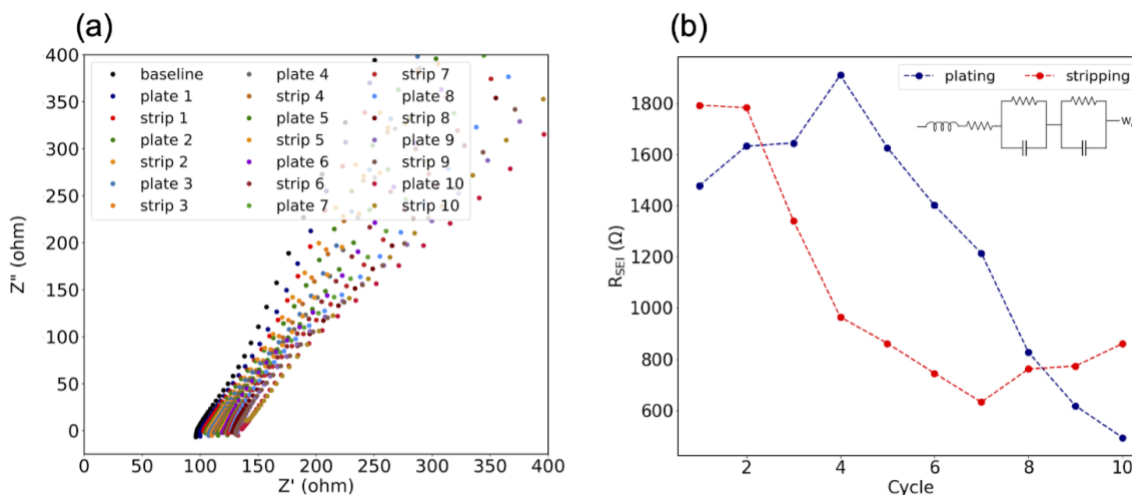


**Figure 5.5** - In situ EIS of calcium electrodes during galvanostatic cycling. a) Nyquist plot from in situ EIS b) Hybrid SEI resistance from in situ EIS. Inset in (b) is equivalent circuit for SEI resistance

To maintain such low overpotentials throughout the course of plating and stripping, the SEI itself should have low resistance. The resistance of the SEI was studied through the use of in situ EIS where the impedance of the SEI was studied as a function of cycling. The first 10 cycles of plating and stripping were studied on the calcium electrode surfaces and the resulting Nyquist plot is shown in Figure 5.5a. The full scale of the Nyquist plot can be found in Figure SI 5.4. An equivalent circuit was used to determine the SEI resistance, the schematic of which is the inset of Figure 5.5b. The circuit includes an inductor which accounts for impedance at high frequencies. The first resistor in the circuit accounts for the bulk resistance of the electrode. Following the first resistor, the first parallel circuit describes the interfacial resistance and the second parallel circuit models the charge transfer. A Warburg element was also included in the equivalent circuit.<sup>32-36</sup> Figure 5b summarizes the SEI resistance over the course of cycling with the  $KPF_6$  electrolyte between the calcium symmetric cell. The SEI resistance increased to above 1800  $\Omega$  on the first cycles of testing, consistent with the formation of the SEI on the calcium electrode surface. Following the formation of the SEI, the resistances decreased to 800  $\Omega$  by cycle 8. The plating

resistance during testing was larger than the stripping resistance. This is consistent with the cycling behavior since the plating SEI would have a thicker layer and therefore a higher resistance. The decrease of the SEI resistance over subsequent cycles would indicate an increase in ionic conductivity.<sup>5</sup> This increase in ionic conductivity is also observed as the evolution of the plating plateau at -0.2 V during the calcium symmetric cell plating and stripping experiment. (Figure 5.1a). The overpotentials and capacities at the -0.2 V plateau increase over the lifetime of testing, consistent with the maximum current response observed in the cyclic voltammetry. The resistance of the SEI stabilized at the end of cycling, indicating the formation and retention of a stable SEI layer.

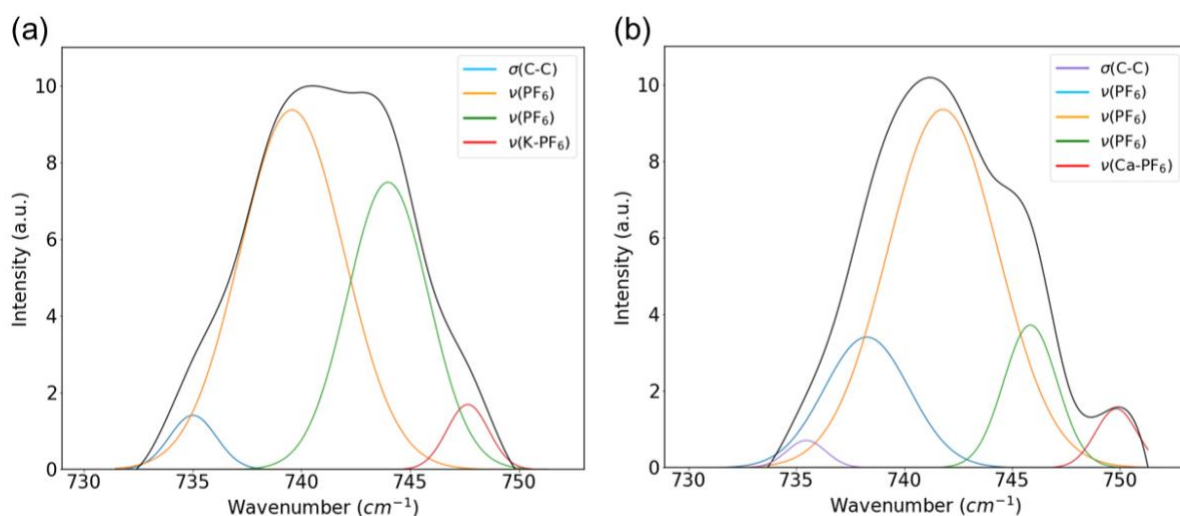


**Figure 5.6** - Raman analysis of electrolyte a) Gaussian fits of  $\text{PF}_6^-$  interactions in  $\text{KPF}_6$  electrolyte (pristine) b) Gaussian fits of  $\text{PF}_6^-$  interactions in  $\text{KPF}_6$  electrolyte (cycled)

The last component analyzed was the  $\text{KPF}_6$  EC/DMC/EMC electrolyte. A transference number experiment was performed on a pristine electrolyte sample using protocols previously described.<sup>17-20</sup> The transference number of the electrolyte was reported to be 0.101. (Figure SI 5.5) This value is consistent with other findings on the transference number of other potassium electrolytes.<sup>37</sup> The low value of the transference number was indicative that the majority of ion movement is accomplished by the  $\text{PF}_6^-$  anion. Focusing on the  $\text{PF}_6^-$  anion interactions, Figure 5.6a shows the

native electrolyte as analyzed under Raman spectroscopy. The results from peak deconvolution reveal a contact-ion pair existing at  $748\text{ cm}^{-1}$ .<sup>38</sup> This contact ion pair interaction was understood to be the interaction between  $\text{K}^+$  and  $\text{PF}_6^-$  ions. Additionally, peaks are observed at 734, 739 and  $744\text{ cm}^{-1}$ . The peaks at 739 and 744 are identified as symmetric  $\text{PF}_6^-$  stretching and are consistent with the interactions of anions with the different solvents.<sup>39-40</sup> The  $734\text{ cm}^{-1}$  peak has been identified as the C-C bond in ethylene carbonate.<sup>41</sup> Following 20 plating and stripping cycles in a symmetric cell, there is a shift of several peaks to higher wavenumbers. The peak at  $735\text{ cm}^{-1}$  is the C-C bond in ethylene carbonate. Peaks observed at 738, 742 and  $746\text{ cm}^{-1}$  are interactions of the  $\text{PF}_6^-$  anion with the solvents of the electrolyte.<sup>39,40,42</sup> The peak shift to  $750\text{ cm}^{-1}$  is a contact ion pair that forms between the  $\text{PF}_6^-$  anion and the uptake of calcium into the electrolyte.<sup>43-44</sup> These shifts in wavenumbers outline how the continued plating and stripping with the hybrid SEI also produces compositional changes in the electrolyte, creating a dual ion system for plating and stripping. Previous research efforts mixing  $\text{Li}(\text{BH}_4)$  and  $\text{Ca}(\text{BH}_4)_2$  as a dual ion electrolyte promoted conversion of the  $\text{Ca}(\text{BH}_4)_2$  into ionic clusters that were more electrochemically favorable for plating and stripping.<sup>45</sup> Similar effects are observed with the evolution of capacities at 0.2 V over the course of cycling. While calcium plating does occur at both 0.2 and 1.8 V overpotentials, the redox activity benchmarked at 0.2 V was determined to be predominantly calcium plating and the 1.8 V overpotential was predominantly potassium. The increase of the capacity at 0.2 V overpotentials reflects the compositional change of the electrolyte and how it translates to increased redox activity at that potential. Inductively Coupled Plasma Mass Spectrometry (ICP-MS) was performed 70 hours into plating and stripping with a symmetric cell. The results from the analysis revealed a calcium concentration of 0.004 M in the cycled electrolyte. As cycling of

the cell would continue, increase of the calcium concentration in the electrolyte would be expected with the increased electrochemical activity at 0.2 V.

## 5.4 Conclusion

We have shown successful plating and stripping with calcium metal electrodes using a native potassium electrolyte while maintaining overpotentials at 2 V. The SEI formed from the galvanostatic cycling plates and strips both calcium and potassium, as observed with XRD, FTIR and EDX. The SEI formed on the calcium electrodes is influenced by the two regions of plating and stripping behavior with Ca, CaF<sub>2</sub> and P<sub>2</sub>O<sub>5</sub> phases forming at the 0.2 V overpotential and K<sub>2</sub>P<sub>2</sub>O<sub>5</sub>F<sub>2</sub> and K phases forming at 1.8 V. The SEI also has a mixture of permanent and transient phases with K and K<sub>2</sub>P<sub>2</sub>O<sub>5</sub>F<sub>2</sub> being removed after stripping while CaF<sub>2</sub> and P<sub>2</sub>O<sub>5</sub> remain. The uptake of calcium into the KPF<sub>6</sub> electrolyte over the course of cycling transition the conducting media to a dual ion system that increases the availability of calcium. The compositional changes to the electrolyte and low interfacial resistance of the SEI allow for increased plating and stripping of calcium and is most notable with the increased capacities at 0.2 V. This work provides demonstration that potassium electrolytes provide similar benefits to the plating and stripping of calcium that has been observed with sodium electrolytes. While the plating and stripping behavior of sodium electrolytes is more concise with all redox activity being observed at a single overpotential, the potassium electrolytes develop an SEI through a more multi-step behavior. Future opportunities with this work can be explored with understanding the dynamics that lead to the development of two distinct regions of redox activity. Other features of this hybrid system that need to be addressed are strategies to lower the overpotentials from 1.8 V. Optimizing the electrolyte to function at 0.2 V is essential for more substantial calcium cycling and for the system to serve as an alternative to such electrolytes such as Ca(BH<sub>4</sub>)<sub>2</sub> in THF. One such optimization that

needs to be explored is different salt and solvent combinations. Another aspect of this hybrid SEI that needs further investigation is lifetime testing of the potassium electrolyte with higher current densities and capacities.

## Supplemental Information

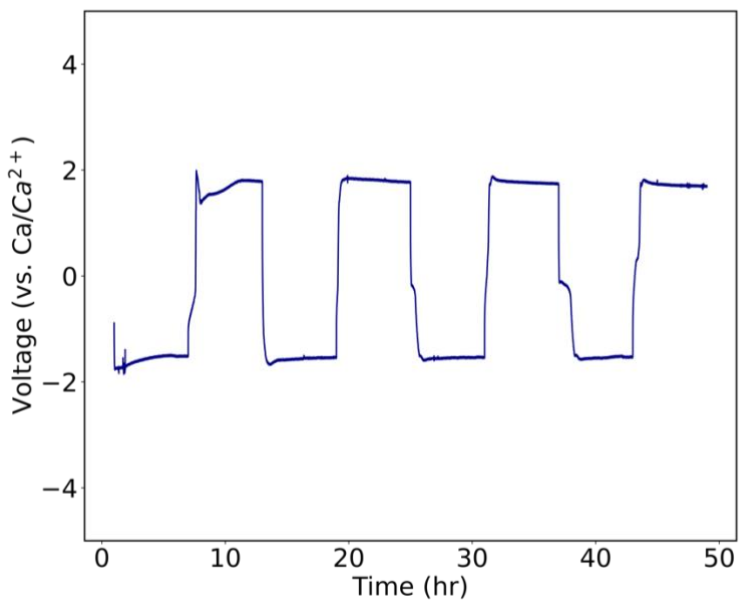


**Figure SI 5.1** – Plating and stripping Ca//Ca symmetric cell with dedicated calcium reference electrode

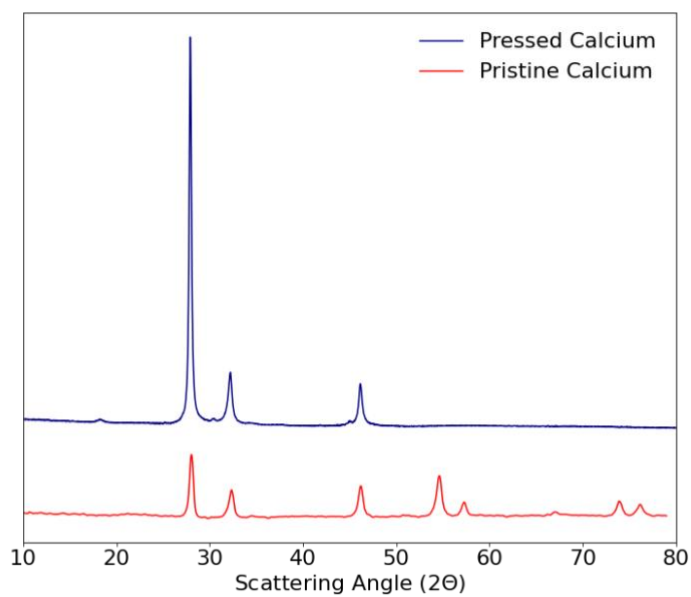


**Figure SI 5.2** - XRD of pristine and pressed calcium pellets

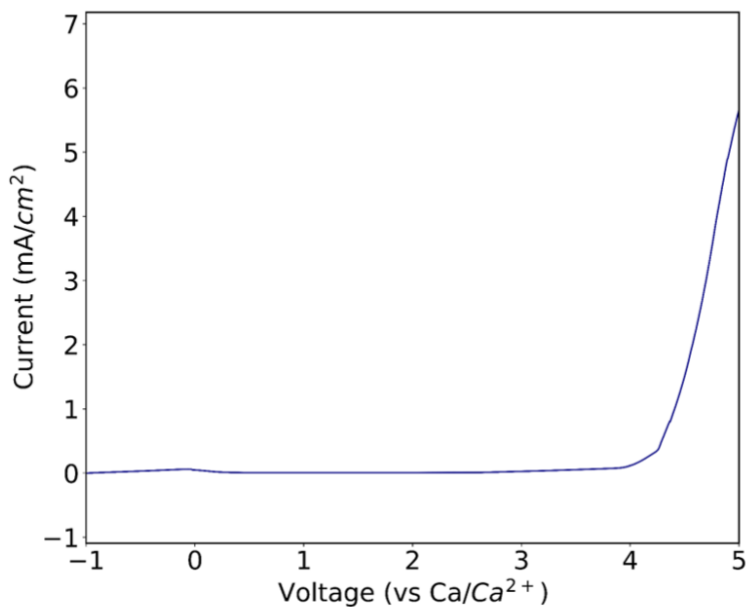


**Figure SI 5.3** - Linear stability window of KPF<sub>6</sub> EC/DMC/EMC using a gold blocking electrode and calcium nonblocking electrode at 0.5 mV/s

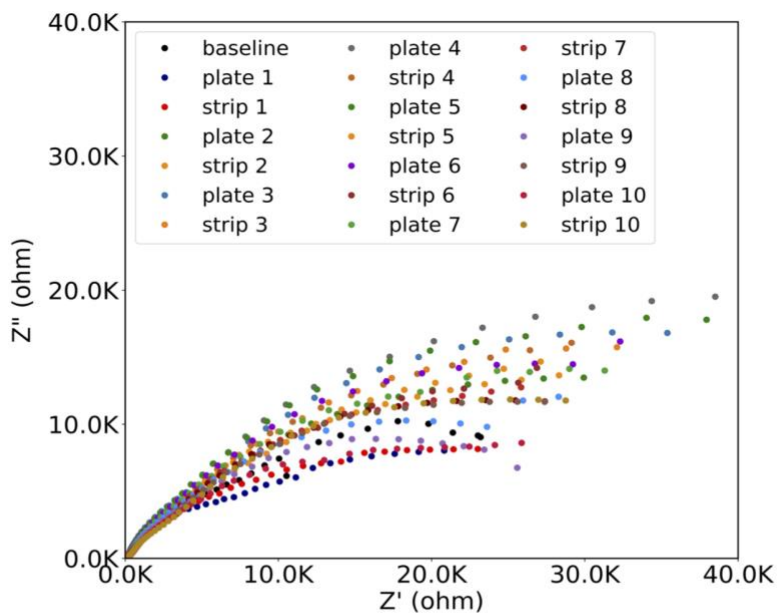


**Figure SI 5.4** - Nyquist plots of impedance for galvanostatic cycling and after each plating and stripping

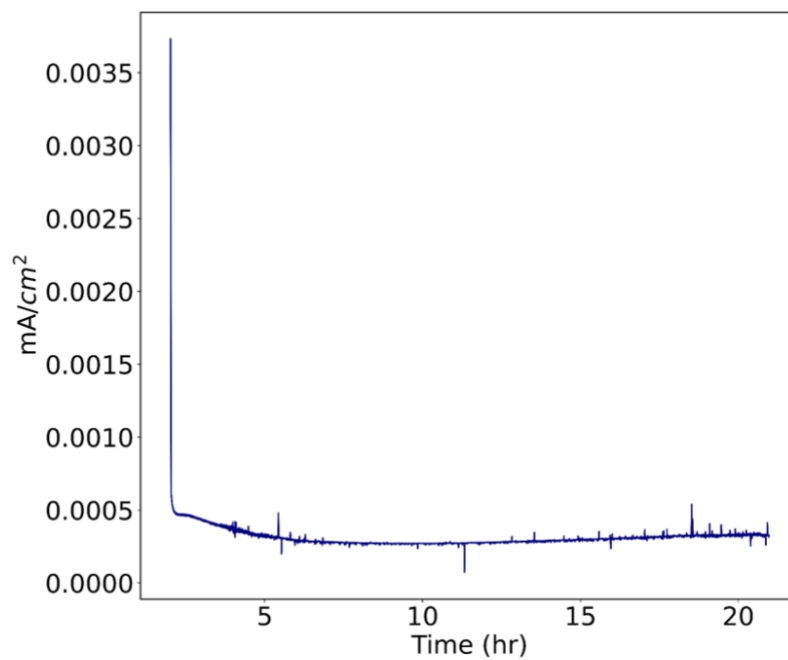


**Figure SI 5.5** - Transference number measurement of KPF<sub>6</sub> EC/DMC/EMC (uncycled)

## References

1. Hosein, I. D. The Promise of Calcium Batteries: Open Perspectives and Fair Comparisons. *ACS Energy Lett.* **2021**, 1560–1565.
2. Song, H.; Wang, C. Current Status and Challenges of Calcium Metal Batteries. *Adv Energy and Sustain Res* **2022**, 2100192.
3. Ponrouch, A.; Frontera, C.; Bardé, F.; Palacín, M. R. Towards a Calcium-Based Rechargeable Battery. *Nat. Mater.* **2016**, *15* (2), 169–172.
4. Song, H.; Su, J.; Wang, C. Hybrid Solid Electrolyte Interphases Enabled Ultralong Life Ca-Metal Batteries Working at Room Temperature. *Adv. Mater.* **2021**, *33* (2), e2006141.
5. Biria, S.; Pathreker, S.; Li, H.; Hosein, I. D. Plating and Stripping of Calcium in an Alkyl Carbonate Electrolyte at Room Temperature. *ACS Appl. Energy Mater.* **2019**, *2* (11), 7738–7743.
6. Biria, S.; Pathreker, S.; Genier, F. S.; Li, H.; Hosein, I. D. Plating and Stripping Calcium at Room Temperature in an Ionic-Liquid Electrolyte. *ACS Appl. Energy Mater.* **2020**, *3* (3), 2310–2314.
7. Shyamsunder, A.; Blanc, L. E.; Assoud, A.; Nazar, L. F. Reversible Calcium Plating and Stripping at Room Temperature Using a Borate Salt. *ACS Energy Letters* **2019**, *4* (9), 2271–2276.
8. Melemed, A. M.; Gallant, B. M. Electrochemical Signatures of Interface-Dominated Behavior in the Testing of Calcium Foil Anodes. *J. Electrochem. Soc.* **2020**, *167* (14), 140543.
9. Kozen, A. C.; Lin, C.-F.; Zhao, O.; Lee, S. B.; Rubloff, G. W.; Noked, M. Stabilization of Lithium Metal Anodes by Hybrid Artificial Solid Electrolyte Interphase. *Chem. Mater.* **2017**, *29* (15), 6298–6307.
10. Araujo, R. B.; Thangavel, V.; Johansson, P. Towards Novel Calcium Battery Electrolytes by Efficient Computational Screening. *Energy Storage Materials* **2021**, *39*, 89–95.
11. Song, H.; Li, Y.; Tian, F.; Wang, C. Electrolyte Optimization and Interphase Regulation for Significantly Enhanced Storage Capability in Ca-metal Batteries. *Adv. Funct. Mater.* **2022**, 2200004.
12. Song, H.; Su, J.; Wang, C. Multi-ions Electrolyte Enabled High Performance Voltage Tailorable Room-temperature Ca-metal Batteries. *Adv. Energy Mater.* **2021**, *11* (10), 2003685.

13. Song, H.; Wang, C. Artificial Hybrid Solid Electrolyte Mediated Ca-metal for Ultra-durable Room-temperature 5 V Calcium Batteries. *Energy Environ. Mater.* **2021**. <https://doi.org/10.1002/eem2.12325>.
14. Fischer, L. M.; Tenje, M.; Heiskanen, A. R.; Masuda, N.; Castillo, J.; Bentien, A.; Émneus, J.; Jakobsen, M. H.; Boisen, A. Gold Cleaning Methods for Electrochemical Detection Applications. *Microelectron. Eng.* **2009**, *86* (4), 1282–1285.
15. Bieker, G.; Winter, M.; Bieker, P. Electrochemical in Situ Investigations of SEI and Dendrite Formation on the Lithium Metal Anode. *Phys. Chem. Chem. Phys.* **2015**, *17* (14), 8670–8679.
16. Lei, Y.; Han, D.; Dong, J.; Qin, L.; Li, X.; Zhai, D.; Li, B.; Wu, Y.; Kang, F. Unveiling the Influence of Electrode/electrolyte Interface on the Capacity Fading for Typical Graphite-Based Potassium-Ion Batteries. *Energy Storage Materials* **2020**, *24*, 319–328.
17. Musil, M.; Vondrák, J. Transference Number Measurements on Gel Polymer Electrolytes for Lithium-Ion Batteries. *ECS Trans.* **2014**, *63* (1), 315.
18. Bruce, P. Conductivity and Transference Number Measurements on Polymer Electrolytes. *Solid State Ionics* **1988**, *28-30*, 918–922.
19. Zugmann, S.; Fleischmann, M.; Amereller, M.; Gschwind, R. M.; Wiemhöfer, H. D.; Gores, H. J. Measurement of Transference Numbers for Lithium Ion Electrolytes via Four Different Methods, a Comparative Study. *Electrochim. Acta* **2011**, *56* (11), 3926–3933.
20. Fong, K. D.; Self, J.; Diederichsen, K. M.; Wood, B. M.; McCloskey, B. D.; Persson, K. A. Ion Transport and the True Transference Number in Nonaqueous Polyelectrolyte Solutions for Lithium Ion Batteries. *ACS Cent Sci* **2019**, *5* (7), 1250–1260.
21. Degen, T.; Sadki, M.; Bron, E.; König, U.; Nénert, G. The HighScore Suite. *Powder Diffr.* **2014**, *29* (S2), S13–S18.
22. Jain, A.; Ong, S. P.; Hautier, G.; Chen, W.; Richards, W. D.; Dacek, S.; Cholia, S.; Gunter, D.; Skinner, D.; Ceder, G.; Persson, K. A. Commentary: The Materials Project: A Materials Genome Approach to Accelerating Materials Innovation. *APL Materials* **2013**, *1* (1), 011002.
23. Khunur, M. M.; Risdianto, A.; Mutrofin, S.; Prananto, Y. P. Synthesis of Fluorite (CaF<sub>2</sub>) Crystal from Gypsum Waste of Phosphoric Acid Factory in Silica Gel. *Bulletin of Chemical Reaction Engineering & Catalysis* **2012**, *7* (1), 71–77.
24. Kiani, A.; Hanna, J. V.; King, S. P.; Rees, G. J.; Smith, M. E.; Roohpour, N.; Salih, V.; Knowles, J. C. Structural Characterization and Physical Properties of P<sub>2</sub>O<sub>5</sub>-CaO-Na<sub>2</sub>O-TiO<sub>2</sub> Glasses by Fourier Transform Infrared, Raman and Solid-State Magic Angle

- Spinning Nuclear Magnetic Resonance Spectroscopies. *Acta Biomater.* **2012**, *8* (1), 333–340.
25. Lambert, J. B.; Shurvell, H. F.; Lightner, D. A.; Cooks, R. G. *Introduction to Organic Spectroscopy*; Macmillan Publishing Company, 1987.
  26. Wang, H.; Wang, H.; Chen, S.; Zhang, B.; Yang, G.; Gao, P.; Liu, J.; Fan, X.; Huang, Y.; Lin, J.; Shen, Z. A Depth-Profiling Study on the Solid Electrolyte Interface: Bis(fluorosulfonyl)imide Anion toward Improved K<sup>+</sup> Storage. *ACS Appl. Energy Mater.* **2019**, *2* (11), 7942–7951.
  27. Fan, L.; Chen, S.; Ma, R.; Wang, J.; Wang, L.; Zhang, Q.; Zhang, E.; Liu, Z.; Lu, B. Ultrastable Potassium Storage Performance Realized by Highly Effective Solid Electrolyte Interphase Layer. *Small* **2018**, *14* (30), e1801806.
  28. Zhuang, G. V.; Yang, H.; Blizanac, B.; Ross, P. N. A Study of Electrochemical Reduction of Ethylene and Propylene Carbonate Electrolytes on Graphite Using ATR-FTIR Spectroscopy. *Electrochem. Solid-State Lett.* **2005**, *8* (9), A441.
  29. Rush, J. J.; Schroeder, L. W.; Melveger, A. J. Dynamics of Sodium and Potassium Bifluoride: Infrared, Raman, and Neutron Studies. *J. Chem. Phys.* **1972**, *56* (6), 2793–2800.
  30. Aziz, M. A. A.; Triwahyono, S.; Jalil, A. A.; Rapai, H. A. A.; Atabani, A. E. Transesterification of Moringa Oleifera Oil to Biodiesel over Potassium Fluoride Loaded on Eggshell Catalyst. *Malaysian Journal of Catalysis* **2016**, 22–26.
  31. Pu, S. D.; Gong, C.; Gao, X.; Ning, Z.; Yang, S.; Marie, J.-J.; Liu, B.; House, R. A.; Hartley, G. O.; Luo, J.; Bruce, P. G.; Robertson, A. W. Current-Density-Dependent Electroplating in Ca Electrolytes: From Globules to Dendrites. *ACS Energy Lett.* **2020**, *5* (7), 2283–2290.
  32. Wen, K.; Liu, L.; Chen, S.; Zhang, S. A Bidirectional Growth Mechanism for a Stable Lithium Anode by a Platinum Nanolayer Sputtered on a Polypropylene Separator. *RSC Adv.* **2018**, *8* (23), 13034–13039.
  33. Liu, Y.; Li, X.; Fan, L.; Li, S.; Maleki Kheimeh Sari, H.; Qin, J. A Review of Carbon-Based Materials for Safe Lithium Metal Anodes. *Front Chem* **2019**, *7*, 721.
  34. Zhao, J.; Wang, L.; He, X.; Wan, C.; Jiang, C. Determination of Lithium-Ion Transference Numbers in LiPF<sub>6</sub>-PC Solutions Based on Electrochemical Polarization and NMR Measurements. *J. Electrochem. Soc.* **2008**, *155* (4), A292.
  35. Steinhauer, M.; Risse, S.; Wagner, N.; Friedrich, K. A. Investigation of the Solid Electrolyte Interphase Formation at Graphite Anodes in Lithium-Ion Batteries with Electrochemical Impedance Spectroscopy. *Electrochim. Acta* **2017**, *228*, 652–658.

36. Gao, P.; Zhang, C.; Wen, G. Equivalent Circuit Model Analysis on Electrochemical Impedance Spectroscopy of Lithium Metal Batteries. *J. Power Sources* **2015**, *294*, 67–74.
37. Zheng, J.; Schkeryantz, L.; Gourdin, G.; Qin, L.; Wu, Y. Single Potassium-Ion Conducting Polymer Electrolytes: Preparation, Ionic Conductivities, and Electrochemical Stability. *ACS Appl. Energy Mater.* **2021**, *4* (4), 4156–4164.
38. Jian, Q.; Wang, T.; Sun, J.; Wu, M.; Zhao, T. In situ Construction of Fluorinated Solid-Electrolyte Interphase for Highly Reversible Zinc Anodes. *Energy Storage Materials* **2022**, *53*, 559–568.
39. Mukai, K.; Inoue, T.; Kato, Y.; Shirai, S. Superior Low-Temperature Power and Cycle Performances of Na-Ion Battery over Li-Ion Battery. *ACS Omega* **2017**, *2* (3), 864–872.
40. Liu, W.; Li, J.; Li, W.; Xu, H.; Zhang, C.; Qiu, X. Inhibition of Transition Metals Dissolution in Cobalt-Free Cathode with Ultrathin Robust Interphase in Concentrated Electrolyte. *Nat. Commun.* **2020**, *11* (1), 3629.
41. Durig, J. R.; Coulter, G. L.; Wertz, D. W. Far-Infrared Spectra and Structure of Small Ring Compounds. Ethylene Carbonate,  $\gamma$ -Butyrolactone, and Cyclopentanone. *J. Mol. Spectrosc.* **1968**, *27* (1), 285–295.
42. Lee, H.; Hwang, S.; Kim, M.; Kwak, K.; Lee, J.; Han, Y.-K.; Lee, H. Why Does Dimethyl Carbonate Dissociate Li Salt Better Than Other Linear Carbonates? Critical Role of Polar Conformers. *J. Phys. Chem. Lett.* **2020**, *11* (24), 10382–10387.
43. Hahn, N. T.; Driscoll, D. M.; Yu, Z.; Sterbinsky, G. E.; Cheng, L.; Balasubramanian, M.; Zavadil, K. R. Influence of Ether Solvent and Anion Coordination on Electrochemical Behavior in Calcium Battery Electrolytes. *ACS Appl. Energy Mater.* **2020**, *3* (9), 8437–8447.
44. Tchitchekova, D. S.; Monti, D.; Johansson, P.; Bardé, F.; Randon-Vitanova, A.; Palacín, M. R.; Ponrouch, A. On the Reliability of Half-Cell Tests for Monovalent (Li<sup>+</sup>, Na<sup>+</sup>) and Divalent (Mg<sup>2+</sup>, Ca<sup>2+</sup>) Cation Based Batteries. *J. Electrochem. Soc.* **2017**, *164* (7), A1384.
45. Hahn, N. T.; Self, J.; Seguin, T. J.; Driscoll, D. M.; Rodriguez, M. A.; Balasubramanian, M.; Persson, K. A.; Zavadil, K. R. The Critical Role of Configurational Flexibility in Facilitating Reversible Reactive Metal Deposition from Borohydride Solutions. *J. Mater. Chem. A Mater. Energy Sustain.* **2020**, *8* (15), 7235–7244.

## **CHAPTER 6**

### **CONCLUSIONS AND FUTURE WORK**

## 6.1 Conclusions

The aim of this dissertation was to: (i) experimentally evaluate the electrochemical activity of transition metal oxide cathodes for calcium-ion batteries (ii) track their structural changes as a function of cycling and (iii) develop an SEI for calcium metal that allows for calcium cycling while mitigating the formation of a passivation layer. In this dissertation, post-spinel cathodes of  $\text{CaFe}_2\text{O}_4$  and  $\text{CaMn}_2\text{O}_4$  were successfully synthesized and evaluated. Their structural developments were tracked with an in situ cell in addition to ex situ characterization methods. Evaluation of the  $\text{CaMn}_2\text{O}_4$  was found to be a promising cathode for calcium-ion batteries while  $\text{CaFe}_2\text{O}_4$  was identified to be a cathode of limited redox activity. Additionally, a hybrid SEI system was explored using a potassium electrolyte. This approach resulted in successfully plating and stripping with calcium electrodes and avoiding the continuous increase of overpotentials that exist with native calcium electrolytes. These findings provide further insight into the field of calcium-ion batteries and calcium-metal batteries.

An in situ cell for operando XRD characterization was designed, fabricated, and validated with lithium-ion battery chemistry.  $\text{LiCoO}_2$  was cycled with a lithium metal anode and the structural changes to the electrode were tracked over cycling. A capacity of 32 mAh/g was cycled with the cathode and structural changes to the  $\text{LiCoO}_2$  were in agreement with previous studies. Glassy carbon was validated as an effective XRD window with the in situ cell. Further optimizations to the work would focus on optimizing the amount of active material in the freestanding electrode to achieve better capacities. This optimization is equally applicable to the  $\text{CaMn}_2\text{O}_4$  and  $\text{CaFe}_2\text{O}_4$  cathodes that were analyzed with the in situ cell.

$\text{CaMn}_2\text{O}_4$  was successfully synthesized and evaluated as a cathode for calcium-ion batteries. The charging of the electrode and structural characterization of it provides important insights into the intercalation chemistry of the post-spinel. Structural changes to the cathode were tracked with in

situ XRD measurements and ex situ techniques. The electrochemical activity of the cathode was further validated by comparing the experimental XRD data to theoretical XRD patterns generated from DFT calculations. The cathode itself was subject to changes in its crystal symmetry during charging from conversion chemistry and disproportionation reactions. Additional changes in crystal symmetry are a result of Jahn-Teller distortions. Using a c-rate of C/200, a total capacity of 100 mAh/g was charged from the  $\text{CaMn}_2\text{O}_4$ . It is also important to note that all electrochemical experiments were performed at room temperature. Future work on the cathode can include improving the amount of active material in the cathode to achieve better capacities along with charging the cathode at elevated temperatures for improving diffusion kinetics. This work on  $\text{CaMn}_2\text{O}_4$  provides an important baseline for the performance of the cathode and serves as motivation for continued exploration of this post-spinel in its use as a calcium-ion cathode.

$\text{CaFe}_2\text{O}_4$  post-spinel was also evaluated as a cathode for calcium-ion batteries. The work performed in this dissertation serves as an experimental validation of the limitations that were expected of  $\text{CaFe}_2\text{O}_4$  from DFT calculations. Theoretical work on this post-spinel concluded the diffusion barrier would not allow for considerable capacity cycling. Even with the use of a slower c-rates on the cathode, minimal structural changes to the cathode were observed with the only notable change being from the intensity increase of (103) lattice planes. The work on  $\text{CaFe}_2\text{O}_4$  establishes a negative result for this transition metal oxide in its role as a cathode for calcium-ion batteries.

The use of  $\text{KPF}_6$  as a salt for calcium-metal batteries was effective in developing a hybrid SEI on calcium metal electrodes and achieving plating and stripping overpotentials below 2 V. The phases formed on the calcium electrode SEI were a composite of calcium, calcium fluoride, phosphorus pentoxide and difluorodiphosphate. Additional characterizations confirmed the uptake of calcium

into the electrolyte as more calcium was plated and stripped throughout the course of cycling. This result demonstrates that potassium has a similar capability to sodium in forming a hybrid SEI that allows for the cycling of calcium while mitigating the continued formation of passivation layers that are present in native calcium electrolytes. This work is an important step towards the implementation of calcium metal anodes and achieving high energy densities with calcium batteries. Future efforts with this work should focus on understanding the development of two distinct regions of redox activity in addition to exploring different salt and solvent combinations.

## **6.2 Future Work**

Regarding the work on cathodes for calcium-ion batteries,  $\text{CaMn}_2\text{O}_4$  post-spinel was a cathode that exhibited promising electrochemical activity. However, some limitations that exist with this cathode are the high diffusion barrier of 1.8 eV, limited capacities, and the phase instabilities that exist from calcium extraction due to Jahn-Teller distortions.<sup>[1,2]</sup> These limitations were evident with the changes of crystal symmetry that occurred because of charging along with the need to use small c-rates to extract larger capacities of calcium from the host structure.

There are several strategies that can be implemented for improving the electrochemical performance of the studied cathodes including the processing of cathodes into single crystals and controlling the fugacities of oxygen within the post-spinels. The use of polycrystalline materials in an electrode is common with batteries. However, polycrystalline electrodes eventually form microcracks that ultimately become grain boundaries and other defects that impact the durability and lifetime of the electrode.<sup>[3,4]</sup> The use of single crystal electrodes has already been studied with lithium-ion batteries and has yielded higher capacities along with improved mechanical and thermal stabilities.<sup>[3-6]</sup> Processing single crystal calcium cathodes has the potential to increase the

operating voltage and capacities of calcium batteries while also providing structural stability that improves the lifetime of the battery. Additional efforts to engineer more favorable cathode performance include controlling the fugacity of oxygen to design vacancies within the crystal structure of the electrode. The use of oxygen vacancies within an electrode not only changes the oxidation state of the transition metal used within the cathode, but also creates new diffusion pathways for calcium to migrate through. Designing such atomic defects within manganese oxide cathodes has reported capacities of 130 mAh/g at room temperature and holds similar potential with other transition metal oxides.<sup>[7,8]</sup>

Other doping strategies include alloying  $\text{CaMn}_2\text{O}_4$  with other transition metals to address the high migration barrier of 1.8 eV and facilitate larger capacity cycling by changing the crystal structure of the post-spinel. Three variants of post-spinel crystal structures exist:  $\text{CaFe}_2\text{O}_4$ -type,  $\text{CaMn}_2\text{O}_4$ -type and  $\text{CaTi}_2\text{O}_4$ -type.<sup>[9]</sup> DFT calculations on simulating cation mobility through post-spinel structures have found the  $\text{CaFe}_2\text{O}_4$ -type crystal structure to possess the lowest diffusion barrier.<sup>[2]</sup> Based on the theoretical evaluations of the post-spinels, better cathode performance for calcium-ion batteries could be achieved if the oxidation states of manganese that enable intercalation chemistry could be combined with the favorable crystal structure of  $\text{CaFe}_2\text{O}_4$ . Efforts at alloying iron and manganese have already been performed and other studies concluding the preferable diffusion of cations into the  $\text{CaFe}_2\text{O}_4$ -type spinel have been established with other battery chemistries.<sup>[10-14]</sup>

The addition of iron to a  $\text{CaMn}_2\text{O}_4$ -type post-spinel structure reorients the crystal structure from  $\text{CaMn}_2\text{O}_4$  to  $\text{CaFe}_2\text{O}_4$  while retaining manganese as the dominant transition metal in the structure. The addition of iron to the crystal structure will not only lower the diffusion barrier from 1.8 eV, but also serve to stabilize manganese in high spin configurations and mitigate Jahn-Teller

distortions as calcium is cycled through the electrode. This alloying effort represents the next step in the exploration of cathodes for calcium-ion batteries and an initial synthesis of the alloyed structure has already been performed and verified.

### 6.2.1 Synthesis of $\text{Ca}_{0.66}\text{Mn}_{1.4}\text{Fe}_{0.6}\text{O}_4$

#### Materials

Calcium Nitrate Tetrahydrate ( $\text{Ca}(\text{NO}_3)_2 \cdot 4\text{H}_2\text{O}$ ), Manganese Nitrate Hydrate ( $\text{Mn}(\text{NO}_3)_2 \cdot x\text{H}_2\text{O}$ ), Iron (III) Nitrate Nonahydrate ( $\text{Fe}(\text{NO}_3)_3 \cdot 9\text{H}_2\text{O}$ ), and Glycine were purchased from Sigma-Aldrich, USA, and used as received.

#### Synthesis

$\text{Ca}_{0.66}\text{Mn}_{1.4}\text{Fe}_{0.6}\text{O}_4$  was synthesized using an auto-combustion synthesis.<sup>[13]</sup> 7 mmol of  $\text{Ca}(\text{NO}_3)_2$ , 14 mmol of  $\text{Mn}(\text{NO}_3)_2$  and 6 mmol of  $\text{Fe}(\text{NO}_3)_3$  were dissolved and mixed together with a total volume of water approximately 25 mL. Following the mixture of all nitrates, 2.1g of glycine was added to the mixture. The glycine was added in quantity to maintain a glycine/metal molar ratio of 2. This would ensure optimum cation chelation. Once the glycine was added to the mixture, the solution was transferred to a beaker and placed on a hot plate, heating it at 100°C. The heating of the solution would cause excess water to evaporate and induce polycondensation of glycine. The beaker was then covered with a 1 L glass beaker to contain the auto-combustion reaction and ensure the containment of the ashes. The temperature of the hot plate was incrementally increased to 250°C for the auto-combustion reaction. Once completed, the ashes were placed in a box furnace and heated to 850°C for 12 hours to obtain the alloyed calcium manganese iron oxide.

## Results

The resulting alloyed structure was analyzed under X-ray diffraction (XRD) using Highscore plus software.<sup>[15]</sup> The synthesized  $\text{Ca}_{0.66}\text{Mn}_{1.4}\text{Fe}_{0.6}\text{O}_4$  was compared to literature values and analyzed with Rietveld refinement.<sup>[16-17]</sup> The results from the analysis confirm the phase of the synthesized product to be the alloyed calcium manganese iron oxide. (Figure 6.1) The space group of the calcium manganese oxide successfully has a  $\text{CaFe}_2\text{O}_4$ -type post-spinel structure with Pnma. The lattice parameters of the post-spinel were refined to be  $a = 9.099943 \text{ \AA}$ ,  $b = 2.883023 \text{ \AA}$  and  $c = 10.958590 \text{ \AA}$ .

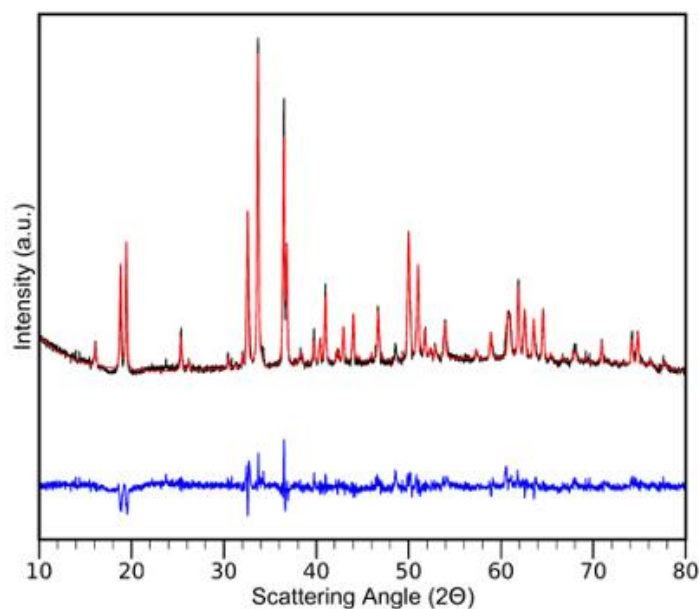


**Figure 6.1** - XRD of synthesized  $\text{Ca}_{0.66}\text{Mn}_{1.4}\text{Fe}_{0.6}\text{O}_4$

Following the successful synthesis of the alloyed structure, future efforts will be aimed at processing the raw materials into an electrode and cycling the electrode with an activated carbon counter electrode in  $\text{Ca}(\text{TFSI})_2$  in DME. The preferable crystal structure of  $\text{CaFe}_2\text{O}_4$  post-spinel is expected to facilitate with faster capacity cycling, and the alloying of iron with manganese, from

theoretical calculations, will help mitigate the phase transitions that occur from Jahn-Teller distortions that are experienced with pure  $\text{CaMn}_2\text{O}_4$  electrodes.<sup>[2]</sup>

## References

1. Dompablo, M. E. A.; Krich, C.; Nava-Avendaño, J.; Biškup, N.; Palacín, M. R.; Bardé, F. A Joint Computational and Experimental Evaluation of  $\text{CaMn}_2\text{O}_4$  Polymorphs as Cathode Materials for Ca Ion Batteries. *Chem. Mater.* **2016**, *28* (19), 6886–6893.
2. Ling, C.; Mizuno, F. Phase Stability of Post-Spinel Compound  $\text{AMn}_2\text{O}_4$  (A = Li, Na, or Mg) and Its Application as a Rechargeable Battery Cathode. *Chem. Mater.* **2013**, *25* (15), 3062–3071.
3. Klein, S.; Bärman, P.; Fromm, O.; Borzutzki, K.; Reiter, J.; Fan, Q.; Winter, M.; Placke, T.; Kasnatscheew, J. Prospects and Limitations of Single-Crystal Cathode Materials to Overcome Cross-Talk Phenomena in High-Voltage Lithium Ion Cells. *J. Mater. Chem. A Mater. Energy Sustain.* **2021**, *9* (12), 7546–7555.
4. Ou, X.; Liu, T.; Zhong, W.; Fan, X.; Guo, X.; Huang, X.; Cao, L.; Hu, J.; Zhang, B.; Chu, Y. S.; Hu, G.; Lin, Z.; Dahbi, M.; Alami, J.; Amine, K.; Yang, C.; Lu, J. Enabling High Energy Lithium Metal Batteries via Single-Crystal Ni-Rich Cathode Material Co-Doping Strategy. *Nat. Commun.* **2022**, *13* (1), 2319.
5. Ran, A.; Chen, S.; Cheng, M.; Liang, Z.; Li, B.; Zhou, G.; Kang, F.; Zhang, X.; Wei, G. A Single-Crystal Nickel-Rich Material as a Highly Stable Cathode for Lithium-Ion Batteries. *J. Mater. Chem. A Mater. Energy Sustain.* **2022**, *10* (37), 19680–19689.
6. Wang, Y.; Wang, E.; Zhang, X.; Yu, H. High-Voltage “Single-Crystal” Cathode Materials for Lithium-Ion Batteries. *Energy Fuels* **2021**, *35* (3), 1918–1932.
7. Kwon, B. J.; Yin, L.; Bartel, C. J.; Kumar, K.; Parajuli, P.; Gim, J.; Kim, S.; Wu, Y. A.; Klie, R. F.; Lapidus, S. H.; Key, B.; Ceder, G.; Cabana, J. Intercalation of Ca into a Highly Defective Manganese Oxide at Room Temperature. *Chem. Mater.* **2022**, *34* (2), 836–846.
8. Torres, A.; Luque, F. J.; Tortajada, J.; Arroyo-de Dompablo, M. E. DFT Investigation of Ca Mobility in Reduced-Perovskite and Oxidized-Marokite Oxides. *Energy Storage Materials* **2019**, *21*, 354–360.
9. Yamanaka, T.; Uchida, A.; Nakamoto, Y. Structural Transition of Post-Spinel Phases  $\text{CaMn}_2\text{O}_4$ ,  $\text{CaFe}_2\text{O}_4$ , and  $\text{CaTi}_2\text{O}_4$  under High Pressures up to 80 GPa. *Am. Mineral.* **2008**, *93* (11-12), 1874–1881.
10. Nolis, G.; Gallardo-Amores, J. M.; Serrano-Sevillano, J.; Jahrman, E.; Yoo, H. D.; Hu, L.; Hancock, J. C.; Bolotnikov, J.; Kim, S.; Freeland, J. W.; Liu, Y.-S.; Poepfelmeier, K. R.; Seidler, G. T.; Guo, J.; Alario-Franco, M. A.; Casas-Cabanas, M.; Morán, E.; Cabana, J. Factors Defining the Intercalation Electrochemistry of  $\text{CaFe}_2\text{O}_4$ -Type Manganese Oxides. *Chem. Mater.* **2020**, *32* (19), 8203–8215.

11. Medina, A.; Pérez-Vicente, C.; Alcántara, R. Spinel-Type  $\text{Mg}_x\text{Mn}_{2-y}\text{Fe}_y\text{O}_4$  as a New Electrode for Sodium Ion Batteries. *Electrochim. Acta* **2022**, *421*, 140492.
12. Zouari, S.; Ranno, L.; Cheikh-Rouhou, A.; Pernet, M.; Strobel, P. Structural and Magnetic Properties of the  $\text{CaFe}_{2-x}\text{Mn}_x\text{O}_4$  Solid Solution. *J. Mater. Chem.* **2003**, *13* (4), 951–956.
13. Lesturgez, S.; Goglio, G.; Duttine, M.; Wattiaux, A.; Durand, E.; Hernandez, J.; Majimel, J.; Demourgues, A. Tuning the Mn and Fe Valence States into New  $\text{Ca}_{0.7}\text{Mn}_{2-x}\text{Fe}_x\text{O}_4$  ( $0 < X \leq 0.60$ ) Solid Solution during Reversible Redox Processes. *Chem. Mater.* **2016**, *28* (14), 4935–4944.
14. Yang, T.; Croft, M.; Ignatov, A.; Nowik, I.; Cong, R.; Greenblatt, M. Stabilization of  $\text{Ca}_{1-\delta}\text{Fe}_{2-x}\text{Mn}_x\text{O}_4$  ( $0.44 \leq X \leq 2$ ) with  $\text{CaFe}_2\text{O}_4$ -Type Structure and  $\text{Ca}^{2+}$  Defects in One-Dimensional (1D) Channels. *Chem. Mater.* **2010**, *22* (21), 5876–5886.
15. Degen, T.; Sadki, M.; Bron, E.; König, U.; Nénert, G. The HighScore Suite. *Powder Diffr.* **2014**, *29* (S2), S13–S18.
16. McCusker, L. B.; Von Dreele, R. B.; Cox, D. E.; Louër, D.; Scardi, P. Rietveld Refinement Guidelines. *J. Appl. Crystallogr.* **1999**, *32* (1), 36–50.
17. Stinton, G. W.; Evans, J. S. O. Parametric Rietveld Refinement. *J. Appl. Crystallogr.* **2007**, *40* (Pt 1), 87–95.

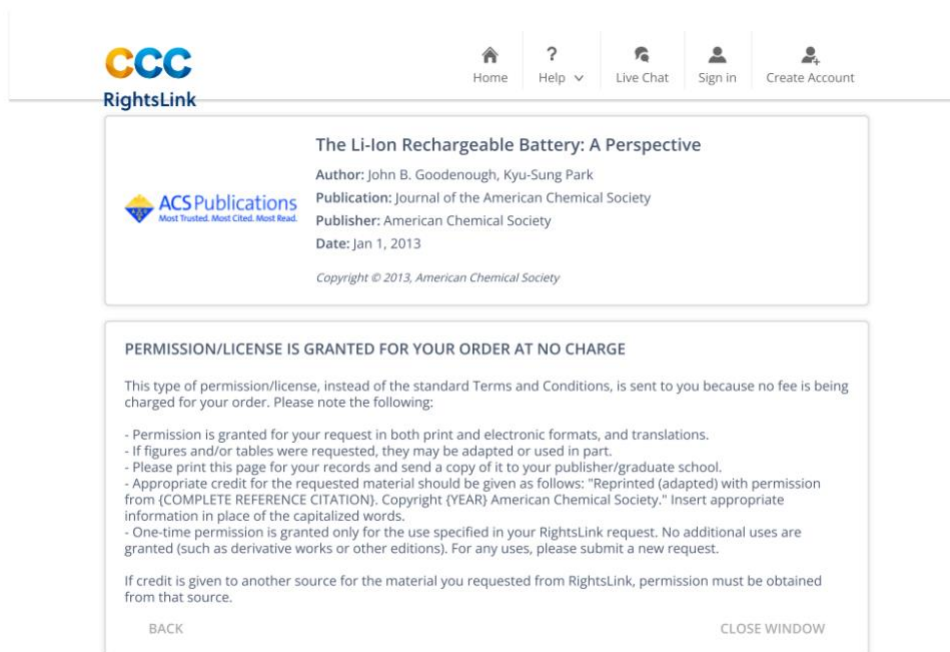
# APPENDICES

# APPENDIX I: PERMISSION FROM ACS

## PUBLICATION FOR FIGURE 1.1

Figure 1.1 extracted from published article:

The Li-Ion Rechargeable Battery: A Perspective



The screenshot shows the CCC RightsLink website interface. At the top, there is a navigation bar with the CCC RightsLink logo on the left and navigation links for Home, Help, Live Chat, Sign in, and Create Account on the right. Below the navigation bar, the main content area displays the following information:

**The Li-Ion Rechargeable Battery: A Perspective**  
Author: John B. Goodenough, Kyu-Sung Park  
Publication: Journal of the American Chemical Society  
Publisher: American Chemical Society  
Date: Jan 1, 2013  
*Copyright © 2013, American Chemical Society*

**PERMISSION/LICENSE IS GRANTED FOR YOUR ORDER AT NO CHARGE**

This type of permission/license, instead of the standard Terms and Conditions, is sent to you because no fee is being charged for your order. Please note the following:

- Permission is granted for your request in both print and electronic formats, and translations.
- If figures and/or tables were requested, they may be adapted or used in part.
- Please print this page for your records and send a copy of it to your publisher/graduate school.
- Appropriate credit for the requested material should be given as follows: "Reprinted (adapted) with permission from (COMPLETE REFERENCE CITATION). Copyright (YEAR) American Chemical Society." Insert appropriate information in place of the capitalized words.
- One-time permission is granted only for the use specified in your RightsLink request. No additional uses are granted (such as derivative works or other editions). For any uses, please submit a new request.

If credit is given to another source for the material you requested from RightsLink, permission must be obtained from that source.

BACK CLOSE WINDOW

# APPENDIX II: PERMISSION FROM ACS

## PUBLICATION FOR FIGURE 1.2

Figure 1.2 extracted from published article:

The Promise of Calcium Batteries: Open Perspectives and Fair Comparisons

ACS ACS Publications C&EN CAS Find my institution Log In

ACS Publications Most Trusted. Most Cited. Most Read. Search text, DOI, authors, etc. My Activity Publications

RETURN TO ISSUE < PREV VIEWPOINT NEXT >

### The Promise of Calcium Batteries: Open Perspectives and Fair Comparisons

Ian D. Hosein\*

Cite this: *ACS Energy Lett.* 2021, 6, 4, 1560–1565  
Publication Date: March 29, 2021  
<https://doi.org/10.1021/acsenerylett.1c00593>  
Copyright © 2021 American Chemical Society  
RIGHTS & PERMISSIONS

Article Views 8714 Altmetric 13 Citations 22  
LEARN ABOUT THESE METRICS

Share Add to Export

PDF (2 MB) Supporting Info (1) » SUBJECTS: Batteries, Calcium, v

ACS Energy Letters

American Chemical Society Publications' copyrights policy is available at:

[https://pubs.acs.org/page/copyright/journals/posting\\_policies.html](https://pubs.acs.org/page/copyright/journals/posting_policies.html)

ACS ACS Publications C&EN CAS Find my institution Log In

ACS Publications Most Trusted. Most Cited. Most Read. Search text, DOI, authors, etc. My Activity Publications

**2. Reuse of Figures, Tables, Artwork, and Text Extracts in Future Works:** Authors may reuse figures, tables, artwork, illustrations, text extracts of up to 400 words, and data from the Author's Submitted, Accepted, or Published Work in which the ACS holds copyright or an exclusive license for teaching or training purposes, in presentations at conferences and seminars, in subsequent scholarly publications of which they are an Author, and for posting on the Author's personal website, university networks, or primary employer's institutional websites, and conference websites that feature presentations by the Author(s) provided the following conditions are met:

- o Appropriate citation to the Published Work is given
- o Modifications to the presentation of previously published data in figures and tables are noted and distinguished from any new data not contained in the Published Work, and
- o Reuse is not to illustrate news stories unrelated to the Published Work
- o Web posting by the Author(s) is for non-commercial purposes (see the definition of Commercial Use below).

To reuse figures, tables, artwork, illustrations, and text from ACS Published Works in general, ACS requests that interested parties use the Copyright Clearance Center Rightslink service. For information see [Instructions for RightsLink](#)

General ACS permission information can be found at [Permissions/RightsLink](#).

# APPENDIX III: PERMISSION FROM ACS CHEMISTRY OF MATERIALS FOR PUBLISHED ARTICLE

## Published Article:

Exploring Calcium Manganese Oxide as a Promising Cathode Material for Calcium-Ion Batteries

<https://pubs.acs.org/doi/10.1021/acs.chemmater.3c00659>

The screenshot shows the ACS Publications interface. At the top left is the ACS Publications logo with the tagline "Most Trusted. Most Cited. Most Read." and a search bar. Navigation links include "My Activity" and "Publications". The article title is "Exploring Calcium Manganese Oxide as a Promising Cathode Material for Calcium-Ion Batteries" by Paul Alexis Chando, Sihe Chen, Jacob Matthew Shellhamer, Elizabeth Wall, Xinlu Wang, Robson Schuarca, Manuel Smeu, and Ian Dean Hosein\*. It includes citation information, publication date (October 6, 2023), DOI, and copyright notice. Metrics for Article Views, Altmetric, and Citations are shown as zero. There are buttons for "Share", "Add to", and "Export". A "PDF (5 MB)" button and "Supporting Info (1)" link are at the bottom. A "Chemistry of Materials" journal cover is visible on the right.

## NOTICE:

Further permissions related to the material excerpted should be directed to ACS

American Chemical Society Publications' copyrights policy is available at:

[https://pubs.acs.org/page/copyright/journals/posting\\_policies.html](https://pubs.acs.org/page/copyright/journals/posting_policies.html)

#### Section I: Scholarly posting & sharing policies

1. **Reuse/Republishing of the Entire Work in Theses or Collections:** Authors may reuse all or part of the Submitted, Accepted or Published Work (**see definitions below**) in a thesis or dissertation that the Author writes and is required to submit to satisfy the criteria of degree-granting institutions. Appropriate citation of the Published Work must be made. If the thesis or dissertation to be published is in electronic format, a direct link to the Published Work must also be included using the [ACS Articles on Request author-directed link](#).

Authors also may reuse the Submitted, Accepted, or Published work in printed collections that consist solely of the Author's own writings; if such collections are to be posted online or published in an electronic format, please contact ACS at [copyright@acs.org](mailto:copyright@acs.org) to inquire about terms for licensed electronic use.

2. **Reuse of Figures, Tables, Artwork, and Text Extracts in Future Works:** Authors may reuse figures, tables, artwork, illustrations, text extracts of up to 400 words, and data from the Author's Submitted, Accepted, or Published Work in which the ACS holds copyright **or an exclusive license** for teaching or training purposes, in presentations at conferences and seminars, in subsequent scholarly publications of which they are an Author, and for posting on the Author's personal website, university networks, or primary employer's institutional websites, and conference websites that feature presentations by the Author(s) provided the following conditions are met:

- Appropriate citation to the Published Work is given
- Modifications to the presentation of previously published data in figures and tables are noted and distinguished from any new data not contained in the Published Work, and
- Reuse is not to illustrate news stories unrelated to the Published Work
- Web posting by the Author(s) is for non-commercial purposes (**see the definition of Commercial Use below**).

To reuse figures, tables, artwork, illustrations, and text from ACS Published Works in general, ACS requests that interested parties use the Copyright Clearance Center Rightslink service. For information see [Instructions for RightsLink](#)

General ACS permission information can be found at [Permissions/RightsLink](#).

# APPENDIX IV: PERMISSION FROM ACS APPLIED ENERGY MATERIALS FOR PUBLISHED ARTICLE

## Published Article:

Plating and Stripping Calcium Metal in Potassium Hexafluorophosphate Electrolyte toward a Stable Hybrid Solid Electrolyte Interphase

<https://pubs.acs.org/doi/10.1021/acsaem.3c00098>

The screenshot shows the article page on the ACS Publications website. At the top, there is the ACS Publications logo and a search bar. Below the logo, there are navigation links for 'My Activity' and 'Publications'. The article title is prominently displayed, followed by the authors' names: Paul Alexis Chando, Jacob Matthew Shellhamer, Elizabeth Wall, Wenlin He, and Ian Dean Hosein\*. The article is marked as 'Open Access'. Metrics for Article Views (834), Altmetric (3), and Citations (-) are shown. There are also links for 'Share', 'Add to', and 'Export'. A 'Supporting Info (1)' link is visible. The subjects listed are Calcium, Electrodes, and Electrolytes. A thumbnail of the journal cover is shown on the right side.

ACS Publications  
Most Trusted. Most Cited. Most Read.

Search text, DOI, authors, etc.

My Activity Publications

RETURN TO ISSUE < PREV ARTICLE NEXT >

### Plating and Stripping Calcium Metal in Potassium Hexafluorophosphate Electrolyte toward a Stable Hybrid Solid Electrolyte Interphase

Paul Alexis Chando, Jacob Matthew Shellhamer, Elizabeth Wall, Wenlin He, and Ian Dean Hosein\*

Cite this: *ACS Appl. Energy Mater.* 2023, 6, 7, 3924–3932  
Publication Date: March 30, 2023  
<https://doi.org/10.1021/acsaem.3c00098>  
Copyright © 2022 The Authors. Published by American Chemical Society. This publication is licensed under [CC-BY 4.0](#).  
[Open Access](#)

Article Views: 834 Altmetric: 3 Citations: -  
[LEARN ABOUT THESE METRICS](#)

Share Add to Export  
RIS

Supporting Info (1) »

SUBJECTS: Calcium, Electrodes, Electrolytes, ▾

ACS Applied Energy Materials

## NOTICE:

Further permissions related to the material excerpted should be directed to ACS

American Chemical Society Publications' copyrights policy is available at:

[https://pubs.acs.org/page/copyright/journals/posting\\_policies.html](https://pubs.acs.org/page/copyright/journals/posting_policies.html)

#### Section I: Scholarly posting & sharing policies

1. **Reuse/Republishing of the Entire Work in Theses or Collections:** Authors may reuse all or part of the Submitted, Accepted or Published Work (**see definitions below**) in a thesis or dissertation that the Author writes and is required to submit to satisfy the criteria of degree-granting institutions. Appropriate citation of the Published Work must be made. If the thesis or dissertation to be published is in electronic format, a direct link to the Published Work must also be included using the [ACS Articles on Request author-directed link](#).

Authors also may reuse the Submitted, Accepted, or Published work in printed collections that consist solely of the Author's own writings; if such collections are to be posted online or published in an electronic format, please contact ACS at [copyright@acs.org](mailto:copyright@acs.org) to inquire about terms for licensed electronic use.

2. **Reuse of Figures, Tables, Artwork, and Text Extracts in Future Works:** Authors may reuse figures, tables, artwork, illustrations, text extracts of up to 400 words, and data from the Author's Submitted, Accepted, or Published Work in which the ACS holds copyright **or an exclusive license** for teaching or training purposes, in presentations at conferences and seminars, in subsequent scholarly publications of which they are an Author, and for posting on the Author's personal website, university networks, or primary employer's institutional websites, and conference websites that feature presentations by the Author(s) provided the following conditions are met:

- Appropriate citation to the Published Work is given
- Modifications to the presentation of previously published data in figures and tables are noted and distinguished from any new data not contained in the Published Work, and
- Reuse is not to illustrate news stories unrelated to the Published Work
- Web posting by the Author(s) is for non-commercial purposes (**see the definition of Commercial Use below**).

To reuse figures, tables, artwork, illustrations, and text from ACS Published Works in general, ACS requests that interested parties use the Copyright Clearance Center Rightslink service. For information see [Instructions for RightsLink](#)

General ACS permission information can be found at [Permissions/RightsLink](#).

# **CURRICULUM VITAE**

---

PAUL ALEXIS CHANDO

031 Link Hall, Syracuse University, NY 13244

Phone: 347.291.7522 Email: [pachando@syr.edu](mailto:pachando@syr.edu)

---

**SUMMARY**

---

Highly motivated chemical engineer with industry and research experience in electrochemistry. I bring a strong background in materials characterization, quality control, and evaluation of battery components and capacitors. Ability to work on multidisciplinary teams for cutting-edge projects at City College of New York and Syracuse University, and adaptable in high-paced environments where responsibilities are constantly evolving. Built and led a new test engineering department from the ground up, which assessed performance of new 3D printers during development cycles and actively engaged in cost-down initiatives of existing products. Effective problem-solving skills to design and execute unique solutions to engineering problems from work experience at MakerBot Industries. Driven to pursue opportunities in energy-based research and actively seeking to develop expertise in battery materials.

**PROFESSIONAL EXPERIENCE**

---

**Syracuse University – Syracuse, NY**

**08/2017 – Present**

**Department of Biomedical and Chemical Engineering**

Graduate Research Assistant

- Synthesized and processed active materials to be used as cathodes in calcium-ion batteries
- Explored electrochemical activity of several calcium-ion battery cathodes in coin cell and beaker cell configurations, performed long-term stability testing, and discovered structural changes in cathodes from galvanostatic cycling

- Designed X-Ray Diffraction test equipment for tracking in situ structural changes of cathodes in calcium-ion batteries
- Created custom fixtures for electrochemical research
- Demonstrated successful plating and stripping with calcium metal electrodes in novel electrolyte formulations and studied the formation of resulting hybrid Solid-Electrolyte Interface (SEI)
- Mentored 5 undergraduate students and 2 masters students in supervised research, spearheaded innovative and suitable research projects, provided guidance and presentation opportunities, taught analytical techniques and good research practices
- Trained graduate and undergraduate students on various health and safety issues with laboratory operations and research
- Managed inventory of various lab supplies for continued operation of lab research
- Established Standard Operating Procedures (SOPs) for executing electrochemical measurements and maintaining equipment
- Redesigned desktop 3D printers for shape memory polymer and bioprinting applications
- Evaluated printability of bioinks using rheological and optical techniques

**RAB Lighting – New York, NY**

**04/2017 – 07/2017**

**Test Engineering Department**

Quality Assurance Engineer

- Executed automated and manual testing of firmware, backend, and frontend
- Coordinated with management and developers on delivering bugfixes and features

**MakerBot Industries – Brooklyn, NY**

**04/2013 – 02/2017**

**Test Engineering Department**

## Quality Test Engineer

- Collaborated with R&D, mechanical, software, product, and sustaining teams to define test objectives for MakerBot products throughout the product development cycle
- Led environmental testing on MakerBot 5<sup>th</sup> Generation products
- Launched failure reports and corrective actions for engineering departments (FRACAS)
- Organized Django database used by the Test Engineering department
- Developed methods to test components, subsystems, and integrated systems by programming test scripts and designing CAD models for test fixtures
- Created performance standards and specifications that would serve as benchmarks for continuous improvement and drive future design
- Documented test reports and procedures that thoroughly detailed test setup, data analysis and results

**The City College of New York – New York, NY**

**08/2010 – 01/2013**

## **Department of Chemical Engineering**

### Graduate Research Assistant

- Engineered novel printing methods for ceramic-polymer capacitors
- Showcased manufacturing scalability of capacitors
- Identified common causes for failure in printed ceramic capacitors
- Investigated nanoparticle aggregates in dielectric film using Atomic Force and Scanning Electron Microscopy
- Examined average nanoparticle size in dielectric using zeta potential analysis
- Analyzed and improved leakage current of printed dielectric

**Rensselaer Polytechnic Institute – Troy, NY**

**05/2006 – 05/2009**

## Department of Physics

Undergraduate Research Assistant

- Quantified average nanoparticle size using surface plasmon resonance
- Implemented several techniques for forming and arranging silver nanoparticles
- Expanded ordering efficiency of silver nanoparticles onto two-dimensional superlattices
- Increased silver nanoparticles phase transfer efficiency to 50%

**University of Illinois at Chicago – Chicago, IL**

**08/2010 – 01/2013**

## Department of Mechanical Engineering

Summer Research Assistant

- Synthesized nanochannels and studied flow through the nanochannels
- Devised theoretical model for two-phase flow in nanochannels

## EDUCATION

---

**Syracuse University – Syracuse, NY**

**2017 – Present**

Doctor of Philosophy – Chemical Engineering – May 2023 (Expected)

GPA – 4.00

*Thesis: Exploring the Electrochemical Performance of Calcium-Ion Batteries with Novel Cathodes and Electrolytes (Thesis advisor: Ian Hosein)*

**The City College of New York – New York, NY**

**2010 – 2013**

Master of Science – Chemical Engineering – January 2013

GPA – 3.14

*Project: Study of Voltage Ramps and Humidity on the Performance of Ceramic Capacitors (Project advisor: Daniel Steingart)*

Bachelor of Science – Chemical Engineering – May 2009

GPA – 3.24

## PATENTS

---

Van Tassel B., Steingart D., Leland E., **Chando P.**, Huang L., O'Brien S. "Prevention of hydrophobic dewetting through nanoparticle surface treatment," U.S. Patent Application 15/624, 152, December 7, 2017

## Selected Peer-Reviewed Publications

- 
1. **Chando, P. A.**; Chen, S.; Shellhamer, J. M.; Wall, E.; Wang, X.; Schuarca, R.; Smeu, M.; Hosein, I. D. "Exploring Calcium Manganese Oxide as a Promising Cathode Material for Calcium-Ion Batteries," *Chem. Mater.* **2023**. <https://doi.org/10.1021/acs.chemmater.3c00659>.
  2. Shellhamer, J. M.; **Chando, P. A.**; Pathreker, S.; Wang, X.; Hosein, I. D. "Unveiling the Potential of Ag<sub>2</sub>S Reference Electrode: Empowering Calcium Electrochemical Reactions," *J. Phys. Chem. C* **2023**. <https://doi.org/10.1021/acs.jpcc.3c04580>.
  3. **Chando, P. A.**; Shellhamer, J. M.; Wall, E.; He, W.; Hosein, I. D. "Plating and Stripping Calcium Metal in Potassium Hexafluorophosphate Electrolyte toward a Stable Hybrid Solid Electrolyte Interphase," *ACS Appl. Energy Mater.* **2023**, 6 (7), 3924–3932.
  4. Genier F., Pathreker S., Adebo P., **Chando P.**, Hosein I.D. "Design of a Boron-Containing PTHF-Based Solid Polymer Electrolyte for Sodium-Ion Conduction with High Na<sup>+</sup> Mobility and Salt Dissociation," *ACS Applied Polymer Materials*, 4 (10), 7645-7663 (2022)

5. Pathreker S., **Chando P.**, Chen F.H., Biria S., Li H., Hosein I.D. “Superhydrophobic Surfaces Developed via Photopolymerization,” *ACS Applied Polymer Materials*, 3 (9), 4661-4672 (2021) [*Cover Article*]
6. Pathreker S., Reed S., **Chando P.**, Hosein I.D. “A study of calcium ion intercalation in perovskite calcium manganese oxide,” *J. Electroanal. Chem.* 874, 114453 (2020)
7. Freeman S., Ramos R., **Chando P.**, Zhou L., Reeser K., Jin S., Soman P., Ye, K. “A bioink blend for rotary 3D bioprinting tissue engineered small-diameter vascular constructs,” *Acta Biomater.* 95, 152–164 (2019)
8. Van Tassell B., Yang S., Le C., Huang L., Liu S., **Chando P.**, Byro A., Liu X., Gerber D.L., Leland E.S., Sanders S., Kinget P.R., Kymissis I., Steingart D., O’Brien S. “Metacapacitors: Printed Thin Film, Flexible Capacitors for Power Conversion Applications,” *IEEE Transactions on Power Electronics*, 31 (4), 2695-2708 (2015)
9. Leland E. S., Van Tassell B., **Chando P.**, Yang S., Tull B., Liu S., Huang L., Kymissis I., Steingart D., O’Brien S. “Metacapacitors: Printed Multilayer Capacitors for High-Frequency On-Chip Power Conversion,” *PowerMEMS 2012* (2012)
10. Martin M.N., Basham J.I., **Chando P.**, Eah S.K. “Charged gold nanoparticles in non-polar solvents: 10-min synthesis and 2D self-assembly,” *Langmuir*, 26 (10), 7410-7417 (2010)
11. Sinha Ray S., **Chando P.**, Yarin A. “Enhanced release of liquid from carbon nanotubes due to entrainment by an air layer,” *Nanotechnology*, UK: IOP Publishing Ltd., 20 (9) (2009)
12. **Chando P.**, Sinha Ray S., Yarin A. "Nanofluidic transport and formation of nano – emulsions," *Journal of Undergraduate Research*, Chicago: University of Illinois at Chicago, 2, 54-60 (2008)

## Selected Abstracts and Conference

---

1. **Chando P.**, Shellhamer J., Hosein I.D. “Plating and Stripping Calcium Metals in Potassium Hexafluorophosphate Electrolytes Towards a Stable Hybrid Solid Electrolyte Interphase,” Oral Presentation, *Materials Research Society*, Boston, MA (2022)
2. **Chando P.**, Shellhamer J., Wall E., Hosein I.D. “Investigation of Transition Metal Oxide Post-Spinels for Calcium-Ion Batteries,” Oral Presentation, *The Electrochemical Society*, Atlanta, GA (2022)
3. **Chando P.**, Shellhamer J., Wall E., Hosein I.D. “Investigation of Transition Metal Oxide Post-Spinels for Calcium-Ion Batteries,” Poster Presentation, *Engineering and Computer Science Research Day*, Syracuse, NY (2022)
4. Wall E., **Chando P.**, Hosein I.D., “Synthesis of Post-Spinel Compounds for Calcium Ion Battery Cathodes,” *AIChE 2021*, Boston, MA, (2021)
5. **Chando P.**, Filip A., Albrecht L., Soman P. “Modification of commercial 3D printers for multi-material printing,” Poster Presentation, *Stevenson Biomaterials Symposium*, Syracuse, NY (2019)
6. Pieri K., **Chando P.**, Soman P., Henderson J. H. “Programming via printing: Printing of ready-to-trigger, biocompatible, shape-memory polymers,” In *Society for Biomaterials Annual Meeting and Exposition 2019: The Pinnacle of Biomaterials Innovation and Excellence - Transactions of the 42nd Annual Meeting* (Transactions of the Annual Meeting of the Society for Biomaterials and the Annual International Biomaterials Symposium; Vol. 40). Society for Biomaterials. (2019)
7. Sinha Ray S., **Chando P.A.**, Yarin A.L. “Characteristics of Flow through Macroscopically Long Carbon Nanotubes”; *Materials Research Society*, San Francisco, CA (2009)

## TEACHING EXPERIENCE

---

**Syracuse University – Syracuse, NY**

**08/2017 – 05/2020**

### **Department of Biomedical and Chemical Engineering**

Teaching Assistant

- BEN 485/685: *Biomaterials and Medical Devices*. Graded assignments and exams in addition to giving guest lectures on special topics
- ECS 104: *Engineering Computational Tools*. Worked closely with the instructor to guide students through problem-based learning projects. Organized grade book for the course while also providing detailed feedback on assignments and giving occasional lectures
- ECS 326: *Engineering Materials, Properties and Processing*. Managed the grade book for the course and designed lesson plans as part of weekly recitation lectures

**The City College of New York – New York, NY**

**01/2012 – 05/2012**

### **Department of Chemical Engineering**

Teaching Assistant

- ChE 22900: *Chemical Engineering Thermodynamics I*. Updated grade book of course with graded assignments and exams. Held regular office hours to answer student questions regarding various topics in the course

## HONORS AND AWARDS

---

Graduate Dissertation Fellowship, Syracuse University	2022
Research Assistantship, Syracuse University	2020 – 2021
Chemical Engineering Honor Society	2008

## POSITIONS OF SERVICE

---

Rheometer Trainer	2017 – 2023
-------------------	-------------

Syracuse Biomaterials Institute – Syracuse, NY

## MENTORED STUDENTS

---

Jingxuan Zhang, <i>Anodes for Calcium-Ion Batteries</i>	2022 – Present
---	----------------

Gabriel Quintero, REU, <i>Investigation of Calcium – Carbon Dioxide Batteries</i>	Summer 2022
---	-------------

Ivan Sarbinov, <i>Hybrid SEI for Plating and Stripping Calcium Metal Batteries</i>	Spring 2022
--	-------------

Jacob Shellhamar, REU, <i>Hybrid Solid Electrolyte Interface for Calcium-Ion Batteries</i>	2021 – Present
--	----------------

Elizabeth Wall, REU, <i>Synthesis of Post-Spinel Compounds for Calcium-Ion Batteries</i>	2021 – 2022
--	-------------

Seth Reed, <i>Cathodes for Calcium-Ion Batteries</i>	2020 – 2021
--	-------------

Jakub A. Kochanowski, <i>Real-Time Cell Tracking</i>	Spring 2019
--	-------------

## PROFESSIONAL ACTIVITY

---

### Membership

Electrochemical Society	2022 – Present
-------------------------	----------------

American Chemical Society	2021 – Present
---------------------------	----------------

American Institute for Chemical Engineers	2016 – 2017
---	-------------

## LICENSES & CERTIFICATIONS

---

Solidworks Mechanical Design – Associate	2015
--	------

Dassault Systèmes

## TECHNICAL SKILLS

---

Battery: Coin-cell and 3-electrode electrochemical cell assembly, Electrode fabrication (current collector and freestanding)

Cell Culture: Basic Cell Culture Techniques with  $C_3H_{10}T_{1/2}$  Cells

Characterization: Atomic Force Microscopy (**AFM**), Differential Scanning Calorimetry (**DSC**), Dynamic Mechanical Analysis (**DMA**), Energy Dispersive Spectroscopy (**EDS**), Fourier Transform Infrared Spectroscopy (**FTIR**), Profilometry, Raman Spectroscopy, Rheometry, Rietveld Refinement, Scanning Electron Microscopy (**SEM**), Tensile Testing, Thermogravimetric Analysis (**TGA**), X-Ray Diffraction (**XRD**)

Electrochemistry: Galvanostatic Measurements, Impedance Spectroscopy, Voltammetry

Engineering: 3D Printing

Software: Arbin, Autodesk Inventor, Django, Docker, GitHub, Highscore Plus, Linux, Mac, MATLAB, Metrohm, Microsoft Office Suite, Minitab, Python, Solidworks, Solartron, TA Universal Analysis, VersaSTAT, Windows XP/7/10

Synthesis: Auto-combustion, Co-Precipitation, Solid-State

## LANGUAGES

---

**English:** Native **French:** Bilingual **Spanish:** Some

**Dual Citizenship:** France and United States